FEUP Universidade do Porto
Faculdade de Engenharia

OPERATIONAL MODAL ANALYSIS AND CONTINUOUS DYNAMIC MONITORING OF FOOTBRIDGES

Wei-Hua Hu

A dissertation presented to the Faculty of Engineering of the University of Porto
for the degree of Doctor in Civil Engineering.
Supervisors: Álvaro Cunha (Full Professor); Elsa Caetano (Associate Professor).

To my family

and my parents

RESUME

Modern footbridges are often slender structures prone to excessive vibrations induced by pedestrians, due to the trend for construction of longer spans, using new materials and satisfying modern aesthetic requirements. Adverse human induced effects may lead to serviceability problems in these structures, affecting the human comfort and the structural integrity and durability. It may be then very useful to monitor the long term dynamic structural behavior, observing and controlling the levels of vibration attained and evaluating the evolution of the structural health condition under operational excitations, taking profit from recent progress occurred in terms of continuous dynamic monitoring systems, automated Operational Modal Analysis and statistical damage detection techniques.

Continuous dynamic monitoring systems, with remote control and tele-transmission, collect vibration data and ambient variables from a structure over a long period of time, and they may be used either simply as alert systems, sending automatic messages whenever some predefined response threshold is exceeded, or as Structural Health Monitoring (SHM) systems. In this case, automated Operational Modal Analysis plays a major role in the automatic estimation of modal parameters allowing the tracking of the time evolution of the most relevant structural dynamic properties, stemming from environmental and operational factors or structural changes due to damage. Damage detection requires then the elimination of environmental and operational effects, which can be achieved using Principal Component Analysis and statistical treatment of corresponding residue errors, leading to a health index that is sensitive to damage.

In this context, this thesis describes the efforts exerted on the development of LabVIEW based software for Operational Modal Analysis, applied either to ambient vibration testing or to continuous dynamic monitoring, by summarizing the corresponding state-of-art output-only modal identification methods, the participation in the real implementation of continuous dynamic monitoring systems, the investigation on the Principal Component Analysis based damage identification procedure and presenting two illustrative applications concerning the continuous dynamic monitoring of two Portuguese lively footbridges. The first application concerns Pedro e Inês footbridge, in Coimbra, where a dynamic monitoring system was

installed at the end of construction with the main purpose of checking the efficiency of the tuned mass dampers implemented to control excessive lateral and vertical vibrations, whereas the second one is focused on the stress-ribbon footbridge of FEUP Campus, where a SHM system was installed to analyze and remove the influence of environmental and operational factors on the modal estimates, and check the feasibility of vibration based damage detection on a efficient and economical basis.

RESUMÉ

Les passerelles à piétons modernes sont souvent des structures minces susceptibles à vibrations excessives, dus à la tendance pour la construction de plus longues envergures, utilisant des nouveaux matériaux et conditions esthétiques inovatives. Les effets défavorables induits par les piétons peuvent mener aux problèmes d'utilité en ces structures, affectant le confort humain et l'intégrité et la longévité structurales. Il peut être alors très utile de surveiller le comportement structural dynamique à long terme, observant et contrôlant les niveaux des vibrations atteints et faisant la evaluation de l'évolution de l'état de santé structural sous des excitations opérationnelles, prenant le bénéfice du progrès récent produit en termes de systèmes de surveillance dynamiques continus, Analyse Modale Opérationnelle automatisée et techniques statistiques de détection de dommages.

Les systèmes de surveillance dynamiques continus, avec télécommande et télé-transmission, rassemblent des données de vibration et des variables ambiantes d'une structure sur une longue période, et ils peuvent être employés simplement en tant que systèmes d'alerte, envoyant les messages automatiques toutes les fois qu'un certain seuil de réponse prédéfini est dépassé, ou en tant que systèmes structuraux de la surveillance de la santé (SHM). Dans ce cas-ci, l'analyse modale opérationnelle automatisée joue un rôle important dans l'évaluation automatique des paramètres modaux permettant le cheminement de l'évolution de temps des propriétés dynamiques structurales les plus appropriées, provenant des facteurs environnementaux et opérationnels ou des changements structurels. La détection de dommages exige alors l'élimination des effets de l'environnement et opérationnels, qui peuvent être réalisée utilisant l'Analyse de Composant Principal et le traitement statistique des erreurs correspondantes de résidu, menant à un index de santé qui est sensible aux dommages.

Dans ce contexte, cette thèse décrit les efforts exercés sur le développement du logiciel basé par LabVIEW pour l'Analyse Modale Opérationnelle, appliqué à l'essai ambiant de vibration ou à la surveillance dynamique continue, en récapitulant les méthodes d'état-de-art d'identification modale correspondantes, la participation dans la vraie exécution des systèmes de surveillance dynamiques continus, la recherche sur le procédé et la présentation d'identification de dommages basé par Analyse de Composant Principal de deux applications

d'illustration au sujet de la surveillance dynamique continue de deux passerelles à piétons au Portugal. La première application concerne la passerelle de Pedro e Inês, à Coimbra, où un système de surveillance dynamique a été installé à la fin de la construction avec le but principal de vérifier l'efficacité des amortisseurs de masse accordés mise en application pour commander des vibrations latérales et verticales excessives, tandis que le second est concentré sur la passerelle du campus de FEUP, où un système de SHM a été installé pour analyser et enlever l'influence des facteurs environnementaux et opérationnels sur les évaluations modales, et vérifier la praticabilité de la détection de dommages basée en mesures dynamiques, sur une base efficace et économique.

RESUMO

Devido à tendência para a construção de vãos maiores, utilizando novos materiais e às actuais exigências de ordem estética, as pontes pedonais modernas são estruturas frequentemente esbeltas e susceptíveis de apresentarem vibrações excessivas induzidas por peões. Os efeitos adversos induzidos pelos peões podem levar a problemas de utilização dessas estruturas, afectando o conforto dos utilizadores, a integridade estrutural e a durabilidade. Pode ser por isso muito útil monitorizar o comportamento dinâmico estrutural de longo prazo, observando e controlando os níveis de vibração atingidos e avaliando a evolução da performance estrutural sob excitações operacionais, tirando partido do progresso recente em termos de sistemas de monitorização contínua dinâmica, da Análise Modal Operacional automatizada e de técnicas estatísticas para detecção de danos.

Os sistemas de monitorização contínua dinâmica, com controle e transmissão de dados remotas, permitem a recolha de dados de vibração e das variáveis ambientais de uma estrutura por um longo período de tempo, podendo ser usados tanto como simples sistemas de alerta, enviando mensagens automáticas sempre que algum valor limite da resposta pré-definido é ultrapassado, como para avaliar a condição estrutural (SHM). Neste último caso, a automatização da Análise Modal Operacional desempenha um papel importante, pois permite o cálculo automático de parâmetros modais, possibilitando o acompanhamento da evolução temporal das propriedades dinâmicas estruturais mais importantes, motivada por factores ambientais e operacionais ou por mudanças estruturais causadas por danos. Em seguida, a detecção de danos exige a eliminação dos efeitos ambientais e operacionais, o que pode ser conseguido usando a Análise de Componentes Principais e o tratamento estatístico dos resíduos correspondentes, possibilitando o cálculo de um índice de saúde estrutural sensível a danos.

Neste contexto, esta tese descreve os esforços desenvolvidos para a criação de um software, baseado em LabVIEW, para Análise Modal Operacional, aplicado no processamento de dados de ensaios de vibração ambiental e provenientes de sistemas de monitorização dinâmica contínua, apresentando o estado-da-arte dos métodos de identificação modal baseados apenas na resposta estrutural, participando na implementação de sistemas de monitorização contínua

dinâmica, investigando a utilidade da Análise de Componentes Principais na identificação de danos e apresentando duas aplicações que ilustram o acompanhamento contínuo de duas pontes pedonais Portuguesas bastante flexíveis. A primeira aplicação trata-se da ponte Pedro e Inês, em Coimbra, onde um sistema de monitorização dinâmica foi instalado no final de construção com o objectivo principal de verificar a eficiência dos sistemas de massas sintonizadas implementados para controlar vibrações laterais e verticais. A segunda aplicação é uma ponte stress-ribbon no Campus da FEUP, onde um sistema de monitorização da condição estrutural foi instalado para analisar e remover a influência de factores ambientais e operacionais sobre as estimativas modais, e para verificar a viabilidade de detecção de danos com base na medição de vibrações de uma forma eficiente e económica.c

ACKNOWLEDGMENTS

This dissertation would not have been possible without the contribution of many people who not only influenced my work, but also supported me in many ways in the last five years of living in Porto.

My first debt of gratitude must go to my advisor, Professor Álvaro Cunha, Head of the Laboratory of Vibrations and Structural Monitoring (ViBest) of FEUP, for supplying all the necessary resources to research, encouraging me to participate in international conferences, and providing fruitful discussions and a rigorous review of the dissertation.

I am grateful to Professor Elsa Caetano, co-supervisor of this thesis. Her trust, knowledge and helpful suggestions, as well as her important contributions on the simulation of damage scenarios of footbridges were especially appreciated.

Special thanks to Prof. Filipe Magalhães, who has kindly cooperated in ambient vibration testing of bridges, and provided me interesting information, discussion and assistance in theoretical developments.

Many thanks to Prof. Carlos Moutinho and Engº António Cardoso for helping me in the conduction of experiments, use of diverse experimental devices, as well as in the construction of monitoring systems.

A special acknowledgement must be also addressed to Professor Wei-Xin Ren and Professor Bao-Chun Chen, from Fuzhou University, China. It was their visit to ViBest / FEUP in 2005 that created the opportunity for me to pursue a doctoral degree at the University of Porto.

I also want to make a general acknowledgement to many other FEUP PhD students and friends that helped me in this research in many ways, and in particular to Joana Delgado, Américo Dimande, Leonel Ramos and Sandro Diord Rescinho.

At the institutional level, I would like to thank the financial support from *Fundação para a Ciencia e a Technologia* (FCT), through the four-year PhD fellowship SFRH/BD/29269/2006 and through the Projects POCTI/ECM/46475/2002 (Vibrations in Cable-Stayed Bridges) and PTDC/ECM/109862/2009 (Advanced Tools for Dynamic Structural Health Monitoring of Bridges and Special Structures, DYNAMO_DEMO).

Moreover, all the support from the construction company Soares da Costa, related with the implementation of the continuous dynamic monitoring system of Pedro e Inês footbridge, is also deeply acknowledged.

I would like to thank my parents in China for supporting me throughout the years and especially for their apprehensions when I was in Portugal. Although far away in distance, we always remained very close.

There are many challenges in life. Some, as this dissertation, you choose for yourself, others are mysteriously trust upon you. At last, but not least, I want to acknowledge to my wife, Shu-Xian Hong and our daughter Bo-Yuan Hu (a special gift from God) for their love, support, encouragement and understanding in dealing with all the challenges.

CONTENTS

1

INTRODUCTION

1.1 RESEARCH CONTEXT

1.1.1 Operational Modal Analysis

Operational Modal Analysis (OMA) consists in the identification of modal parameters of a structural system without measuring a controlled input excitation. Therefore, it is also known as Output-only Modal Analysis. The motivation to carry out OMA tests emerged initially from Civil Engineering, because it is difficult and expensive to artificially excite constructions such as buildings, bridges or dams in order to obtain induced vibration levels exceeding the structural response due to traffic or wind. However, OMA has been also widely used in other fields, like mechanical engineering or aerospace engineering. An extensive overview of applications of OMA with different scopes can be found in (Cunha et al, 2007; Hermans et al, 1999).

Generally, OMA methods can be classified in two types: One of them comprehends the operational modal analysis methods used to process data from ambient vibration tests. Another one involves the long-term automated operational modal analysis methods, used to process continuous dynamic monitoring signals.

In ambient vibration tests, the structural ambient response is captured by one or more reference sensors at fixed positions, together with a set of roving sensors placed at different measurement points along the structure in different setups. The collected structural response

is processed by two main groups of operational modal identification methods, consisting of non-parametric and parametric methods in both frequency and time domains. The purpose of the ambient vibration tests is the identification of structural dynamic properties in order to calibrate and update the finite element models, as well as build a baseline for structural continuous dynamic monitoring.

Long-term automated operational modal analysis techniques mainly comprise a structural continuous dynamic monitoring system and fully automated output-only modal identification tools. The continuous dynamic monitoring system includes a series of permanently installed sensors such as strain gauges, displacement transducers, accelerometers, temperature sensors, video cameras, etc, collecting structural responses and environmental variations in operational conditions over a long period of time. The continuous dynamic monitoring system not only provides vibration data for automated modal analysis, but also can be used to build a relatively simple alert system or to accurately characterise the structural performance, for instance evaluating experimentally fatigue damage. Automated modal identification procedures are responsible for processing the accumulated continuous monitoring vibration signals, excluding any user interaction, and tracking the variations of structural dynamic properties in order to reflect long term structural dynamic behaviour. In recent years, automated operational modal analysis has gathered raising attentions with the formulation of algorithms relying on control theory and conventional signal processing techniques. Fruitful development of theory and applications is reviewed in (Rainieri and Fabbrocino, 2009).

Combined with continuous dynamic monitoring technology, long term automated operational modal analysis, integrated with an appropriate damage detection strategy, can be implemented into a complete vibration-based structure health monitoring system with the specific purpose of determining the current state of the structural health condition.

The increasing interest in the investigation and application of OMA led to the emergence of several conferences developed in recent years specifically focused on OMA, as is the case of the International Operational Modal Analysis Conference (IOMAC).

1.1.2 Vibration-based Structural Health Monitoring

Structural Health Monitoring (SHM) requires the integration of sensing and possibly also actuation devices to allow the loading and damaging conditions of a structure to be recorded, analyzed, localized, and predicted in a way that nondestructive testing (NDT) becomes an integral part of the structure and a material (Boller et al, 2009). Damage identification is the key aspect in SHM. *Damage* means the occurrence of changes to the material and/or geometric connectivity, which adversely affect the performance of the system. Usually, four levels of damage identification are discriminated (Rytter, 1993).

Level 1-detection: Is the structure damaged or not?

Level 2-location: Where is the damaged area located?

Level 3-quantification: What is the extent of damage?

Level 4-prediction: What is the remaining service life of the structure?

Damage identification procedures, also named as damage prognosis, may generally be classified as either physical-based or data-based approaches, though typically a combination of them is usually employed (Figure 1.1, Farrar and Lieven, 2007). In physical-based approaches, the analytical model of the system is proposed. Parameters of such model associated with damage are updated so that the predicted system response may be correlated with experimental measurements in damage state. Finite Element updating methods are example of physical-based techniques (Friswell and Mottershead, 1995). On the contrary, data-based methods mainly rely on the comparison between current measurements and previous responses collected in healthy conditions, typically by means of feature extraction and statistical pattern recognition methods (Farrar and Worden, 2007). Physical-based techniques require more computational efforts than data-based assessments, while with data-based approaches is more difficult to identify the nature of the structural damage. Therefore, the combination of both approaches is useful to acquire confidence and efficiency in the evaluation of the system health state.

Vibration-based structural health monitoring is one of the SHM approaches widely used in Civil Engineering applications due to its ‘output only’ nature. The core issue of this

methodology is to detect the changes of the meaningful features extracted from the structural response, for example, the variations of natural frequencies. This problem is always complicated due to two aspects: the first one is the implementation of automated OMA approaches in order to extract useful dynamic properties from a large amount of vibration signals (Rainieri and Fabbrocino, 2009); the second one is that the ambient variations of the system caused by environmental and operational conditions should be separated from changes induced by system damage, because the former may mask early subtle structural modifications. An efficient methodology for removing the variability due to the environment in operational conditions is thus required for reliable damage identification on the basis of statistical analysis. (Sohn, 2007).

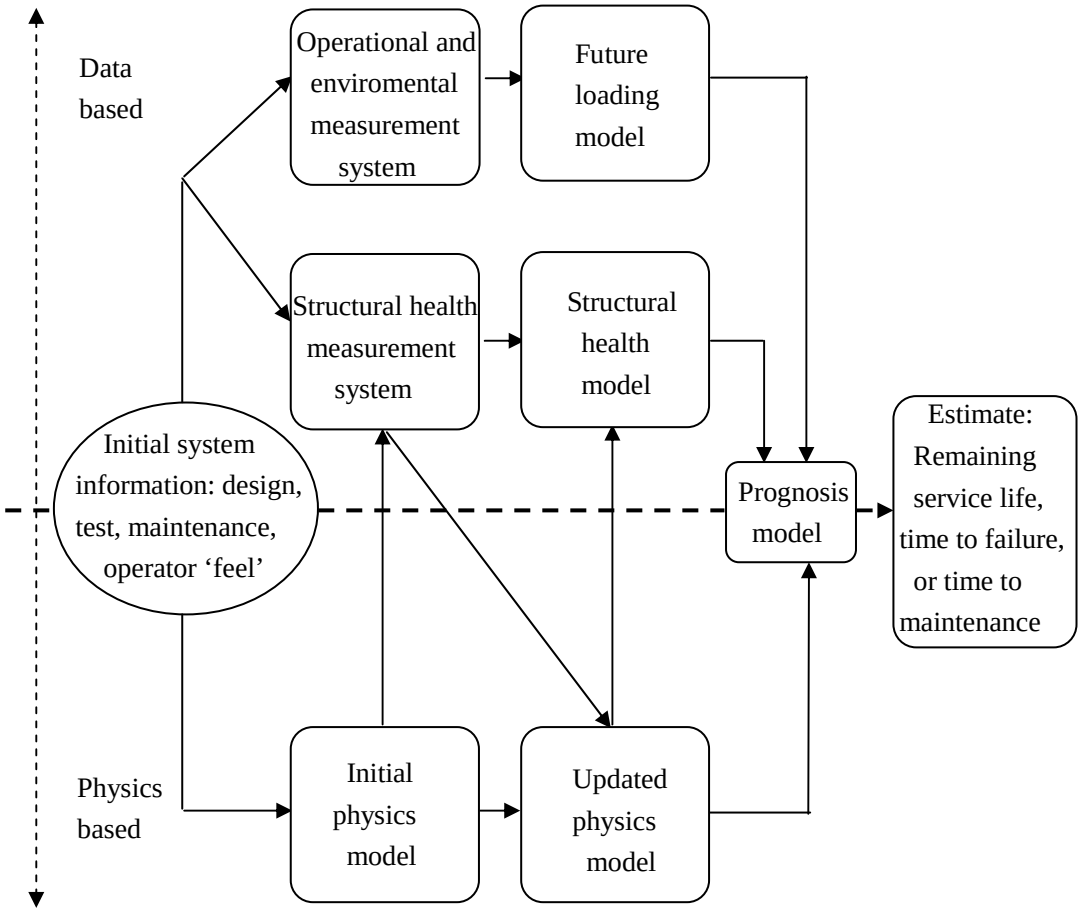

Figure 1.1 The general components of a damage prognosis process (Farrar and Lieven, 2007)

1.2 OBJECTIVES AND MAIN CONTRIBUTIONS

1.2.1 Motivations and objectives

The promising prospective of SHM inspired many researchers all over the world. Recent overviews, theory development and practical applications can be found in (Sohn et al, 2003; Worden and Farrar, 2007; Boller et al, 2009). Most of the applications of SHM are dedicated to large suspension, cable-stayed or highway bridges. Rather rare research is reported concerning the development of low-cost and compact vibration-based SHM for footbridges, with the intention of understanding the long term dynamic behaviour, investigating the environmental effects and attempting to detect early subtle structural changes in operational conditions.

Modern footbridge structures tend to be lively structures due to the increasing strength of new materials, longer spans and greater slenderness for aesthetic requirements. These construction trends lead to vibration serviceability problems, footbridges becoming more susceptible to excessive sway motions resulted from moving crowds. For example, the excessive lateral vibrations were clearly perceived by pedestrians in the opening day of the Millennium Bridge in London on 10th June 2000 (Dallard et al, 2001). This fact motivated the development of important investigations on footbridge vibrations, as clearly evidenced by the International Footbridge Conference, launched in 2002 in Paris, and subsequent editions in Venice (2005) and Porto (2008). A review on footbridges research can be found in (Živanović et al, 2005) and a recent a book on Footbridge Vibration Design was edited by (Caetano et al, 2009). Considerable footbridge research attentions are paid to different aspects, namely, vibration source, path and receivers. However, the long term dynamic behaviour of footbridges under operational conditions has not been extensively investigated and well understood yet. For example, the influence of walking people on footbridge vibration properties, such as natural frequencies and modal damping ratios. Besides, though excessive vibration induced by pedestrians is regarded as a serviceability problem, it also may lead to early structural changes in normal operational conditions.

The Laboratory of Vibrations and Structural Monitoring (ViBest) of the Faculty of Engineering of University of Porto (FEUP) has developed extensive research and consultancy projects on footbridges during the last ten years, focusing on the design and control of footbridge vibrations (SYNPEX, 2008; Caetano et al, 2010a,b), which is a field that may require the implementation of continuous dynamic monitoring systems to clarify the long term dynamic behaviour of footbridges in operational conditions.

In this context, the objectives of this thesis are concerned with such issues:

(i) Understanding and comparison of main OMA methods;

(ii) Implementation of these methods into a user-friendly toolkit for OMA and application of it to existing bridges, evidencing the change of dynamic properties caused by structural modifications and ambient factors;

(iii) Development of a toolkit for continuous dynamic monitoring, installation of continuous dynamic monitoring systems on bridges and their application to two slender footbridges in Portugal, the Pedro e Inês footbridge over Mondego river in Coimbra, equipped with passive control devices, and the stress-ribbon footbridge of FEUP campus;

(iv) Application of a damage detection procedure to the continuous dynamic monitoring data in order to remove the environmental effects and detect simulated structural damage.

1.2.2 Contributions of the Thesis

To achieve the above mentioned objectives, the thesis is dedicated to solve these problems and its contributions are the following:

(i) Nearly all frontier operational modal analysis techniques are reviewed synthetically. Generally, they are classified as frequency and time domain approaches, depending on the primary data type: frequency spectra of data using Fourier Transforms, or data in time domain. In order to better explain how the modal parameters can be estimated from measured signals, an ambient vibration test of a 3-story metallic frame is performed in laboratory, the corresponding experimental signals being processed by each method;

(ii) A user- friendly toolkit for operational modal analysis is developed by implementing different modal identification methods. Moreover, an additional toolkit for automated operational modal analysis is also implemented on the basis of appropriate interpretation of

stabilization diagrams excluding any user interaction, allowing to track the evolution of the modal parameters estimated from continuous monitoring data;

(iii) Different operational modal analysis approaches are applied to ambient vibration test data from a roadway bridge and two footbridges. In these applications, comparisons of the estimated modal parameters before and after structural modifications show that the identified natural frequencies of different orders may reflect those structural changes, which indicates the possibility of detecting damage based on the measurement of frequency shifts. However, significant effects of environmental factors on frequency estimates are also observed. Therefore, the continuous dynamic monitoring and the implementation of automated operational modal analysis tools are necessary to investigate and remove the influence of environmental factors;

(iv) Participate in the implementation and development of continuous dynamic monitoring systems for two footbridges. On the basis of long term monitoring data, the behaviour of footbridges in operational conditions are thoroughly investigated in both time and frequency domains: maximum vibration levels are monitored as a serviceability index; waterfall plots characterize the distributions of frequency components; averaged vibration levels are used to evaluate the pedestrian traffic intensity and ambient temperature is also observed. The relations between modal parameters estimated by automatic operational modal analysis and environmental factors are studied. Linear and nonlinear environmental effects revealed by analyzing continuous monitoring results suggest that such influences should be removed for confident damage identification;

(v) Linear Principal Component Analysis (PCA) is used to remove the environmental effects from damage events under operational conditions. Linear PCA not only naturally distinguishes the linear environmental effects on dynamic properties, but also efficiently removes the nonlinear influences on natural frequencies if highly linear relations are observed among them. The Novelty analysis on the residue errors provides a statistical indication for structural damage. The potential of this method is demonstrated by successful detection of different simulated damage scenarios.

1.3 ORGANIZATION OF THE THESIS

A chapter-by-chapter overview is presented in the following and inherent logic relations of them are manifested.

Chapter 1 introduces the investigation background and motivations, highlights the main work, as well as the organization of the thesis.

Chapter 2 begins with the classical dynamic vibration equations and Finite Element models, transforms the structural vibration to modal model defined in system identification. Different parametric and non-parametric system identification approaches in both frequency and time domains are presented. An ambient vibration test of a metallic laboratorial frame is performed and experimental data is used to illustrate the abstract system identification theory.

Chapter 3 describes the implementation of a user-friendly toolkit integrating different system identification methods for OMA. In addition, a toolkit based on an automated OMA algorithm is also developed and proposed for processing a large amount of continuous monitoring data.

Chapter 4 presents three cases of application of OMA using different system identification approaches. Comparisons of dynamic properties before and after structural changes suggest that the natural frequencies are sensitive enough to reflect such changes. However, environmental factors can also influence the dynamic properties. Therefore, continuous dynamic monitoring is required to investigate the long term structural behavior and the environmental influences.

Chapter 5 is focused on the investigation of the long term dynamic behaviour and of the environmental effects on the dynamic properties of footbridges under normal operational conditions, taking into account the maximum vibration levels, distributions of frequency components, and tracking of the variations of dynamic properties and environmental variables in order to clarify their relations.

Chapter 6 discusses the removal of the environmental influences and damage identification. It is observed that linear PCA not only eliminates the linear effects, but also discards the nonlinear influences if natural frequencies of different modes are linearly related.

The simulated progressive damage of the two footbridges analyzed is successfully detected on the basis of statistical analysis of the residual errors.

Chapter 7 ends the thesis with some conclusions and perspectives for further investigations relevant in the field of vibration-based SHM.

The organization of this thesis can be further illustrated in Figure 1.2.

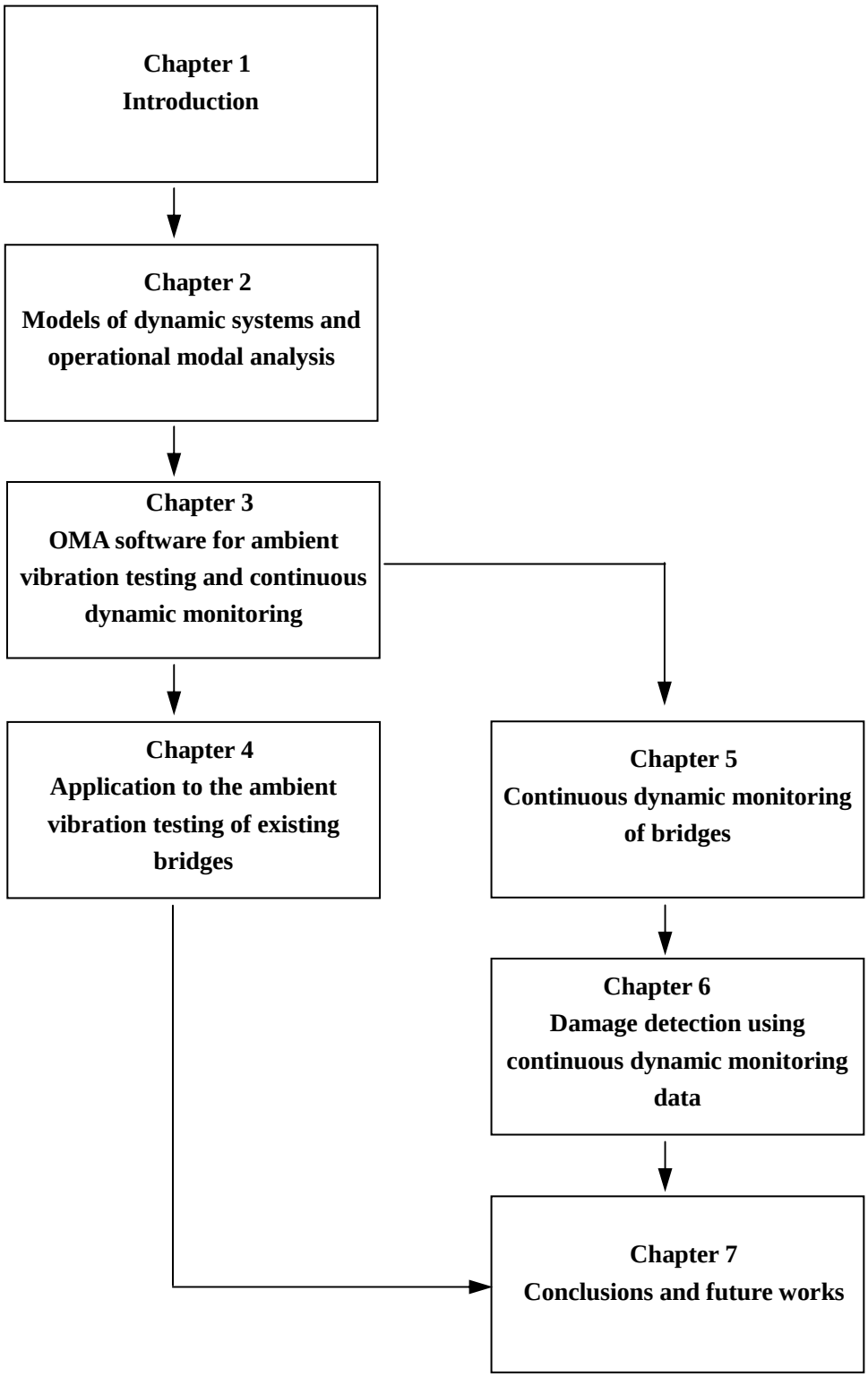

Figure 1.2 Organization of the thesis

2

MODELS OF DYNAMIC SYSTEMS AND OPERATIONAL MODAL ANALYSIS

2.1 INTRODUCTION

In past two decades, operational modal analysis (OMA), stemming from traditional experimental modal analysis (EMA) in mechanical engineering and time series analysis (TSA) in systems control engineering, has drawn great attention in the civil engineering community with applications in bridges, buildings, towers, etc (Cunha et al, 2006,2007).

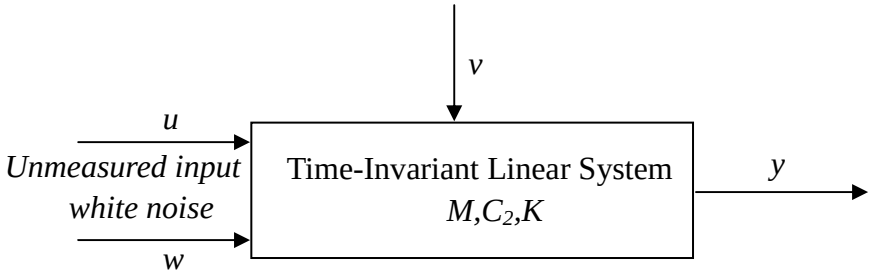

Figure 2.1 A system with output *y*; the input, comprising a determined input *u* and measured disturbance *w*, is assumed as white noise; *v* is an unmeasured disturbance

OMA is also called as output-only '*system identification*'. A *system* is an object in which different kinds of variables interact and produce observable signals, illustrated by Figure. 2.1. The observable signals (*y*) that are of interest to use are usually called *outputs*. The *system* is also affected by external stimuli. External signals that can be manipulated by the observer are defined as determined inputs (*u*). Others are called *disturbances* and can be divided into those that are directly measured (*w*) and those that are only observed through their influence on the

output (*v*). The distinctions between inputs (*u*) and measured or unmeasured disturbances (*w*, *v*) is often less important for the modelling process.

The notion of a *system* is a broad concept. In this thesis, a system is specified as a civil engineering structure. In OMA of civil engineering, the structures are naturally excited by ambient excitation forces e.g. wind, traffic, seismic activity, etc., which are difficult or even impossible to be measured. Elimination of this ambient excitation is often impossible and applying an artificial measurable force which exceeds the natural excitation is expensive and sometimes difficult. In these cases, only structural responses (*y*) are measured. The basic assumption of OMA is that the output response is a realization of a stochastic process and the unmeasured input is a white noise.

OMA directly evolved from traditional EMA, which can be regarded as a classical input-output approach, where the extraction of modal parameters is based on frequency response functions (FRFs), derived in frequency domain, or on the equivalent impulse response functions (IRFs), in time domain, using input-output measurements. Moving from one domain to the other is a matter of applying Fourier Transform. There are many technical publications on input-output modal identification (EMA) developed in last three decades. These methods are generally classified as frequency domain or time domain approaches. The frequency domain methods, based on the measurement of FRFs, comprise the simple 'peak-picking' (PP) or 'peak-amplitude' technique, the complex mode indicator function (CMIF) method (Shih et al, 1988) and the polyreference least squares complex frequency (P-LSCF) procedure (Guillaume et al, 2003). In parallel, the IRFs in time domain are normally calculated from the FRFs by an inverse Fourier transform, which leads to time domain methods comprehending the least-squares complex exponential (LSCE) method (Brown, 1979), the polyreference complex exponential (PRCE) method (Vold et al, 1982), the multiple reference Ibrahim time domain (MRITD) technique (Fukuzono, 1986) and the eigensystem realization algorithm (ERA) procedure (Juang and Pappa, 1985; Longman and Jung, 1989). In 1998, the unified matrix polynomial approach (UMPA) was proposed (Allemang et al, 1998). It demonstrates that most of the abovementioned techniques, both in the frequency and time domains, are particular cases of a more general polynomial formulation, and this helps to clarify the similarities among the various methods. More

comprehensive and detailed discussion of these methods can be found in (Heylen et al, 1995; Maia et al, 1997; Ewins, 2000).

In early 1990s, the Natural Excitation Technique (NexT) was proposed (James, 1992). It is a significant breakthrough for modal identification, because only output measurements in the case of natural excitation are used for modal parameters estimation. The underlying principle of the NExT technique is that correlation functions (COR) between the responses can be expressed as a sum of decaying sinusoids. Each decaying sinusoid has a damped natural frequency and damping ratio that is identical to the one of the corresponding structural mode. Therefore, CORs can be employed as IRFs to estimate modal parameters, which means that a modal identification procedure from traditional EMA can be further adopted for OMA. For example, in time domain, by replacing IRFs with CORs, ERA methods can be developed to NExT-ERA technique (Akaike, 1974; Benveniste and Funche, 1985; Aoki, 1987). This method is also named as Covariance driven Stochastic Subspace Identification (SSI-COV) method (Peeters, 2000). Similarly, in frequency domain, output spectra can be modeled in a similar way as FRFs under the assumption that the input is white noise. By replacing the FRFs matrix with the output spectral matrix, the traditional CMIF method and p-LSCF procedure evolved to frequency domain decomposition (FDD) method (Brincker et al, 2000,2001) and Polyreference Least Squares Complex Frequency techniques (PolyMAX®, Peeters, 2004,2005), respectively.

Apart from EMA in mechanical engineering, OMA in civil engineering also root in TSA in control engineering because TSA methods model dynamic systems directly from output measurements, such as the auto-regressive moving average (ARMA) time series model and stochastic state-space (SS) model. It is demonstrated that the ARMA model is equivalent to the stochastic state-space model (Akaike, 1974; Basseville, 1985), however, the identification technique of stochastic SS model is better than of ARMA model because no non-linear search is required and computational complexity is dramatically reduced. The most important techniques for identifying ARMA model is the prediction-error method (PEM) (Ljung, 1999). By minimizing the prediction errors, the modal parameters identification is a nonlinear optimization problem, which makes ARMA model identification rather difficult to apply, especially for large dimension structures. Despite this drawback, efforts have been still made

to apply PEM to identify modal parameters in civil engineering (Andersen, 1997). In the 1990´s, stochastic subspace identification (SSI) technique was developed in control engineering (Van Overschee, 1996). It starts by projecting the row space of the 'future' outputs into the row space of 'past' outputs, factorization of the projecting matrix leading to Kalman filter state sequence, which can be utilized to estimate system matrix by least square (LS) techniques. The identification procedure avoids non-linear iteration and is numerically reliable and effective. SSI has been adopted successfully for OMA in civil engineering (Peeters, 2000). Because of using the stochastic response data to identify modal parameters directly, it is also named Data driven Stochastic Subspace Identification (SSI-DATA).

A standard OMA procedure require the consideration of three basic entities: (1) a set of measured output responses, (2) candidate models and (3) methodologies for the identification of the candidate models using the output data. In OMA testing, the only available information about the dynamic behaviour of a structure are the output measurements. Different identification methods based on mathematical models in OMA are capable to provide accurate estimates of the modal parameters of the structure from output response. However, it is necessary to obtain some kind of comprehension of how all kinds of models, both in frequency domain and time domain, relate to the modal parameters, that is, how they relate to the lumped mass-spring parameter model in structural analysis and how modal parameters can be identified by these models.

The main purpose of this chapter is to provide such understanding. Therefore, this chapter starts with the description of the simple multi-degree-of freedom vibration model and the finite element model of vibration systems, subsequently, the analytical models are converted to frequency domain models and time domain state-space models. The corresponding modal parameters identification procedures are illustrated and clarified with application of these complex techniques to output measurements of a steel frame in laboratory. Finally, the performances of different OMA approaches are compared.

2.2 MULTI-DEGREE-OF-FREEDOM SYSTEMS

The dynamic behaviour of a mechanical system can be often idealized by discretizing in n_m masses connected by springs and dampers (DOFs), the corresponding motion being described by the following matrix differential equations:

$$M\ddot{q}(t) + C_2\dot{q}(t) + Kq(t) = f(t) = B_l u(t) \tag{2.1}$$

where $M, C_2, K \in \mathbb{R}^{n_m \times n_m}$ are the mass, damping and stiffness matrices; $q(t)$, $\dot{q}(t)$, $\ddot{q}(t) \in \mathbb{R}^{n_m}$ are displacement, velocity and acceleration vectors at continuous time *t*, respectively; $f(t) \in \mathbb{R}^{n_m}$ is the excitation force vector, which can be factorized into a matrix $B_l \in \mathbb{R}^{n_m \times m}$ specifying the locations of inputs and an input vector $u(t) \in \mathbb{R}^m$。In a practical modal experiment，output measurements are only a set of responses measured from well selected points, and not all n_m DOFs described in FE model.

It is assumed that measurements are acquired at *l* points. In general case, the response can be measured using accelerometers, velocity or displacement transducers. In that case the observation equation $y(t)$ is expressed as:

$$y(t) = C_a\ddot{q}(t) + C_v\dot{q}(t) + C_d q(t) \tag{2.2}$$

where $y(t) \in \mathbb{R}^l$ are the outputs and $C_a, C_v, C_d \in \mathbb{R}^{l \times n_m}$ are the selection matrices for the accelerations, velocities and displacements. These matrices contain only zeros and a few ones, indicating which output is measured as an acceleration, velocity or displacement. For example, if only accelerometers are used, $C_a = I$, $C_v = 0$ and $C_d = 0$.

In structural analysis, e.g., finite element (FE) analysis, the structure is discretized in a set of elements. The global mass matrix M and stiffness matrix *K* are obtained directly from the geometry and material properties. However, it is impossible to assemble the damping matrix C_d in the same way as *M* and *K* due to lack of reliable material constants representing the global damping behaviour of structure. Damping matrix C_d can be modelled as symmetry and ordinary form: proportional damping and general viscous damping.

Example

An example of a metallic frame is introduced to illustrate the theoretical concepts, described in this chapter. It is composed by 3 rigid iron masses connected to each other and to the base through aluminium columns by connection elements, which are clamped at nodes 1-6 and the base (Figure 2.2).

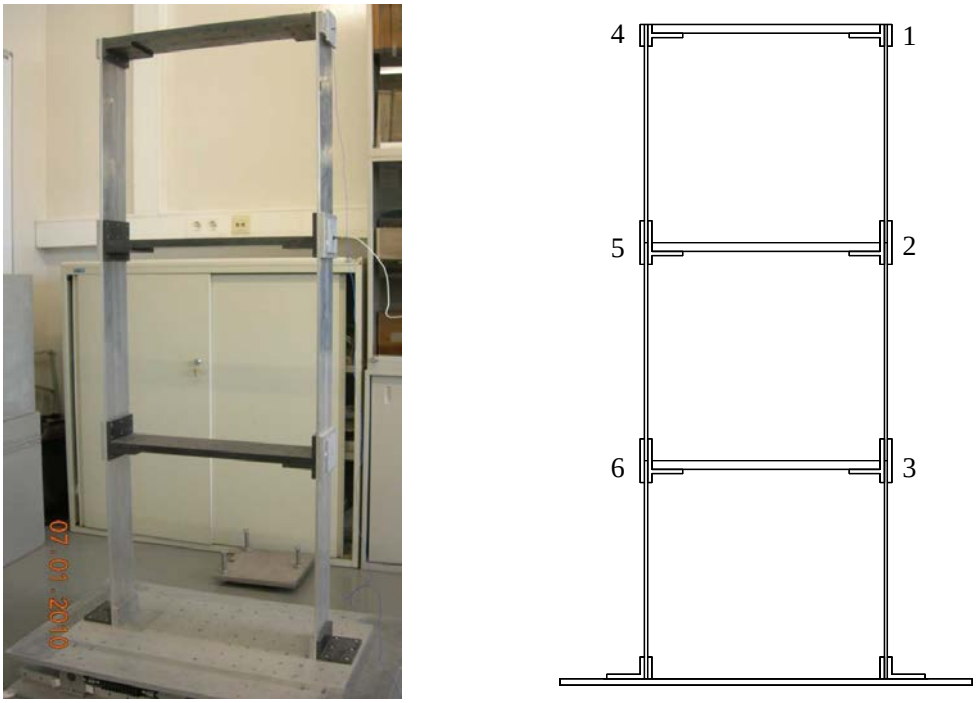

(a) Photo (b) Schematic lateral view

Figure 2.2 General view of the metallic frame

2.2.1 Undamped free vibration systems

Assuming the free vibration of an undamped system, equation (2.1) is transformed by ignoring the damping matrix C_d and the external excitation $f(t)$:

$$M\ddot{q}(t) + Kq(t) = 0 \tag{2.3}$$

Substituting the general solution $q(t) = \phi_i e^{\lambda_i t}$ in equation (2.3) leads to

$$K\phi_i = M\phi_i(-\lambda_i^2) \tag{2.4}$$

where $\phi_i \in \mathbb{R}^{n_m}$ $(i = 1,2,...,n_m)$ is an eigenvector and λ_i^2 is an eigenvalue. In an undamped vibration system, an eigenvalue is usually denoted as the square of an undamped natural

frequency ω, that is

$$\lambda_i = j\omega_i \tag{2.5}$$

Equation (2.4) can be expressed in the following complete solution:

$$K\Phi = M\Phi\Omega^2 \tag{2.6}$$

where $\Phi = \lfloor \phi_1, ..., \phi_{n_m} \rfloor \in \mathbb{R}^{n_m \times n_m}$ is the eigenvector matrix and $\Omega = \left[\backslash \omega_{i \backslash} \right] \in \mathbb{R}^{n_m \times n_m}$ is a diagonal eigenfrequency matrix. According to orthogonality properties

$$\Phi^T M\Phi = \left[\backslash m_{i \backslash} \right], \quad \Phi^T K\Phi = \left[\backslash k_{i \backslash} \right] \tag{2.7}$$

from which

$$\omega_i^2 = k_i / m_i$$

where m_i and k_i are the modal mass and modal stiffness, respectively. The superindex '*T* ' denotes transpose of a matrix.

It is important to realize that the eigenvalue matrix Ω is unique, because eigenfrequencies are fixed quantities, while the eigenvector matrix Φ is subject to indeterminate scaling factors, which affect the amplitude of the eigenvectors ϕ_i. There are many scaling and normalization processes of Φ, the most common is to modal identification being mass-normalization. The mass-normalized eigenvector matrix is written as $[\Phi]_{nor}$ and has the particular property

$$\Phi_{nor}^T M\Phi_{nor} = I_{n_m}, \quad \Phi_{nor}^T K\Phi^T = \Omega^2 \tag{2.8}$$

where I_{n_m} is an identity matrix of dimension of $n_m \times n_m$.

Matrices Φ and Ω describe the dynamic characteristics of the dynamic system. Hence, they constitute the *modal model*. Eigenvector ϕ_i is also called the *i*-th *mode shape* corresponding to the *i*-th undamped *natural frequency* ω_i. It is noted that in the undamped case the eigenvectors are real modal vectors.

Example

The metallic frame is idealized as a 3 degree of freedom undamped vibration model. In the current analysis, the density and modulus of elasticity of both aluminum and iron are evaluated as

$\rho_A = 2.7E10^3 kg/m^3, E_A = 65\text{Gpa}$ and $\rho_I = 7.7E10^3 kg/m^3, E_I = 210\text{Gpa}$, respectively. The total mass of each level, including the iron mass, the mass of each half part of support columns and the mass of connection elements, is calculated as $m_1 = m_2 = 15.67kg$ and $m_3 = 13.28kg$. The stiffness provided by aluminium column are 167.2kN/m, 167.2kN/m and 83.6kN/m. The mass and stiffness matrices have the following expression:

$$M = \begin{bmatrix} 15.67 & 0 & 0 \\ 0 & 15.67 & 0 \\ 0 & 0 & 13.28 \end{bmatrix} kg, \qquad K = \begin{bmatrix} 167.2 & -83.6 & 0 \\ -83.6 & 167.2 & -83.6 \\ 0 & -83.6 & 83.6 \end{bmatrix} kN/m$$

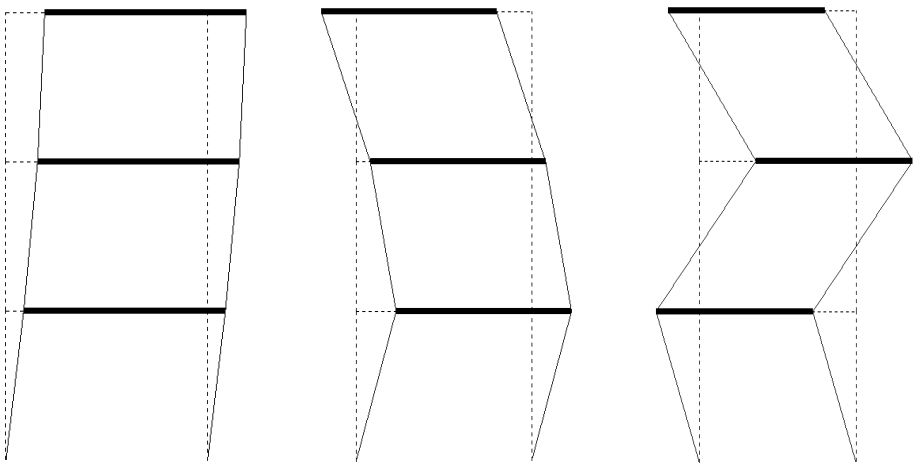

$f_1 = 5.40Hz$ $f_2 = 14.93Hz$ $f_3 = 21.16Hz$

F**igure 2.3** Natural frequencies and modal shapes

According to equation (2.6), the eigenfrequency matrix Ω and the eigenvector matrix Φ are evaluated. The modal results are shown in Figure 2.3.

2.2.2 Proportional damping systems

In a more general case of free vibration of a damped system, it is necessary to introduce some assumptions concerning the damping characters. Usually the damping is assumed as proportional, which means that the damping matrix C_2 is assumed as a linear combination of the mass and stiffness matrices, which is also called Rayleigh damping:

$$C_2 = aM + \beta K \tag{2.9}$$

where a, β are two scalar constants, then the equation of motion can be written in the form:

$$\Phi^T M\Phi\ddot{q}_p(t) + \Phi^T C_2\Phi\dot{q}_p(t) + \Phi^T K\Phi q_p(t) = 0 \tag{2.10}$$

where $q_p(t) = \Phi^{-1}q(t)$ is a coordinate transformation. Assuming damping is small, it is acceptable to neglect the off diagonal elements in C_2 and it can be diagonalized as:

$$\Phi^T C_2\Phi = \lfloor c_{i\backslash} \rfloor = \lfloor 2\xi_i\omega_i m_{i\backslash} \rfloor \tag{2.11}$$

where $\xi_i = c_i/2m_i\omega_i$ is the modal damping ratio.

The solution of equation (2.10) with proportional damping has a form similar to the one of an undamped model $q_p(t) = \phi_{pi}e^{\lambda_i t}$. Substituting this solution and equation (2.11) into equation (2.10) leads to a series of independent equations:

$$\lambda_i^2 + 2\xi_i\omega_i\lambda_i + \omega_i^2 = 0 \tag{2.12}$$

yielding the following solution:

$$\lambda_i, \lambda_i^* = -\xi_i\omega_i \pm j\sqrt{1-\xi_i^2}\,\omega_i \tag{2.13}$$

where superindex '*' denotes complex conjugate.

The particular advantage of using a proportional damping model in structural analysis is that the mode shapes are identical and the natural frequencies are similar to those of the simple undamped system. In fact, it is possible to derive the modal property of a proportional damping system by analyzing the undamped version and making a correction for the presence of the damping. However, it should be noted that it is only valid under the assumption that damping is distributed over the structure in the same way as the mass and the stiffness, which does not happen in real structures with local dampers, e.g. bridges with tuned mass damper (TMDs). In order to model the damping mechanisms more accurately, another approach is introduced in the next section, assuming general viscous damping.

2.2.3 General viscous damping systems

In case of a vibration model with general viscous damping, the damping matrix C_2 can not be diagonalized. In order to solve the eigenvalue problem, it is necessary to recast equation (2.1) into so-called *state-space* form, the second order equation being reformulated as a first order equation.

Define a *state vector* $x(t)$ of order $n=2n_m$, containing both the displacement vector $q(t)$ and the velocity vector $\dot{q}(t)$,

$$x(t) = \begin{bmatrix} q(t) \\ \dot{q}(t) \end{bmatrix} \tag{2.14}$$

Assuming the solution is $q(t) = \phi_{gi} e^{\lambda_i t}$,

$$x(t) = \begin{bmatrix} q(t) \\ \dot{q}(t) \end{bmatrix} = \begin{bmatrix} \phi_{gi} \\ \lambda_i \phi_{gi} \end{bmatrix} e^{\lambda_i t} = \varphi_i e^{\lambda_i t}, \quad \dot{x}(t) = \begin{bmatrix} \dot{q}(t) \\ \ddot{q}(t) \end{bmatrix} = \begin{bmatrix} \lambda_i \phi_{gi} \\ \lambda_i^2 \phi_{gi} \end{bmatrix} e^{\lambda_i t} = \lambda_i \varphi_i e^{\lambda_i t} \tag{2.15}$$

Equation (2.1) can be then rewritten in state-space form as:

$$P\dot{x}(t) + Qx(t) = F \tag{2.16}$$

where

$$P = \begin{bmatrix} C_2 & M \\ M & 0 \end{bmatrix}, \quad Q = \begin{bmatrix} K & 0 \\ 0 & -M \end{bmatrix}, x(t) = \begin{bmatrix} q(t) \\ \lambda_i q(t) \end{bmatrix}, F = \begin{pmatrix} B_l \\ 0 \end{pmatrix} u(t)$$

Substituting equation (2.15) in equation (2.16), this leads to a generalized eigenproblem when $f(t)=0$,

$$P\Lambda_{com}\Psi + Q\Psi = 0 \tag{2.17}$$

whose solution comprises a set of $n=2n_m$ eigenvalues, appearing in complex conjugate pairs.

Denoting the eigenvalues as $\Lambda \in \mathbb{C}^{n_m \times n_m}$ and the conjugate pairs as $\Lambda^* \in \mathbb{C}^{n_m \times n_m}$, the corresponding complex eigenvectors are

$$\varphi = \begin{bmatrix} \Phi \\ \Phi\Lambda \end{bmatrix}, \quad \varphi^* = \begin{bmatrix} \Phi^* \\ \Phi^*\Lambda^* \end{bmatrix} \tag{2.18}$$

Λ_{com} and Ψ have following structure:

$$\Lambda_{com} = \begin{bmatrix} \Lambda & 0 \\ 0 & \Lambda^* \end{bmatrix} = \begin{bmatrix} \lambda_i & 0 \\ 0 & \lambda_i^* \end{bmatrix}, \quad \Psi = [\varphi, \varphi^*] = \begin{bmatrix} \Phi & \Phi^* \\ \Phi\Lambda & \Phi^*\Lambda^* \end{bmatrix} \tag{2.19}$$

where Λ and $\Phi \in \mathbb{C}^{n_m \times n_m}$ are the eigenvalues and eigenvectors of the original second order system. Substituting Λ_{com} and Ψ into equation (2.17) and it becomes

$$M\Lambda^2\Phi + C_2\Lambda\Phi + K\Phi = 0 \tag{2.20}$$

It is noted that eigenvectors matrix Φ can not diagonalize the matrices *M*, C_2 and *K* as happen when proportional damping is assumed. However, complex eigenvalues of (2.20) λ_i are written as those analogous to proportional damping system:

$$\lambda_i, \lambda_i^* = -\xi_i \omega_i \pm j\sqrt{1-\xi_i^2}\,\omega_i \tag{2.21}$$

Pre and post-multiplying equation (2.16) by the eigenvector matrix Ψ, it is found that:

$$\Psi^T P \Psi \dot{q}_{mc}(t) + \Psi^T Q \Psi q_{mc}(t) = 0 \tag{2.22}$$

where $q_{mc}(t) = \Psi^{-1} x(t)$ is the modal coordinate transformation. According to orthogonality conditions, matrices *P* and *Q* are diagonalized:

$$\Psi^T P \Psi = \left[{}^{\backslash} a_{i\backslash} \right], \quad \Psi^T Q \Psi = \left[{}^{\backslash} b_{i\backslash} \right] \tag{2.23}$$

where $\left[{}^{\backslash} a_{i\backslash} \right]$ and $\left[{}^{\backslash} b_{i\backslash} \right]$ are modal *a* matrix and modal *b* matrix, respectively.

Substituting (2.23) in (2.17) and pre-multiplying by $[\Psi]^T$ yields

$$\Lambda_{com} = \left[{}^{\backslash} \lambda_{i\backslash} \right] = -\left[{}^{\backslash} b_i / a_{i\backslash} \right] \tag{2.24}$$

2.3 FINITE ELEMENT MODELING

The dynamic behavior of complex structures is generally analyzed by means of the Finite Element Method (FEM), which leads to an eigenvalue problem that is solved in terms of modal parameters (natural frequencies, modal damping ratios and mode shapes).

The limitation of the FEM lies in the increase of model size required to properly describe complex structures with sufficient detail, which leads to high model construction and calculation times. More important restriction is inherent inaccuracy in modelling including model structure, parameter and order errors. To address these limitations, an experimental approach to modal analysis was developed to yield results which can be either as a model, or to validate and improve the FEM (Frisell and Mottershead, 1995). The resulting EMA and OMA approach have become a standard element of the mechanical product design and engineering process.

Example

The finite element model of the metallic frame was developed with ANSYS software. The iron beams and aluminum columns were simulated with beam4 element, and the connection elements were modeled as concentrated masses with mass21 element. The numerical results are exhibited in Figure 2.4.

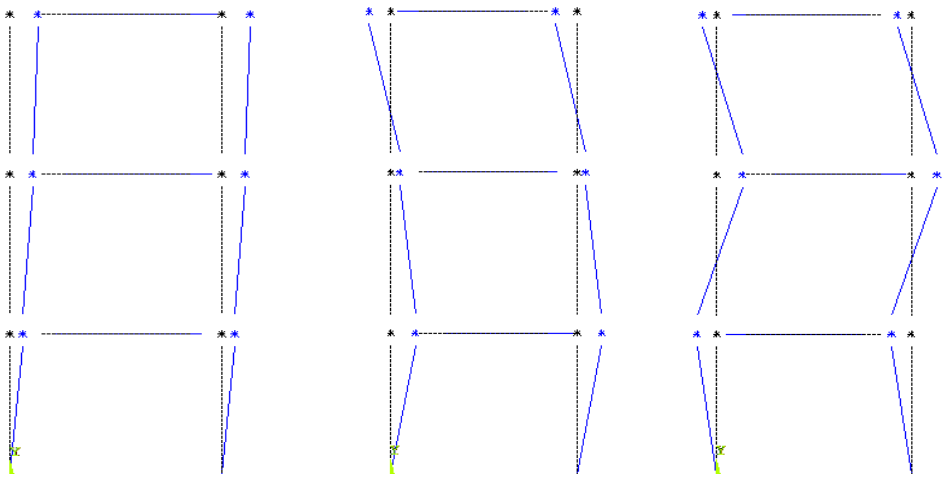

$f_1 = 5.35Hz$ $f_2 = 15.02Hz$ $f_3 = 21.66Hz$

Figure 2.4 Calculated natural frequencies and modal shapes

2.4 FREQUENCY DOMAIN MODELS

A standard OMA procedure consists of three basic stages: (1) Conduction of ambient vibration test under operational conditions and collection of output responses; (2) Consideration of a set of candidate models; (3) Application of methodologies in model fitting using the output data. The candidate models in OMA can be classified based on the domain in which the data is treated resulting in 'frequency domain models' and 'time domain models'. In time domain, the output responses can be used directly to build the model, while in frequency domain models it is necessary to perform a spectrum analysis by Fourier transform. In this section, the frequency models and corresponding algorithms will be introduced.

Example

In order to illustrate the complex candidate models of OMA, a vibration experiment of the metallic frame was performed in laboratory. It is assumed that the lateral response on nodes 1 and 4, 2 and 5, as well as on 3 and 6 are equal. So, only acceleration signals in nodes 1,2 and 3 were measured.

The signal acquisition system used in the experiment consists of piezoelectric accelerometers,

signal conditioners and a data acquisition equipment, as shown in Figure 2.5 (a-c). The acceleration signals were measured with sensors (PCB 352A10 and PCB 352C68) and amplified with ICP sensor signal conditioner. The signals were sampled by National Instruments data acquisition equipment (cDAQ-9172 and NI 9234) which connected to a computer. The frame was excited manually by a hammer (PCB 086C03) occasionally. The experiment was divided in 2 setups and node 1 was selected as reference point. The first setup comprehended the vibration signal measured at nodes 1 and 2, while the second setup collected data from nodes 1 and 3. The duration of each setup was 15 minutes and the sampling frequency was 500Hz.

(a) Sensor (PCB 352A10) at node 1

(b) Sensor (PCB 352C68) at node 2

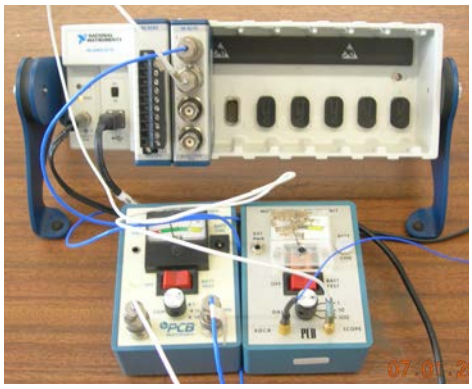

(c) ICP signal conditioner (480D06 and 480E09) and
NI data acquisition equipment (cDAQ-9172 and NI 9234)

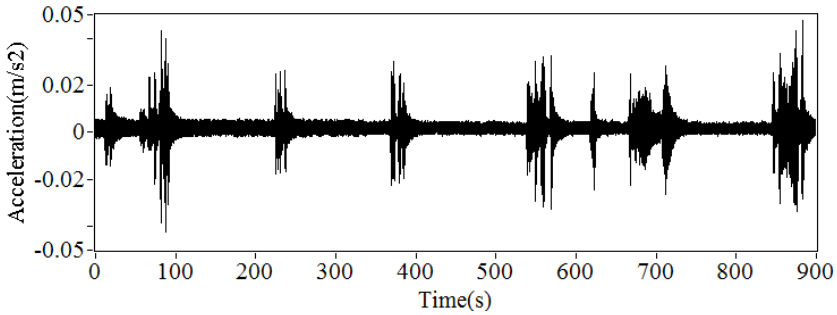

(d) Acceleration signal measured at node 1 in setup 1

Figure 2.5 Sensors, signal conditioner, data acquisition equipment and measured signal

The application of Laplace transform in continuous time domain leads to the classical Frequency Response Function (FRF) in frequency domain. In frequency domain analysis, the FRF can be decomposed in two different forms of fraction, representing two different models. In one of them is the FRF can be expressed as a Partial Fraction Description (PFD) model, which is also called pole-residue parameterization. The modal frequency and modal damping can be estimated from the poles, whose modal shapes can be extracted from decomposition of residue. In another model is the FRF is described as a Right Matrix Fraction Description (RMFD) model. Identification of this model is based on the minimization of an equation error between the measured and modelled FRF matrix. After linearization, modal parameters can be extracted by linear Least Squares (LS) approach.

Typical for operational modal analysis is that only discrete and finite output measurements are available. Dealing with real random responses requires converting continuous time domain models to discrete domain, and introducing concept of spectrum and spectrum estimation algorithm in frequency domain, which are the basis for further application of frequency domain models for operational modal analysis. On one hand, in PFD model, the input spectra matrix is assumed as a constant matrix, therefore, poles and residues can be identified by estimation of an output spectra matrix based on response measurements. On the other hand, using an output spectral matrix instead of a FRF matrix to build RMFD model also leads to accurate identification of modal parameters by linear LS method.

2.4.1 Laplace transform and transfer function

The Laplace transform converts time-variant differential equations to algebraic ones, which are easier to manipulate. The one-sided Laplace transform of a function $x(t)$, denoted as $X(s)$, is defined as

$$X(s)=\mathbf{L}[x(t)]=\int_0^\infty x(t)e^{-st}dt \tag{2.25}$$

where $s=\mathbb{C}$ is a complex quantity known as the Laplace variable. According to important property of the Laplace transform

$$\mathbf{L}[\,\dot{x}(t)\,]=sX(s)-x(0) \tag{2.26}$$

Applying the Laplace transform to equation (2.1) leads to

$$\mathbf{L}\left[M\ddot{q}(t)+C_d\dot{q}(t)+Kq(t)\right]=M\left[s^2X(s)-sx(0)-\dot{x}(0)\right]+C_d\left[sX(s)-x(0)\right]+KX(s)$$

$$=(Ms^2+C_ds+K)X(s)-Msx(0)-M\dot{x}(0)-Cx(0) \tag{2.27}$$

and

$$\mathbf{L}\left[f(t)\right]=F(s) \tag{2.28}$$

If the initial displacement and velocity are equal to 0 ($x(0)=0$ and $\dot{x}(0)=0$), equations (2.27) and (2.28) can be expressed as the ratio of the transformed response to the transformed excitation:

$$H(s)=\frac{Q(s)}{F(s)}=\frac{1}{Ms^2+C_ds+K}=\frac{1}{Z(s)}=Z^{-1}(s) \tag{2.29}$$

where $Z(s)$ is the dynamic stiffness.

The denominator of equation (2.29) Ms^2+C_ds+K is identical to equation (2.20) yielding roots s_i expressed as Λ . Substituting s_i and the modal coordinates $q_{mc}(t)=\Psi^{-1}x(t)$ in equation (2.16), and pre-multiplying by Ψ^T

$$(s_i\Psi^TP\Psi+\Psi^TQ\Psi)q_{mc}(t)=\Psi^TF \tag{2.30}$$

According to orthogonality conditions shown in equations (2.23) and (2.24), it leads to:

$$q_{mc}(t)=(s_i\left[\backslash a_{i\backslash}\right]-\left[\backslash a_{i\backslash}\right]\Lambda_{com})^{-1}\Psi^TF \tag{2.31}$$

Introducing $V_d=\left[\Phi \quad \Phi^*\right]$, $\Psi=\begin{bmatrix}V_d\\V_d\Lambda_{com}\end{bmatrix}$ and considering $q_{mc}(t)$ in (2.31), equation (2.14) becomes:

$$x(t)=\begin{Bmatrix}q(t)\\\lambda_iq(t)\end{Bmatrix}=\Psi q_{mc}(t)=\begin{bmatrix}V_d\\V_d\Lambda_{com}\end{bmatrix}\left[s_i\left[\backslash a_{i\backslash}\right]-\left[\backslash a_{i\backslash}\right]\Lambda_{com}\right]^{-1}\begin{bmatrix}V_d\\V_d\Lambda_{com}\end{bmatrix}^T\begin{bmatrix}f(t)\\0\end{bmatrix} \tag{2.32}$$

The upper part of equation (2.32) is

$$q(t)=[V_d]\left[s_i\left[\backslash a_{i\backslash}\right]-\left[\backslash a_{i\backslash}\right]\Lambda_{com}\right]^{-1}[V_d]^T\,f(t) \tag{2.33}$$

Applying the Laplace transform to equation (2.33) yield

$$Q(s)=[V_d]\left[s\left[\backslash a_{i\backslash}\right]-\left[\backslash a_{i\backslash}\right]\Lambda_{com}\right]^{-1}[V_d]^T\,F(s) \tag{2.34}$$

Then, transform function $H(s)$ in Partial Fraction Expansion (PFE) is obtained:

$$H(s)=\frac{Q(s)}{F(s)}=V_d\left[s\left[\backslash a_{i\backslash}\right]-\left[\backslash a_{i\backslash}\right]\Lambda_{com}\right]^{-1}V_d^T=\sum_{i=1}^{n_m}\left(\frac{1}{a_i}\frac{\phi_i\phi_i^T}{s-\lambda_i}+\frac{1}{a_i^*}\frac{\phi_i^*\phi_i^H}{s-\lambda_i^*}\right)$$

$$=\sum_{i=1}^{n_m}\left(\frac{\phi_i\gamma_i^T}{s-\lambda_i}+\frac{\phi_i^*\gamma_i^H}{s-\lambda_i^*}\right)$$

$$=\sum_{i=1}^{n_m}\left(\frac{R_{ri}}{s-\lambda_i}+\frac{R_{ri}^*}{s-\lambda_i^*}\right) \tag{2.35}$$

The transform function $H(s)$ is described as a sum of modal contributions, which is called *modal decomposition*.

In classical modal analysis, λ_i,λ_i^* are named as system poles and coincide with equation (2.21):

$$\lambda_i,\lambda_i^*=-\xi_i\omega_i\pm j\sqrt{1-\xi_i^2}\,\omega_i$$

ϕ_i , γ_i and R_{ri} are defined as *mode shape vector*, *mode participation vector* and *residue*, respectively. A so-called '*modal model*' is characterised by natural frequencies ω_i, modal damping ratios ξ_i, mode shapes ϕ_i and *mode participation factors* γ_i.

The equation (2.29) can also be expressed as

$$H(s)=(Z(s))^{-1}=\frac{Z_{adj}(s)}{|Z(s)|} \tag{2.36}$$

where the numerator $Z_{adj}(s)$ (the adjoint matrix) is an ($n_m\times n_m$) matrix containing polynomials in *s* of order $2(n_m-1)$, and the denominator is a polynomial in *s* of order $2n_m$. Therefore, equation (2.36) can also be written as (Verboven, 2002)

$$H(s)=\frac{B_{ri}(s)}{A_{ri}(s)}=\frac{\begin{bmatrix}B_{r(1,1)}(s) & \cdots & B_{r(1,n_m)}(s)\\ \vdots & \ddots & \vdots\\ B_{r(n_m,1)}(s) & \cdots & B_{r(n_m,n_m)}(s)\end{bmatrix}}{A_{ri}(s)} \tag{2.37}$$

which is called a *common denominator model* or also *scalar matrix fraction description.* This expression can also be considered as a special case of multivariable transfer function models

described using a Right Matrix Fraction Description (RMFD) (Kailath, 1980; Guillaume et al, 1996)

$$H(s) = B_{ri}(s)(A_{ri}(s))^{-1} \tag{2.38}$$

Based on this relation, the modal participation factor can be estimated directly together with poles. Afterwards, the mode shape can be estimated by linear least-squares frequency domain (LSFD) method.

2.4.2 Fourier transform and Frequency Response Function (FRF)

If the complex Laplace variable s is restricted to purely imaginary value $s = j\omega$, where ω is any frequency of interest, the Laplace transform is converted into the Fourier transform:

$$X(j\omega) = \mathbf{F}[x(t)] = \int_0^\infty x(t)e^{-j\omega t}dt \tag{2.39}$$

The FRF can be denoted replacing s by $j\omega$ in the transform function. It can be written in PFD, also in *modal decomposition* form:

$$H(j\omega) = \sum_{i=1}^{n_m}\left(\frac{R_{ri}}{j\omega - \lambda_i} + \frac{R_{ri}^*}{j\omega - \lambda_i^*}\right) \tag{2.40}$$

and in RMFD

$$H(j\omega) = B_r(j\omega)(A_r(j\omega))^{-1} \tag{2.41}$$

The Fourier transform is a mathematical tool that converts a time signal into the frequency domain, and its great popularity in practical application stems from the efficient algorithm known as Fast Fourier Transform (FFT) (Cooley and Tukey, 1965).

Example

In current research, traditional EMA was also performed using the metallic three story frame. The transient force excitation was applied by a hammer and the acceleration response at node 1 was recorded with a sampling frequency of 500Hz, as shown in Figure 2.6 (a). The force and free decay acceleration signals within 120 seconds were measured and are shown in Figures 2.6 (b) and (c). The calculated **FRF** is shown in Figure 2.6 (d). The frequencies corresponding to the peaks of the FRF are 5.29Hz, 15.18Hz and 22.35Hz, respectively.

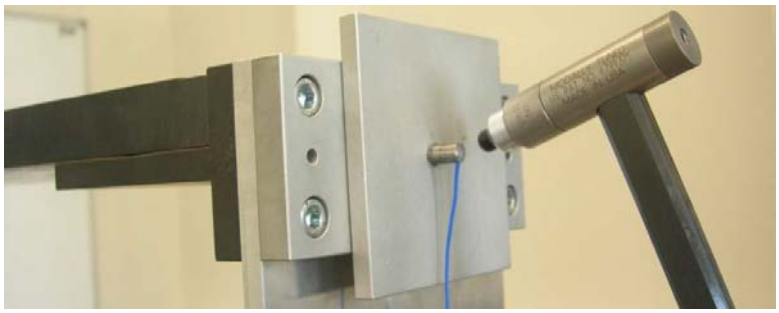

(a) Measurement of force input and acceleration response at node 1

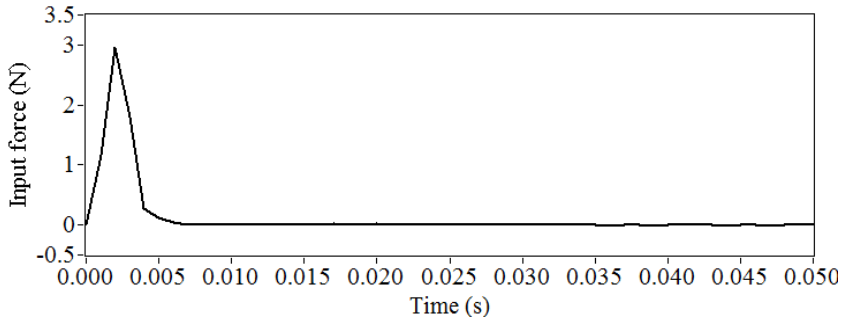

(b) Impulse excitation applied by hammer (PCB 086C03)

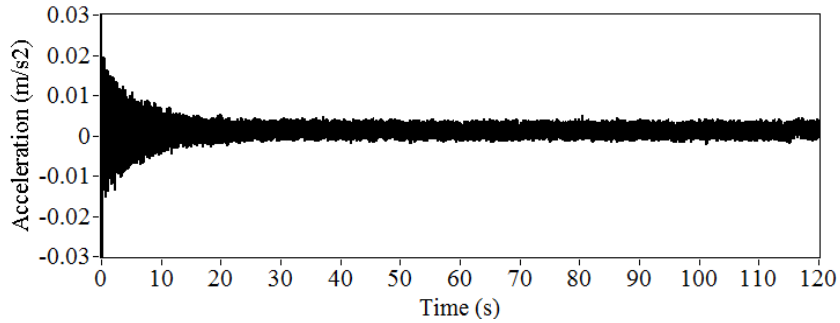

(c) Acceleration response when applying impulse excitation

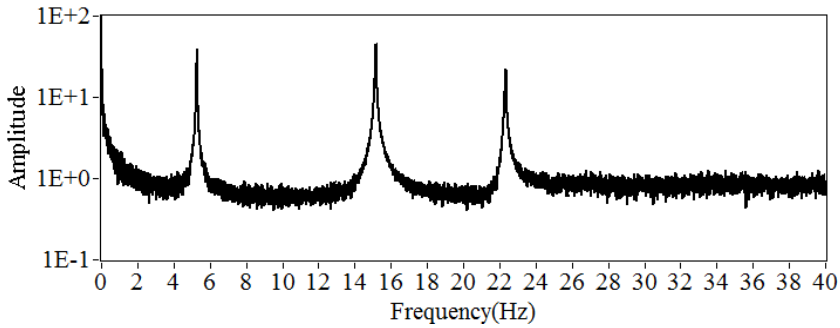

(d) Amplitude of FRF relating the impulse excitation and the acceleration response at node 1

Figure 2.6 Measurements of input and output signals as well as resulting FRF

2.4.3 Sampling, *z*-transform, Discrete Time Fourier Transform and Discrete Fourier Transform

In previous sections all equations are expressed in terms of infinite length in continuous time or frequency, but in experimental world observations of inputs and outputs are finite length in discrete time because of data-acquisition mode. In order to fit models to real measurements, it is then necessary to convert the above models to discrete time form. It is assumed that measurements are observed at the *sampling instants* $t_k = k\Delta t$, k=0,1,2…N-1$\in \mathbb{N}$, where internal Δt is called *sampling interval*. Most often, *a zero-order hold* (ZOH) assumption is adopted, which means that the response, for example the displacement $q(t)$, is piecewise constant between the sampling instants:

$$q(t) = q_k \,, k\Delta t \le t < (k+1)\Delta t \tag{2.42}$$

Under this assumption, the equation of motion is converted as:

$$M\ddot{q}_k + C_d\dot{q}_k + Kq_k = f_k \tag{2.43}$$

where $q_k, \dot{q}_k, \ddot{q}_k$ and f_k are the sampled displacement, velocity, acceleration and force vectors.

The *z*-transform can be considered as a discrete equivalent of the Laplace transform. One-sided *z*-transform is defined as:

$$X(z) = \mathbf{Z}\left[x_k\right] = \sum_{k=0}^{+\infty} x_k z^{-k} \tag{2.44}$$

where $z \in \mathbb{C}$ is a scalar complex variable. An important property of the *z*-transform is:

$$\mathbf{Z}\left[x_{k+1}\right] = z(X(z) - x_0) \tag{2.45}$$

Assuming that initial condition is $x_0 = 0$, a forward shift in time domain corresponds to a multiplication by *z* in the *z*-domain,

$$\mathbf{Z}\left[x_{k+1}\right] = zX(z) = z\,\mathbf{Z}\left[x_k\right] \tag{2.46}$$

The Discrete-Time Fourier transform (DTFT) is the discrete equivalent of the Fourier transform shown in (2.39),

$$X(e^{j\omega\Delta t}) = \mathbf{F}[x_k] = \sum_{k=0}^{+\infty} x_k e^{-j\omega k\Delta t} \tag{2.47}$$

Comparing equations (2.47) and (2.44), it is observed that the **DTFT** is a special case of *z*-transform when z is restricted to $z = e^{j\omega\Delta t}$, which is the evaluation of the z-transform around the unit circle in the complex plane.

In practical evaluation of the inputs and outputs during an experiment, only finite length sequences with *N* points are available. Thus, equation (2.47) may be modified as

$$X(e^{j\omega\Delta t}) = \mathbf{F}[x_k] = \sum_{k=0}^{N-1} x_k e^{-j\omega k\Delta t} \tag{2.48}$$

If *N* is a power of 2, $X(e^{j\omega\Delta t})$ can be efficiently computed at uniformly-spaced discrete frequencies

$$\omega = \frac{l_n}{N}\frac{2\pi}{\Delta t}, (l_n = 0,..., N-1) \tag{2.49}$$

across one period (2π) by using FFT. $X(e^{j\omega\Delta t})$ is now recognized a Discrete Fourier Transform (DFT). By using **DFT,** a finite length discrete signal in time domain is converted discrete frequency spectrum.

2.4.4 Spectrum and spectrum estimation

As input is unknown in OMA testing, power spectra are frequently used to identify the system model and extract modal parameters. In this section, spectrum analysis and practical aspects of spectrum estimation technique are introduced.

The power spectrum is defined as the Fourier transform of the autocorrelation function $R_s(t)$, if the signal can be treated as a stationary stochastic process,

$$S_s(j\omega) = \int_{-\infty}^{+\infty} R_s(t) e^{-j\omega t} dt \tag{2.50}$$

In OMA, it is assumed that the excitation (input) is a zero mean $\mathbf{E}[x(t)] = 0$, white noise sequence. The autocorrelation function can be written as,

$$R_{xx}(\tau) = E[x(t)x(t+\tau)] = R_{xx}\delta(\tau) \tag{2.51}$$

where τ is the time lag, $R_{xx}(\tau) \in \mathbb{R}^{m \times m}$ is a constant matrix and $\delta(\tau)$ is the Dirac delta function. The inherent property of this function is:

$$\int_{-\infty}^{+\infty} f(t)\delta(t-a)dt = f(a) \tag{2.52}$$

for any function *f*(*t*) which is continuous at time *a*.

Considering the property of Dirac delta function, the power spectrum of unknown input is a constant matrix also called 'flat' spectrum matrix.

$$S_{xx}(j\omega) = \int_{-\infty}^{+\infty} R_{xx}(t)e^{-j\omega t}dt = S_{con} \tag{2.53}$$

Again, return to real experimental world and recall that the output measurements. The measured output vector in *l* selected points is discreted as y_k, and thus output correlation matrices $R_r \in \mathbb{R}^{l \times l}$ are defined as:

$$R_r = E\left[y_{k+r} y_k^T\right] \tag{2.54}$$

where *r* is an arbitrary time lag similar to τ in continuous time. If the measured output vector with *N* points is assumed as an ergodic random process $y_k, k = 0,1,...N-1 \in \mathbb{N}$, the correlation matrices are estimated as:

$$\hat{R}_r = \frac{1}{N}\sum_{k=0}^{N-1} y_{k+r} y_k^T \tag{2.55}$$

The spectrum of a stochastic process is defined as the double sided *z*-transform of R_r:

$$S_{yy}(z) = \sum_{r=-\infty}^{+\infty} R_r z^{-r} \tag{2.56}$$

The property of discrete autocorrelation function R_r is

$$R_{-r} = R_r^T \tag{2.57}$$

Thus, the spectrum (2.56) can be rewritten as

$$S_{yy}(z) = S_{yy}^+(z) + (S_{yy}^+(z^{-1}))^T \tag{2.58}$$

where

$$S_{yy}^+(z) = R_0/2 + \sum_{r=1}^{+\infty} R_r z^{-r} \tag{2.59}$$

The so-called half spectrum, having a positive time lag *r*, can be calculated by DTFT in

equation (2.47) as

$$S_{yy}(e^{j\omega\Delta t}) = R_0/2 + \sum_{r=1}^{+\infty} R_r z^{-j\omega r\Delta t} \tag{2.60}$$

In real experiments only a finite number of data is available, and so the spectrum indicated in equation (2.60) can not be directly computed up to infinity. Consequently, the spectrum used in practice is estimated by finite sample sequence using DFT. The most popular spectrum estimation method may be *weighted averaged periodogram* (*modified Welch's periodogram*) (Welch, 1967) and *weighted correlogram* (Tukey and Blackman, 1958). The term *weighted* in these two methods means that a window function is applied to the signal (Hamming, Hanning,…) to reduce leakage. The *averaged periodogram* operates directly on the output signal sequences, while the *correlogram* approach first estimates the correlations in time-domain and then the power spectra are obtained by transferring the correlations to the frequency-domain.

The *weighted averaged periodogram* method starts with dividing output sequences into L segments of M_s samples as

$$L \le N/M_s \tag{2.61}$$

Each segment $y_{Ms}^{\ell}(m_s)$ are formed as

$$y_{Ms}^{\ell}(m_s) = y(m_s + (\ell-1)M_s)\begin{cases} 0 \le m_s \le M_s - 1 \\ 1 \le \ell \le L \end{cases} \tag{2.62}$$

The L modified or windowed periodogram can be defined as

$$S_{yy\ell}(e^{j\omega\Delta t}) = \frac{1}{\sum_{m_s=0}^{M_s-1} |win(m_s)|^2} \left(\sum_{m_s=0}^{M_s-1} win(m_s) y_{M_s}^{\ell}(m_s) e^{-j\omega m_s\Delta t}\right)\left(\sum_{m_s=0}^{M_s-1} win(m_s) y_{M_s}^{\ell}(m_s) e^{-j\omega m_s\Delta t}\right)^T \tag{2.63}$$

where *win* means window function (Hanning, Hamming,…) to reduce leakage. If M_s is a power of 2, the spectrum of this segment is efficiently calculated by DFT at the discrete frequency points

$$\omega = \frac{\ell}{M_s}\frac{2\pi}{\Delta t}, \ell = 0,1,...,M_s - 1 \tag{2.64}$$

The spectrum estimation S_{yy} is computed by averaging all spectra based on L segments

of sequence y_k .

$$\hat{S}_{yy} = \frac{1}{L}\sum_{\ell=1}^{L} S_{yy\ell}(e^{j\omega\Delta t}) \tag{2.65}$$

$\hat{S}_{yy}$ is the asymptotically unbiased estimate of the spectrum. Because the window functions reduce the contributions of the data at the beginning and at the end of the record, introducing an overlap between the adjacent segments is advisable.

Another correlogram approach starts by estimating the correlation functions as indicated in equation (2.55). Then, the correlation functions are transferred to the frequency-domain by taking the DFT to obtain the power spectrum.

$$\hat{S}_{yy} = \sum_{r=-L}^{L} w_k \hat{R}_k e^{-j\omega r\Delta t} \tag{2.66}$$

In this section, the spectrum analysis and spectrum estimation techniques are introduced. The spectrum of stationary stochastic output is primary data in frequency domain OMA.

Example

The acceleration signal measured at node 1, shown in Figure 2.5 (d), consists of 500×900=450000 data samples. The autocorrelations of the signal $\hat{R}_r$ were estimated with equation (2.55) and time lag *r*=0, 1,…, 16384. Only the time lag $r \geq 0$ is plotted in Figure 2.7 (a).

The spectrum of the signal was estimated by both *weighted averaged periodogram* and *weighted correlogram* methods. In the application of *weighted correlogram* method, the estimated autocorrelations $\hat{R}_r$ (r=0, 1, …, 16384) were multiplied by a Hanning window before application of **FFT,** according to equation (2.66). The resulting estimated spectrum, with frequency resolution 500/16384=0.03Hz, is shown in Figure 2.7 (b). The *weighted averaged periodogram* method was also used to estimate the spectrum, as shown in Figure 2.7 (c). 442368 of a total of 450000 sample points were used and divided into 54 segments of 16384 points with 50% overlapping; after multiplication by a Hanning window, **FFT** was applied to each segment. Finally, the 54 FFTs were averaged to yield the spectrum estimates with frequency resolution 500/16384=0.03Hz.

Comparing the spectrum estimated by the *weighted averaged periodogram* and the *weighted correlogram* methods, it is observed that the spectrum yielded by the *weighted averaged periodogram* is smoother because of multiple averages.

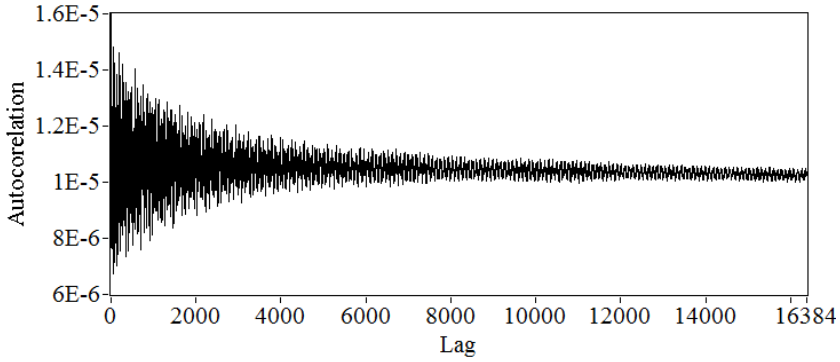

(a) Estimation of autocorrelation of response measured at node 1

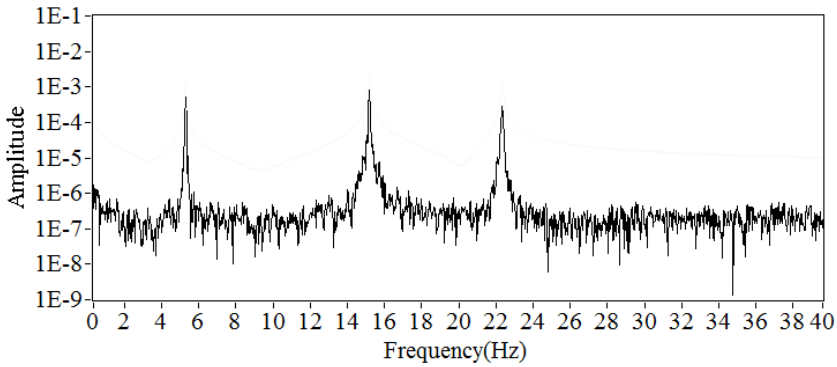

(b) Spectrum estimation using weighted correlogram method

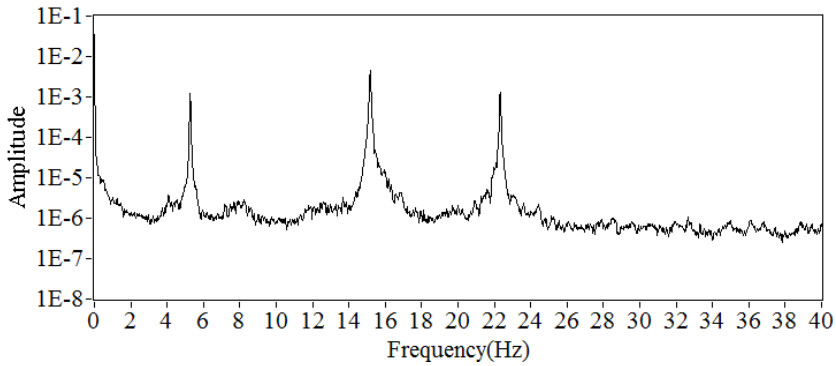

(c) Spectrum estimation using weighted averaged periodogram method

Figure 2.7 Estimation of output correlation and spectrum

2.4.5 Model reduction

In real operational modal analysis, the ambient vibration experiment is always *band-limited*, which means that the signal only contains information over a certain frequency band. Only modes whose frequencies are within the bandwidth will show up in data and

certain modes out of bandwidth are eliminated. This is called model reduction in operational modal analysis.

Recall equation (2.40), the FRF can be rearranged with components within the bandwidth and parts out of the bandwidth as

$$H(j\omega) = \sum_{i=1}^{n_{re}} \left(\frac{R_i}{j\omega - \lambda_i} + \frac{R_i^*}{j\omega - \lambda_i^*}\right) + \sum_{i=n_r+1}^{n_m} \left(\frac{R_i}{j\omega - \lambda_i} + \frac{R_i^*}{j\omega - \lambda_i^*}\right) \tag{2.67}$$

where n_{re} is the number of retained modes. In identification from experimental data, only modal parameters located in the test frequency range are estimated, while the contributions of out-of-band modes corresponding to the second part of the right hand side of equation (2.67) are neglected as

$$H(j\omega) = \sum_{i=1}^{n_r} \left(\frac{R_i}{j\omega - \lambda_i} + \frac{R_i^*}{j\omega - \lambda_i^*}\right) \tag{2.68}$$

The modal reduction is then a step closer to real experimental world.

2.4.6 Frequency domain models

a) *Half positive power spectra matrix*

In OMA, the relation between the constant input spectrum S_{con} and the output spectrum S_{yy}^+ can be expressed as (Bendat and Piersol, 1980):

$$S_{yy}^+(j\omega) = H(j\omega) S_{con} H(j\omega)^H \tag{2.69}$$

where $S_{yy}^+(j\omega) \in \mathbb{C}^{l \times l}$ and $S_{con} \in \mathbb{C}^{m \times m}$ are the power spectra matrices of the output and input measurements, and *l*, *m* are the number of output and input responses. $H(j\omega) \in \mathbb{C}^{l \times m}$ is the FRF matrix. The superscript $(\,)^H$ denotes complex conjugate and transpose.

The equation (2.69) leads to a simple *non-parametric* frequency domain spectrum model derived from the FRF in PFE form, and a more complex *parametric* model based on FRF in RMFD format. In this paragraph, two models widely used in current frequency domain OMA are introduced. The purpose of OMA in frequency domain is to identify these models and extract modal parameters based on the output spectra matrix S_{yy}.

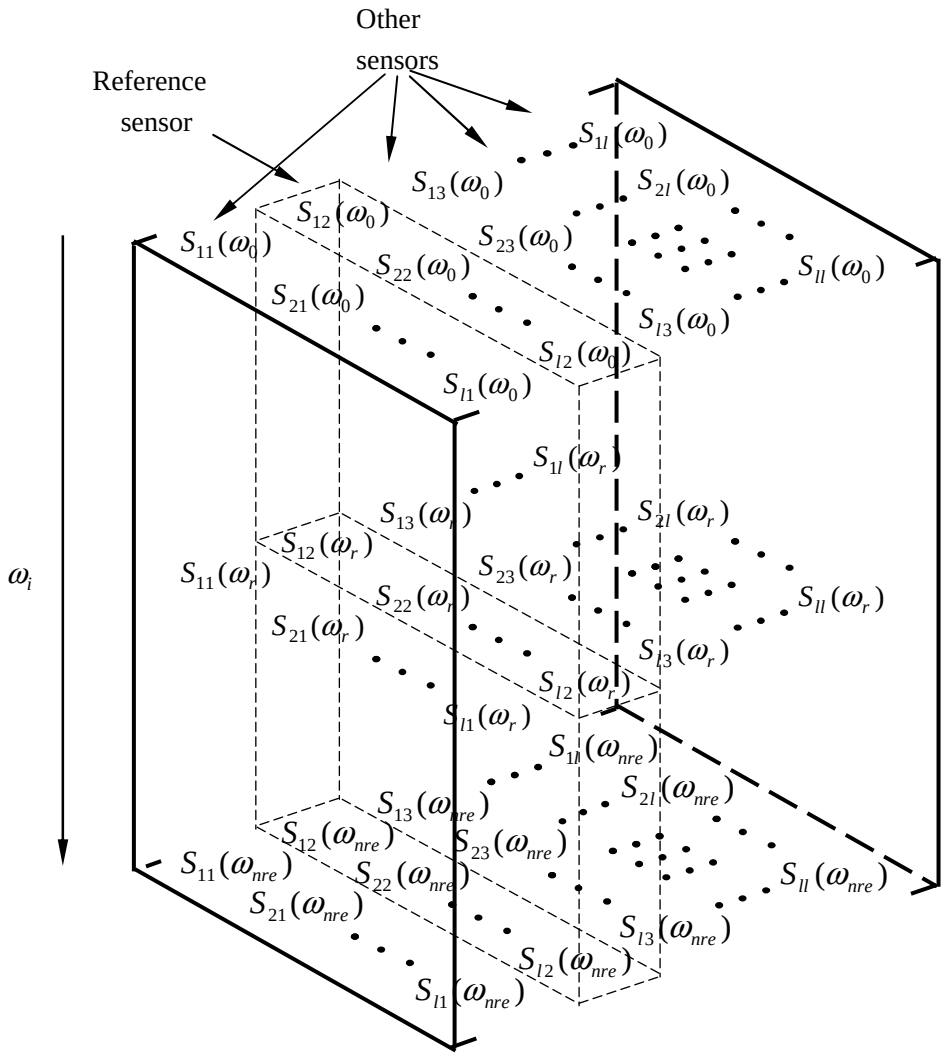

Figure 2.8 Schematic for interpretation of spectra matrix

Example

The half positive power spectra is a 3-dimension matrix consisting of auto and cross power spectra based on the experimental signals acquired in each setup. Considering that only 2 sensors were used in each setup of the ambient vibration test of the frame, the output spectrum S_{yy}^{+} can be written, according to Figure 2.8, as

$$S_{yy}^{+}(j\omega) = \sum_{i=0}^{n_{re}} \begin{bmatrix} S_{11}(\omega_i) & S_{12}(\omega_i) \\ S_{21}(\omega_i) & S_{22}(\omega_i) \end{bmatrix}$$

where $\begin{bmatrix} S_{11}(\omega_i) & S_{12}(\omega_i) \\ S_{21}(\omega_i) & S_{22}(\omega_i) \end{bmatrix}$ refer a sub-matrix at discrete frequency points ω_i. $S_{11}(\omega_i), S_{22}(\omega_i)$ are the auto power spectra calculated by experimental acceleration signals, while $S_{12}(\omega_i), S_{21}(\omega_i)$

correspond to cross power spectra. $\sum_{i=0}^{n_{re}}$ represents that the half positive power spectra $S_{yy}^{+}(j\omega)$ comprehends sub-matrix at all discrete frequency points ω_i ($i=0,1\ldots,n_{re}$).

b) *Half positive power spectra model in PFD*

Substituting the equation (2.68) into equation (2.69), the output spectra matrix $S_{yy}(j\omega)$ is evaluated at discrete frequency points as follows

$$S_{yy}(j\omega)=\sum_{i=1}^{n_r}\sum_{s=1}^{n_r}\left(\frac{\phi_i\gamma_i^T}{j\omega-\lambda_i}+\frac{\phi_i^*\gamma_i^H}{j\omega-\lambda_i^*}\right)S_{con}\left(\frac{\phi_s\gamma_s^T}{j\omega-\lambda_s}+\frac{\phi_s^*\gamma_s^H}{j\omega-\lambda_s^*}\right)^H \tag{2.70}$$

Multiplying the two partial fraction factors and making use of the Heaviside partial fraction theorem, the output spectra $S_{yy}(j\omega)$ can be converted to the partial fraction form (Hermans and Van der Auweraer,1999; Peeters, 2000; Brincker,2001).

$$S_{yy}(j\omega)=\sum_{i=1}^{n_r}\left(\frac{\phi_i g_i^T}{j\omega-\lambda_i}+\frac{\phi_i^* g_i^H}{j\omega-\lambda_i^*}+\frac{g_i\phi_i^T}{-j\omega-\lambda_i}+\frac{g_i^*\phi_i^H}{-j\omega-\lambda_i^*}\right) \tag{2.71}$$

where $g_i\in\mathbb{C}$ is the *operational reference vecto*r for mode *i*, which replaces the modal participation factors in cases where only output responses are available in OMA. The power spectra matrix derived above has a 4-quadrant symmetry because the OMA modal model contains $\lambda_i,-\lambda_i,\lambda_i^*$ and $-\lambda_i^*$ as poles, positive (λ_i,λ_i^*) and negative ($-\lambda_i,-\lambda_i^*$). The power spectra matrix $S_{yy}(j\omega)$, modally decomposed into 4-quadrant symmetric terms, is called full power spectra matrix.

The counterpart of the full power spectra matrix $S_{yy}(j\omega)$ in time domain is the correlation function matrix

$$C_{yy}(\tau)=\sum_{i=1}^{n_r}\left(\phi_i g_i^T e^{\lambda_i\tau}+\phi_i^* g_i^H e^{\lambda_i^*\tau}-g_i\phi_i^T e^{-\lambda_i|\tau|}-g_i^*\phi_i^H e^{-\lambda_i^*|\tau|}\right) \tag{2.72}$$

In this equation, the first two terms, having positive poles, correspond to positive time lags, whereas the last two terms, with negative poles, correspond to the negative time lags.

The full power spectra matrix is normally estimated by the spectrum estimation methods introduced in section 2.4.4. Because the power spectra matrix is estimated from a limited amount of data in OMA, which are typically characterised by significant noise levels, a

tradeoff must be made between stochastic uncertainties and bias errors introduced by leakage. The drawbacks caused by the spectrum estimation methods can be overcome by the unbiased estimation of correlation functions with only positive lags according to equation (2.54) (Hermans et al, 1998; Cauberghe, 2004). The fist two terms in equation (2.72) are kept as

$$C_{yy}^{\tau}(\tau) = \sum_{i=1}^{n_r} (\phi_i g_i^T e^{\lambda_i \tau} + \phi_i^* g_i^H e^{\lambda_i^* \tau}) \tag{2.73}$$

Its counterpart in the frequency domain can be written as

$$S_{yy}^{+}(j\omega) = \sum_{i=1}^{n_r} (\frac{\phi_i g_i^T}{j\omega - \lambda_i} + \frac{\phi_i^* g_i^H}{j\omega - \lambda_i^*}) \tag{2.74}$$

The output spectra matrix with only positive poles is called *half positive power spectra* matrix.

The first kind of frequency model begins from some mathematical manipulation of equation (2.71) under assumption of light damping. The term $\phi_i g_i^T$ in equation (2.71) is a function of the modal parameters and the constant power spectrum matrix of the unknown random input excitation

$$\phi_i g_i^T = (\phi_i \gamma_i^T)\, S_{con} (\sum_{s=1}^{n_r} \frac{\phi_s \gamma_s^T}{j\omega - \lambda_s} + \frac{\phi_s^* \gamma_s^H}{j\omega - \lambda_s^*})^H \tag{2.75}$$

When λ_s approaches $\lambda_i = -\xi_i \omega_i + j(1-\xi_i^2)^{1/2} \omega_i$ (equation 2.21), the contribution of the *i-th* mode is given by

$$\phi_i g_i^T = \frac{(\phi_i \gamma_i^T) S_{con} (\phi_i \gamma_i^T)^H}{2\xi_i \omega_i} \tag{2.76}$$

If damping ratio is low, $\phi_i g_i^T$ becomes proportional to the mode shape as

$$\phi_i g_i^T \propto (\phi_i \gamma_i^T) S_{con} (\phi_i \gamma_i^T)^H = d_i \phi_i \phi_i^H \tag{2.77}$$

where d_i is a scalar constant.

Around a certain frequency ω_i, only a limited number of modes contribute significantly and these modes are denoted as $Sub(\omega)$. Thus, the half positive power spectra matrix S_{yy}^{+} can be expressed in PFD form as

$$\underset{\omega \to Sub(\omega_i)}{S_{yy}^{+}(j\omega)} = \sum_{i \in Sub(\omega)} \left(\frac{d_i \phi_i \phi_i^H}{j\omega - \lambda_i} + \frac{d_i \phi_i \phi_i^H}{j\omega - \lambda_i^*} \right) \tag{2.78}$$

According to this equation, a relation between the output spectrum, the system poles λ_i, λ_i^* and the mode shape ϕ_i is established, which leads to the identification algorithm of *peak-picking* and *frequency domain decomposition*.

c) *Half positive power spectra model in RMFD*

The frequency model described in equation (2.78) is only valid for a slightly damped structure. In order to estimate modal parameters of highly damped structures, another frequency model derived from RMFD shown in equation (2.41) is proposed (Peeters et al, 2004). It is observed that the half positive spectra matrix $S_{yy}^{+}(j\omega)$ is similar to the $H(j\omega)$ and they are parameterized in the same way. Therefore, The left side of equation (2.41), $H(j\omega)$, can be replaced by positive power spectra considering only the positive lags of the output spectra matrix $S_{yy}^{+}(j\omega)$.

Assuming there are *l* outputs and *m* of them are regarded as 'input', positive output spectra $S_{yy}^{+}(j\omega) \in \mathbb{C}^{l \times m}$ can be modelled in RMFD form as

$$S_{yy}^{+}(j\omega) = B_{ri}(j\omega)(A_{ri}(j\omega))^{-1} \tag{2.79}$$

where $B_{ri}(j\omega) \in \mathbb{C}^{l \times m}$ is the numerator matrix polynomial and $A_{ri}(j\omega) \in \mathbb{C}^{m \times m}$ is the denominator matrix polynomial. They are defined as

$$\begin{aligned} B_{ri}(j\omega) &= \sum_{r=0}^{p} \Omega_r(\omega) \beta_r \\ A_{ri}(j\omega) &= \sum_{r=0}^{p} \Omega_r(\omega) a_r \end{aligned} \tag{2.80}$$

in which $\Omega_r(\omega)$ are the polynomial basis function and *p* is the user defined polynomial order. A p^{th} order model based on *m* outputs contains *mp* poles. Theoretically, the indication of the model order can be counted as twice the number of peaks in the frequency-plot of a non-parametric spectrum. It is also provided more accurate by the CMIF in which a frequency plot of the singular values of a non-parametric spectrum estimates. However, in practice it is

better to over-specify the model order, a stabilization diagram being used to extract modal parameters from this model, which will be further discussed in next section.

For a discrete-time domain model, the functions $\Omega_r(\omega)$ are usually defined as

$$\Omega_r(\omega) = e^{-j\omega\Delta tr} \tag{2.81}$$

where Δt is the sampling time.

The polynomial coefficients $\beta_r \in \mathbb{R}^{l\times m}$ and $\alpha_r \in \mathbb{R}^{m\times m}$ are the parameters to be estimated and are assembled in following matrices:

$$\beta_o = \begin{pmatrix} \beta_{o0} \\ \beta_{o1} \\ \dots \\ \beta_{op} \end{pmatrix} \in \mathbb{R}^{(p+1)\times m} \ (o = 1,2,\dots,l), \alpha = \begin{pmatrix} \alpha_0 \\ \alpha_1 \\ \dots \\ \alpha_p \end{pmatrix} \in \mathbb{R}^{m(p+1)\times m}, \theta = \begin{pmatrix} \beta_1 \\ \beta_2 \\ \dots \\ \beta_l \\ \alpha \end{pmatrix} \in \mathbb{R}^{(l+m)(p+1)\times m} \tag{2.82}$$

From this model, the output spectra $S_{yy}^{+}(j\omega)$ can be written as function of the coefficient $S_{yy}^{+}(\omega_k, \theta)$. By fitting the measured output spectra $S_{yy}^{+}(j\omega)$ with this model by coefficient θ at each frequency point ω_k, the system poles λ_i and *operational reference vecto*r g_i can be estimated. From this frequency model, a *poly-reference least squares frequency domain* algorithm is used to identify modal parameters.

Completing this section with two frequency domain models in equations (2.78) and (2.79), the path has now been paved for a discussion on the modal identification techniques.

2.4.7 Summary

This section presents half positive power spectra frequency domain models in both *PFD* and *RMFD* form. The evolution from analytical second order vibration equation to OMA frequency models is in following steps: converting analytical model to transfer function in continuous time domain and to classical FRF in discrete-time domain. The introductions of sampling , DFT technique, spectrum estimation and model reduction are further step to real experimental world. Finally, frequency models based on half positive power spectra in different forms leads to different identification methods that will be discussed

comprehensively in next section.

2.5 FREQUENCY DOMAIN MODAL IDENTIFICATION METHODS

In the context of operational modal analysis (OMA) in civil engineering, structures such as bridges and buildings are excited by unmeasured input forces and only output measurements are available. Under the assumption that the input is a stochastic process (e.g. white noise), the structural behaviour can be idealized by mathematical models in the frequency domain proposed, as described in previous section, in order to establish the relation between the output spectra matrix and the structural modal parameters. In this chapter, an overview of the main frequency domain modal identification methods is presented. They comprise *peak-picking* (PP) and *frequency domain decomposition* (FDD) algorithms and *poly-reference least squares complex frequency* (p-LSCF) technique. The PP and FDD methods are called *nonparametric* method, because modal parameters are estimated by just looking at signal-based features without fitting or estimating a parametric model. Despite their simplicity and quickness, *nonparametric* methods are rather subjective in estimating modal parameters. On the contrary, p-LSCF is called a *parametric* method. A right matrix fraction model is selected and it is parameterized as a function of a parameter vector θ. By fitting this model with spectra of the output measurements in a linear least square (LS) sense, θ is determined and further leads to the estimation of modal the parameters more accurately.

2.5.1 Peak-picking (PP)

The Peak-Picking (PP) is the simplest and most popular approach to estimate structural modal parameters in OMA. The key step of this method is the natural frequencies are simply taken from the observation of the peaks on the graphs of the magnitude of the spectrum plot under the basic assumption that the modes have well-separated frequencies. Assuming that the spectrum around any frequency ω_i is dominated by a single mode, equation (2.78) can be expressed as:

$$S_{yy}(j\omega) = -\frac{d_i \phi_i \phi_i^H}{\xi_i \omega_i} \tag{2.83}$$

By defining the scalar constant α_i as:

$$\alpha_i = -\frac{d_i}{\xi_i \omega_i} \tag{2.84}$$

The approximated spectrum at resonance can be expressed as:

$$S_{yy}(j\omega) \approx \alpha_i \phi_i \phi_i^H \tag{2.85}$$

From the point of view of Peak-Picking method, the interpretation of equation (2.85) is that at the resonance frequency ω_i, each column (or equivalently row) of the spectra matrix can be considered as an estimate of the observed mode shape up to some scaling factor, as shown in Figure 2.3. If the column (or row) corresponds to a DOF of the structure that is situated at a node of a certain mode, this mode can not be identified. In order to that ensure all of the natural frequencies of a structure are identified, a practical implementation of the Peak-Picking method was firstly developed by Felber (1993). It is suggested to consider the averaged normalized power spectrum density (ANPSD) of all measured locations, which means the diagonal elements of the spectrum matrix $S_{yy}^{+}(j\omega)$.

The determination of damping ratios is then usually based on the half-power bandwidth method. However, this is a rather inaccurate procedure. Using simple peak-picking method, the damping ratio is likely difficult to be determined.

When peak-picking method is applied to identify modal shapes, instead of estimating the spectrum matrix $S_{yy}^{+}(j\omega)$, only the spectra between the reference sensor and all sensors are calculated. The reason is that only one column (or row) of the spectrum matrix suffices to obtain the mode shape estimates. Some refinements of the peak-picking method are also proposed in (Felber, 1993). Coherence function between two sensors can assist in selecting natural frequencies, because the coherence function tends to be 1 around the resonance damped frequencies. The phase angles of the cross spectra are also helpful for determining the damped natural frequencies since the phase angles should be either 0° or 180°.The detailed procedure for identifying modal parameters can be found in (Felber, 1993).

Example

Before applying various modal identification methods, the experimental data sampled at 500Hz were pre-processed: They were decimated with factor 5 to reduce the size of data from 450000 to 90000 samples. The data were filtered with an eight-order Chebyshev type I lowpass filter with a cutoff frequency of 0.8*500/5/2=40Hz. Afterwards, the data were resampled with a lower sampling rate f_s=500/5=100Hz. Subsequently, the decimated data were detrended to remove the linear component.

When the preprocessed signals were treated by peak-picking method, the spectrum matrix was estimated by the *weighted averaged periodogram* method. 81920 of total 90000 sample points were used and divided into 9 segments of 16384 points with 50% overlapping; after multiplication by a Hanning window, **FFT** was applied to each segment. Finally, the 9 FFTs were averaged to yield the spectrum estimates with frequency resolution 100/16384=0.006Hz. The trace of the spectrum matrix is shown in Figure 2.9. Actually, it is the sum of auto power spectra produced by each signal acquired from individual sensors. The frequencies are easily identified by picking the peaks: 5.28Hz, 15.18Hz and 22.35Hz. The corresponding modal identification results are listed and compared with those yielded from other methods in Table 1 at the end of this chapter.

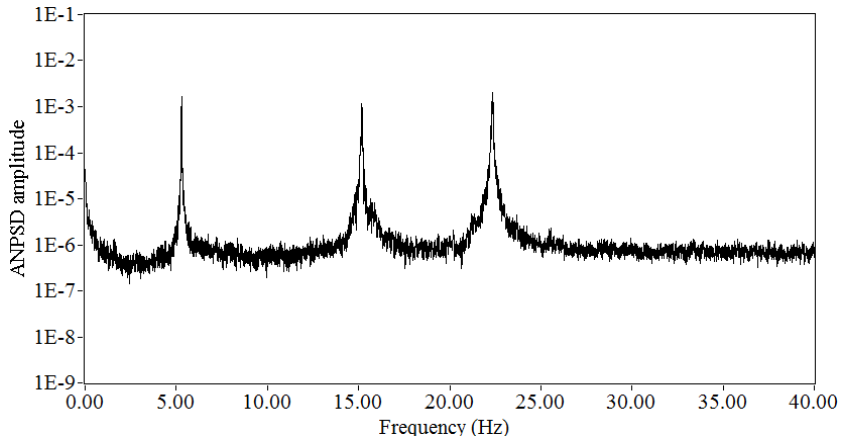

Figure 2.9 The trace of the spectrum matrix

The peak-picking method may be the most widely used method in civil engineering because of its simplicity. Many civil engineering cases exist where the method was successfully applied in (Cunha et al, 2006, 2007). Despite its popularity, the disadvantages of peak-picking method are obvious: the assumption of this method is that damping is low and the modes are well-separated, violation of these assumptions leading to erroneous results. Instead of identifying mode shapes, only *operational deflection shapes* are determined. For

closely-spaced modes, such an operational deflection shape will be the superposition of multiple modes. For structures like towers, the peak-picking method may become problematic, since the bending modes along any of the two principle axes modes are likely to have closely-spaced frequencies. Other disadvantages are that the selection of the damped natural frequencies can become a subjective task if the spectrum peaks are not very clear and the estimation of damped natural frequencies are constrained by the frequency resolution.

In order to overcome these drawbacks of peak-picking method, a more advanced procedure named Frequency Domain Decomposition (FDD) was developed as an alternative.

2.5.2 Frequency Domain Decomposition (FDD)

The key step of FDD method is the Singular Value Decomposition (SVD) of the spectra matrix at each discrete frequency ω_i. The SVD is a mathematic tool that is typically used for counting the rank of a matrix, because the number of non-zero singular values equals the rank of the matrix. It is also interpreted in modal analysis that the FRF or spectrum matrix evaluated at a certain frequency is only determined by a few modes, and the number of these modes coincides with the rank of the spectrum matrix. Originally, the SVD of the spectrum matrix was used as a tool to count the number of modes of a vibrating system subjected to natural excitation (Prevosto, 1982). Subsequently, this method was applied to FRFs to count the number of modes in modal testing and it was named as Complex Mode Indication Function (CMIF). It was also extended to identify the modal parameters from FRFs (Shih, 1988). Similarly, SVD of output spectra matrix was further developed to estimate modal parameters in OMA (Brincker et al 2000, 2001).

When applying the FDD method for modal parameters identification, the first step is also the estimation of the half positive spectra matrix S_{yy}^{+} based on output measurements. Then, by taking the SVD of S_{yy}^{+} at each discrete frequency ω_i, it can be decomposed as follows:

$$S_{yy}^{+}(j\omega_i) = U(\omega_i)S(\omega_i)U_i^{H}(\omega_i) \tag{2.86}$$

where $S(\omega_i)$ is a diagonal matrix holding the singular values sorted in descending order $s(\omega_{ij}),\ j = 1,2,...,l$. $U(\omega_i) = [u_1(j\omega_i), u_2(j\omega_i), ...u_l(j\omega_i)]$ is an unitary matrix holding the

singular vectors $u_j(j\omega_i)$.When the frequency approaches a certain resonance frequency ω_r, the power spectra matrix can be approximately decomposed as a rank one matrix

$$S^{+}_{\substack{yy \\ \omega\to\omega_r}}(j\omega_r)=\begin{bmatrix} S_{11}(\omega_r) & S_{12}(\omega_r) & \cdots & S_{1l}(\omega_r) \\ S_{21}(\omega_r) & S_{22}(\omega_r) & \cdots & S_{2l}(\omega_r) \\ \vdots & \vdots & \vdots & \vdots \\ S_{l1}(\omega_r) & S_{l2}(\omega_r) & \cdots & S_{ll}(\omega_r) \end{bmatrix} \xrightarrow{SVD} s_{11}(\omega_r)u_1(\omega_r)u_1^H(\omega_r) \qquad (2.87)$$

If only one mode is dominating at the resonance frequency ω_r, the corresponding singular vector $u_1(\omega_r)$ is an estimate of the corresponding mode shape with unitary normalization.

$$\hat{\phi}_r = u_1(\omega_r) \qquad (2.88)$$

and the corresponding singular value is the auto power spectra function of the corresponding single degree of freedom (SDOF) system associated with equation (2.78).

In the case of repeated modal frequencies, the rank of the power spectra matrix is equal to the multiplicity number of the modes. Therefore, the singular value which is a function of frequencies sorted in descending order can be adopted as the modal indication function. Modal frequencies can be located by the peaks of the singular value plots. Mode shapes can be obtained from the corresponding singular vectors assuming the mode shapes are orthogonal. Because SVD has the ability to separate the signal space from noise space, the modes can be indicated from singular value plots with noisy measurements, and closely spaced modes or even modes with repeated modal frequencies can be easily detected.

Initially, FDD could only estimate modal frequencies and mode shapes. To identify modal damping ratio, the enhanced FDD (EFDD) technique was proposed (Brincker et al, 2001). After estimating mode shapes according to equation (2.88), the corresponding singular value is the auto power spectral density function of the corresponding single degree of freedom system. This power spectral density function is identified around the peak by comparing the mode shape estimation $\hat{\phi}$ with the singular vectors for the frequency lines around the peak. If a singular vector is found that has high Modal Assurance Criterion (MAC) value with $\hat{\phi}$ the corresponding singular value consists of the SDOF auto spectra function.

From the fully or partially identified SDOF auto spectra function, an approximation of the correlation function of the SDOF system is obtained by taking the spectral density function back to time domain by inverse FFT. From this free decay function in time domain, the natural frequency and the damping is found by estimating crossing times and logarithmic decrement. Firstly, all peaks p_k on the correlation function are found. The logarithmic decrement σ is calculated as

$$\sigma = \frac{1}{k} \ln\left(\frac{p_0}{p_k} \right) \tag{2.89}$$

where p_0 is the initial peak value of the correlation function and p_k is the *k*th peak. And the damping ratio is estimated by

$$\xi = \frac{\sigma}{\sqrt{\sigma^2 + 4\pi^2}} \tag{2.90}$$

The damped natural frequency ω_d is found by making a linear regression between the crossing times and the times corresponding to the peaks. The natural frequency ω is found by

$$\omega = \frac{\omega_d}{\sqrt{1-\xi^2}} \tag{2.91}$$

Example

The SVD was applied to the estimated spectrum matrix constructed with the preprocessed experimental signals of the metallic frame. Figure 2.10 shows the singular values as a function of frequency. Because only two sensors were used to record the experimental signal in each setup, a 2×2 output spectrum matrix S_{yy}^{+} (as the example discussed in in section 2.4.6) yields 2 singular value vectors according to equation (2.86). The first singular value vector reached peaks at about 5.18Hz, 15.12Hz and 22.33Hz,

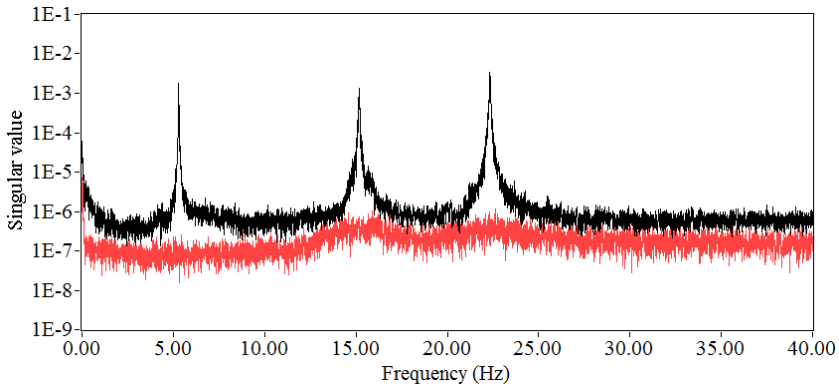

Figure 2.10 Singular values produced by EFDD method

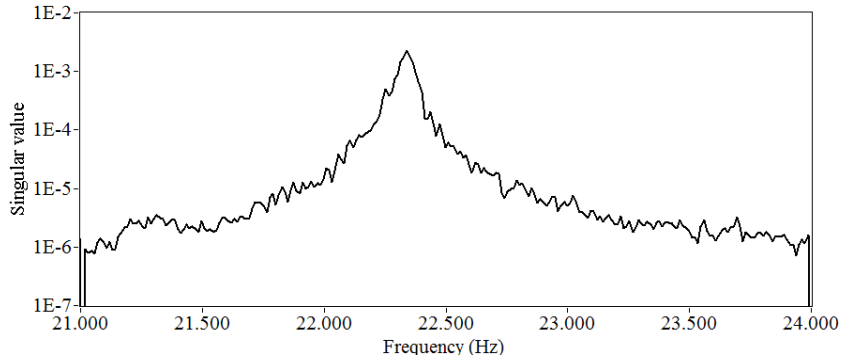

(a) Singular values around 22.32Hz with MAC value higher than 0.8

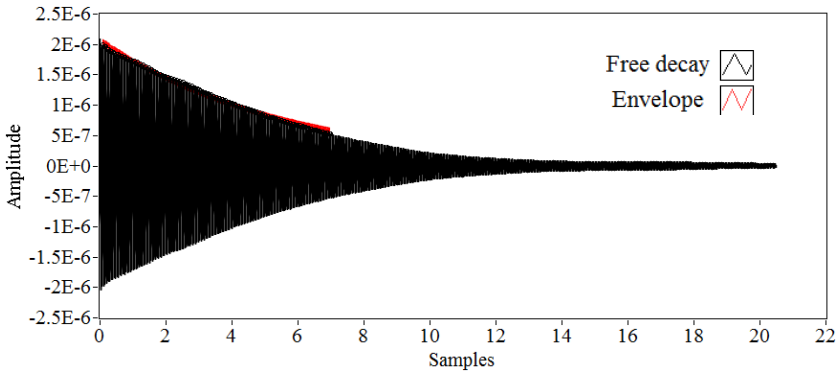

(b) Time domain free decay function obtained by inverse FFT and estimated damping envelope

Figure 2.11 Selected singular values and corresponding free decay function

The peak around 22.32Hz was picked and mode shape $\hat{\phi}_{22.32Hz}$ was estimated. The singular vectors of the neighbouring frequency lines around the peak were compared with the mode shape $\hat{\phi}_{22.32Hz}$ by calculating the MAC value. The frequency lines with MAC value higher than 0.8 were selected and regarded as the auto correlation function of a SDOF system, as shown Figure 2.11 (a).

By applying inverse FFT to the selected frequency lines, the free decay function in time domain is obtained (Figure 2.11 (b)). The natural frequency and the damping were evaluated by estimating

crossing times and logarithmic decrement of the fitted envelope according to functions (2.89-2.91). The detailed estimation results are presented at the end of this chapter.

The basic assumption of FDD is that the structure is lightly damped. Moreover, only truncated data near the peak of the singular value plot are utilized for the inverse FTT to calculate approximate correlation functions of the corresponding SDOF system, which may cause bias error in damping estimation. To estimate damping ratio were accurately, the *poly-reference least squares complex frequency* (p-LSCF) algorithm for identification of modal parameters based on half positive output spectra matrix was proposed from the frequency model in RMFD (Peteers et al, 2005).

2.5.3 Poly-reference Least-Squares Complex Frequency Domain (p-LSCF)

Originally, the least-squares complex frequency-domain (LSCF) estimation method was introduced to find initial values for the iterative maximum likelihood method (Guillaume et al, 1998). The method estimates a so-called common-denominator transfer function model. Lately it was found that these “initial values” yielded already very accurate modal parameters with a very small computational effort. A thorough analysis of different variants of the common-denominator LSCF method can be found in (Verboven, 2002). A complete background on frequency-domain system identification can be found in (Pintelon and Schoukens, 2001).

a) *Equation error formulation*

The frequency model in RMFD is summarized from equation (2.79)-(2.82). The purpose of p-LSCF method is to identify all unknown model coefficients θ in equation (2.82) based on the power spectra matrix $S_{yy}^{+}(j\omega_i)$ from output measurements, which can be done by minimizing the following non-linear least-squares (NLS) equation errors $\varepsilon_o^{NLS}(\omega_i,\theta)\in\mathbb{C}^{l\times m}$:

$$\varepsilon_o^{NLS}(\omega_i,\theta)=w_o(\omega_i)(B_o(\omega_i,\beta_o)A^{-1}(\omega_i,\alpha)-S_{yy}^{+}(\omega_i)) \tag{2.92}$$

where $\omega_i, i=1,2,...,N_f$ are the discrete frequencies at which $S_{yy}^{+}(j\omega_i)$ are available.

$$w_0(\omega)=\frac{1}{\sqrt{\mathrm{var}\{S_{yy}^{+}(\omega_i)\}}}$$

is the scalar weighting function, which can further improve the quality of the estimates because it allows to take into account different data quality that may exist between different outputs.

The equation errors ε_o^{NLS} for all outputs and all discrete frequency points ω_i are combined in following scalar cost function:

$$\ell^{NLS}(\theta) = \sum_{o=1}^{l}\sum_{i=1}^{N_f} tr\left\{\varepsilon_o^{NLS}(\omega_i,\theta)^H \varepsilon_o^{NLS}(\omega_i,\theta)\right\} \tag{2.93}$$

where $tr\{\ \}$ is the trace of a matrix. The cost function is minimized by putting the derivatives of equation (2.93) with respect to the unknown model coefficients θ equal to zero. It is obvious that this leads to non-linear equations when equation (2.92) is used for the equation errors directly. The non-linear least-squares (NLS) problem can be approximated by a linear least-squares (LS) one by right-multiplying equation (2.92) with the numerator matrix polynomial *A*, yielding equation errors $\varepsilon_o^{NLS}(\omega_i,\theta) \in \mathbb{C}^{l\times m}$ that are linear in the parameters:

$$\begin{aligned}\varepsilon_o^{NLS}(\omega_i,\theta) &= w_o(\omega_i)(B_o(\omega_i,\beta_o) - S_{yy}^{+}(\omega_i)A(\omega_i,\alpha)) \\ &= w_o(\omega_i)\sum_{r=0}^{p}(\Omega_r(\omega_i)\beta_{or} - \Omega_r(\omega_i)S_{yyo}^{+}(\omega_i)\alpha_r)\end{aligned} \tag{2.94}$$

The equation errors at all discrete points are stacked in a matrix $E_o^{LS}(\theta) \in \mathbb{C}^{N_f\times m}$:

$$E_o^{LS}(\theta) = \begin{pmatrix} \varepsilon_o^{LS}(\omega_1,\theta) \\ \varepsilon_o^{LS}(\omega_2,\theta) \\ \dots \\ \varepsilon_o^{LS}(\omega_{N_f},\theta) \end{pmatrix} = (X_o \quad Y_o)\begin{pmatrix}\beta_o \\ \alpha\end{pmatrix} \tag{2.95}$$

where

$$X_o = \begin{pmatrix} w_o(\omega_1)(\Omega_o(\omega_1)\dots\Omega_p(\omega_1)) \\ \dots \\ w_o(\omega_{N_f})(\Omega_o(\omega_{N_f})\dots\Omega_p(\omega_{N_f})) \end{pmatrix} \in \mathbb{C}^{N_f\times(p+1)},$$

$$Y_o = \begin{pmatrix} -w_o(\omega_1)(\Omega_o(\omega_1)\dots\Omega_p(\omega_1)) \otimes S_{yyo}^{+}(\omega_1) \\ \dots \\ -w_o(\omega_{N_f})(\Omega_o(\omega_{N_f})\dots\Omega_p(\omega_{N_f}) \otimes S_{yyo}^{+})(\omega_{N_f}) \end{pmatrix} \in \mathbb{C}^{N_f\times(p+1)} \tag{2.96}$$

where $\otimes$ denotes the Kronecker product.

b) *Reduced normal equations*

The linearized equation errors $\ell^{LS}(\theta)$ can be formulated in the similar way as equation (2.93)

$$\ell^{LS}(\theta) = \sum_{o=1}^{l}\sum_{i=1}^{N_f} tr\left\{\varepsilon_o^{LS}(\omega_i,\theta)^H \varepsilon_o^{LS}(\omega_i,\theta)\right\} \tag{2.97}$$

Minimizing this cost function leads to a weighted linear least square (LS) problem. Substituting equations (2.95) and (2.96), the cost function can be written as:

$$\begin{aligned}\ell^{LS}(\theta) &= \sum_{o=1}^{l} tr\left\{(E_o^{LS}(\theta))^H E_o^{LS}(\theta)\right\} \\ &= \sum_{o=1}^{l} tr\left\{(\beta_o^T \quad \alpha^T)\begin{pmatrix} X_o^H \\ Y_o^H \end{pmatrix}(X_o \quad Y_o)\begin{pmatrix}\beta_o \\ \alpha\end{pmatrix}\right\} \\ &= tr\left\{\theta^T J^H J\theta\right\}\end{aligned} \tag{2.98}$$

where $J \in \mathbb{C}^{lN_f \times (l+m)(p+1)}$ is the so-called Jacobian matrix

$$J = \begin{pmatrix} X_1 & 0 & \dots & 0 & Y_1 \\ 0 & X_2 & \dots & 0 & Y_2 \\ \dots & \dots & X_3 & \dots & \dots \\ 0 & 0 & \dots & X_4 & Y_l \end{pmatrix} \tag{2.99}$$

In the case of real-value coefficients θ, it can be shown that the expression $J^H J$ can be substituted by its real part $\mathrm{Re}(J^H J) \in \mathbb{R}^{(l+m)(p+1)\times(l+m)(p+1)}$ and the cost function (2.98) becomes:

$$\ell^{LS}(\theta) = tr\left\{\theta^T \,\mathrm{Re}(J^H J)\theta\right\} \tag{2.100}$$

with:

$$\mathrm{Re}(J^H J) = \begin{pmatrix} R_1 & 0 & \dots & 0 & S_1 \\ 0 & R_2 & \dots & 0 & S_2 \\ \dots & \dots & \dots & \dots & \dots \\ 0 & 0 & \dots & R_l & S_l \\ S_1^T & S_2^T & \dots & S_l^T & \sum_{o=1}^{l} T_o \end{pmatrix} \tag{2.101}$$

in which

$$R_0 = \mathrm{Re}(X_o^H X_o) \in \mathbb{R}^{(p+1)\times(p+1)}$$

$$S_0 = \mathrm{Re}(X_o^H Y_o) \in \mathbb{R}^{(p+1)\times m(p+1)} \tag{2.102}$$

$$T_0 = \mathrm{Re}(Y_o^H Y_o) \in \mathbb{R}^{m(p+1)\times m(p+1)}$$

The cost function (2.100) is minimized by putting its derivatives with respect to the unknown polynomial coefficients equal to zero:

$$\begin{aligned} \frac{\partial \ell^{LS}(\theta)}{\partial \beta_o} &= 2(R_o \beta_o + S_o \alpha) = 0 \\ \frac{\partial \ell^{LS}(\theta)}{\partial \alpha} &= 2\sum_{o=1}^{l}(S_o^T \beta_o + T_o \alpha) = 0 \end{aligned} \tag{2.103}$$

If the denominator polynomial α is computed by above equation, the system poles and operational reference factors can be estimated. Firstly, the least squares (LS) problem can be reduced by eliminating the β_o coefficient equation (2.103)

$$\beta_o = -R_o^{-1} S_o \alpha \tag{2.104}$$

Yielding the so-called reduced normal equation

$$\left\{2\sum_{o=1}^{l}(T_o - S_o^T R_o^{-1} S_o)\right\}\alpha = 0 \tag{2.105}$$

Defining $M = \left\{2\sum_{o=1}^{l}(T_o - S_o^T R_o^{-1} S_o)\right\} \in \mathbb{R}^{m(p+1)\times m(p+1)}$, then

$$M\alpha = 0 \tag{2.106}$$

This equation can be solved for the denominator polynomial α. In order to avoid finding the trivial solution $\alpha = 0$, the following constraint is imposed:

$$\alpha_p = I_m \tag{2.107}$$

where I_m is the $m \times m$ identity matrix. The other denominator polynomial coefficients can be found by least-square (LS) estimation:

$$M(1:mp, 1:mp)\begin{pmatrix} \alpha_0 \\ \alpha_1 \\ \cdots \\ \alpha_{p-1} \end{pmatrix} = -M(1:mp, mp+1:m(p+1)) \tag{2.108}$$

The estimation of α is given by

$$\hat{\alpha}_{LS} = \begin{pmatrix} \alpha_0 \\ \dots \\ \alpha_{p-1} \\ I_m \end{pmatrix} \tag{2.109}$$

c) *Estimation of modal parameters*

Once the system order p is specified and $\hat{\alpha}_{LS}$ is known, the system poles and operational reference factors are retrieved as the eigenvalues and eigenvectors of its companion matrix:

$$\begin{pmatrix} 0 & I & \dots & 0 & 0 \\ 0 & 0 & \dots & 0 & 0 \\ \dots & \dots & \dots & \dots & \dots \\ 0 & 0 & \dots & 0 & I \\ -\alpha_0^T & -\alpha_1^T & \dots & -\alpha_{p-2}^T & -\alpha_{p-1}^T \end{pmatrix} V = V\Lambda \tag{2.110}$$

The operational reference factors are the last m rows of $V \in \mathbb{C}^{mp \times mp}$, the eigenvalue matrix $\Lambda \in \mathbb{C}^{mp \times mp}$ contains the mp system poles $e^{-\lambda_i \Delta t}$ on its diagonal. They are related with natural frequencies ω_i and damping ratios ξ_i as equation (2.21)

$$\lambda_i, \lambda_i^* = -\xi_i \omega_i \pm j\sqrt{1-\xi_i^2}\,\omega_i$$

the p-LSCF stabilization diagram is constructed efficiently by formulating the equation (2.110) and lower order problems can then be solved by considering submatrices of appropriate dimensions.

The interpretation of the stabilization diagram yields a set of poles and corresponding operational reference vector g_i. The mode shapes can then be estimated by

$$S_{yy}^+(j\omega) = \sum_{i=1}^{n_r} \left(\frac{\phi_i g_i^T}{j\omega - \lambda_i} + \frac{\phi_i^* g_i^H}{j\omega - \lambda_i^*} + \frac{LR}{j\omega} + (j\omega)UR \right) \tag{2.111}$$

where $LR, UR \in \mathbb{R}^{l \times m}$ are the lower and upper residue, respectively. They are introduced to reflect the influence of the out-of-band modes as discussed in equation (2.67). The only unknown elements in equation (2.111) are the mode shape ϕ_i and the lower and upper residues. They can be solved in a linear least-squares (LS) sense. This procedure is commonly

called Least Squares Frequency Domain (LSFD) method. (Heylen et al, 1995)

Example

The poly-reference least-squares complex frequency-domain (p-LSCF) method was applied to the preprocessed experimental signals of metallic frame. Firstly, the half positive spectra matrix $S_{yy}^{+}(j\omega_i)$ was estimated with weighted correlogram method, with maximum time lags L=2048 and an exponential window. Next, a stabilization diagram was constructed by considering RMFD models with the polynomial order p= 0,1,…20. Because l=2, these models have 2,4,…,60 poles. According to equation (2.110), the discrete-time eigenvalues μ_i (diagonal elements of V) and operational reference vector g_i (last m rows of V) were computed. The frequencies and damping ratios are related to the discrete-time eigenvalues as

$$\mu_i, \mu_i^* = \exp((-\xi_i\omega_i \pm j\sqrt{1-\xi_i^2}\,\omega_i)\Delta t)$$

The mode shapes ϕ_i were estimated with the linear least-squares method by equation (2.111).

The stabilization diagram is shown in Figure 2.12. The user defined criteria are 1% for frequencies, 3% for both damping and operational reference factors. The symbol ´o´ in red represents a stable pole.

The trace of the half positive spectra matrix $S_{yy}^{+}(j\omega_i)$ is also plotted as a visual aid to select the stable poles though they are not related with the p-LSCF method. Inspection of Figure 2.12 shows that most of the stable poles concentrate around 5.28Hz, 15.16Hz and 22.34Hz. The detailed estimation results are presented at the end of this chapter.

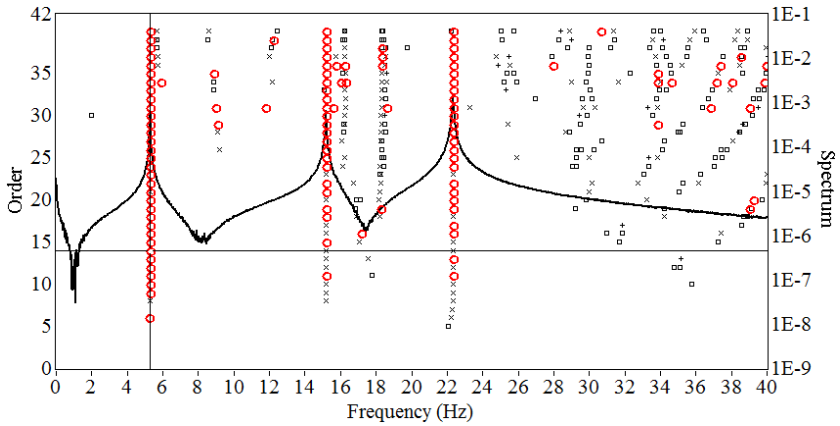

Figure 2.12 Stabilization diagram obtained with the p-LSCF method

2.5.4 Frequency-domain maximum likelihood identification

Beyond the previously discussed frequency models and algorithms, a frequency-domain Maximum Likelihood (ML) approach for the extraction of modal parameters from output measurements was also proposed by (Hermans et al 1998; Guillaume et al 1999). Maximum likelihood identification is an optimization-based method that estimates the parameters of a model by minimizing an error norm. During the last years attention has been paid to the optimization of the frequency domain maximum likelihood method. A detailed discussion on the application of this method to identify parametric frequency domain models and successful industrial OMA applications of frequency domain ML identification can be found in (Parloo,2003; Cauberghe, 2004).

2.5.5 Summary

This section reviews the main frequency domain modal identification algorithms. The classical peak-picking technique is faster and straightforward but it is less accurate for a complex structure because of low frequency resolution, difficulty to identify closely spaced modes and failure to identify real mode shapes. To overcome these drawbacks, FDD method was proposed, whose key feature consists in performing SVD of the output power spectra matrix. However, bias error exists in damping estimation, because only truncated data near the peak of the singular values plot are used for inverse FFT to calculate approximate correlation functions of the corresponding SDOF system. Both PP and FDD methods belong to *non-parametric* modal identification methods and the estimation results are less accurate because no mathematic model is proposed to be fitted for parameter identification. On the contrary, the p-LSCF modal identification approach based on *parametric* model was developed. The specific advantage of this method is that high-order and highly damped systems with large modal overlap can be identified and thus the drawbacks of non-parametric methods are overcome.6

2.6 TIME DOMAIN MODELS

Time domain state-space (SS) and ARMA models originate from control engineering. These models reveal the inherent relation between modal model of vibration systems and output measurements. Without converting from the signals to frequency domain, the modal parameters can be fitted directly from time series analysis (TSA) based on *parametric* models. It is utmost useful to inspect these time domain representations of vibration signals. The modal identification results estimated by these models in time domain can be correlated with the results produced by frequency domain models.

2.6.1 Continuous-time state-space model

a) *The state equation*

Recall the second order vibration equation in state-space form (2.16)

$$P\dot{x}(t) + Qx(t) = F$$

$$P = \begin{bmatrix} C_d & M \\ M & 0 \end{bmatrix},\ Q = \begin{bmatrix} K & 0 \\ 0 & -M \end{bmatrix}, x(t) = \begin{bmatrix} q(t) \\ \lambda_i q(t) \end{bmatrix}, F = \begin{pmatrix} B_l \\ 0 \end{pmatrix} u(t)$$

$\dot{x}(t)$ is obtained by pre-multiplying by P^{-1}

$$\dot{x}(t) = A_c x(t) + B_c u(t) \tag{2.112}$$

where the sub index '*c*' denotes continuous time, $A_c \in \mathbb{R}^{n\times n}$ is the state matrix and $B_c \in \mathbb{R}^{n\times m}$ is the input matrix. They are given by

$$A_c = -P^{-1}Q = \begin{pmatrix} 0 & I \\ -M^{-1}K & -M^{-1}C \end{pmatrix},\ B_c = P^{-1}\begin{pmatrix} B_l \\ 0 \end{pmatrix} = \begin{pmatrix} 0 \\ M^{-1}S \end{pmatrix} \tag{2.113}$$

b) *The observation equation*

In a practical vibration experiment, accelerations $\ddot{q}(t)$, velocities $\dot{q}(t)$ and displacements $q(t)$ may be measured simultaneously in well selected *l* positions as described in equation (2.2).

$$y(t) = C_a \ddot{q}(t) + C_v \dot{q}(t) + C_d q(t)$$

Using the second order equation of motion (2.2) and the definition of the state vector $x(t)$ in equation (2.14), the observation equation (2.2) can be expressed as

$$y(t) = C_c x(t) + D_c u(t) \tag{2.114}$$

where subindex '*c*' denotes continuous time, $C_c \in \mathbb{R}^{l \times n}$ is the output matrix and $D_c \in \mathbb{R}^{l \times m}$ is the direct transmission matrix.

$$C_c = (C_d - C_a M^{-1} K \quad C_v - C_a M^{-1} C_2), D_c = C_a M^{-1} B_l \tag{2.115}$$

Combining equations (2.112) and (2.114), the classical continuous-time state-space (SS) model is given by

$$\begin{aligned} \dot{x}(t) &= A_c x(t) + B_c u(t) \\ y(t) &= C_c x(t) + D_c u(t) \end{aligned} \tag{2.116}$$

The equation of motion is written in state-space form and it can also be used to compute the response $y(t)$ of the structure with a given input $u(t)$.

2.6.2 Discrete-time state-space model

It is necessary to convert the state-space model expressed in the continuous time domain to discrete time domain, in order to fit the models to discrete measurements. In section 2.4.3, the concepts of sampling and assumption of zero-order hold (ZOH) have been introduced. The continuous-time state-space model described in equation (2.116) can be then converted to the discrete-time state-space model:

$$\begin{aligned} x_{k+1} &= A x_k + B u_k \\ y_k &= C x_k + D u_k \end{aligned} \tag{2.117}$$

where $x_k = x(k\Delta t) = \begin{pmatrix} q_k \\ \dot{q}_k \end{pmatrix}$ is the discrete-time state vector consisting of the sampled displacements and velocities; u_k, y_k are the sampled input and output vectors; *A*,*B*,*C* and *D* are the discrete state matrix, discrete input matrix, discrete output matrix and direct transmission matrix, respectively. They can be expressed by their continuous-time counterparts as:

$$A = e^{A_c \Delta t}, B = \int_0^{\Delta t} e^{A_c \tau} \delta\tau B_c = (A - I) A_c^{-1} B_c$$
$$C = C_c, D = D_c \tag{2.118}$$

The classical derivation of the above relations can be found in (Juang, 1994)

a) *Modal parameters*

The purpose of this section is to reveal the relations between matrices *A* and *C* and the modal parameters, including natural frequencies ω_i, modal damping ratios ξ_i and mode shapes ϕ_i.

It is observed that the state matrix A_c in continuous-time state-space model in equation (2.113) comprises all information about the structural system. According to orthogonality conditions of *P* and *Q* in equation (2.23), as well property in equation (2.24), A_c is rewritten as a standard eigenvalue problem.

$$A_c = -P^{-1}Q = -\Psi\left[\backslash 1/a_i \backslash\right]\Psi^T \Psi^{-T}\left[\backslash b_i \backslash\right]\Psi^{-1} = \Psi\Lambda_{com}\Psi^{-1} \tag{2.119}$$

where Λ_{com} and Ψ are complex eigenvalue and eigenvector matrices defined in equation (2.19) as

$$\Lambda_{com} = \begin{bmatrix} \Lambda & 0 \\ 0 & \Lambda^* \end{bmatrix} = \begin{bmatrix} \backslash\lambda_i \backslash & 0 \\ 0 & \backslash\lambda_i^* \backslash \end{bmatrix}, \quad \Psi = \left[\varphi, \varphi^*\right] = \begin{bmatrix} \Phi & \Phi^* \\ \Phi\Lambda & \Phi^*\Lambda^* \end{bmatrix}$$

which is called modal decomposition of matrix A_c.

The matrix *A* in discrete-time stochastic state-space model is found by inserting the modal decomposition of the continuous state matrix A_c into equation (2.118)

$$A = e^{A_c \Delta t} = e^{\Psi\Lambda_c\Psi^{-1}\Delta t} = \Psi e^{\Lambda_c \Delta t}\Psi^{-1} = \Psi\Lambda_d\Psi^{-1} = \Psi\left[\backslash \mu_i \backslash\right]\Psi^{-1} \tag{2.120}$$

where

$$\mu_i = e^{\lambda_i \Delta t}$$

Thus, the system poles are determined as

$$\lambda_i = \frac{\ln(\mu_i)}{\Delta t} \tag{2.121}$$

The connection between λ_i, ω_i and ξ_i is specified in equation (2.21).

A *similarity transformation* of the *state vector* $x(t)$ to the (complex) *modal state vector*

$x^m(t) \in \mathbb{C}^n$ is defined as:

$$x(t) = \Psi x^m(t) \tag{2.122}$$

The corresponding discrete time format is

$$x_k = \Psi x_k^m \tag{2.123}$$

The *modal state-space model* in discrete time format is obtained by inserting the modal decomposition of A in equation (2.117)

$$\begin{aligned} x_{k+1}^m &= \Lambda_d x_k^m + L^T u_k \\ y_k &= V x_k^m + D u_k \end{aligned} \tag{2.124}$$

where L^T and V are the discrete modal participation matrix and the observed mode shape matrix, given by

$$\begin{aligned} L^T &= \Psi^{-1} B \\ V &= C\Psi \end{aligned} \tag{2.125}$$

The relation between the observed mode shape matrix V and the mode shape matrix Φ of the second order equation of motion (2.1) can be clarified by inspecting $V = C\Psi$ based on the definition of C (equation (2.118)), C_c (equation (2.115)) and Ψ (equation (2.19)).

$$V = C\Psi = C_c\Psi = (C_d - C_a M^{-1}K \quad C_v - C_a M^{-1}C_2)\begin{bmatrix} \Phi & \Phi^* \\ \Phi\Lambda & \Phi^*\Lambda^* \end{bmatrix} \tag{2.126}$$

If only displacements are measured, $C_a = C_v = 0$, the mode shape matrix V becomes

$$V = C_d(\Phi \quad \Phi^*) \tag{2.127}$$

If only velocities are measured $C_a = C_d = 0$, V yields

$$V = C_v(\Phi\Lambda \quad \Phi^*\Lambda^*) \tag{2.128}$$

If output measurements are only specified as accelerations, which is the most widely used in vibration experiment, V can be derived by also considering equation (2.19) as

$$V = C_a(\Phi\Lambda^2 \quad \Phi^*\Lambda^{*2}) \tag{2.129}$$

From equations (2.127-2.129), C_d, C_v and C_a are selecting the components of the mode shape corresponding to the output positions. Λ, Λ^* and Λ^2, Λ^{*2} are diagonal matrices that

are only scales of mode shape Φ. It is concluded that observed mode shape matrix V denotes the part of mode shapes from output measurements.

This section reveals the relation between matrices *A* and *C* and the modal parameters. Once matrices *A* and *C* are identified from the state-space model, modal parameters including natural frequencies ω_i, modal damping ratios ξ_i and modal shapes ϕ_i will be obtained.

b) *Model reduction*

As experiments are performed using a certain sampling frequencies, only the contribution of a limited number of modes is acquired. The model reduction can be derived by eliminating higher modes from the modal state-space model. The discrete time modal state-space model in equation (2.124) is divided with the n_r to-be-retained modes and n-n_r eliminated modes as

$$\begin{matrix} n_r \\ n-n_r \end{matrix} \updownarrow \begin{pmatrix} x_{k+1}^r \\ x_{k+1}^e \end{pmatrix} = \begin{pmatrix} \Lambda_d^r & 0 \\ 0 & \Lambda_d^e \end{pmatrix} \begin{pmatrix} x_k^r \\ x_k^e \end{pmatrix} + \begin{pmatrix} L^r \\ L^e \end{pmatrix}^T u_k$$

$$y_k = \begin{pmatrix} V^r & V^e \end{pmatrix} \begin{pmatrix} x_k^r \\ x_k^e \end{pmatrix} + Du_k \tag{2.130}$$

where x_k^r is the discrete-time state vector of the reduced system and x_k^e is the state vector to be eliminated. The *modal decomposition* of direct transmission term *D* can be expressed as a sum of *n* rank-one matrices as (Peeters, 2000).

$$\begin{aligned} D = D_c &= V_c \Lambda_c^{-1} L_c^T = V(\Lambda_d - I)^{-1} L^T \\ &= D^r + D^e \\ &= V^r (\Lambda_d^r - I)^{-1} L^{r^T} + V^e (\Lambda_d^e - I)^{-1} L^{e^T} \end{aligned} \tag{2.131}$$

Model reduction can be obtained by putting next states that have to be eliminated equal to the current state $x_{k+1}^e = x_k^e$. By introducing the resulting of x_k^e into the observation equation, the reduced modal state-space model is obtained as

$$\begin{aligned} x_{k+1}^r &= \Lambda_d^r x_k^r + L^{r^T} u_k \\ y_k &= V^r x_k^r + D^r u_k \end{aligned} \tag{2.132}$$

The reduced model reflects the real experimental world, where only the modes within a certain frequency bandwidth are contained in the experimental data.

2.6.3 Discrete-time stochastic state-space model

The discrete-time state-space model in equation (2.118) shows that the system is only driven by the input u_k. However, the noise in real measurements has to be considered to model the vibration system accurately. Therefore, stochastic components cab be modeled and the *discrete-time combined deterministic-stochastic state-space model* (Van Overschee and De Moor, 1996) is obtained as

$$\begin{aligned} x_{k+1} &= Ax_k + Bu_k + w_k \\ y_k &= Cx_k + Du_k + v_k \end{aligned} \tag{2.133}$$

where $w_k \in \mathbb{R}^n$ represents the noise caused by disturbances and modelling inaccuracies and $v_k \in \mathbb{R}^l$ means the measurement noise due to sensor inaccuracy.

In real experiments, it is impossible and unimportant to distinguish the terms in u_k and the noise terms w_k and v_k in equation (2.134). By incorporating Bu_k and w_k, Du_k and v_k as stochastic input, equation (2.134) becomes a *discrete-time stochastic state-space model* as:

$$\begin{aligned} x_{k+1} &= Ax_k + w_k \\ y_k &= Cx_k + v_k \end{aligned} \tag{2.134}$$

It is assumed that unmeasured signal vectors w_k and v_k are white zero mean, and their covariance matrices having the following property:

$$\mathbf{E}\left[\begin{pmatrix} w_p \\ v_p \end{pmatrix}\begin{pmatrix} w_q^T & v_q^T \end{pmatrix}\right] = \begin{pmatrix} Q & S \\ S^T & R \end{pmatrix}\delta_{pq} \tag{2.135}$$

where **E** is the expected value operator; δ_{pq} is the Kronecker delta, which means that $\delta_{pq} = 1$ if $p = q$, otherwise $\delta_{pq} = 0$; p,q are two arbitrary time instants.

The discrete-time stochastic state-space model in equation (2.134) assumes implicitly that the input is modelled by a white noise. If this assumption of white noise is not valid, for example, if the input contains some dominating frequency components, these frequency components can not be separated from the eigenfrequencies of the system, appearing as spurious poles of the state matrix A (Petters, 2000).

2.6.4 Properties of stochastic systems

In this section, the main properties of linear time invariant stochastic system are briefly summarized. These properties lead to different identification algorithms that will be described in section 2.7. More detailed and complete derivation can be found in (Van Overschee and De Moor, 1996).

It is assumed that the stochastic process x_k is stationary

$$E[x_k] = 0, \quad E[x_k x_k^T] = \Sigma \tag{2.136}$$

where the state covariance matrix Σ is independent of the time *k*. In this section, the *forward model* and *forward innovation model* are introduced, which leads to *covariance driven subspace stochastic identification* and data *driven subspace stochastic identification*.

a) *Forward model*

Since noise terms w_k and v_k in equation (2.133) are zero mean white noise vector sequences and independent of x_k, then

$$E[x_k w_k^T] = 0, E[x_k v_k^T] = 0 \tag{2.137}$$

Recall the definition of output correlation matrices in equation (2.54)

$$R_i = E[y_{k+i} y_k^T]$$

where *i* is an arbitrary time lag. The 'next state-output' covariance matrix $G \in \mathbb{R}^{n \times l}$ is defined as

$$G = E[x_{k+1} x_k] \tag{2.138}$$

From equations (2.135), (2.137)-(2.139), it is be deduced that

$$\begin{aligned} \Sigma &= E[x_{k+1} x_{k+1}^T] = A\Sigma A^T + Q \\ R_0 &= E[y_k y_k^T] = C\Sigma C^T + R \\ G &= E[x_{k+1} y_k^T] = A\Sigma C^T + R \end{aligned} \tag{2.139}$$

and for $i = 1,2...$

$$\begin{aligned} R_i &= CA^{i-1}G \\ R_{-i} &= G^T (A^{i-1})^T C^T \end{aligned} \tag{2.140}$$

This equation reveals an important relation between the output covariance sequence and system matrices *A* and *C*, which means that *A* and *C* can be identified by decomposing the estimated output covariance matrix. This property leads to the *covariance driven subspace stochastic identification* algorithm.

b) *Forward innovation model*

The *discrete-time stochastic state-space model* can be converted into a *so-called forward innovation model* by applying a Kalman filter to the stochastic SS model in equation (2.135). The Kalman filter is described in many books. A nice explanation can be found in (Juan, 1994). The purpose of the Kalman filter is to estimate the optimal prediction of the state vector x_{k+1}, denoted as Kalman filter state vector $\hat{x}_{k+1}$. It is given as

$$\begin{aligned} x_{k+1} &= Ax_k + Ke_k \\ y_k &= Cx_k + e_k \end{aligned} \tag{2.141}$$

where e_k are called innovations sequence, the corresponding covariance matrix being

$$E\left[e_k e_k^T\right] = R_0 - CPC^T$$

K is the Kalman gain

$$K = (G - APC^T)(R_0 - CPC^T)^{-1}$$

and *P* is the forward state covariance matrix. It can be solved by *discrete Riccati equation*

$$P = APA^T + (G - APC^T)(R_0 - CPC^T)^{-1}(G - APC^T)^T$$

Based on this forward innovation model, the *data driven subspace stochastic identification* method is proposed to identify the state matrices *A* and *C*.

2.6.5 ARMA model

In time domain OMA, a more classical auto-regression moving average (ARMA) model can also be employed (Ljung,1999). The basic idea of time series analysis is to identify a system and predict its present and future response from the information of its past inputs and outputs. Instead the second order differential equation (2.1), a linear and time-invariant

vibration system is represented by a finite difference equation. It can be derived by eliminating the state vector x_k from the forward innovation state-space model in equation (2.141). An ARMA model can be expressed as

$$y_k + \alpha_1 y_{k-1} + ... + \alpha_{n_a} y_{k-n_a} = e_k + \beta_1 e_{k-1} + ... + \beta_{n_b} e_{k-n_b} \tag{2.142}$$

where the left side is called the Auto-Regression (AR) part and the right side is the Moving Average (MA) part. y_k is the output vector and e_k is a input white noise vector, α_i, β_i are AR and MA coefficients, respectively. The physical meaning of an ARMA model is the follows: the term $\alpha_i y_{k-i}$ signifies the weighted contribution of the historical sample y_{k-i} to the present response y_k, and the term $\beta_i e_{k-i}$ represents the weighted contribution of the historical input e_{k-i} to the present response y_k. Therefore, the ARMA model describes the input–output relationship of a measured structure. In essence, the ARMA model is equivalent to the stochastic state space model and then it will not be discussed in detail. More details and applications can be found in (Ljung, 1999; Andersen, 1997).

2.6.6 Summary

In this section it is described how a structural system subjected to white noise excitation can be parameterized by a stochastic state space model in time domain. The relation between a state space model and a modal model is revealed and thus modal parameters can be identified from the state space model. The concept of model reduction is also explained in state-space model, which makes a closer step to the real experiment field. Introduction of important properties of the state space model pave a solid path for the different time domain identification techniques. Apart from the state-space model, an equivalent ARMA model is also briefly described.

2.7 TIME DOMAIN MODAL IDENTIFICATION METHODS

In this section modal identification methods involving time domain mathematical models of vibrating systems are explained. Instead of transforming the time domain data to spectra in frequency domain, output measurements are directly assigned to time domain models to

extract modal parameters. The main concern is related with the stochastic subspace identification (SSI) methods. A first group of algorithms is called covariance-driven SSI methods, because the output covariance matrix is used as primary data, which is based on the factorization property in equation (2.140). Another group is named data-driven SSI methods, because they identify models directly from the time signals, which stems from the Kalman filter state sequence shown in equation (2.141).

2.7.1 'Past' and 'Future' part of experimental signal

Before explaining the identification algorithm, the data reduction and smoothing procedure for dividing experimental signal into 'past' and 'future' part is introduced. The Toeplitz and Hankel matrices consist of these two parts of signals.

In a real experiment, only discrete samples of time signal y_k (k=0,1…,N. $N \to \infty$) are available. To determine experimental mode shapes, modal test always involve a batch of measurement setups. In each setup, l sensors (mostly accelerometers) are placed at certain nodes of the structure. The discrete samples y_k can be described as a samples matrix:

$$y_k = \left[y_m^n\right] = \begin{bmatrix} y_1^n \\ y_2^n \\ \vdots \\ y_l^n \end{bmatrix} = \begin{bmatrix} y_1^0 & y_1^1 & \cdots & y_1^N \\ y_2^0 & y_2^1 & \cdots & y_2^N \\ \vdots & \vdots & \vdots & \vdots \\ y_l^0 & y_l^1 & \cdots & y_l^N \end{bmatrix} \tag{2.143}$$

where y_m^n refers the *n-th* (n=0,1,…N) sample points from the *m-th* (m=1,2,…,l) sensor in a certain setup. The Hankel matrix $H \in \mathbb{R}^{2li \times j}$ can be divided into a *past* part Y_p and a *future* part Y_f in equation (2.144).

$$H_{0|2i-1} = \frac{1}{\sqrt{j}} \begin{pmatrix} y_0 \\ y_1 \\ \vdots \\ y_{i-1} \\ y_i \\ y_{i+1} \\ \vdots \\ y_{2i-1} \end{pmatrix} = \begin{pmatrix} y_{1\to l}^0 & y_{1\to l}^1 & \cdots & y_{1\to l}^{j-1} \\ y_{1\to l}^1 & y_{1\to l}^2 & \cdots & y_{1\to l}^{j} \\ \cdots & \cdots & \cdots & \cdots \\ y_{1\to l}^{i-1} & y_{1\to l}^{i} & \cdots & y_{1\to l}^{i+j-2} \\ \hline y_{1\to l}^{i} & y_{1\to l}^{i+1} & \cdots & y_{1\to l}^{i+j-1} \\ y_{1\to l}^{i+1} & y_{1\to l}^{i+2} & \cdots & y_{1\to l}^{i+j} \\ \cdots & \cdots & \cdots & \cdots \\ y_{1\to l}^{2i-1} & y_{1\to l}^{2i} & \cdots & y_{1\to l}^{2i+j-2} \end{pmatrix} = \begin{pmatrix} Y_{0|i-1} \\ Y_{i|2i-1} \end{pmatrix} = \begin{pmatrix} Y_p \\ Y_f \end{pmatrix} \begin{matrix} "past" \\ "future" \end{matrix} \tag{2.144}$$

where the number of block rows i is a user defined index which is theoretically larger than the

maximum order of the system. It is noted that the matrix $H_{0|2i-1}$ consists of 2*li* rows since each block row include *l* (number of output measurement) rows. The number *j* is typically equal to N-2i+2, which implies that all samples are used.

The subscripts of $Y_{i|2i-1}, Y_{0|i-1}$ and $Y_{i|2i-1}$ are subscripts of the first and last element in the first column of the block Hankel matrix. The subscripts *p* and *f* stand for *past* and *future*. The past matrix $Y_{0|i-1}$ and future matrix $Y_{i|2i-1}$ are defined by splitting the Hankel matrix H in two parts with *i* block rows. Another division is defined by omitting the first block row of $Y_{i|2i-1}$ and adding these block rows to the last block row to $Y_{0|i-1}$, which can be explained as

$$H_{0|2i-1} = \frac{1}{\sqrt{m}} \begin{pmatrix} y_0 \\ y_1 \\ \vdots \\ y_i \\ y_{i+1} \\ y_{i+2} \\ \vdots \\ y_{2i-1} \end{pmatrix} = \left(\begin{array}{cccc} y_{1\to l}^{0} & y_{1\to l}^{1} & \cdots & y_{1\to l}^{j-1} \\ y_{1\to l}^{1} & y_{1\to l}^{2} & \cdots & y_{1\to l}^{j} \\ \cdots & \cdots & \cdots & \cdots \\ y_{1\to l}^{i} & y_{1\to l}^{i+1} & \cdots & y_{1\to l}^{i+j-1} \\ \hline y_{1\to l}^{i+1} & y_{1\to l}^{i+2} & \cdots & y_{1\to l}^{i+j} \\ y_{1\to l}^{i+2} & y_{1\to l}^{i+3} & \cdots & y_{1\to l}^{i+j+1} \\ \cdots & \cdots & \cdots & \cdots \\ y_{1\to l}^{2i-1} & y_{1\to l}^{2i} & \cdots & y_{1\to l}^{2i+j-2} \end{array} \right) = \begin{pmatrix} Y_{0|i} \\ \hline Y_{i+1|2i-1} \end{pmatrix} = \begin{pmatrix} Y_p^+ \\ \hline Y_f^- \end{pmatrix} \begin{matrix} \text{"}past\text{"} \\ \hline \text{"}future\text{"} \end{matrix} \quad (2.145)$$

2.7.2 Covariance-driven SSI method

The covariance-driven SSI problem is actually called stochastic realization method. System realization, whose purpose is to recover or identify the system matrices, was developed in 1960s. Classical contribution in deterministic system realization for recovering the system matrices from Impulse Response Functions (IRF) is outlined in (Ho and Kalman, 1966). Refinements of the method were further developed by introducing singular value decomposition (SVD) as a tool to reduce the noise inference in the IRF measurements (Zeiger and McEwen, 1974; Kung, 1978). The SVD-based system realization was firstly adapted for modal identification and named as Eigensystem Realization (ERA) (Juang and Pappa, 1984). In parallel, stochastic system realization was also developed based on discrete-time stochastic state-space equation (Akaike, 1974), and was extended to apply to modal identification in middle of 1980s (Benveniste and Fuche, 1985).The key feature of the stochastic system

realization is the system decomposition of the COV matrix instead of the IRF matrix, which is identical to the Natural Excitation Technique (NExT) proposed by (James et al, 1992). The principle of NExT suggests that correlation function (COR) of the random response of the structure subjected to natural excitation can be expressed as a summation of decaying sinusoids whose damped natural frequency, damping ratio and mode shape is identical to the one of the corresponding structural mode, therefore, COR can be employed as IRF to extract modal parameters in OMA. Actually, IRF, COR, Free Decay Response (FDR), as well as Random Decrement signature (RDD) can all be expressed as modal superposition or modal decomposition. Hence, major modal identification procedures developed in traditional EMA, such as the Least Square Complex Exponential (LSCE) and the Ibrahim time domain (ITD) methods, can be employed in OMA, which correspond to so-called Instrumental Variable method (Ljung, 1999). In this thesis, the covariance-driven SSI method is introduced.

a) *Factorization Property of output covariance*

The Covariance-driven SSI method is based on the factorization property of output covariance shown in equation (2.140). Substituting equations (2.120) and (2.125) in equation (2.140):

$$\begin{aligned} R_i &= CA^{i-1}G \\ &= C\Psi\Lambda_d^{i-1}\Psi^{-1}G \\ &= V\Lambda_d^{i-1}G_m \end{aligned} \tag{2.146}$$

where Λ_d is the discrete eigienvalue matrix and Ψ is eigenvectors, V is the modal output matrix determining the mode shapes. G_m is the 'next modal state-output' covariance matrix , which is similar to the modal participation matrix L in EMA. It is noted that the modal participation matrix can not be identified by G_m because of lacking of knowledge of the input.

It is observed that Λ_d and V, that is the undamped natural frequencies, modal damping ratios and mode shapes can be estimated by output covariance R .

The definition of the output covariance R is given in equation (2.54)

$$R_i = E\left[y_{k+i}y_k^T\right]$$

In reality the output covariance R is estimated as $\hat{R}$ in equation (2.55), because only a finite number N of data is available.

$$\hat{R}_i = \frac{1}{N}\sum_{i=0}^{N-1} y_{k+i} y_k^T$$

b) *Stochastic realization theory*

This section presents the main procedure of the covariance-driven SSI method, which is similar to the classical stochastic realization theory. Firstly, the estimated output covariance $\hat{R}_i$ are gathered in a block Toeplitz matrix as

$$T_{1|i} = Y_f (Y_p)^T = \begin{pmatrix} R_i & R_{i-1} & \cdots & R_1 \\ R_{i+1} & R_i & \cdots & R_2 \\ \vdots & \vdots & \vdots & \vdots \\ R_{2i-1} & R_{2i-2} & \cdots & R_i \end{pmatrix} \tag{2.147}$$

Applying the factorization property shown in equation (2.140) yields:

$$\begin{aligned} T_{1|i} &= \begin{pmatrix} C \\ CA \\ \vdots \\ CA^{i-1} \end{pmatrix} \begin{pmatrix} A^{i-1}G & A^{i-2}G & \dots & G \end{pmatrix} \\ &= O_i \Gamma_i \end{aligned} \tag{2.148}$$

where $O_i \in \mathbb{R}^{li \times n}$ and $\Gamma_i \in \mathbb{R}^{n \times li}$ are the extended observability and controllability matrix, respectively and given by:

$$\begin{aligned} O_i &= \begin{bmatrix} C & CA & ... & CA^{i-1} \end{bmatrix}^T \\ \Gamma_i &= \begin{bmatrix} A^{i-1}G & A^{i-2}G & ... & G \end{bmatrix} \end{aligned} \tag{2.149}$$

Applying the singular value decomposition (SVD) to matrix $T_{1|i}$ to reduce noise effect, lead to:

$$T_{1|i} = USV^T = \begin{pmatrix} U_1 & U_2 \end{pmatrix} \begin{pmatrix} S_1 & 0 \\ 0 & 0 \end{pmatrix} \begin{pmatrix} V_1^T \\ V_2^T \end{pmatrix} = U_1 S_1 V_1^T \tag{2.150}$$

where $U \in \mathbb{R}^{li \times li}$ and $V \in \mathbb{R}^{li \times li}$ are orthonormal matrices ($U^T U = UU^T = I_{li}, V^T V = VV^T = I_{li}$) and $S \in \mathbb{R}^{li \times li}$ is a diagonal matrix containing the positive singular values in descending order. SVD is a mathematical tool to estimate the rank of a matrix, which is determined by the

number of non-zero singular values. By omitting the non-zero singular values and corresponding singular vectors, the Toeplitz matrix $T_{1|i}$ is reduced to the product of $U_1 \in \mathbb{R}^{li \times n_r}$, $S_1 \in \mathbb{R}^{n_r \times n_r}$,

and $V_i \in \mathbb{R}^{n_r \times li}$. By comparing equation (2.148) and (2.150), O_i and Γ_i can be expressed as

$$\begin{aligned} O_i &= U_1 S_1^{1/2} \\ \Gamma_i &= S_1^{1/2} V_1^T \end{aligned} \tag{2.151}$$

From the definition of the extended observability matrix O_i and the reversed extended controllability Γ_i in equation (2.149), matrix C can obtained from the first l rows of matrix O_i and G is the last l columns of matrix Γ_i:

$$\begin{aligned} C &= O_i(1:l,:) \\ G &= \Gamma_i(:,l(i-1)+1:li) \end{aligned} \tag{2.152}$$

Two possible methods are proposed to determine the state transition matrix A. One of the methods consists in calculating the matrix A from the decomposition property of a shifted block Toeplitz matrix (Zeiger and McEwen, 1974):

$$T_{2|i+1} = O_i A \Gamma_i \tag{2.153}$$

where the shifted matrix $T_{2|i+1_i}$ is composed of covariance $R_k\,(k = 2,3...,2i)$. According to equation (2.151) and (2.153), matrix A is computed as

$$A = O_i^{\dagger} T_{2|i+1} \Gamma_i^{\dagger} = S_1^{-1/2} U_1^T T_{2|i+1} (S_1^{1/2} V_1^T)^{\dagger} \tag{2.154}$$

where † denotes the Moore-Penrose-inverse of a matrix.

Another method is proposed by (Kung, 1978). Matrix A is then computed by exploiting the shift structure of the extended observability matrix O_i:

$$A = O_i(1:l(i-1),:)^{\dagger} O_i(l+1:li,:) \tag{2.155}$$

Once matrix A and C are identified, the undamped frequencies, damping ratios and mode shapes can further be estimated by equations (2.120),(2.121) and (2.125):

$$A = \Psi \left[\backslash \mu_{i \backslash} \right] \Psi^{-1}$$

$$\lambda_i = \frac{\ln(\mu_i)}{\Delta t}, \omega_i = |\lambda_i| \frac{|\lambda_i|}{2\pi}, \quad \xi_i = \frac{-\mathrm{Re}(\lambda_i)}{\omega_i} \tag{2.156}$$

$$V = C\Psi$$

It is noted that the matrices A and C and the modal parameters are considered as estimated results, because in real experiments the measurements are not infinite and the output covariance actually are just an estimation of $\hat{R}_i$.

Theoretical, the rank of the Toeplitz matrix is the order of the system. With perfect noise-free data, the minimum order realization can be easily obtained by keeping only the non-zero Toeplitz singular values, as discussed in equation (2.150). With real or noise-contaminated data, however, the Toeplitz matrix tends to be full rank, thus making the problem of determining a minimum-order state-space model non-trivial. In this context, it is expected that there would be a significant drop in the singular values representing the "true" order of the system, while it rarely happens with real data. A reduced-order model obtained by retaining only 'significant' singular values tends to be poor in accuracy. In practice, an efficient procedure consists in construct the stabilization diagram, as already introduced in section 2.5.3. For the SSI-COV method, the SVD of the Toeplitz matrix $T_{1|i}$ once and the system matrices and the system poles in different order are determined by models including different number of singular values and the vectors. By comparing the poles corresponding to a certain model order with the poles of a one-order-low model, the stable poles are found and a stabilization diagram is efficiently constructed. The modal parameters are determined by interpreting the stabilization diagram.

Example

The SSI-COV method was applied to the preprocessed experimental data of the metallic frame structure. The output covariance $\hat{R}_i$ were estimated with a lag i=1,2,…,2i-1 with i=20 (an experience parameter defined according to user) to construct the $li \times li$ (40×40) Toeplitz matrix (equation 2.147). The singular values, yielded from the SVD of the Toeplitz matrix (equation 2.150) with a log scale, are plotted in Figure 2.13. After preprocessing of the experimental data, only 3 DOF were retained and the true model order is 6. It is also observed from Figure 2.13 that 6 singular values are significant, existing a "gap" between the 6th and 7th singular values, representing the true model order in the

processed experimental data . (equation 2.147)

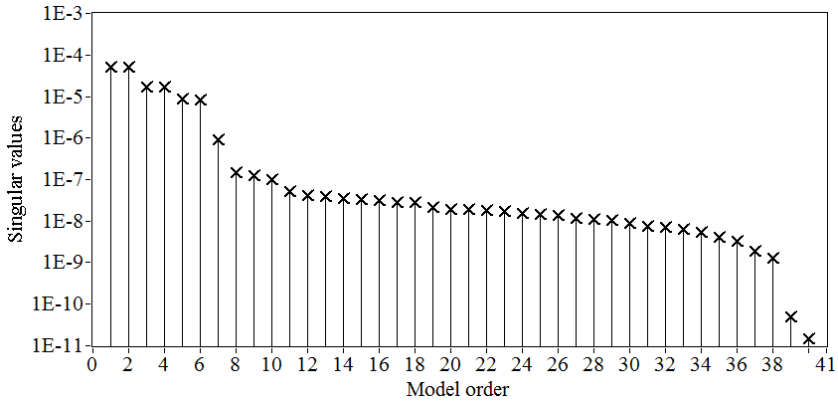

Figure 2.13 Singular values of the covariance Toeplitz matrix

A stabilization diagram was constructed by identifying the state-space model with orders n=2,3,…,40. The user defined criteria were 1% for frequencies, 3% for both damping and mode shape correlations. The symbol ´o´ in red represents a stable pole. The trace of the spectrum matrix is also plotted as a visual aid to select the stable poles though they are not related with the SSI-COV method. Inspection of Figure 2.14 shows that most of the stable poles concentrate around 5.28Hz, 15.16Hz and 22.34Hz. The modal parameters were computed from the identified model matrices *A* and *C* (equation 2.156). Detailed estimation results are presented at the end of this chapter.

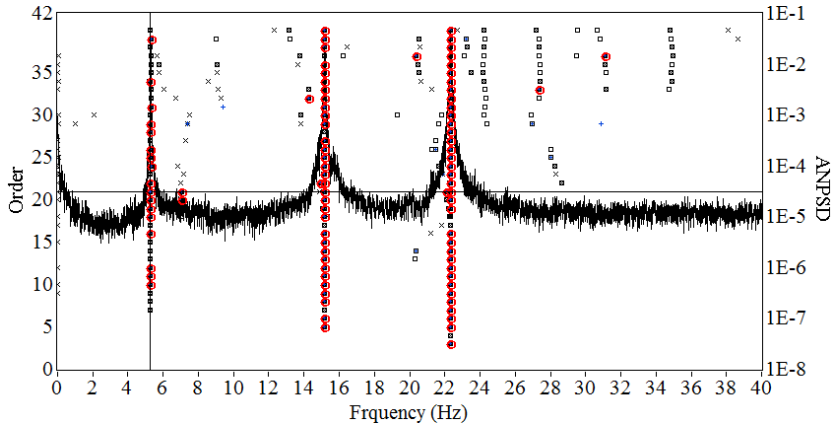

Figure 2.14 Stabilization diagram yielded by the SSI-COV method

2.7.3 Data-driven SSI method

Alternatively, modal parameters can be identified by data-driven SSI method by Overschee and De Moor. Detailed description of this method can be found in (Van Overschee and De Moor, 1996; Ljung, 1999). Instead of computing output covariance of output measurements, the data-driven SSI method starts with projecting the row space of future outputs into the row space of past outputs. Actually, the purpose of both covariance and

projections in different methods is to cancel out the uncorrelated noise. The following steps in data-driven SSI method are SVD and Least Squares, similar to covariance-driven SSI method. The principles of data-driven SSI algorithm are the Kalman filter states and the factorization property of projection matrix.

a) *Kalman Filter States*

The Kalman filter states play a crucial role in data-driven SSI method. The purpose of Kalman filter is to estimate the Kalman filter state $\hat{x}_k$ together with the observation of the outputs up to time *k*-1, system matrices and the noise covariance according to the forward innovation model indicated in section 2.6.4. If the initial state estimates $\hat{x}_0 = 0$, the initial covariance of the state estimates $P_0 = E\left[\hat{x}_0 \hat{x}_0^T\right] = 0$ and the output measurements $y_0, y_1 ... y_{k-1}$ are observed. The non steady state Kalman filter state estimates $\hat{x}_k$, the Kalman filter gain matrix K_{k-1} and Kalman state covariance matrix P_k can be derived as

$$\begin{aligned} \hat{x}_k &= A\hat{x}_{k-1} + K_{k-1}(y_{k-1} - C\hat{x}_{k-1}) \\ K_{k-1} &= (G - AP_{k-1}C^T)(R_0 - CP_{k-1}C^T)^{-1} \\ P_k &= AP_{k-1}A^T + (G - AP_{k-1}C^T)(R_0 - CP_{k-1}C^T)^{-1}(G - AP_{k-1}C^T)^t \end{aligned} \tag{2.157}$$

The Kalman filter state sequence $\hat{X}_i \in \mathbb{R}^{n \times j}$ is defined as

$$\hat{X}_i = (\hat{x}_i \quad \hat{x}_{i+1} \quad ... \quad \hat{x}_{i+j-1}) \tag{2.158}$$

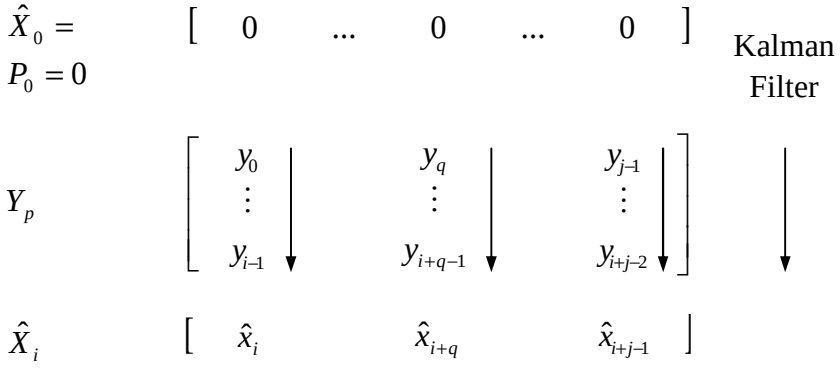

Figure 2.15 Non-steady Kalman filter state estimation based on output measurements

This sequence in equation (2.158) can be written as a linear combination of the past output measurements and is generated by a batch of non-steady state Kalman filters working

in parallel on each columns of the block Hankel matrix of past outputs Y_p, which is illustrated in Figure 2.15. This observation implies that the Kalman filter state sequence $\hat{X}_i$ can be determined directly from output data (Van Overschee and De Moor , 1996).

b) *Factorization Property of Projection Matrix*

The projection matrix is defined as projecting the row space of future outputs onto row space of past outputs

$$\mathrm{P} = Y_f / Y_p = Y_f (Y_p)^T (Y_p (Y_p)^T)^{\dagger} Y_p \tag{2.159}$$

where $Y_f \in \mathrm{R}^{li \times j}$, $Y_p \in \mathrm{R}^{li \times j}$ are the block Hankel matrices containing *future* and *past* outputs, respectively. The projection matrix is also equal to the product of the extended observability matrix O_i and the Kalman filter state sequence $\hat{X}_i$,

$$\mathrm{P} = O_i \hat{X}_i \tag{2.160}$$

This relation is based on the main theorem of SSI, whose proof is of (Van Overschee and De Moor, 1996). From equations (2.159) and (2.160), it is observed that the Kalman filter state sequence $\hat{X}_i$ can be determined by projecting the future outputs on past outputs.

It is noted that the equation (2.159) is just the definition and projection can not computed straightforward. In practice, the projection is computed by *RQ* factorization based on the Hankel matrix defined in equations (2.144) and (2.145),

$$Y_{0|2i-1} = \mathrm{P} = Y_f / Y_p = Y_f^+ / Y_p^- = RQ^T \tag{2.161}$$

where $Q \in \mathbb{R}^{j \times j}$ is an orthonormal matrix and $R \in \mathbb{R}^{2li \times j}$ is a lower triangular matrix.

Projecting the row space of future outputs Y_f onto row space of past outputs Y_p can be achieved by the *RQ* factorization of projection P_i:

$$\mathrm{P}_i = Y_f / Y_p = \begin{array}{c} \\ li \\ l \\ l(i-1) \end{array} \begin{array}{c} \begin{array}{ccc} li & l & l(i-1) \end{array} \\ \begin{pmatrix} R_{11} & 0 & 0 \\ R_{21} & R_{22} & 0 \\ R_{31} & R_{32} & R_{33} \end{pmatrix} \end{array} \begin{array}{c} j \to \infty \\ \begin{pmatrix} Q_1^T \\ Q_2^T \\ Q_3^T \end{pmatrix} \\ \begin{array}{c} li \\ l \\ l(i-1) \end{array} \end{array} \tag{2.162}$$

Substituting equation (2.162) in equation (2.159), projection matrix P_i is expressed by the product of *R* and *Q* submatrices as:

$$\mathrm{P}_i = \begin{pmatrix} R_{21} \\ R_{31} \end{pmatrix} Q_1^T \tag{2.163}$$

Similarly, projection P_{i-1} is computed by the alternative expression of future outputs Y_f^- and past outputs Y_p^+:

$$\mathrm{P}_{i-1} = \begin{pmatrix} R_{31} & R_{32} \end{pmatrix} \begin{pmatrix} Q_1^T \\ Q_2^T \end{pmatrix} \tag{2.164}$$

The factorization property applied to projecting matrices play a crucial role in data-driven SSI method. Once the projection of matrix P_i and P_{i-1} are available, the structure modal parameters can be estimated using these matrices.

c) *Estimation of system matrix*

Again, SVD is applied to estimate the rank of projection matrix. Theoretically, the rank is equal to the system order *n* and the number of the non-zero singular values. After omitting the zero singular values and corresponding singular vectors, the projection matrix is given as:

$$\mathrm{P}_i = U_1 S_1 V_1^T \tag{2.165}$$

where $U \in \mathrm{R}^{li \times li}$, $S \in \mathrm{R}^{li \times li}$ and $V \in \mathrm{R}^{li \times li}$. This step explains why these algorithms are called *subspace algorithms*: Only the subspaces consisting of singular vectors corresponding to non-zero singular values of the projection matrix are used to identify the system matrices.

Combining equations (2.160) and (2.165), the extended obsevability O_i is given by

$$O_i = U_1 S_1^{1/2} \tag{2.166}$$

Substituting equation (2.160) into equation (2.165),

$$\hat{X}_i = O_i^{\dagger} P_i \tag{2.167}$$

In order to identify system matrices *A* and *C*, another projection matrix is introduced by shifting one block row down in the Hankel matrix,

$$\mathrm{P}_{i-1} = Y_f^- / Y_p^+ = O_{i-1} \hat{X}_{i+1} \tag{2.168}$$

The extended observability matrix O_{i-1} is simply obtained by deleting the last *l* rows of O_i,

$$O_{i-1} = O_i\ (1 : l(i-1),:) \tag{2.169}$$

The state sequence $\hat{X}_{i+1}$ can be derived as

$$\hat{X}_{i+1} = O_{i-1}{}^{\dagger} \mathrm{P}_{i-1} \tag{2.170}$$

Substituting state sequences $\hat{X}_{i+1}$ and $\hat{X}_i$ into stochastic state-space model (2.134), yields

$$\begin{pmatrix} \hat{X}_{i+1} \\ Y_{i|i} \end{pmatrix} = \begin{pmatrix} A \\ C \end{pmatrix} \hat{X}_i + \begin{pmatrix} W_i \\ V_i \end{pmatrix} \tag{2.171}$$

where W_i, V_i are residuals, and $Y_{i|i} \in \mathbb{R}^{l \times j}$ is the *i*-th block row of the Hankel matrix. It is easily written, according to *RQ* submatrices in equation (2.161),

$$Y_{i|i} = \begin{pmatrix} R_{31} & R_{32} & R_{33} \end{pmatrix} \begin{pmatrix} Q_1^T \\ Q_2^T \\ Q_3^T \end{pmatrix} \tag{2.172}$$

By now, state sequences $\hat{X}_{i+1}$, $\hat{X}_i$ and block row $Y_{i|i}$ are calculated from output measurements, and system matrices *A* and *C* can be computed by the least square method:

$$\begin{pmatrix} A \\ C \end{pmatrix} = \begin{pmatrix} \hat{X}_{i+1} \\ Y_{i|i} \end{pmatrix} \hat{X}_i{}^{\dagger} \tag{2.173}$$

Identification of matrices *A* and *C* is sufficient to estimate the modal parameters following the equation (2.156) discussed in section 2.6.2. System poles and mode shapes are given as

$$A = \Psi \left[\backslash \mu_{i \backslash} \right] \Psi^{-1}$$

$$\lambda_i = \frac{\ln(\mu_i)}{\Delta t}, \omega_i = \frac{|\lambda_i|}{2\pi}, \quad \xi_i = \frac{-\mathrm{Re}(\lambda_i)}{\omega_i}$$

$$V = C\Psi$$

It is noted that the the matrices *A* and *C* identified from output measurements are only an estimation (denoted as $\hat{A}$ and $\hat{C}$) of the 'true' system matrices, because only finite data length is available.

Due to noise of the measurements in practice, the model order *n* can not be determined

by simply counting the number of non-zero singular values of matrix S_1 (equation 2.165). The expected 'gap' between successive singular values is also not obvious in real experiments. To solve the order determination problem, the stabilization diagram used in P-LSCF and SSI-COV are implemented again. Models of different order are then obtained and used to construct a stabilization diagram by considering a different number of singular values and corresponding vectors in equation (2.165). Modal parameters are estimated by interpreting the stabilization diagram.

Example

The SSI-DATA method was also applied to the preprocessed experimental data. The experience parameter *i* was set as 20, like in the SSI-COV method. The first step of SSI-DATA is to gather the output measurements in a block Hankel matrix with $2il \times N$ (80×89961). Next the *R*-factor of Hankel matrix is computed to construct the projection matrix P_i. The singular values of the SVD of the projection matrix P_i (equation 2.164) are shown in Figure 2.16. It is also observed from Figure 2.13 that 6 singular values are significant and that there is a "gap" between the 6^{th} and 7^{th} singular values, representing the true model order in the processed experimental data.

A stabilization diagram was constructed identifying state-space models of orders n=2,3,...,40. The user defined criterions are 1% for frequencies, 3% for both damping and mode shape correlations. The symbol ´o´ in red represents a stable pole. The trace of the spectrum matrix is also plotted as a visual aid to select the stable poles. It is clear from Figure 2.17 that most of the stable poles concentrate around 5.28Hz, 15.16Hz and 22.34Hz. The modal parameters were computed from the identified model matrices *A* and *C* (equation 2.156), and the detailed estimation results are presented at the end of this chapter.

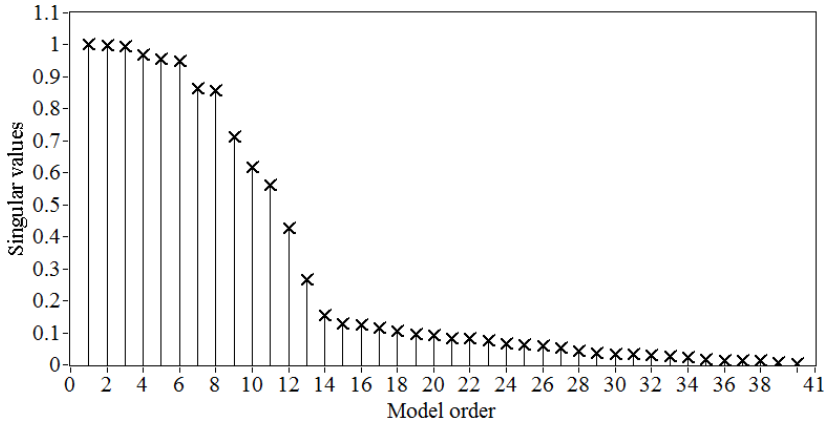

Figure 2.16 Singular values of the projection matrix

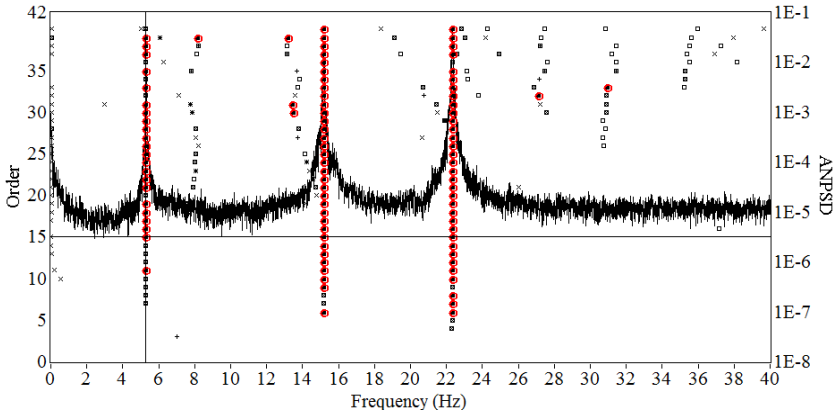

Figure 2.17 Stabilization diagram obtained with the SSI-DATA method

A complete system identification procedure comprises not only the estimation of matrices *A* and *C*, but also of matrices *G*, R_0. Identification of full state-space matrices *A*, *C*, *G* and R_0 in data driven SSI method leads to a postprocessing procedure including spectrum analysis, modal decomposition and prediction errors.

2.7.4 Summary

In this section, two stochastic subspace identification methods based on output measurements from a system subjected to stochastic excitation are introduced. Both approaches share similar procedures for modal parameters estimation. In the covariance-driven SSI method, original output measurements stem from *l* sensors and *N* samples in each sensor. The Toeplitz matrix $T_{1|i} = Y_f Y_p$ based on covariance between 'future outputs' and 'past outputs' reduce the data matrix from $l \times N$ to $li \times li$.In the data-driven SSI algorithm, a similar data reduction procedure is used by projecting the row space of future outputs to row space of past outputs $\mathrm{P} = Y_f / Y_p$, which is obtained by *RQ*-factorization of the data Hankel matrix. Following the data reduction procedure, SVD is utilized in both approaches to reveal the order of the system and reduce noise inference. However, the true system order is difficult to determine, because of noise effect in practical measurements. An efficient stabilization diagram is used to identify a whole set of models of different orders. Finally, the system matrices *A* and *C* in both approaches are estimated by Least Square technique and modal parameters are thus estimated.

There are also some differences between the covariance-driven SSI method and the

data-driven SSI approach. The construction of the Toeplitz matrix in the covariance-driven SSI is much faster than the *QR*-factorization of the Hankel matrix. Theoretically, the data-driven approach is numerically more robust due to its square root algorithm, comparing the matrix square up in covariance-driven SSI method. Apart from these differences, postprocessing tools such as closed-form solution of spectrum and modal decomposition of total response are also available in data-driven SSI approach (Petters, 2000).

2.8 COMPARISON OF DIFFERENT MODELS AND MODAL IDENTIFICATION METHODS

This section presents a comparison between the modal parameters computed or estimated by different models and modal identification methods. A modal test of a metallic frame was described in section 2.2. On the one side, the experimental data acquired can be used to clarify the complex theory previous described. On the other side, modal parameters computed by theoretical and numerical models can also be used to get confidence on the estimates achieved by different operational modal identification methods in both frequency and time domains. Besides, a systematic comparison of the modal identification results can be used to evaluate the performance of different operational modal identification techniques. So, the practical implementation of the identification models and identification methods was introduced to illustrate the theoretical development. Table 2.1 synthesizes natural frequencies, modal damping ratios and mode shape results. It is noted that the damping ratio can not be computed directly by analytical models, being only estimated by experimental methods. The damping ratio results estimated by PP method are not listed because the half-power bandwidth damping ratio estimation method is not reliable and the EFDD method evolved from PP method can provide more objective and accurate estimation of modal damping ratios.

Theoretically, PP and EFDD modal identification techniques are usually classified as *non-parametric* estimation methods as pointed out in section 2.5.5, because they do not employ a parametric model in the search for a best description, which induces that the identification procedure becomes a relatively subjective task in case of noisy civil engineering experimental data or weakly-excited modes. For example, the half-power bandwidth damping

ratio estimation method is not reliable and only operational deflection shapes are identified instead of mode shapes. EFDD method can enhance the PP method by applying SVD to the spectra matrix, allowing for a rather objective estimation process especially for closely spaced modes. However, the quality of modal damping ratios and mode shape estimates depends on the selected singular vector around the resonance. On the contrary, the p-LSCF, SSI-COV and SSI-DATA are categorized as *parameter* estimation methods. The linear structural system is parameterized as a model using a parameter vector (matrix). Structural modal parameters identification then becomes a problem of estimating the parameter vector (matrix). For example, during the process of application of p-LSCF, FRF of a linear system are parameterized as RMFD model with polynomial coefficients α_r and β_r. By determining theses coefficients, solving a least squares problem, the modal parameters are estimated. Stochastic subspace algorithms (SSI-COV and SSI-DATA) begin idealizing the linear system using state space models with system matrices *A*, *B*, *C* and *D*. Modal parameters can be estimated by identifying system matrices *A* and *C* using least squares techniques. Besides, these parametric methods employ the stabilization diagram to identify the parametric model, allowing separating the true system poles from spurious ones and extract the modal parameters confidently.

Computation speed is another index to evaluate the performance of these modal identification techniques. PP method may be the fastest computation algorithm because the spectrum estimation consumes very short time. Thus, PP is especially suitable to check the quality of the experimental dates in the filed because of its rapidity. The computation time of EFDD, P-LSCF and SSI-COV are moderate. All three approaches require two stages to identify the modal parameters. The first step of EFDD and p-LSCF methods consists in estimating the half positive power spectra matrix. During the second stage, SVD and linear LS are applied in EFDD and p-LSCF, respectively. In the first stage of SSI-COV, a Toeplitz matrix can be computed by FFT rapidly. Afterwards, the SVD and LS mathematic algorithms are adopted for modal parameters estimation. The computation efficiency of these three methods is similar. Comparing with the four approaches previous mentioned, SSI-DATA algorithm is relatively slow owing to the *QR* factorization of the large size of Hankel matrix.

Considering the numerical accuracy and efficiency of these five modal estimation approaches, it may be recommended that for baseline (one time) operational modal analysis of structures, different methods are adopted, so that the results can be crosschecked, while for automatic modal identification of continuous dynamic monitoring data, it is advised that both the p-LSCF method in frequency domain and SSI-COV approach in time domain are employed, in order to achieve the most accurate modal estimates in a reasonable time.

Table 2.1 Modal parameter results computed by theoretical and numerical models, as well as those estimated by different experimental models and methods

Method		Frequency (Hz)	Damping (%)	Mode shape ϕ_1		
				ϕ_{11}	ϕ_{21}	ϕ_{31}
Analytical	Theoretical	5.40	/	1	0.82	0.46
	Numerical	5.35	/	1	0.81	0.45
Experimental	PP	5.28	/	1	0.88	0.48
	FDD	5.28	0.18	1	0.87	0.48
	P-LSCF	5.28	0.20	1	0.87	0.48
	SSI-COV	5.28	0.19	1	0.87	0.48
	SSI-DATA	5.28	0.19	1	0.88	0.48

Method		Frequency (Hz)	Damping (%)	Mode shape ϕ_2		
				ϕ_{12}	ϕ_{22}	ϕ_{32}
Analytical	Theoretical	14.93	/	1	-0.40	-1.14
	Numerical	15.02	/	1	-0.41	-1.14
Experimental	PP	15.18	/	1	-0.44	-1.22
	FDD	15.17	0.18	1	-0.44	-1.21
	P-LSCF	15.17	0.19	1	-0.43	-1.22
	SSI-COV	15.16	0.21	1	-0.44	-1.21
	SSI-DATA	15.16	0.21	1	-0.44	-1.21

Method		Frequency (Hz)	Damping (%)	Mode shape ϕ_3		
				ϕ_{13}	ϕ_{23}	ϕ_{33}
Analytical	Theoretical	21.16	/	1	-1.81	1.38
	Numerical	21.66	/	1	-1.82	1.39
Experimental	PP	22.35	/	1	-1.92	1.47
	FDD	22.33	0.12	1	-1.93	1.47
	P-LSCF	22.33	0.13	1	-1.88	1.46
	SSI-COV	22.32	0.11	1	-1.89	1.45
	SSI-DATA	22.33	0.12	1	-1.89	1.47

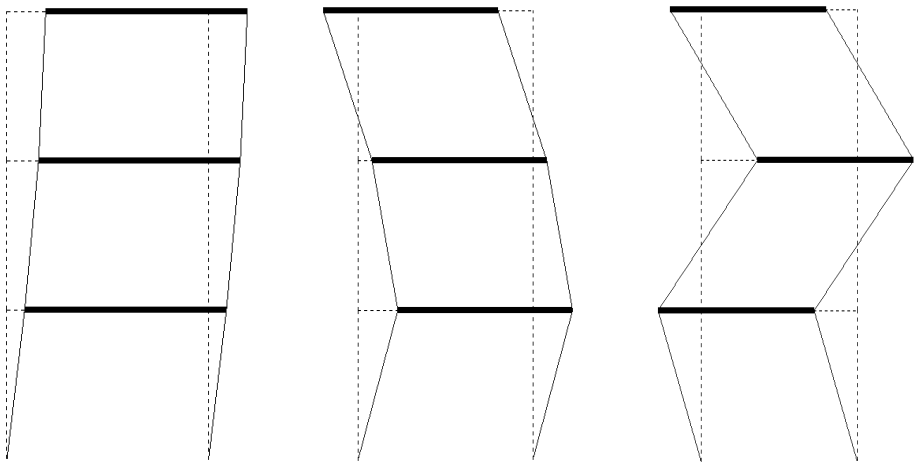

F**igure 2.18** Model shapes identified using SSI-COV

2.9 CONCLUSION

This chapter presents a state of art of operational modal analysis (OMA) and describes in detailed five of the most relevant methods. The relation between OMA and analytical formulations of analysis, as well as the connection between OMA and EMA are described to further clarify the theoretic foundation of modal identification based on output-only measurements. A modal test of a laboratory frame was performed to enhance the understanding of abstract concepts of the theory described. Finally, the performance of different OMA methods is briefly compared. This synthesis was essential to create a solid foundation for the implementation and application of these OMA methods to the real structures, in particular in the context of long-term structural health monitoring.

3

OMA SOFTWARE FOR AMBIENT VIBRATION TESTING AND CONTINUOUS DYNAMIC MONITORING

3.1 INTRODUCTION

Although some of the most relevant modal identification methods for Operational Modal Analysis (OMA) have been already introduced in chapter 2, it is important to refer how to implement these algorithms for application to structures in a friendly and frequent way. In this context, several commercial modal identification software packages have been developed worldwide based on these modal identification algorithms such as the Ambient Response Testing and Modal Identification Software (ARTeMIS, 2010). However, these dedicated software packages have some drawbacks in a research environment, since it is impossible to access the implementation of these algorithms and is not straightforward to add own developments for further application particularly related with automated modal identification for continuous dynamic monitoring. Moreover, there are also many toolboxes in a connection program for MATLAB-related third party productions, for example, Structural Dynamics Toolbox (SDTools, 2008) and MACEC (MACEC, 2011). However, the former only handles with experimental modal analysis (EMA), which is not suitable for the output-only OMA applications. Although the latter provides both EMA and OMA components, it does not comprise any possibility for automatic continuous dynamic monitoring, whose tasks involve automatic processing of massive acquired data, as well as the complex management and access of the results. Besides, all of these commercial software packages and toolboxes are

only dedicated to signal processing, not combining themselves with specific hardware for data acquisition. Therefore, it is clear the necessity to develop new programs aiming not only the structural modal identification and continuous monitoring, but that can be also integrated with data acquisition hardware to constitute a complete vibration-based continuous structural health monitoring system (Hu et al, 2007, 2008, 2010).

In this thesis, new computational tools for structural modal identification and long-term dynamic monitoring, developed in NI LabVIEW (National Instruments, Laboratory Virtual Instrument Engineering Workbench) environment, are described. They consist of two independent toolkits: SMI (Structural Modal Identification) toolkit is used for one time structural modal identification, whereas CSMI (Continuous Structural Modal Identification) toolkit is applied for continuous monitoring of structural systems. SMI toolkit is a user-friendly toolkit, implementing different system modal identification methods such as PP, EFDD, SSI-COV and SSI-DATA. This toolkit offers the possibility of data loading and preprocessing, system identification and model shape visualization. By pushing buttons, the user is guided through the whole process of structural modal parameters identification. CSMI toolkit is used for continuous dynamic monitoring comprising three components: an automated signal processing sub-toolkit, including automated vibration level detection algorithm and system identification based on SSI-COV approach; a database to organize the analytical results, in text and graph format, generated from signal processing sub-toolkit; and a user-friendly results visualization toolkit to access the analytical results conveniently. The CSMI toolkit can automatically search and process latest signal file, organize results and publish them.

NI LabVIEW software was chosen as the basic environment to develop these toolkits for OMA and long-term dynamic monitoring because that, on the one hand, it is an open environment offering computation, visualization and programming tools. On the other hand, it is convenient to link with a variety of NI data acquisition hardware.

3.2 OVERVIEW OF NI LabVIEW SOFTWARE

NI LabVIEW (National Instruments, Laboratory Virtual Instrument Engineering Workbench) is a graphical programming language that uses icons instead of lines of text to create applications. In contrast to text-based programming languages, such as Visual Basic, C++, JAVA and Matlab, where instructions determine the order of program execution, LabVIEW uses dataflow programming, where the flow of data determines the execution.

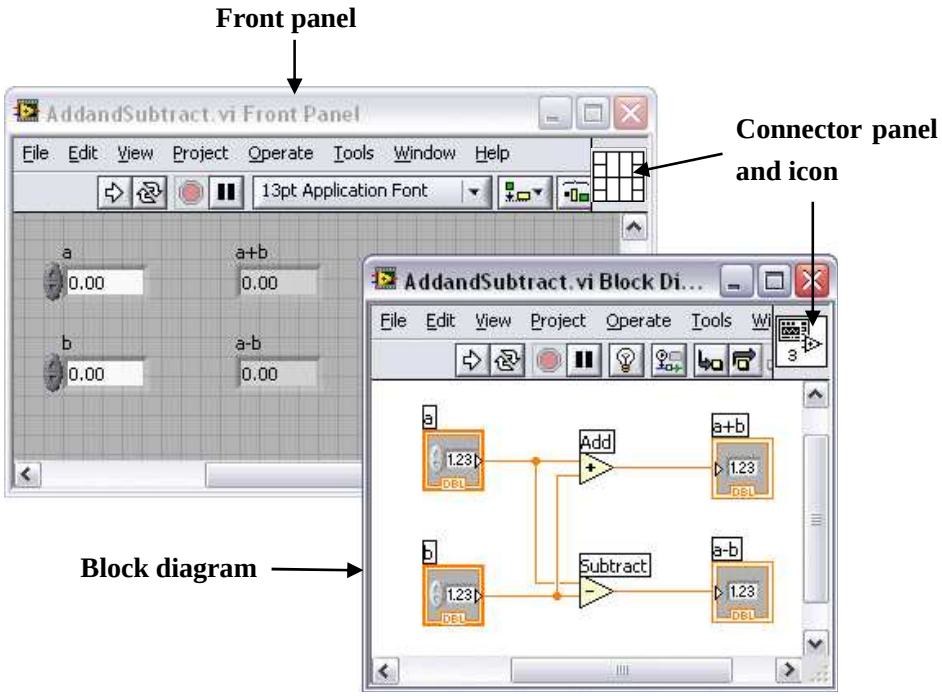

Figure 3.1 An example of front panel, block diagram, icon and connector panel

LabVIEW programs are called virtual instruments (VIs) because their appearance and operation imitate physical instruments, such as oscilloscopes and multimeters. A VI contains the following three components:

- Front panel, serving as the user interface;
- Block diagram, which contains the graphical source code that defines the functionality of the VI;
- Icon and connector pane that identifies the interface to the VI so that one can use the VI in another VI. A VI within another VI is called a subVI. A subVI corresponds to a

subroutine in text-based programming languages.

A simple example of VI including front panel, block diagram, icon and connector panel is shown in Figure 3.1.

The front panel is an interface built with controls and indicators, which are the interactive input and output terminals of the VI, respectively. Controls are knobs, push buttons, dials, and other input mechanisms. Indicators are graphs, LEDs, and other output displays. Controls simulate instrument input mechanisms and supply data to the block diagram of the VI. Indicators simulate instrument output mechanisms and display data the block diagram acquires or generates. Associated with the front panel, codes using graphical representation of functions are implemented to control the front panel objects. The block diagram contains such graphic source code, which comprehends terminals, nodes, wires and structures. The terminals represent the data type of the control and indicator in the front panel. The nodes are objects that have inputs and/or outputs and perform operations. They are analogous to statements, operators, functions, and subroutines in text-based programming languages. The wires transfer data among block diagram objects and the structures are graphical representations of the loop and case statements of text-based programming languages. The icon and the connector pane are built to customize a VI as a subVI. An icon is a graphical representation of a VI. The connector pane is a set of terminals that corresponds to the controls and indicators, similar to the parameters list of a function call in text-based programming languages. The connector defines inputs and outputs wired to the VI so that it can be used as a subVI (LabVIEW, 2010).

LabVIEW not only contains a comprehensive set of tools for acquiring, analyzing, displaying, and storing data, as well as tools for coding troubleshooting, but also several add-on software toolsets for developing specialized applications. Besides, it can be used to communicate conveniently with National Instruments (NI) hardware such as data acquisition, vision, and motion control devices, as well as GPIB, PXI, VXI, RS232, and RS485 equipments. All of these characters and advantages of LabVIEW software facilitate user involvement for the design and development of system in context of operational modal analysis and continuous dynamic measurements based structural health monitoring.

3.3 SMI TOOLKIT

This SMI toolkit was constructed with a main panel shown in Figure 3.2, comprising four main options: loading files, preprocessing, system identification and visualization of mode shapes. To perform each task, a new window is open and after finishing the desired task, the user can choose and return to the main menu to proceed with the following task.

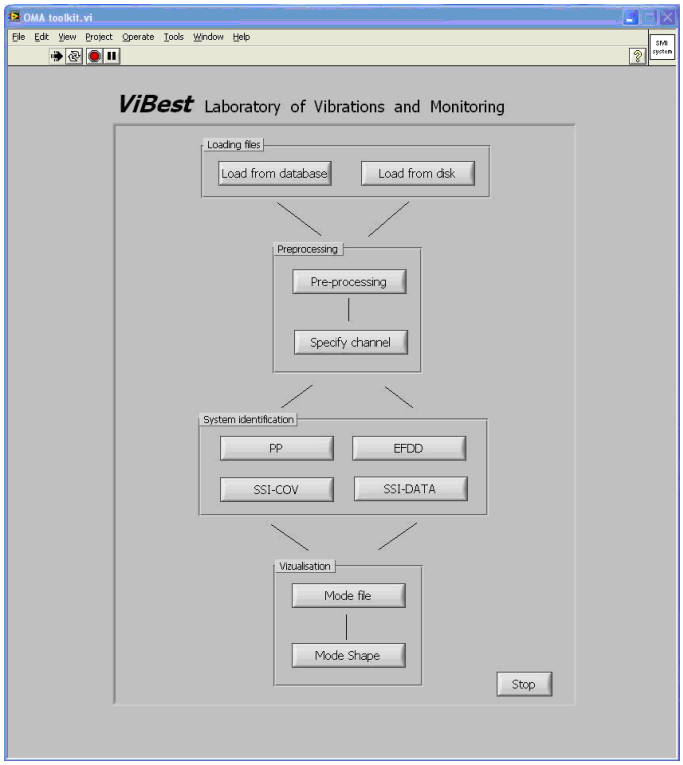

Figure 3.2 Main panel of SMI toolkit

3.3.1 Loading files

The toolkit provides two options to import signal files for modal identification: (i) load data from a database developed based on SQL (Structured Query Language) program or (ii) load signal files directly from local disk. After loading the signal files and defining the sampling frequency, the selected signals are listed and some signal information, such as signal length, maximum and minimum value and corresponding time or mean and variance values are detected or computed automatically. The user has also the choice to visualize the waveform graph of the selected signals in time domain. These functions are indicated in the

loading files menu shown in Figure 3.3.

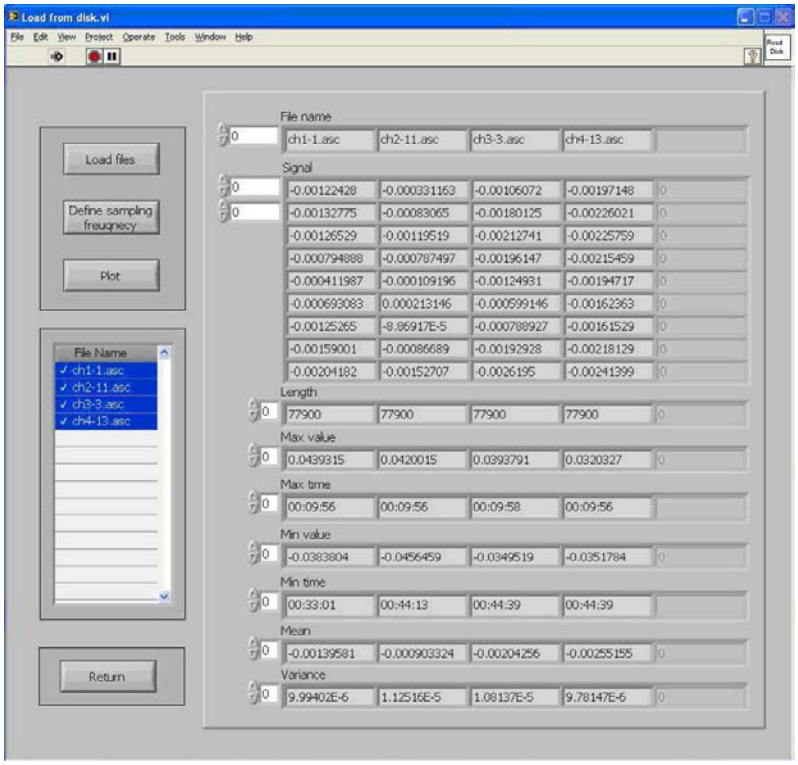

Figure 3.3 Loading files menu

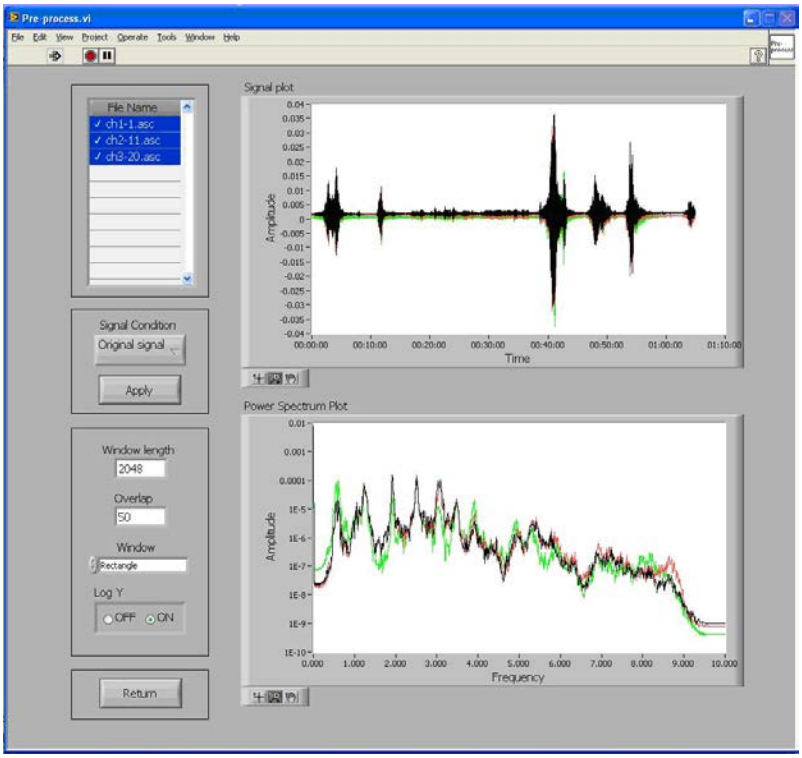

Figure 3.4 Preprocessing menu

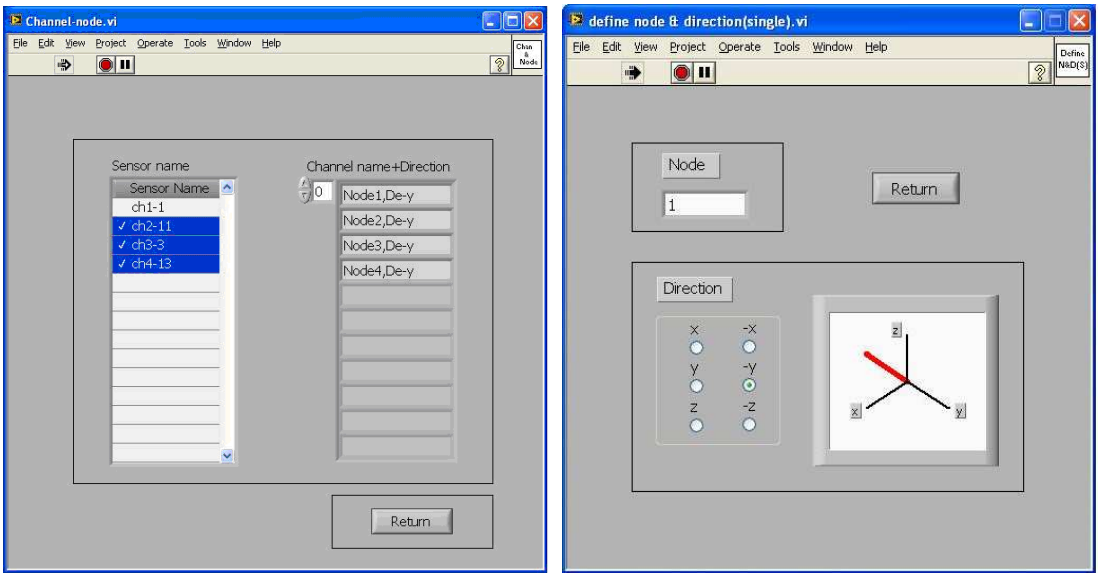

Figure 3.5 Menu for specification of the location and axis information of each channel

3.3.2 Preprocessing

After loading files, the user can begin the pre-processing task using the menu shown in Figure 3.4. Pre-processing is the data treatment before system identification and it highly influences the results. Functions such as signal decimation, detrend, digital filtering and FFT analysis have been implemented. The user can define the window length, overlapping and different windows for FFT analysis. The NPSD (normalized power spectrum density) graphs of each signal file have been also integrated. The effect of each function in the preprocessing procedure can be observed immediately after taking the choice.

For generating mode shapes, it is essential to incorporate the physical location and axis information of the measurement points. For that purpose the user can employ the window shown in Figure 3.5, specifying the location and axis of each channel.

3.3.3 System identification

Four complementary methods have been implemented in this toolkit: Peak-Picking (PP), Enhanced Frequency Domain Decomposition (EFDD), Covariance-driven and Data-driven Stochastic Subspace Identification methods (SSI-COV and SSI-DATA).

If the user chooses the PP method, a window with averaged normalized power spectrum (ANPSD) graph opens, as shown in Figure 3.6. The user can then choose the peaks in the

ANPSD graph and operational deflection shapes are determined according to the selected frequencies.

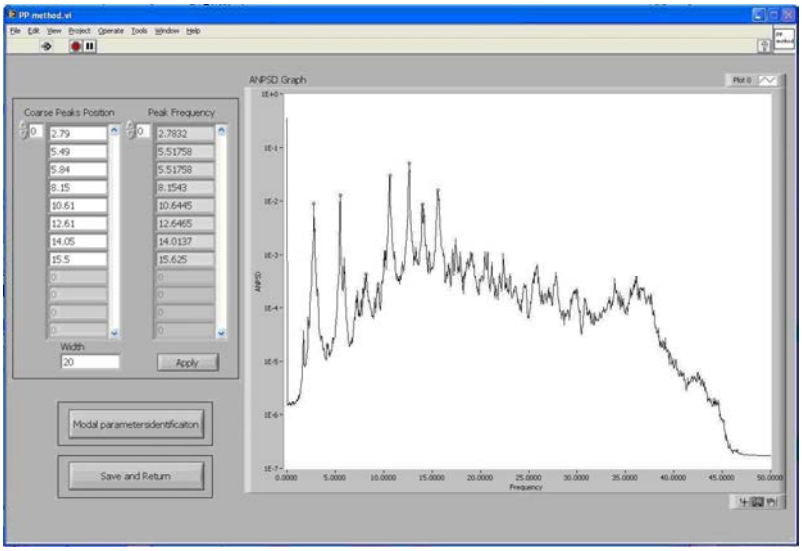

Figure 3.6 Peak-Picking menu

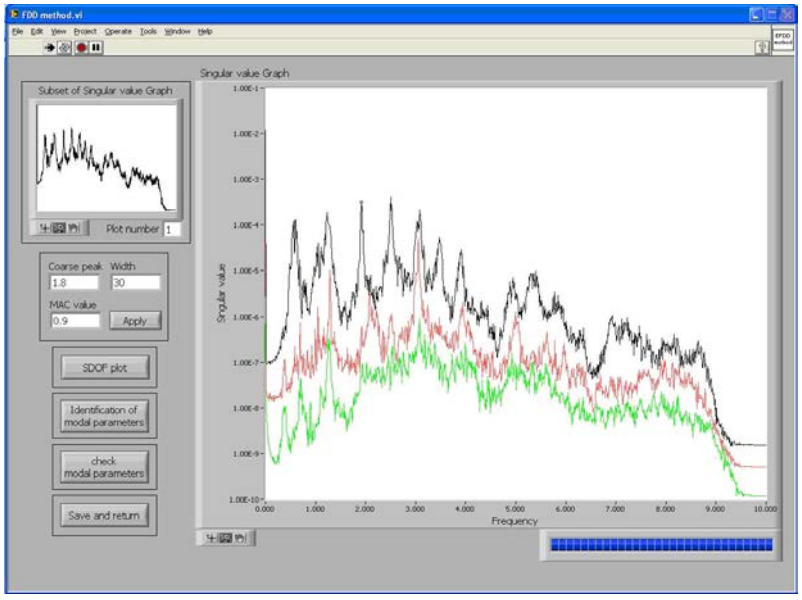

Figure 3.7 SVD curves obtained through EFDD menu

The second method is EFDD. Firstly, the singular value curves of spectrum matrices are calculated and plotted as shown in Figure 3.7. The user can select resonance peaks in different SVD curves. Then, a proper segment of SVD curve is selected near each resonance peak, based on a MAC criterion, and the corresponding free decay time domain curve is obtained using an inverse FFT. After application of spline interpolation on the free decay curve, a

smoother graph is obtained for curve fitting. By defining two proper peaks, a logarithmic decrement line will fit all the peak points of the free decay curve and refined natural frequency and damping ratio estimates can be obtained.

Beyond the above mentioned two identification algorithms in frequency domain, the SSI-COV and SSI-DATA methods in time domain have been also incorporated in this toolkit. Since SSI-COV and SSI-DATA share some similar procedures, a common interface window has been introduced. In the former case, for instance, the user should first specify expected maximum model order *n* and choose the model order range. After computation, a stabilization diagram as shown in Figure 3.8 is constructed. Then, the user can specify stricter stabilization criteria for better quality of the stabilization diagram. User can select a series of stable poles in a stabilization column, which corresponds to a certain resonance frequency. For visual reference, the ANPSD plot is represented together with that diagram.

3.3.4 Visualization

The identified mode shapes are graphically represented in specified menu (Figure 10), which offers the following possibilities: scrolling through all modes, representation of undeformed structure, 3D-view with different viewpoint and distance. The physical location and axis information were attributed to the channels in previous step (see section Preprocessing). Before visualization, a grid of nodes and the connection between the nodes in terms of beams and surfaces need to be defined.

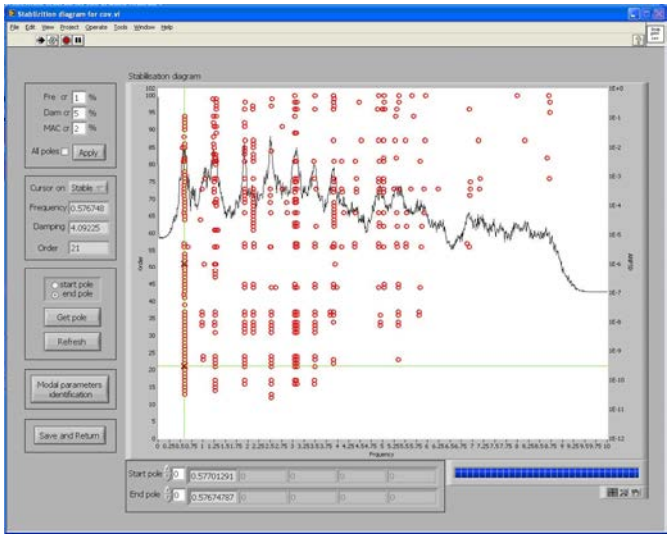

Figure 3.8 Stabilization diagram obtained through SSI-COV menu

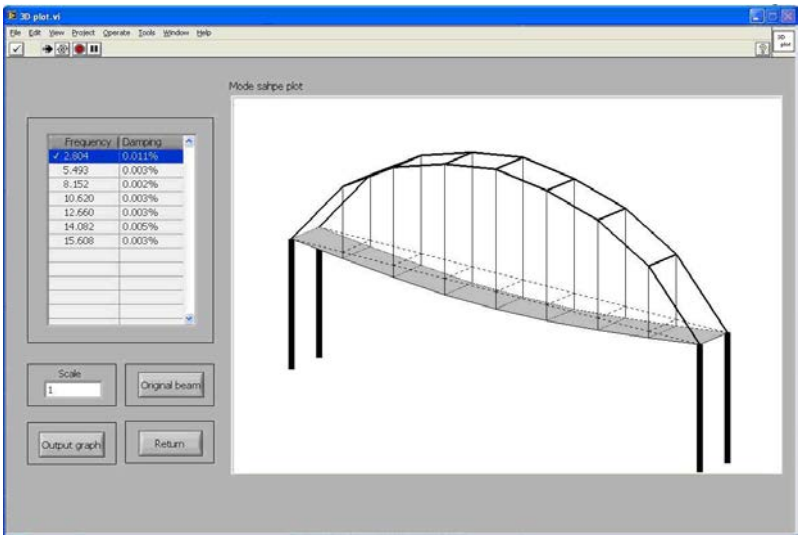

Figure 3.9 Mode shape visualization menu

3.4 CSMI TOOLKIT

CSMI toolkit is an automated signal processing, system identification, data management and result visualization program, with the main purpose of dealing with corresponding three different challenges in structure continuous dynamic monitoring: (1) automatic signal processing and system identification; (2) appropriate organization of the massive amount of signal files and analysis results; (3) easy visualization and access of analysis results via Internet. To achieve the goals, this program is divided into three parts as shown in Figure 3.10. First of all, an automated signal processing and system identification sub-toolkit is proposed without any manual operation and generating a series of results. Secondly, those analysis results, including text and graphic files are automatically saved into a database based on user-defined file folders in Window system for organizing massive results. Subsequently, a user-friendly graphic user interface (GUI) sub-toolkit provides immediate access to the analysis results by specifying different options such as time, position of the accelerometers, etc. This GUI toolkit may be published within the framework of a webpage, being useful in the context of remote monitoring by Internet.

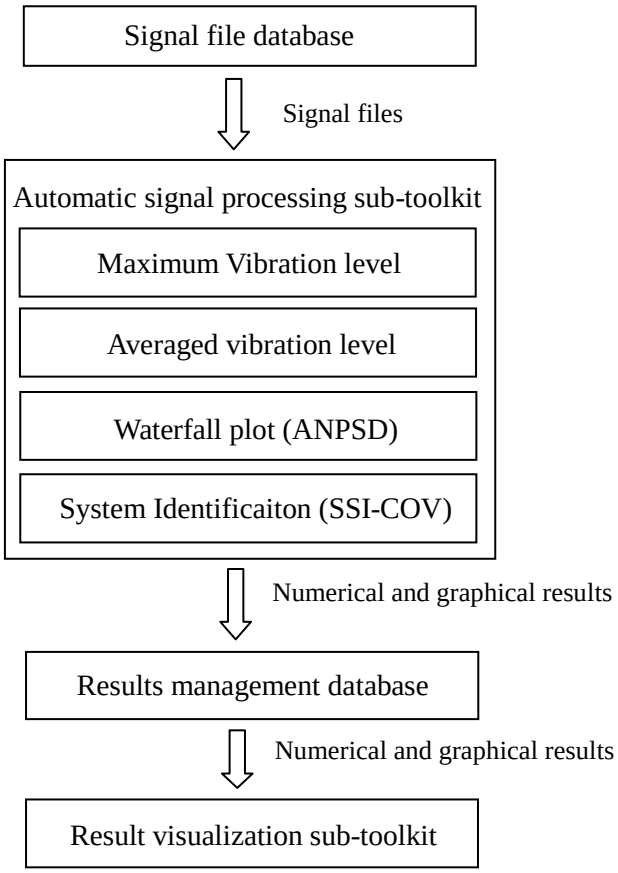

Figure 3.10 Architecture of CSMI

3.4.1 Automated signal processing sub-toolkit

a) *Algorithm for evaluation of averaged vibration level*

The purpose of evaluation of vibration level is to investigate if some vibration comfort limits are exceeded and analysis the effect of traffic intensity on the modal properties. A typical response comprehending acceleration signals from different sensors is shown in Figure 3.11.

The procedures of the proposed algorithm are the follows:

(i) Firstly, the envelope of each acceleration signal acquired from each individual accelerometer is calculated by Peak Detection Virtual Instrument (VI) based on multi-resolution wavelet analysis (LabVIEW, 2010). Using this VI, the peaks as well as valleys of the signal are detected, and the envelop is obtained. An example is shown in Figure 3.12.

(ii) Subsequently, the absolute averaged values of the envelope curve of each accelerometer in every hour are calculated.

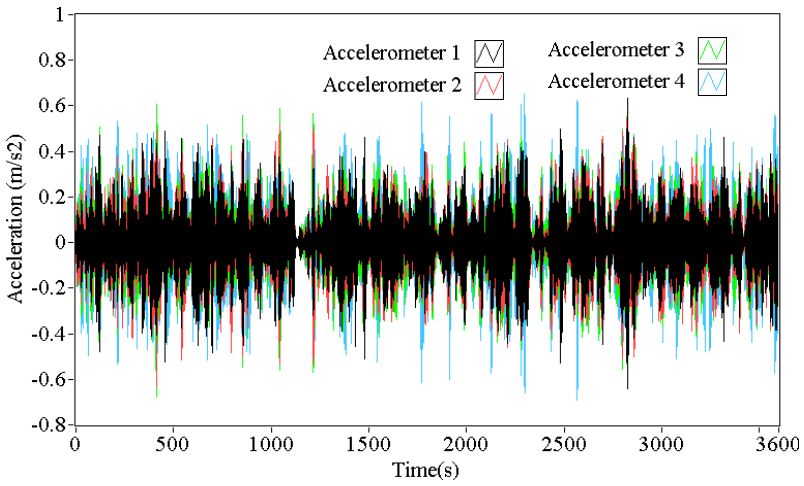

Figure 3.11 Typical acceleration time series

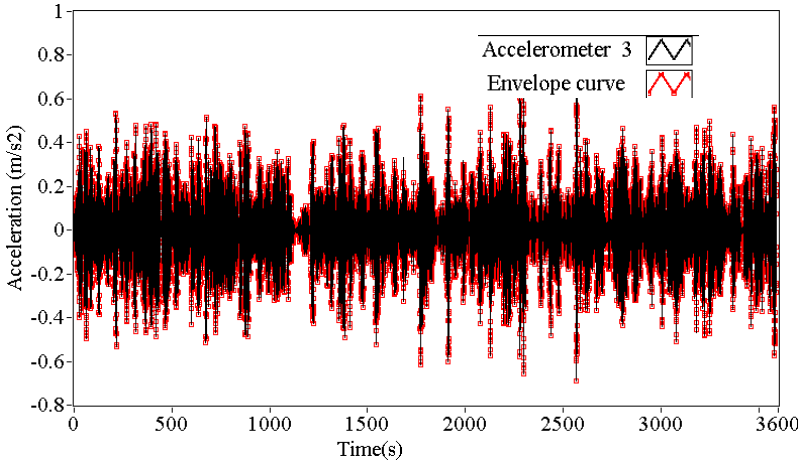

(a) Signal and its envelope

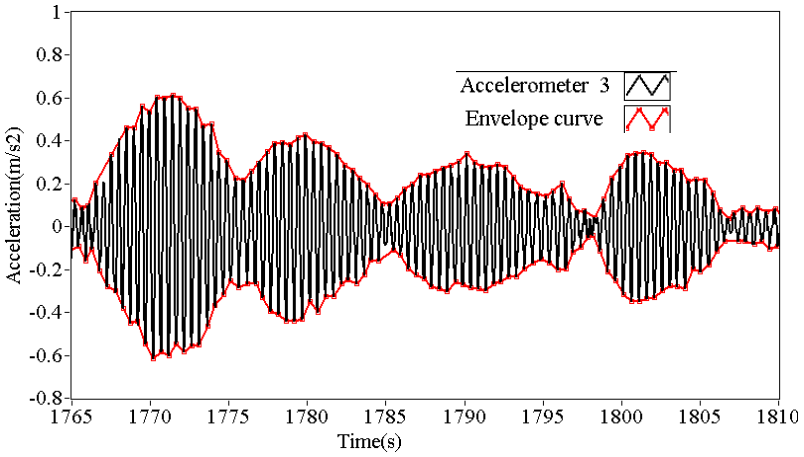

(b) Part of signal and its envelope

Figure 3.12 Signal from one accelerometer and its envelope

Figure 3.13 (a) shows the distribution of averaged acceleration amplitude from each accelerometer in one day. Averaged acceleration amplitudes from all the accelerometers are averaged again to obtain a global indicator or the vibration levels in every hour, as shown in Figure 3.13 (b). Figure 3.13 (c) plots the averaged acceleration amplitude in one month. It is clearly observed that consecutive peaks are presented in five working days and low vibration levels are exhibited at weekends. Yearly averaged vibration levels are evaluated in Figure 3.13 (d). Using this procedure, the vibration level under normal operational conditions is appraised efficiently.

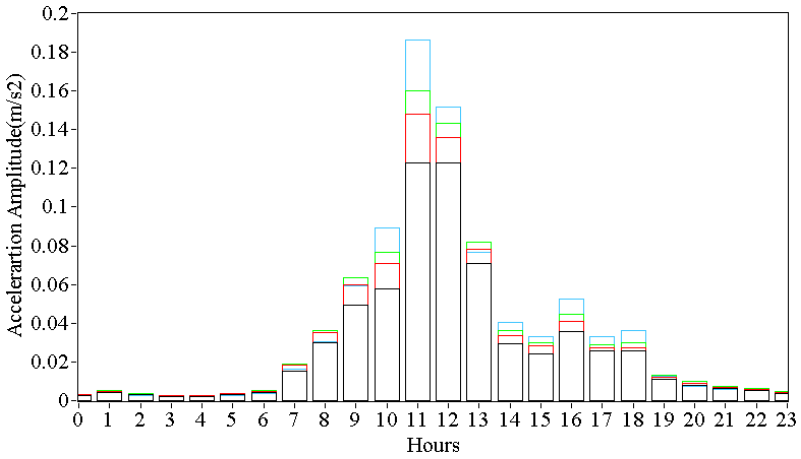

(a) Averaged amplitudes at each accelerometer during one day

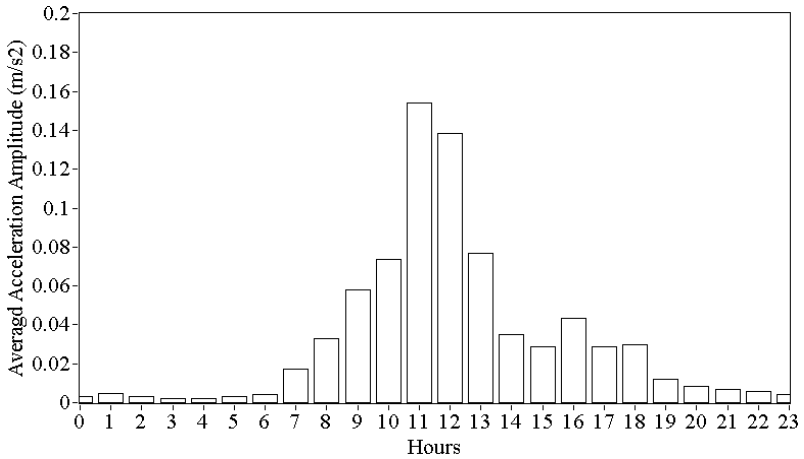

(b) Averaged amplitudes at all accelerometers

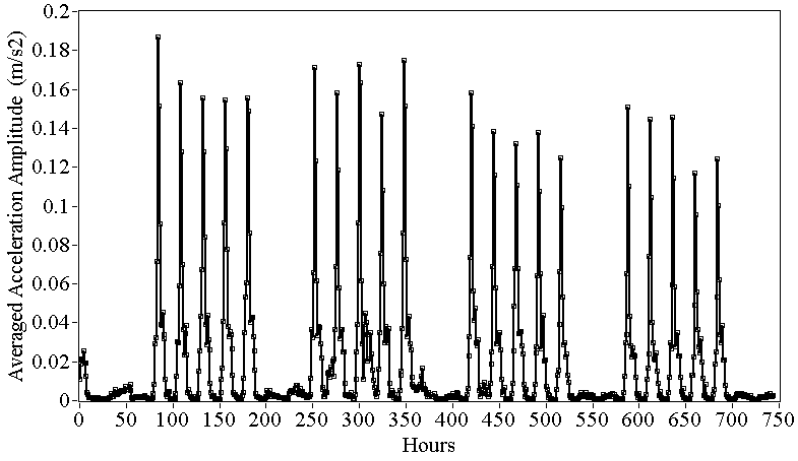

(c) Averaged amplitudes in all accelerometers in one month

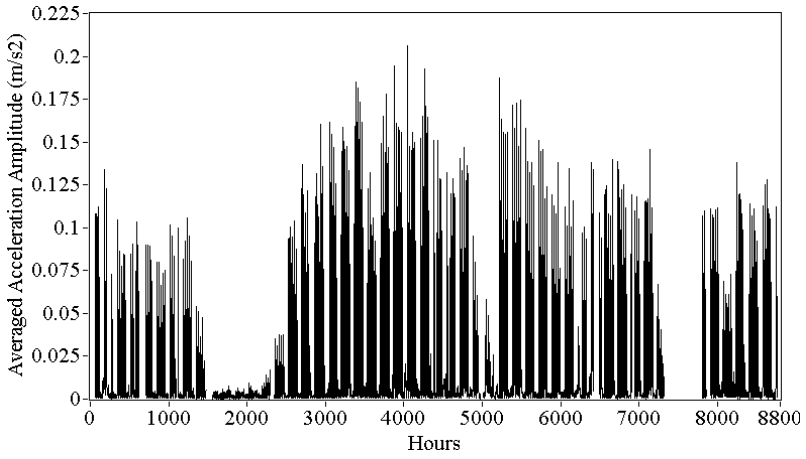

(d) Yearly averaged amplitude

Figure 3.13 Averaged acceleration amplitude in all accelerometers during one year

b) *Detection of maximum vibration level*

The accuracy of monitoring the vibration amplitude by picking the peaks directly may be disturbed by occasional spike noise. Therefore, the maximum vibration levels are detected by calculating the averaged vibration level of the absolute envelope in a user-defined short interval. The first step is also to detect the envelope of the vibration signals as described in the algorithm in evaluation of averaged vibration level. In a short user-defined time duration (eg. 1 second), the absolute envelope values are averaged. An example of averaged absolute envelope and zoom part are plotted in Figure 3.14 (a) and (b), respectively. In every hour, the maximum vibration level is detected and thus the daily maximum values are obtained. The monitoring results corresponding to each month and each year are obtained shown in Figure

3.14 (c) and (d). These values are used to describe the maximum acceleration response of bridges under normal operational conditions.

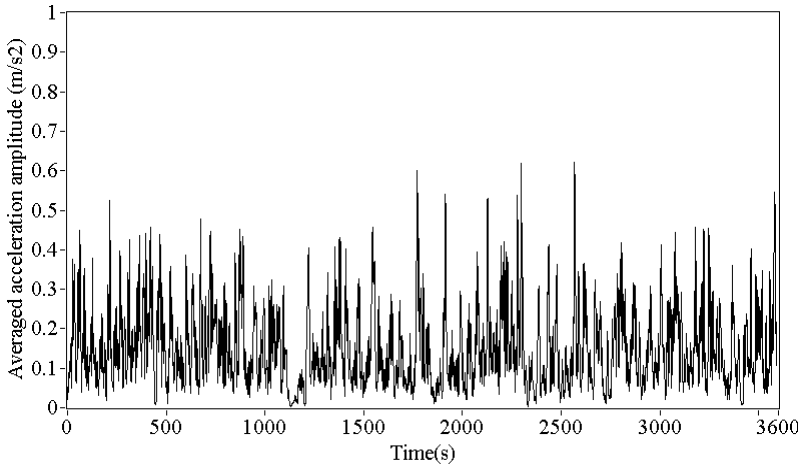

(a) Averaged absolute envelope within certain time interval

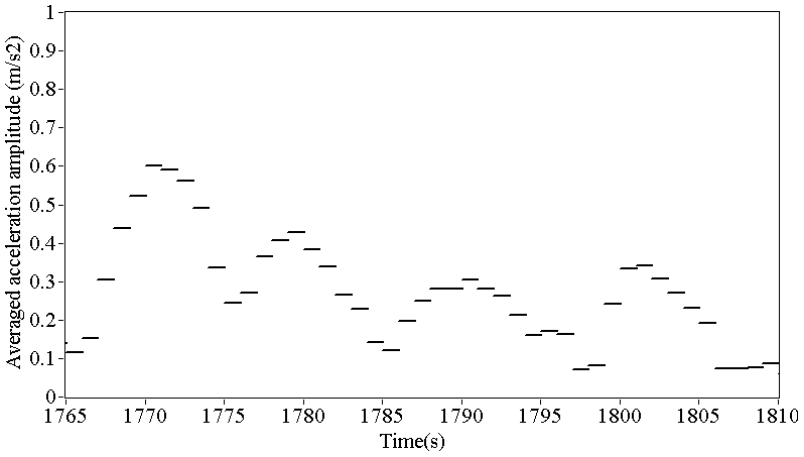

(b) Part of averaged absolute envelope within certain time interval

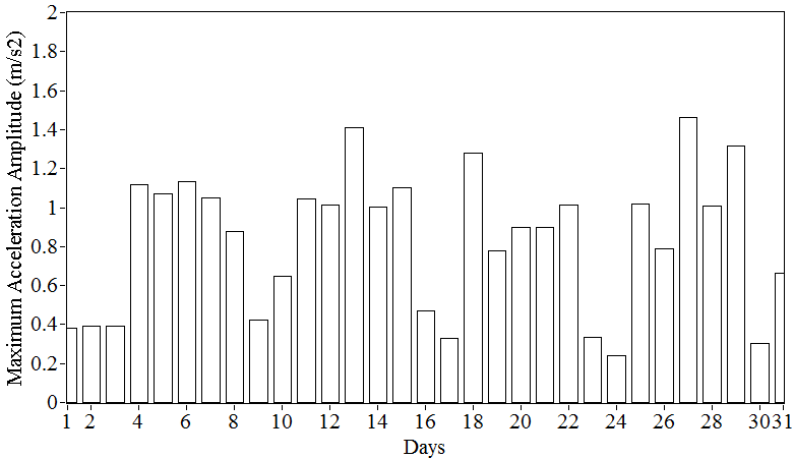

(c) Maximum amplitude in one month

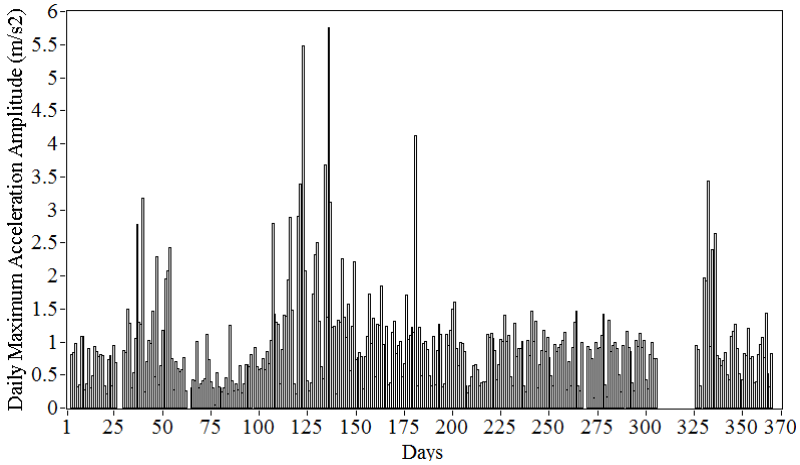

(d) Maximum amplitude in one year

Figure 3.14 Vertical maximum acceleration amplitude

c) *Waterfall plot*

CSMI also performs systematic frequency domain analysis of acquired data. By arranging sequences of ANPSD spectral estimates besides each other, 3D waterfall plots are obtained as shown in Figure 3.15 (a). 2D waterfall plots, as a top view of the 3D versions, can be also plotted, as indicated in Figure 3.15 (b). From 2D and 3D waterfall plots, the frequency component distribution is easily captured, allowing the observation of time variation of natural frequencies, as well as the identification of different intensity periods.

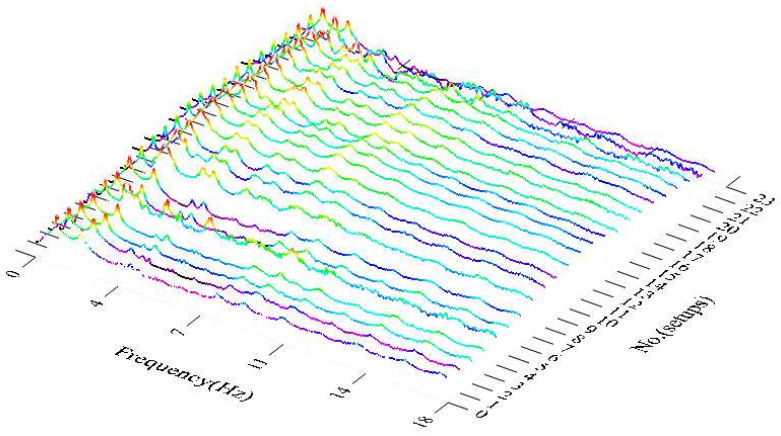

(a) 3D Waterfall plot (log scale)

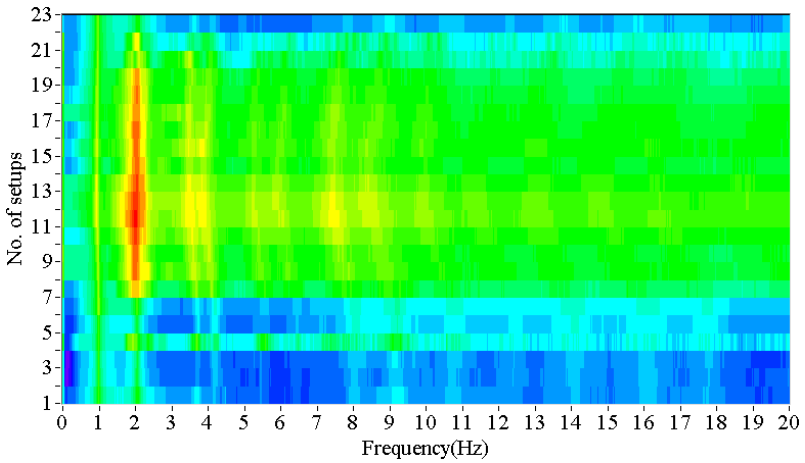

(b) 2D Waterfall plot (log scale)

Figure 3.15 Waterfall plots

d) *Automatic SSI-COV algorithm*

The automatic system identification procedure based on SSI-COV algorithm is implemented in the CSMI toolkit. It comprehends two steps: (i) construction of stabilization diagram and (ii) cleaning of stabilization diagram.

(i) Construction of stabilization diagram: The state-space model is estimated using correlation functions with a maximum length of i points. The maximum system order is n and the stable poles within certain system orders (m, $m+j$, $m+2j$,…, n, where m is the user defined lowest order and j is the increment of order) are considered. Poles are labeled as stable if the relative differences in the natural frequency (δf), modal damping ratio ($\delta\xi$) and modal assurance criterion (*MAC*) values between poles of consecutive orders are below the following threshold values:

$$\delta f \le 1\%, \quad \delta\xi \le 10\%, \quad (1-MAC)\times\% \le 5\%$$

Otherwise, the poles are classified as spurious or numerical. At the same time, the poles having unrealistic damping ratios (e.g $\xi \ge 10\%$) are discarded.

(iii) Cleaning of stabilization diagram: The stabilization diagram inevitably contains spurious or numerical poles which interfere with the automated estimation of modal parameters. It is observed (e.g. Figure 3.16 (a)) that the spurious poles are isolated, while the stable poles are concentrated around the structural natural frequencies. Therefore, the number of

spurious poles is smaller than the number of stable poles representing structure modes. In order to sort out these spurious poles, the procedure of cleaning of the stabilization diagram is implemented by treating all poles between *m* and *n* order as follows: (a) Different groups are established by examining the different modal parameters represented by the poles in the *m* order; (b) In the $(m+j)$ order, the new poles are incorporated into the corresponding groups if the relative difference of modal parameters is smaller than the threshold prescribed in step (i), however, if there are any poles in $(m+j)$ order which do not match with any groups defined in the previous step, a new group is assigned; (c) Step (b) is applied to the poles from $(m+2j)$ to *n* order and all poles are grouped; (d) Subsequently , a plot like the one presented in Figure 3.16 (b) is created through counting the number of poles inside each group and averaging all the frequency results of the same group. By inspecting this figure, it is observed that the stable poles representing structural modes are grouped together and the corresponding numbers are relatively large, while the spurious numerical poles are clustered in groups with a small number of elements. (e) Finally, a threshold for the numbers of poles *p* is prescribed and the groups whose number of elements is smaller than this threshold are removed. A stabilization diagram obtained after the application of the cleaning procedure is shown in Figure 3.16 (c). According to the information represented by the stabilization poles, the plot reflecting the relation between damping ratios and natural frequency estimates is displayed in Figure 3.16 (d). The modal parameters are estimated by averaging the frequencies, damping ratio and mode shape vectors within the selected groups of poles. The parameters of the algorithm *i, j, m, n* and *p* used for the automated modal identification in each application are defined by the user according to the quality of the continuous dynamic monitoring results.

According to the automatically identified results, the long term variation of natural frequencies and the modal damping ratios is obtained, as shown in Figure (a)-(d).

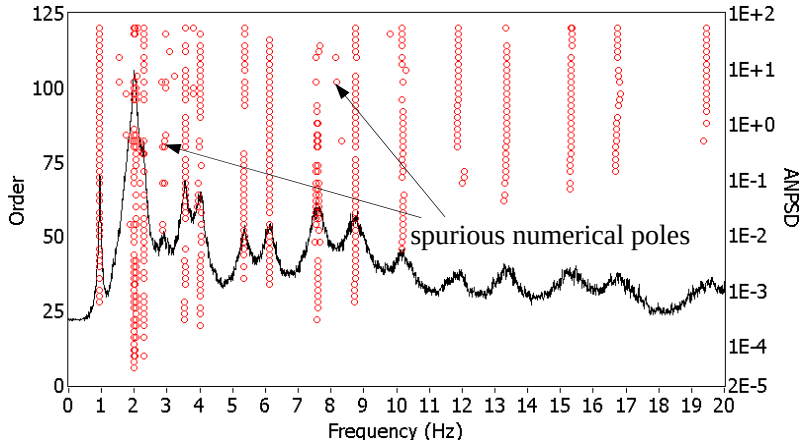

(a) Stabilization diagram

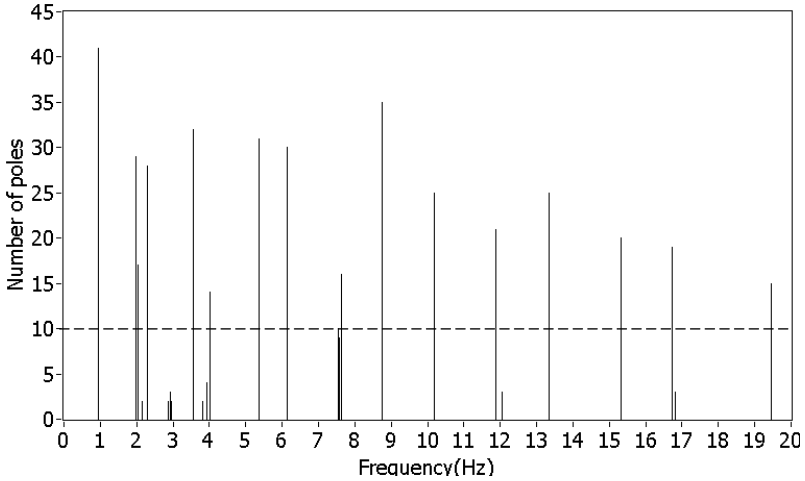

(b) Number of grouped poles

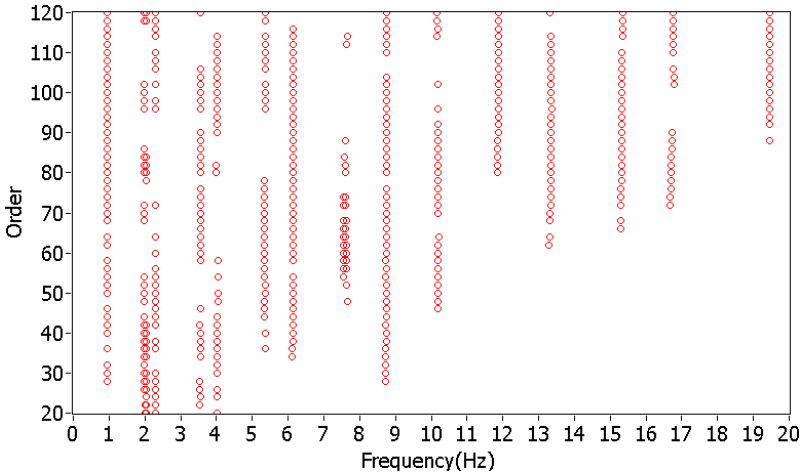

(c) Cleaning of stabilization diagram

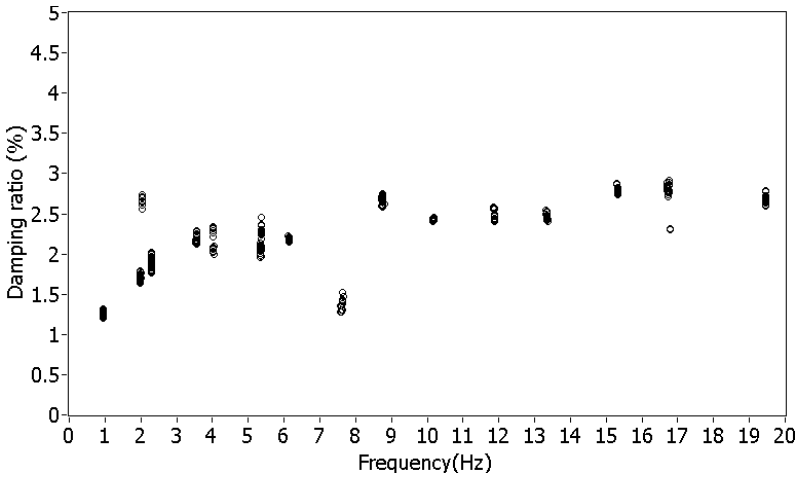

(d) Relation between natural frequencies and modal damping ratios estimates

Figure 3.16 Identification of physical modes based on automatic interpretation of stabilization diagrams provided by SSI-COV method

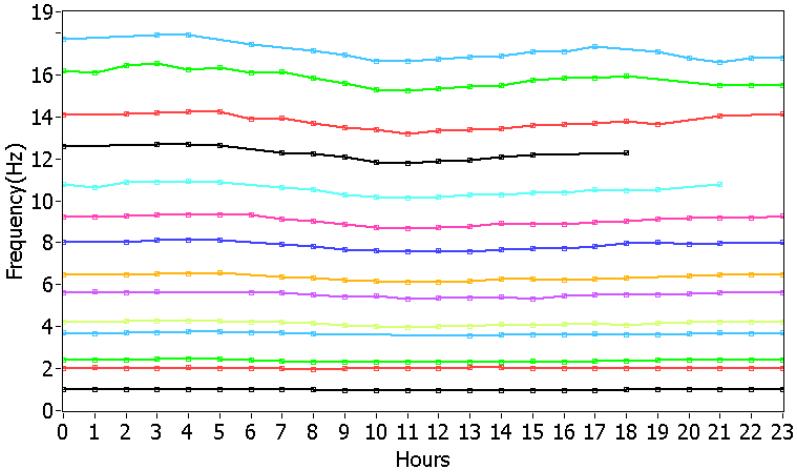

(a) Variation of natural frequencies during one day

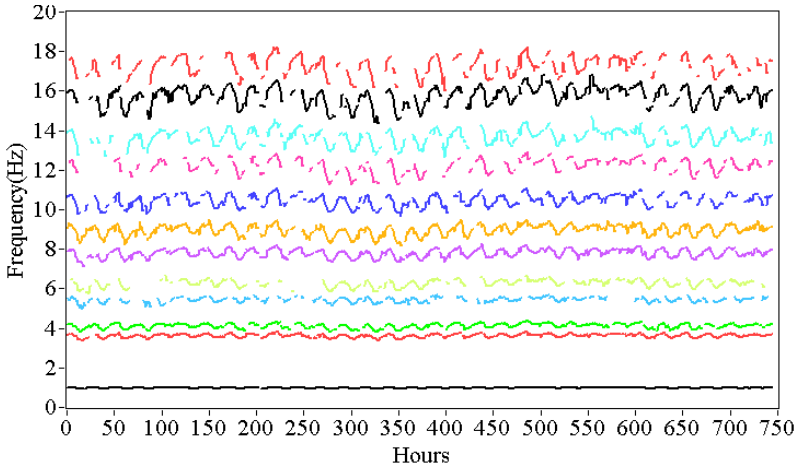

(b) Variation of nature frequencies during one month

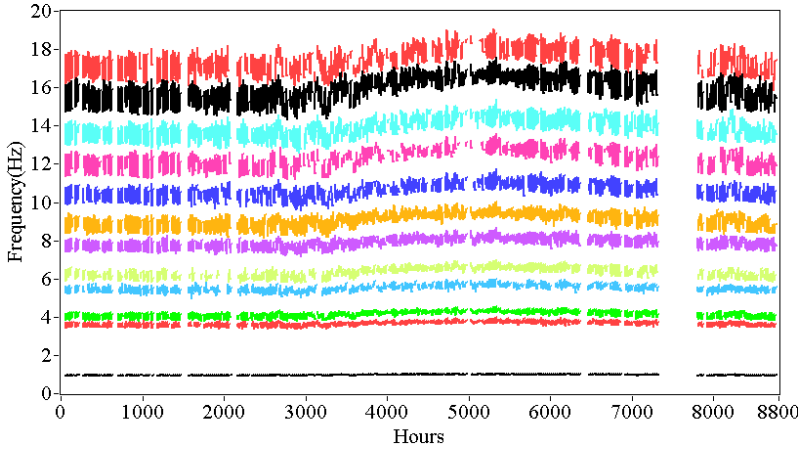

(c) Variation of natural frequencies during one year

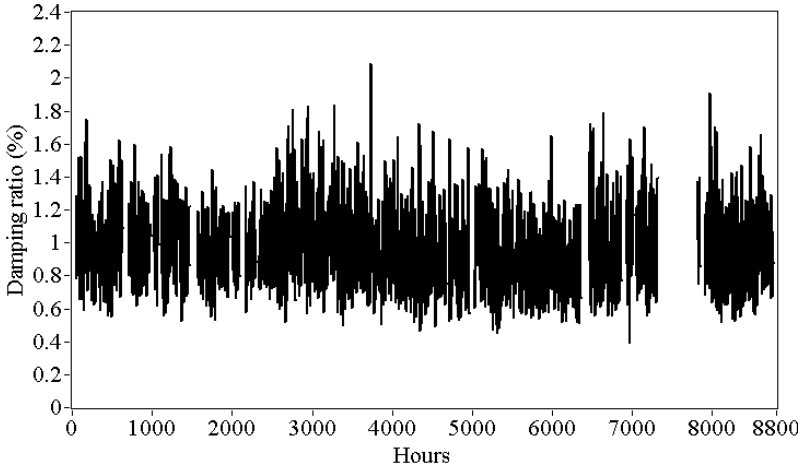

(d) Variation of the 1st modal damping ratio during one year

Figure 3.17 Variation of modal properties

3.4.2 Results management database

The results management system is a series of cascading hierarchical folders created in Window system. The main folder consists of three subfolders, ‘time domain’, ‘waterfall plot’ and ‘ssicov’, for saving the information stemming from the corresponding signal processing operations. They have similar structure, though they integrate different subfolders for saving different results. All specified directories for saving the processed results are conveniently implemented in the automated signal processing toolkit. When this toolkit operates, the processed results, both in TEXT format and PNG (Portable Network Graphics) format, are saved to local disk automatically. The size of each TEXT file is less than 10Kb and PNG file is no more than 15Kb. It is convenient to create new folders, as well as the corresponding save

directories used by the automated signal processing toolkit for application of the monitoring system to other structures.

3.4.3 Results visualization sub-toolkit

With the purpose of allowing a rapid and easy access of the user to long term dynamic monitoring results, the results visualization sub-toolkit was specially designed with a main panel and a series of subpanels.

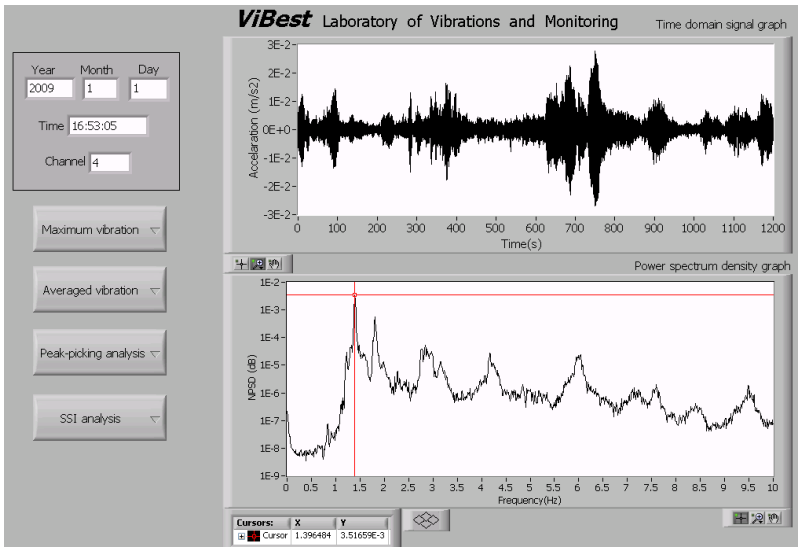

(a) Main panel

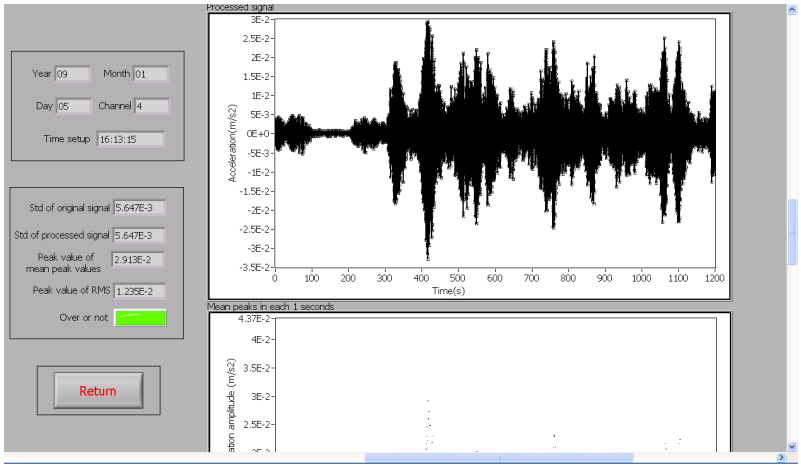

(b) Subpanel: Maximum vibration, current setup

Figure 3.18 Results visualization toolkit

Figure 3.18 (a) shows the main panel comprising three components: (a) five numerical indicators; (b) four pull down menus, and (c) two graph indicators. The user can specify

different time and channels in five numerical indicators to load the corresponding acceleration signals, using the ‘Time domain signal graphic’ indicator. In the meanwhile, the graphic of the normalized power spectrum density (NPSD) is also calculated and shown in ‘Power spectrum density graphic’ indicator. A red cursor in this graphic indicator can be used to detect the frequency values around each peak in PSD graphic and the frequency content of the vibration signal is clarified. The user can also apply ‘zoom’ and ‘move’ functions to search some more interesting parts of the plots shown using two graphic indicators. Four pull down menus, consisting of ‘Maximum vibration’, ‘Averaged vibration’, ‘Peak-picking analysis’ and ‘SSI analysis’, were included to load the results, both in PNG format and TEXT format, which are pre-processed by the automated signal processing toolkit and saved in the results management database. The user may click the menus, choose different options and enter a series of subpanels. One subpanel, ‘Current setup’ of main panel ‘Maximum vibration’, is shown in Figure 3.18 (b). In this way, the user can load all pre-processed results. The graphics are loaded directly and the analysis results are shown in table indicator on the left side of the subpanel, allowing the user to easily examine the analysis results, as well as the information when and where they occurred. By pushing ‘Return’ button in red, the user goes back to the main panel and makes another choice. The results visualization toolkit can also be linked by webpage, which permits the user to easily control this toolkit and access long term monitoring results via Internet.

3.5 CONCLUSION

This chapter introduces two toolkits developed in LabVIEW software for structural modal identification and continuous dynamic monitoring. The LabVIEW software was selected as development environment because of two advantages: One of them is that it is a graphical programming language offering a series of tools for acquiring, analyzing, displaying, and storing data, as well as several add-on software toolsets for developing specialized applications. Another reason is that it can be used to communicate conveniently with National Instruments (NI) hardware. These features and advantages of LabVIEW software facilitate the user to design and develop the system in the context of operational modal analysis and long

term structural health monitoring.

SMI (Structural Modal Identification) toolkit was developed for regular modal identification of structures, involving the implementation of the peak-picking (PP), frequency domain decomposition (FDD), covariance-driven and data-driven stochastic subspace identification (SSI) algorithms. It provides the possibility of pre-processing, system identification with different methods and results visualization with a user friendly interface.

In addition, CSMI (Continuous Structural Modal Identification) toolkit was developed for continuous dynamic monitoring. It consists of an automated signal processing sub-toolkit, results management database and results visualization sub-toolkit. Automated signal processing sub-toolkit searches the latest setup signal file, detects maximum vibration and averaged amplitudes both in vertical and lateral directions, and identifies the modal parameters continuously based on the covariance driven stochastic subspace identification (SSI-COV) methods. Based on continuously processed results in each setup, daily and monthly variations of maximum vibration amplitudes, averaged vibration amplitudes, as well as of modal parameters are also generated. All these analysis results are saved and organized in the results management database both in TEXT format and PNG format. The results visualization sub-toolkit allows the user rapidly to access these results and examine the short and long term behaviour of the structure.

4

APPLICATION TO THE AMBIENT VIBRATION TESTING OF EXISTING BRIDGES

4.1 INTRODUCTION

After introducing the theoretical background and corresponding implementations of OMA (Operational Modal Analysis), this chapter presents some applications to the dynamic testing of existing bridges. The first application is concerned with the evaluation of the change of modal properties induced by the rehabilitation of the centenary metallic roadway bridge over Douro River, at Pinhão. The second case study characterises the identification of modal parameters before and after the installation of Tuned Mass Dampers (TMDs) at Pedro e Inês footbridge, over the Mondego River at Coimbra. The last one depicts the variations of the modal results of a lively stress-ribbon footbridge in FEUP campus, by analyzing data from three ambient vibration tests performed in March 2003, October 2004 and October 2009.

4.2 OMA OF PINHÃO BRIDGE

4.2.1 Description of Pinhão Bridge

The Pinhão roadway Bridge crosses over the Douro River at the Pinhão village, located in the north of Portugal, and open to public in 1906. Nowadays, the bridge still plays a significant role in the road network linking the two banks of the Alto Douro wine region, also presenting a relevant historical heritage value, since it is part of the landscape of the Alto

Douro Wine Region, where was classified as World Heritage by UNESCO in 2001. Figure 4.1 shows an overview of this roadway bridge.

(a) Global view of Pinhão Bridge

(b) Location of Pinhão

(c) Overview of Village of Pinhão

(d) View of bridge from below

(e) View of bridge deck and select truss structure

Figure 4.1 Overview of Pinhão Roadway Bridge

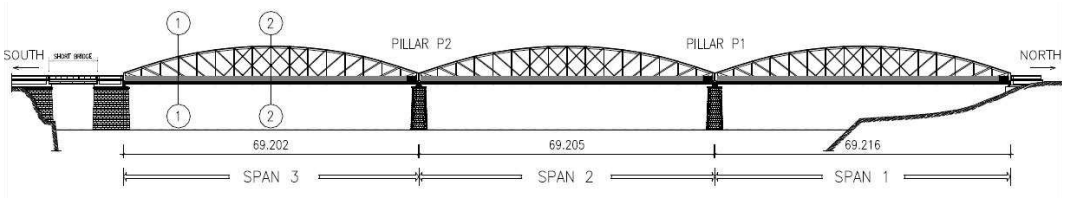

(a) Lateral view

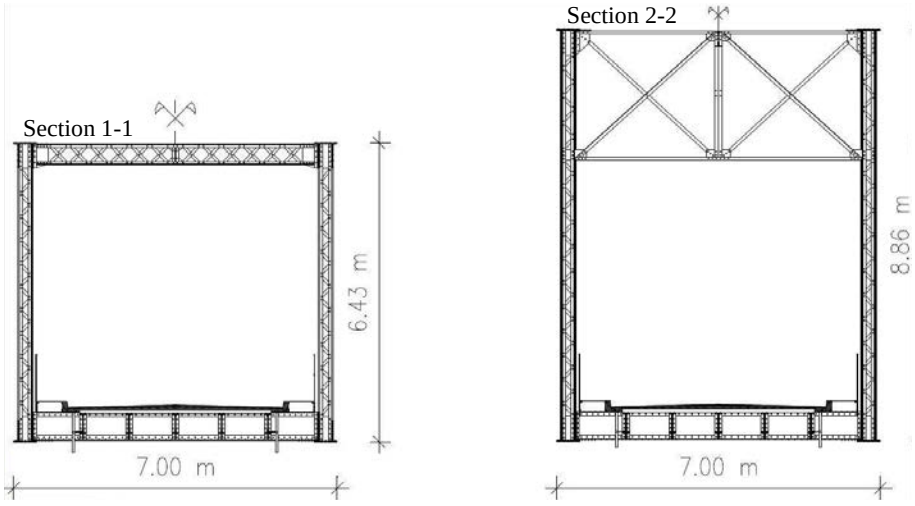

(b) Sections 1-1 and 2-2

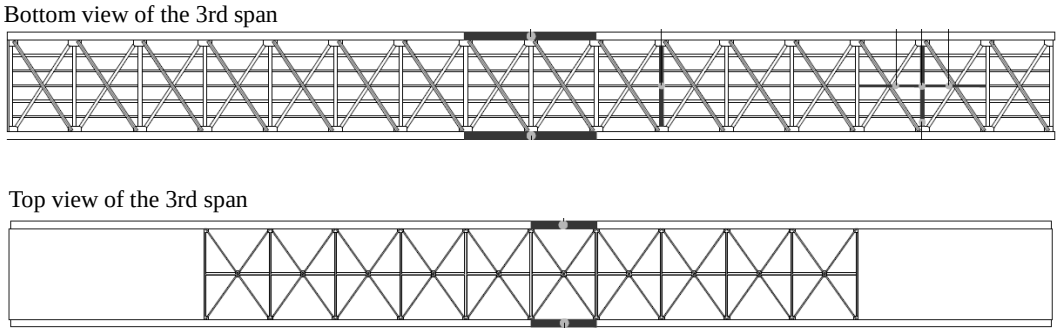

(c) Bottom and top plan view of deck in the 3rd span

Figure 4.2 Schematic representation of Pinhão roadway Bridge

Figure 4.2 (a), (b) depicts the characteristics of the bridge and corresponding cross sections. The bridge consists of a steel truss structure with three identical simply supported spans, presenting a total length of 207.623m and 8.86m of total height at the three mid-spans. The deck is approximately 7m wide between the two girders outer planes, and 0.75m high, throughout the longitudinal axis, including the 0.08m concrete and 0.02m asphalt layers, respectively. The deck area occupied by the two traffic lanes are 4.68m large, and are resting on a steel grid accomplished by 5 longitudinal and 17 transversal beams in each span. The two sidewalks are 0,675m wide, having a lateral handrail 1m height. The supporting grid beams

presented an “I” cross-section achieved by assembling plates and angles connected with rivets. Between each pair of transversal deck beams, there were two bracing bars “X” arranged (see Figure 4.2 (c)), materialised by double angles rivet connected. In each girder, for each span, the lower and upper chords are connected by columns and diagonals. The columns are formed by two pairs of laced angles, while diagonals were achieved by pairs of parallel rectangular cross bars. In each span, the lateral sway of both girders is prevented by truss bracings connecting them at the top.

Due to the aging and lack of efficient maintenance of the bridge in long history, the structure presented some anomalies related with the significant vibration of some of its elements, existence of cracks in the joints of the granite masonry at the support pillars, occurrence of material corrosion and degradation of the bearing supports, as shown in Figure 4.3 (Costa et al, 2008).

(a) Deterioration in the deck lower elements

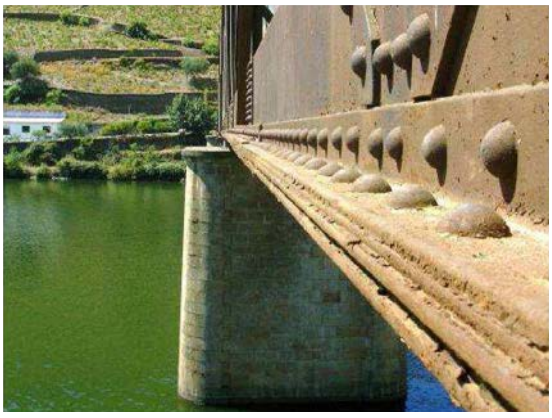

(b) Steel delaminating in the girders lower chords

(c) Poor conservation state of the bearings

(d) Heavy corrosion in the contact area of support

Figure 4.3 Examples of damage

In the year 2004 the bridge owner ordered a study to evaluate the bridge rehabilitation procedure. In this study, static load tests were carried out. The parameters observed during the field test include deflections of the deck, strains of the structural members, longitudinal displacements of the bearing supports and their rotations. A three dimensional finite-element model was developed by the team of the Faculty of Engineering of the University of Porto that conducted the static test of the Pinhão Bridge (www.fe.up.pt/labest), and the calculated values were correlated with the results from the static load tests. In the meanwhile, two ambient vibration tests were performed by Laboratory of Vibration and Structural Monitoring (www.fe.up.pt/vibest) in similar conditions before and after the rehabilitation with the purpose of calibrating the finite-element model. The detailed rehabilitation procedure is described in (Costa et al, 2008).

In this dissertation, the OMA of the data acquired from these two ambient vibration tests is performed to reflect the change of modal parameters caused by the structural rehabilitation.

4.2.2 Ambient vibration tests

During the two ambient vibration tests performed before and after rehabilitation, four tri-axial 18-bit seismographs were used (Figure 4.4). These devices comprised very sensitive internal force balance accelerometers (linear behaviour from DC to 100 Hz), analogue to digital converters with 18 bit (to guarantee a good resolution), batteries that enabled the possibility of autonomy for one day of tests, memories materialized by removable Compact Flash cards that permit a fast download of the acquired data. The external GPS sensor was used to deliver a very accurate time so that the seismographs could work independently and synchronously. With these equipments, the cables were avoided and the labour associated with the preparation of the dynamic test was drastically minimized.

In order to obtain a good characterization of the mode shapes, the accelerations at 7 cross sections on both sides of the deck were measured in each span (Figure 4.5). Two of the four units were fixed at reference points (points 3 and 13), whereas the other two were successively placed at the remaining 12 points, scanning the bridge deck in 6 consecutive setups for each span, measuring the acceleration along the 3 orthogonal directions (Figure 4.6).

For each setup, time series of 13 minutes were collected with a sampling frequency of 100 Hz, value that was imposed by the filters of the acquisition equipment.

Figure 4.4 Seismograph and external GPS

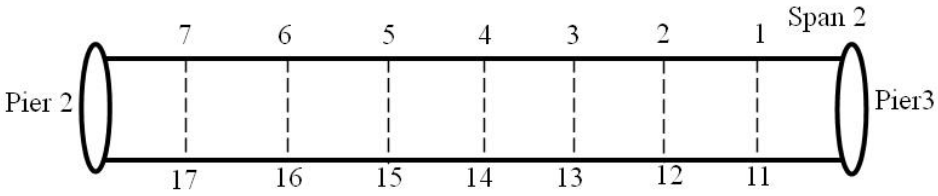

Figure 4.5 Measurement points used in the ambient vibration test

Figure 4.6 Position of the measuring devices during one setup

Since the three spans of the bridge are structurally independent and identical, they were also tested independently and the modal estimates are similar (Magalhães et al, 2006). In this study, only the experimental data acquired from the middle span of the bridge was analyzed.

The ambient tests were developed under normal operational conditions without inducing significant restrictions in the bridge. So it was possible to quantify the level of the vibrations motivated by the traffic. Figure 4.7 shows, for instance, the acceleration measured in the downstream point of section 4. In this graphic, the passage of a vehicle can easily be identified, which motivated a relatively high vertical acceleration 0.052 m/s^2. It is also

observed from the graphic that the level of lateral accelerations is approximately 1/10 of the vertical accelerations, which may partially explain the lower quality of the identified lateral mode shapes.

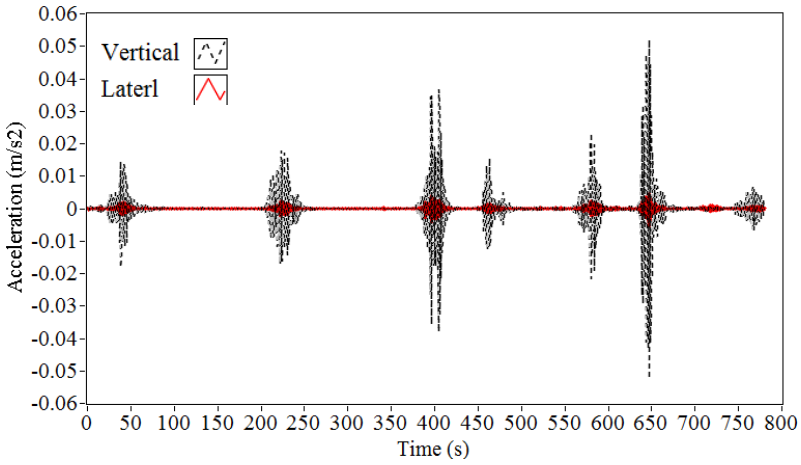

Figure 4.7 Measured acceleration signals in vertical and lateral directions during ambient vibration test after rehabilitation

4.2.3 Operational Modal Analysis before and after rehabilitation

The SMI toolkit was used to analyze the experimental data acquired in the ambient vibration tests performed before and after rehabilitation. First, the collected signals were de-trended to remove linear effects and decimated with a factor of 2 to reduce the size (sampling frequency converted to 50Hz). Then, the PP, EFDD, SSI-COV and SSI-DATA methods were employed for OMA, as shown in Figures 4.8 and 4.9 for vertical and lateral test data, respectively. With regard to PP and EFDD methods in frequency domain, a window length of 4096 points was used, leading to a frequency resolution of 50/4096=0.012Hz in the spectral estimates, with application of Hanning window and overlapping of 50%. When using SSI-COV and SSI-DATA methods in time domain, the stochastic subspace model was calculated with the time lag parameter i (used for evaluation of the output covariance $\hat{R}_i$) equal to 40. A stabilization diagram was constructed by identifying state-space models for orders n=2,3,...,100. The user defined criteria are 1% for frequencies, 5% for both damping and mode shape correlations.

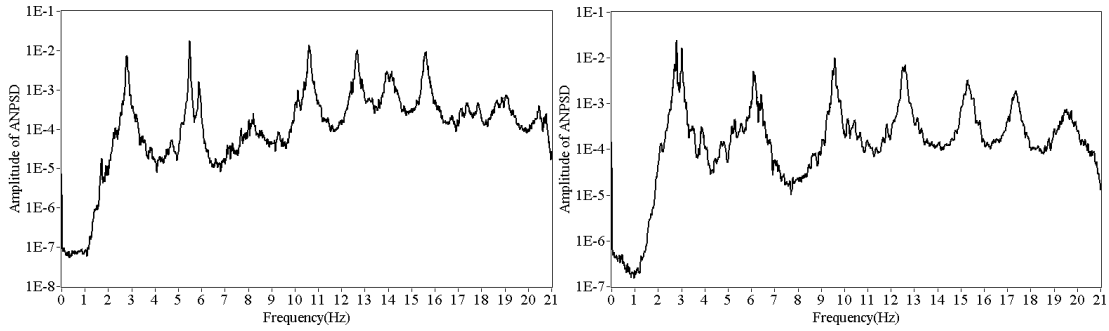

(a) ANPSD before rehabilitation (b) ANPSD after rehabilitation

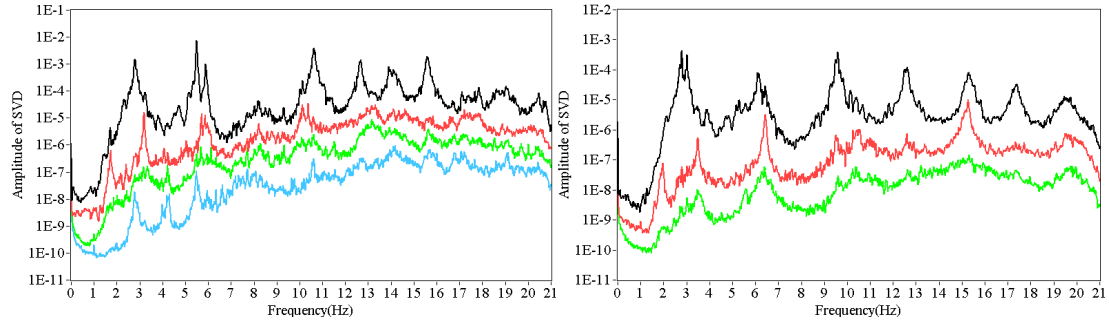

(c) Averaged SVD curves before rehabilitation (d) Averaged SVD curves after rehabilitation

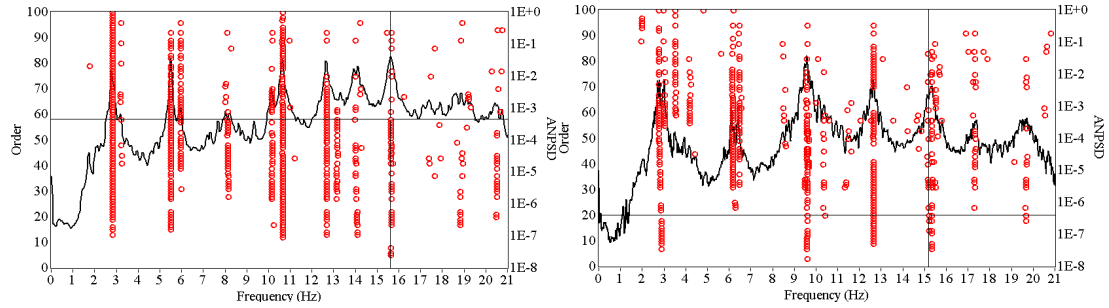

(e) Stabilization diagram produced by SSI-COV before rehabilitation

(f) Stabilization diagram produced by SSI-COV after rehabilitation

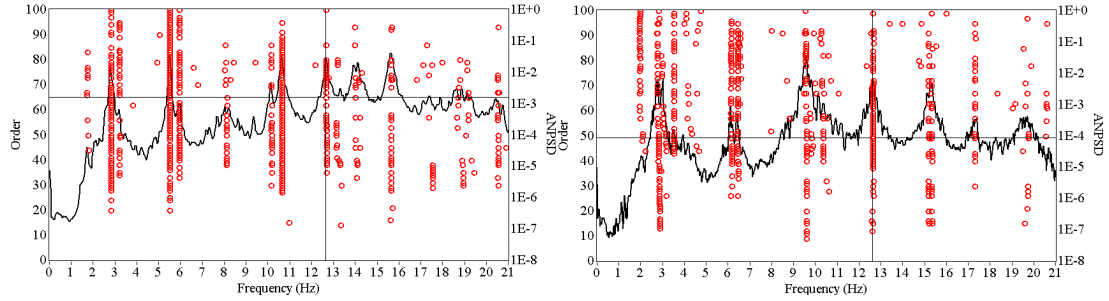

(g) Stabilization diagram produced by SSI-DATA before rehabilitation

(h) Stabilization diagram produced by SSI-DATA after rehabilitation

Figure 4.8 OMA of vertical test data acquired before and after rehabilitation by PP, EFDD, SSI-COV and SSI-DATA methods

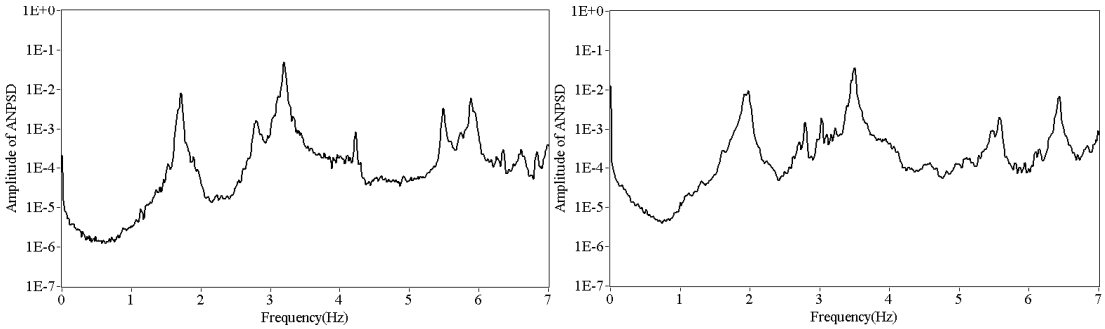

(a) ANPSD before rehabilitation (b) ANPSD after rehabilitation

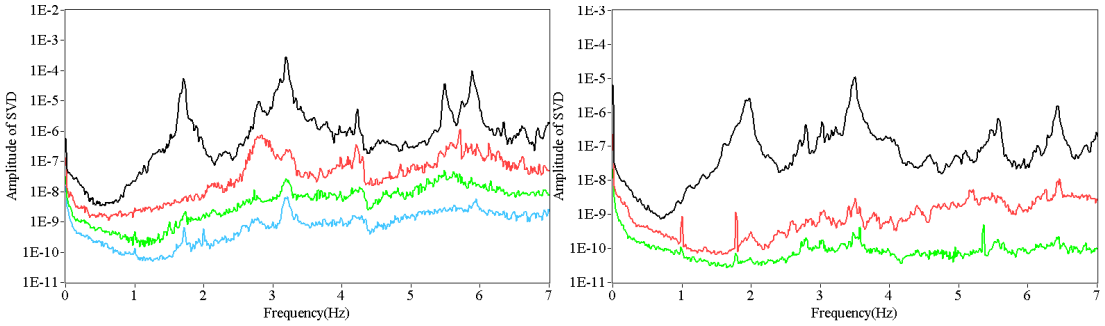

(c) Averaged SVD curves before rehabilitation (d) Averaged SVD curves after rehabilitation

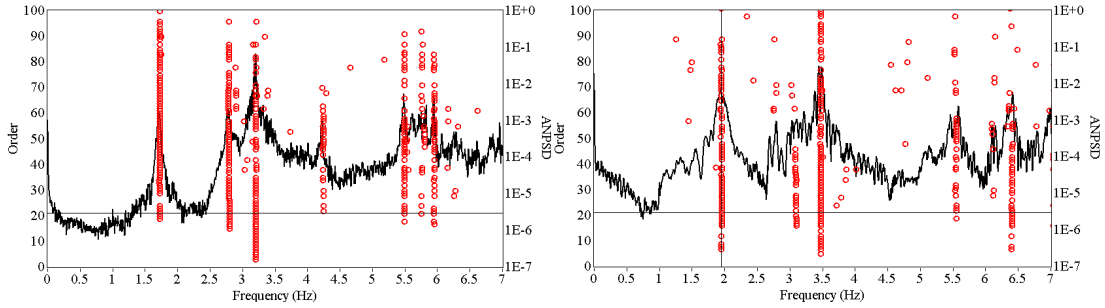

(e) Stabilization diagram produced by SSI-COV before rehabilitation

(f) Stabilization diagram produced by SSI-COV after rehabilitation

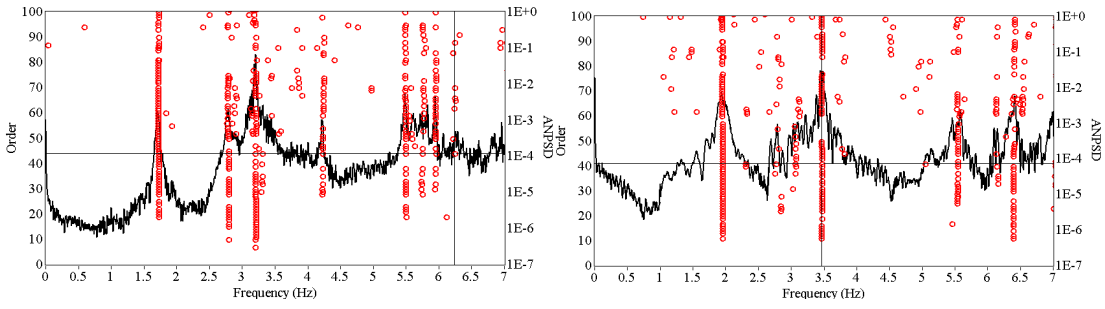

(g) Stabilization diagram produced by SSI-DATA before rehabilitation

(h) Stabilization diagram produced by SSI-DATA after rehabilitation

Figure 4.9 OMA of lateral test data acquired before and after rehabilitation by PP, EFDD, SSI-COV and SSI-DATA methods

Table 4.1 Comparison of modal parameters identified by different methods and computed by finite element analysis before rehabilitation of Pinhão bridge

Mode		Modal Identification results							*FEM*
		PP	EFDD		SSI-COV		SSI-DATA		
		Freq (Hz)	Freq (Hz)	Damp. (%)	Freq (Hz)	Damp. (%)	Freq (Hz)	Damp (%)	Freq (Hz)
V	1	2.80	2.80	1.15	2.80	1.35	2.80	1.33	2.87
	2	5.49	5.49	0.32	5.49	0.35	5.49	0.36	5.22
	3	8.15	8.15	2.50	8.17	2.87	8.19	2.66	8.34
	4	10.61	10.62	0.53	10.61	0.54	10.62	0.55	11.28
	5	12.66	12.66	0.55	12.64	0.59	12.65	0.60	12.88
	6	14.05	14.08	0.75	14.07	1.1	14.08	1.06	/
	7	15.60	15.61	0.50	15.60	0.52	15.61	0.58	/
T	1	5.94	5.94	0.33	5.93	0.57	5.92	0.58	6.66
L	1	1.71	1.72	1.21	1.71	0.87	1.71	0.83	1.69
	2	3.20	3.20	0.70	3.19	0.65	3.20	0.67	3.38
	3	4.22	4.23	0.41	4.22	0.41	4.22	0.41	4.31

Table 4.2 Comparison of modal parameters identified by different methods after rehabilitation of Pinhão bridge

Mode		Modal Identification results						
		PP	EFDD		SSI-COV		SSI-DATA	
		Freq (Hz)	Freq (Hz)	Damp (%)	Freq (Hz)	Damp (%)	Freq (Hz)	Damp (%)
V	1	2.83	2.82	0.78	2.84	2.56	2.85	2.34
	2	6.13	6.13	0.67	6.14	1.52	6.13	1.41
	3	9.58	9.58	0.83	9.59	0.88	9.58	0.75
	4	12.56	12.56	0.85	12.58	0.90	12.58	0.82
	5	15.33	15.31	0.95	15.33	0.93	15.34	1.02
	6	17.35	17.35	0.90	17.33	1.14	17.34	0.93
	7	19.57	19.57	0.91	19.56	1.46	19.58	1.44
T	1	6.42	6.43	0.43	6.42	0.50	6.42	0.55
L	1	1.96	1.96	1.60	1.97	1.55	1.96	1.52
	2	3.49	3.49	0.78	3.49	0.74	3.48	0.75
	3	5.54	5.54	0.82	5.56	0.85	5.55	0.81

1st vertical mode

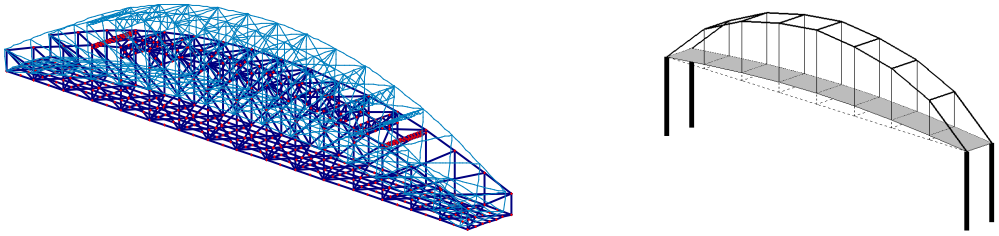

2nd vertical mode

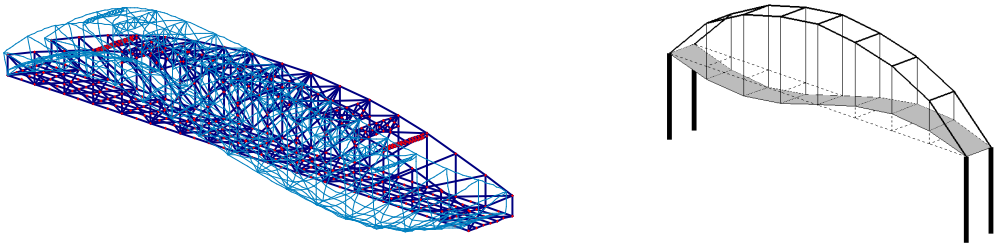

3rd vertical mode

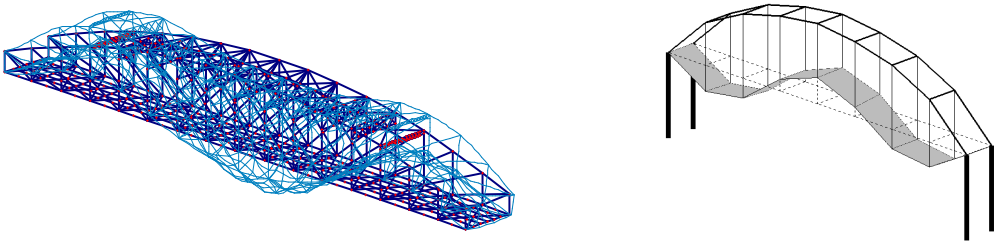

4th vertical mode

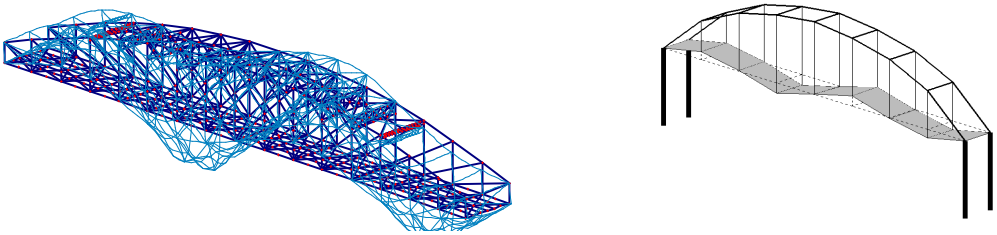

5th vertical mode

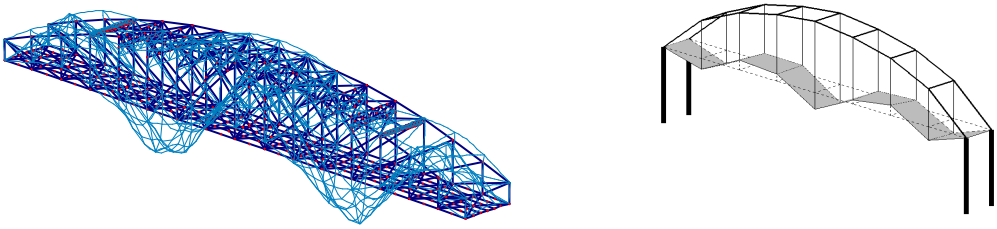

(a) Vertical mode shapes

1st torsion mode

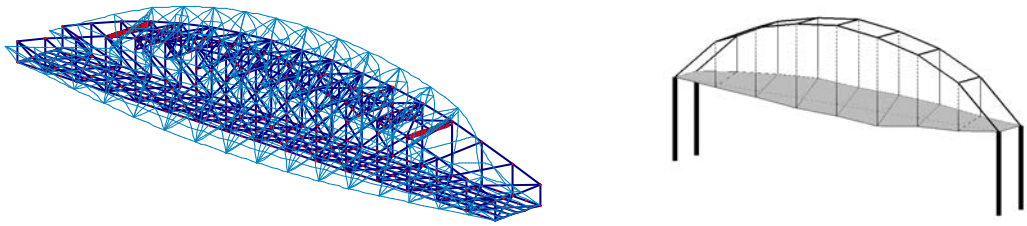

(b) Torsion mode shape

1st lateral mode

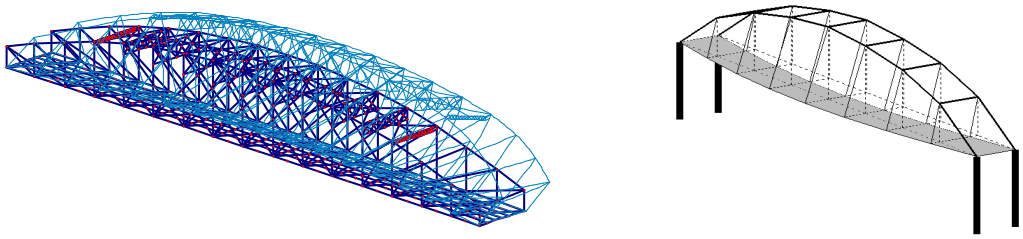

2nd lateral mode

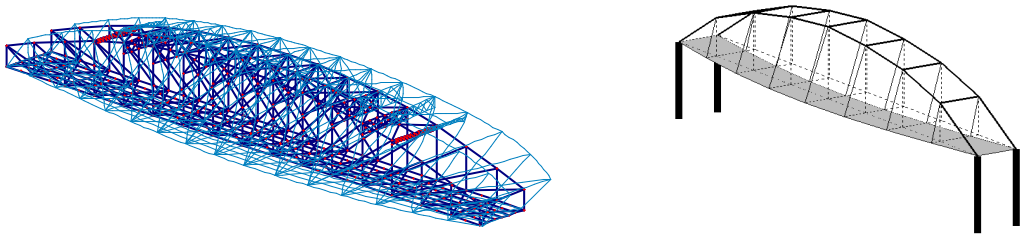

3rd lateral mode

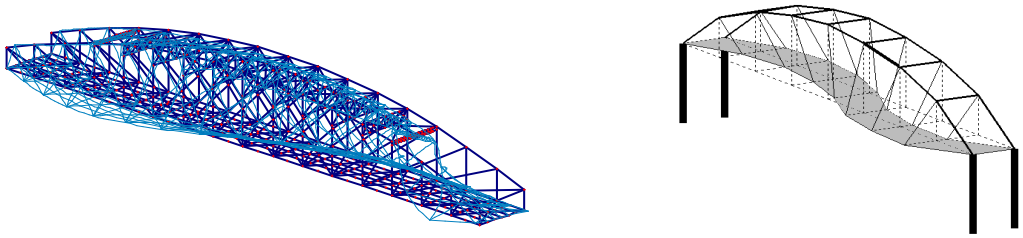

(c) Lateral mode shapes

Figure 4.10 Mode shapes calculated by Finite Element analysis (left side) and identified by OMA (right side)

The identified modal frequencies and damping ratios before and after rehabilitation are listed in Table 4.1 and Table 4.2, where 'V', 'T' and 'L' represent vertical, torsion and lateral modes. Before rehabilitation, a finite element model was also constructed and the corresponding frequency results are listed in Table 4.1. Comparing the modal results in Table

4.1 and Table 4.2, it is observed that identical modal frequencies are estimated by PP, EFDD, SSI-COV and SSI-DATA. With regard to the damping estimation, both SSI-COV and SSI-DATA produced similar results which are in reasonable agreement with those produced by EFDD method. Before and after rehabilitation, similar modal shapes were also identified by the SMI toolkit. Figure 4.10 shows the modal shapes identified by SSI-COV method before rehabilitation and those calculated using the structure analysis software Robot Millennium (Costa, 2008).

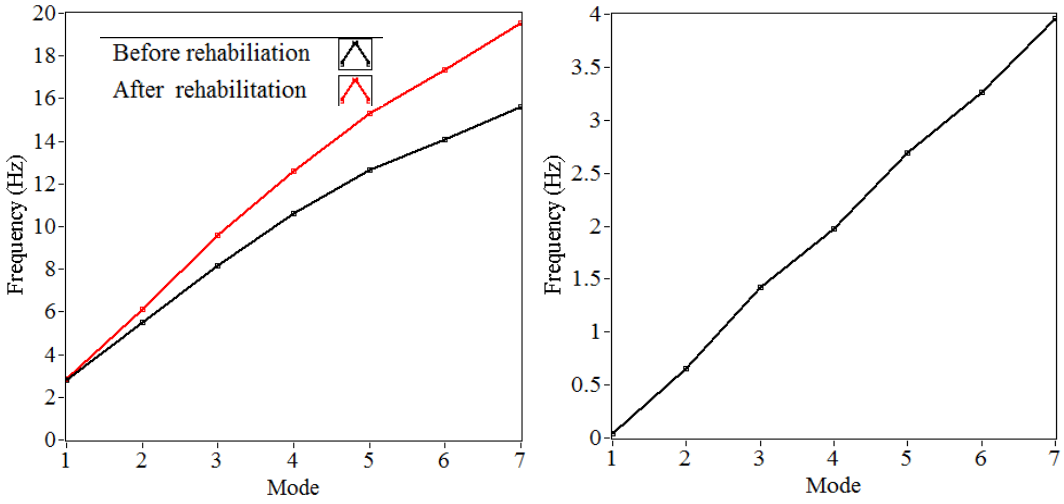

(a) Vertical natural frequencies (b) Increase of vertical natural frequencies

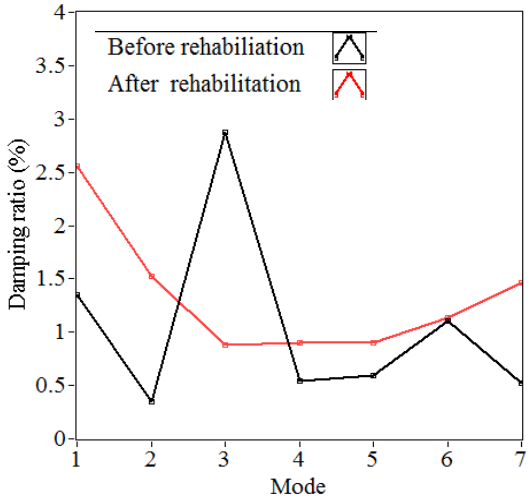

(c) Vertical damping ratios

Figure 4.11 Comparison of identified vertical frequencies and damping ratios before and after rehabilitation (SSI-COV method)

The changes of natural frequencies may reflect the variation of the bridge's stiffness or modification of boundary conditions caused by rehabilitation works. Comparison of vertical and lateral modal frequencies obtained by SSI-COV method is shown in Figure 4.11. For the vertical modes, it is found that the 1st natural frequency increases from 2.804Hz to 2.920Hz, while the 7th modal frequency changes from 15.608Hz to 19.570Hz, which means that higher modal frequencies are more sensitive to the structural modification. On the contrary, no clear trend is observed by comparing the estimation results of damping ratios before and after rehabilitation (Figure 4.11 (c)). The damping ratios in mode 1, 2, 4, 5 and 7 increase after rehabilitation while the one of mode 3 decreases. Similar trend is also observed in lateral and torsion modes.

4.3 OMA OF PEDRO E INÊS FOOTBRIDGE

4.3.1 Description of Pedro e Inês footbridge

The Pedro e Inês footbridge (Figure 4.12) is located in the centre of the City Park developed along the two banks of the river Mondego, at Coimbra, and was inaugurated in November 2006. This infrastructure, conceived to become a landmark for the city and to contribute to the quality of a new leisure area, was designed by Adão da Fonseca, leading a team from Afassociados, in collaboration with Cecil Balmond, leading the architectural team from Ove Arup (Afassociados and OveArup).

The 275m long slender steel footbridge is composed by a 110 m span central parabolic arch raising 9.40m above the water level, two lateral parabolic half arches with a span of 64m as well as an approaching span of 30.5m on the west bank and a transition span of 6m on the east bank (Figure 4.13 (a)). A distinctive feature of the bridge is the anti-symmetrical development of both arches and deck cross-sections along the longitudinal axis of the bridge (Figures 4.13 (b)). The continuously supported deck has a width of 4m and is formed by a L-shaped box cross section whose top flange is a composite steel-concrete slab 0.11m thick (Figure 4.13 (c), section B). In the lateral spans, arch and deck generate a rectangular box cross-section 4m x 0.90m. (Figure 4.13 (c), section C). In the central part of the bridge, each L-shaped box cross-section and corresponding arch "meet" to form a rectangular box

cross-section 8m x 0.90m (Figure 4.13 (c), section D), leading to the creation of a central square with 8mx8m at mid-span.

(a) Location of Coimbra

(b) Coimbra city and Pedro e Inês footbridge

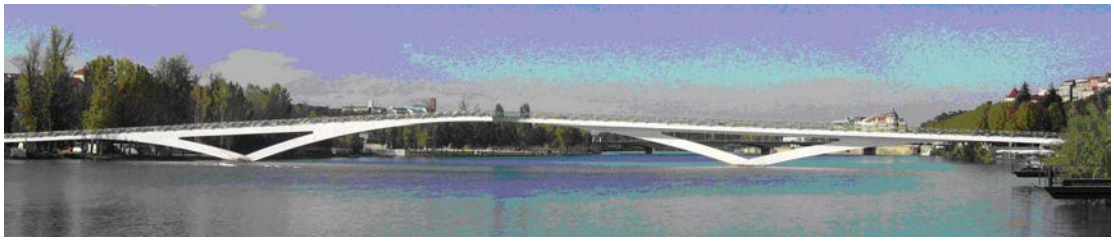

(c) General view of the Pedro e Inês footbridge

(d) Perspectives of the bridge

Figure 4.12 Overview of Pedro e Inês footbridge

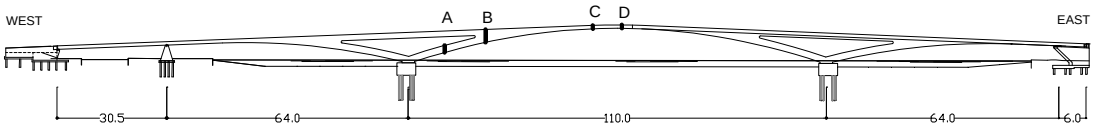

(a) Elevation view (dimensions in m)

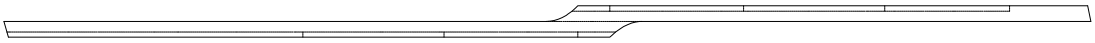

(b) Plan view

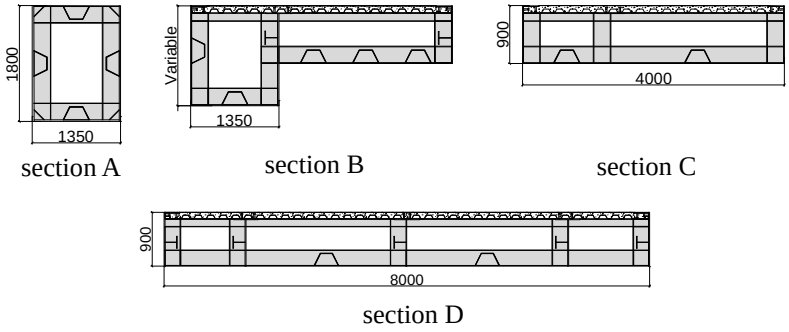

(c) Cross-sections (dimensions in mm)

Figure 4.13 Schematic representation of Pedro e Inês footbridge

Another structural feature is the poor horizontal stiffness provided by the foundations. The central arch is supported by two groups of vertical piles with a depth of about 30m. The horizontal stiffness provided by these foundations is low due to poor mechanical characteristics of soil layers beneath the river bed. Consequently, the arch-effect is expected to be reduced, leading to mixed arch/girder behaviour as explained in Figure 4.14 (Dimande et al, 2011). The supports provided at the abutments and at the left bank intermediate column allow the longitudinal displacement of the deck and block the transversal movements.

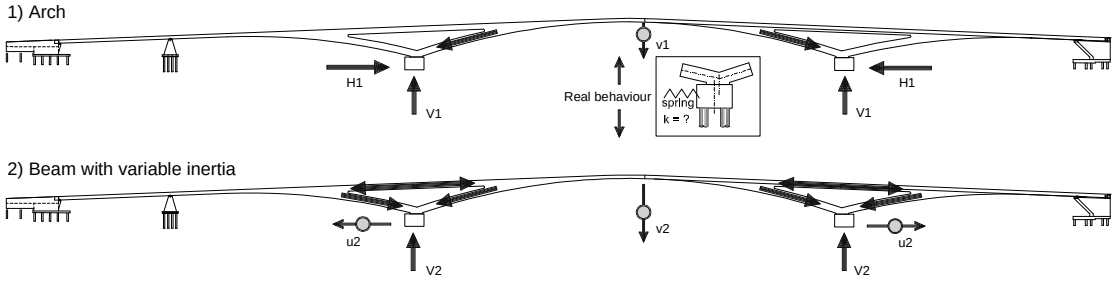

Figure 4.14 Influence of the soil foundation characteristics on bridge structural behaviour

4.3.2 Ambient vibration tests

The investigation conducted at design stage showed that this relatively long and slender footbridge would be prone to vertical and lateral vibrations induced by the action of pedestrians, requiring implementation of a control system based on a set of lateral and vertical Tuned Mass Dampers (TMDs) (Caetano et al, 2010). Two ambient vibration tests were performed before and after the installation of the control devices and non-structural elements, such as the handrails, the glass panels and timber pavements, in order to accurately characterize the dynamic behaviour of the footbridge and allow the design of the TMDs. The former test was developed in April 2006, before the installation of TMDs and non-structural elements. The latter was performed in November 2006, after the complete construction of the footbridge, including all installation of the TMDs and non-structural elements.

The strategy and testing procedure were similar in the two tests. Both of them were developed based on the use of four high sensitivity triaxial seismographs, including force-balance accelerometers and 18-bit A/D converters, duly synchronized through external GPS sensors (Figure 4.15). The 20 sections indicated in Figure 4.16 were instrumented. Except for sections 9, 10 and 11, where accelerations were measured at both sides of the deck (upstream and downstream), to better characterize torsional effects, vibrations were just recorded at the longitudinal axle of the deck. Taking into account the mode shapes predicted numerically, three reference points were considered in the ambient vibration test (points 1, 6 and 8). Three seismographs were permanently placed at these points, while a fourth one was used to measure the response of the bridge successively at the remaining measurement points, during 16 minutes in each setup, in a total 19 setups. All the acceleration time series were acquired using a sampling rate of 100Hz, which was imposed by the anti-aliasing filters of the acquisition system.

The ambient test was developed under normal operational conditions, so it was possible to quantify the level of the vibrations motivated by the ambient excitation such as pedestrians and wind. Figure 4.17 presents measured vertical and lateral acceleration signals recoded in the second ambient vibration test. It is also observed from the graphic that the level of the

lateral accelerations is similar to the order of magnitude of vertical accelerations, which may reflect the mixed arch/girder behaviour duo to the poor horizontal stiffness in the foundations.

Figure 4.15 Seismograph and external GPS

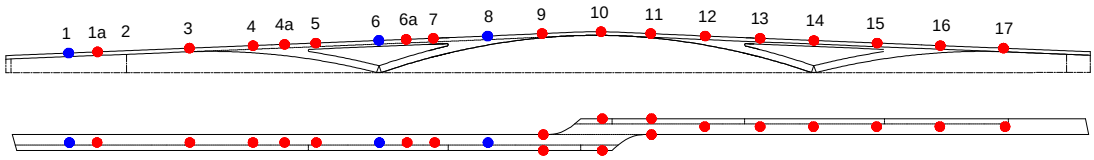

Figure 4.16 Instrumented sections: lateral and top view
(reference points are indicated in blue)

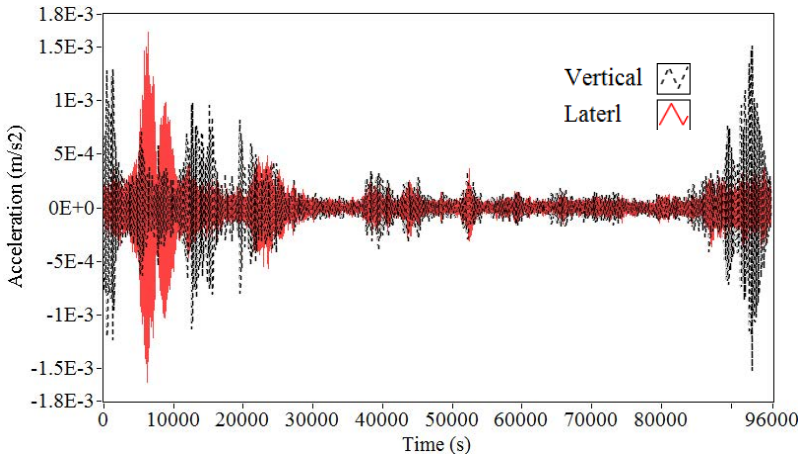

Figure 4.17 Measured acceleration signals in both vertical and lateral direction

4.3.3 Operational Modal Analysis at different construction stages

The original intent of the two ambient vibration tests was to accurately evaluate the dynamic properties of the footbridge before and after the implementation of the TMDs, as well as the installation of non-structural elements. This section shows the change of modal properties between these two stages.

During the phase of the preprocessing of experimental data, collected signals were de-trended to remove the linear effect and decimated with a factor of 5 to reduce the size (sampling frequency was thus converted from 100Hz to 20Hz).

Table 4.3 Modal parameters identified by EFFD and SSI-DATA methods before installation of TMDS and non-structural elements

Mode	Modal Identification results			
	EFDD		SSI-DATA	
	f [Hz]	ξ [%]	f [Hz]	ξ [%]
1	0.91	0.89	0.91	0.56
2	1.54	0.73	1.54	0.84
3	1.88	0.67	1.87	1.06
4	1.95	0.82	1.94	1.04
5	2.05	0.62	2.05	0.57
6	2.54	1.98	2.53	2.26
7	2.88	1.13	2.86	2.41
8	3.18	0.90	3.18	1.11
9	3.36	0.38	3.35	0.28
10	3.57	0.39	3.57	0.35

The data collected in the ambient vibration test performed in April 2006, before installation of TMDs and non-structural elements, was processed using the Enhanced Frequency Domain Decomposition (EFDD) technique and the Data Driven Stochastic Subspace Identification (SSI-DATA) implemented in the Artemis software. (Magalhães, F. et al, 2007) In the application of the EFDD method, the auto and cross spectra were evaluated using a frequency resolution of about 0.01Hz. In the application of the SSI-DATA method, the data was fitted by stochastic subspace models of order between 2 and 100. Table 4.3 summarizes the results identified by the applied output-only identification methods, showing the average values of the identified natural frequencies and modal damping ratios. The natural frequencies estimated by both methods are almost coincident. But, the modal damping ratios still present some differences. The first 10 mode shapes identified by the SSI-COV method are represented in Figure 4.20, using lateral and top views and comparing with those estimated from data collected at the ambient vibration test after the installation of TMDs.

The data acquired in the second ambient vibration test, conducted in November 2006, was treated by SMI toolkit with PP, EFDD, SSI-COV as well as SSI-DATA methods. In the application of frequency domain analysis, it was adopted a resolution of about 0.01Hz, an

overlapping of 50% and a Hanning window when calculating the auto and cross spectrum. The vertical and lateral global ANPSD (Averaged Normalized Power Spectrum Density) spectra and SV (Singular Values) curves, which were produced by averaging the ANPSD or SV diagrams from each setup, as shown in Figure 4.18 (a)-(b) and Figure 4.19 (a)-(b). There are four singular value curves, because the signals were acquired from 4 different channels in each setup, which led to a 4×4 spectrum matrix for singular value decomposition. The time domain methods were also employed to identify modal parameters. The stochastic subspace model was calculated with the time lag parameter *i* equal to 40. The data was fitted by stochastic subspace models of order between 2 and 100. With criteria 1% for frequencies and mode shape correlations, 3% for both damping, the stabilization diagrams are produced by both Covariance and Data driven SSI methods, as shown in Figure 4.18 (c)-(d) and Figure 4.19 (c)-(d).

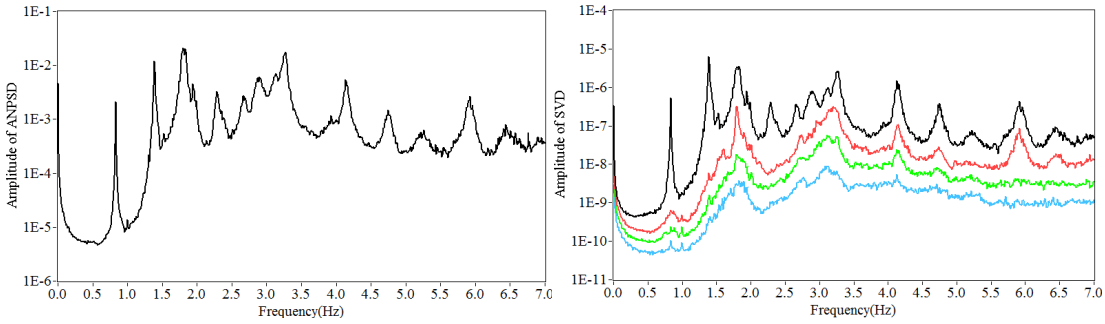

(a) ANPSD (b) Averaged SV curves

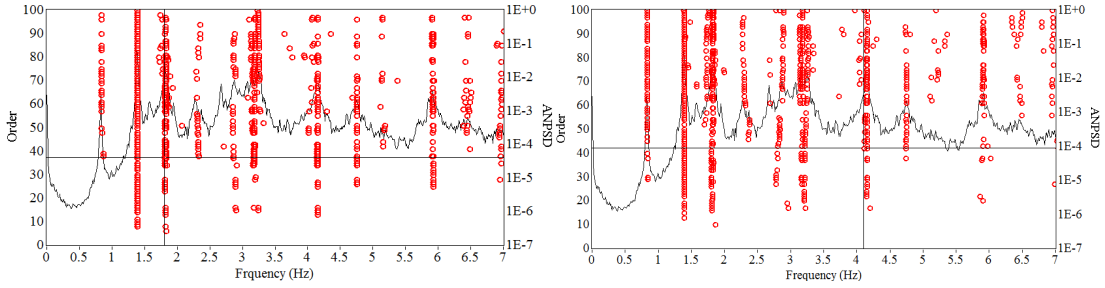

(c) Stabilization diagram produced by SSI-COV (d) Stabilization diagram produced by SSI-DATA

Figure 4.18 OMA of vertical test data acquired before installation of TMDs and non-structural elements by PP, EFDD, SSI-COV and SSI-DATA methods

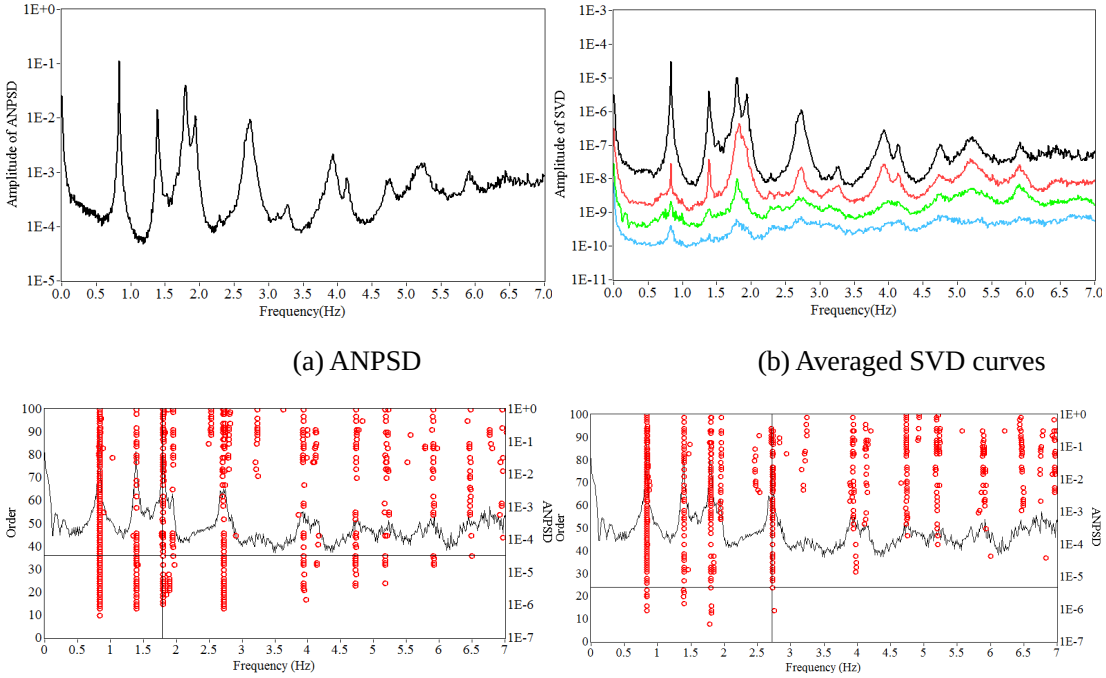

(a) ANPSD (b) Averaged SVD curves

(c) Stabilization diagram produced by SSI-COV (d) Stabilization diagram produced by SSI-DATA

Figure 4.19 OMA of lateral test data acquired after installation of TMDs and non-structural elements by PP, EFDD, SSI-COV and SSI-DATA methods

Table 4.4 Comparison of modal parameters identified by different methods after installation of TMDs and non-structural elements

Mode	Modal Identification results						
	PP	EFDD		SSI-COV		SSI-DATA	
	Fre (Hz)	Fre (Hz)	Damp (%)	Fre (Hz)	Damp (%)	Fre (Hz)	Damp (%)
1	0.83	0.83	0.76	0.83	0.41	0.83	0.42
2	1.39	1.39	0.71	1.39	0.57	1.39	0.56
3/4	1.80	1.80	1.16	1.81	1.28	1.81	1.09
5	1.94	1.94	0.93	1.95	1.18	1.95	1.02
6	2.28	2.29	1.73	2.29	1.45	2.29	1.65
7	2.69	2.69	0.85	2.69	1.17	2.69	1.09
8	2.90	2.90	1.37	2.88	2.11	2.88	2.04
9	3.13	3.12	0.44	3.11	1.70	3.13	2.00
10	3.26	3.26	1.00	3.25	1.08	3.25	1.27

The modal results identified by different methods are summarized in Table 4.4. The identified frequencies obtained by different methods are almost coincident, while the modal damping ratios estimates are a little different from EFDD to SSI methods. Similar modal shapes are provided by PP, EFDD and SSI-COV methods. Figure 4.20 shows the

corresponding coupled modal shapes identified by SSI-COV methods, together with those achieved before the installation of TMDs. Modal shapes identified before installation of TMDs are similar to those after installation of TMDs except for the 3rd and 4th modal shape. It seems that after installation of TMDs and non-structural elements those modes combined into a new 3rd mode. The peculiar geometry of the bridge marked by assuming in plane view and deck cross section led to less intuitive mode shapes, most of them having vertical and lateral components simultaneously.

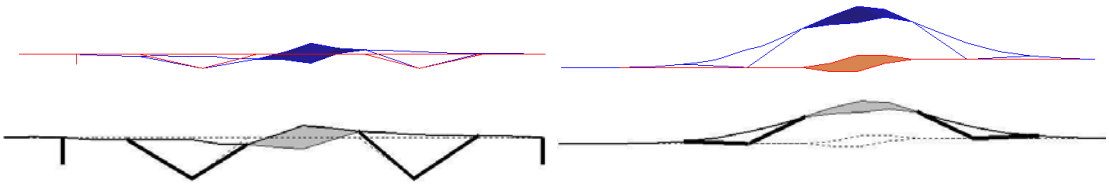

1st mode

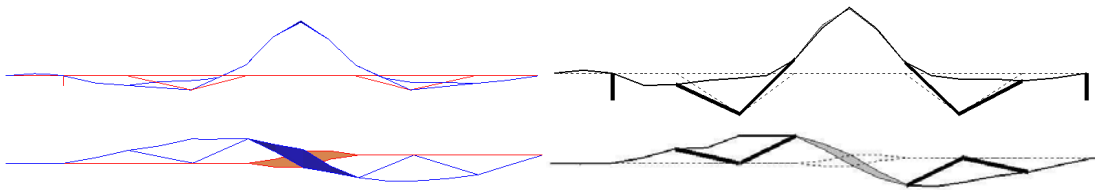

2nd mode

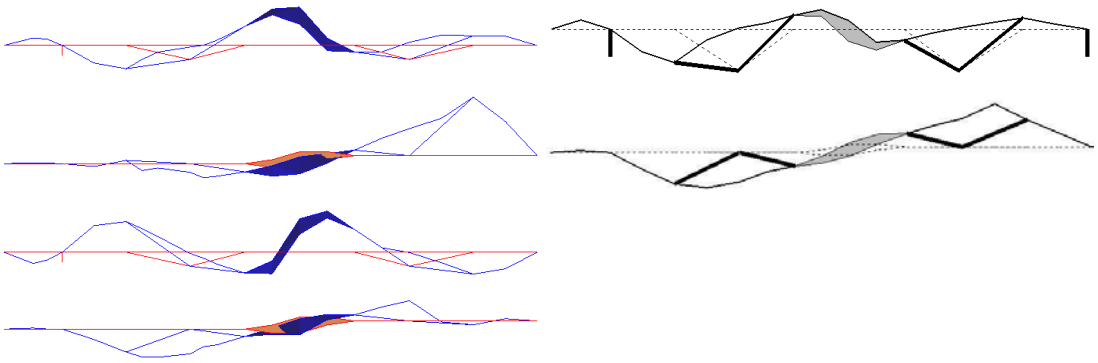

3rd /4th mode

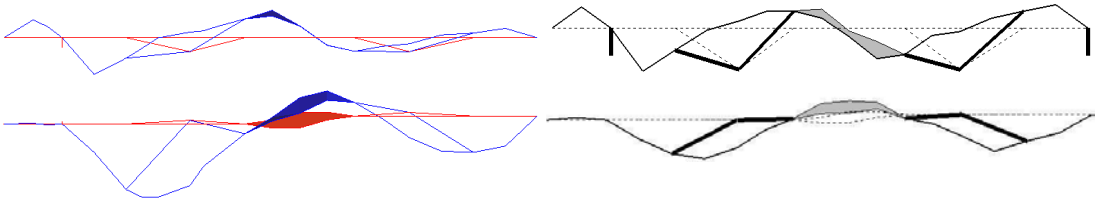

5th mode

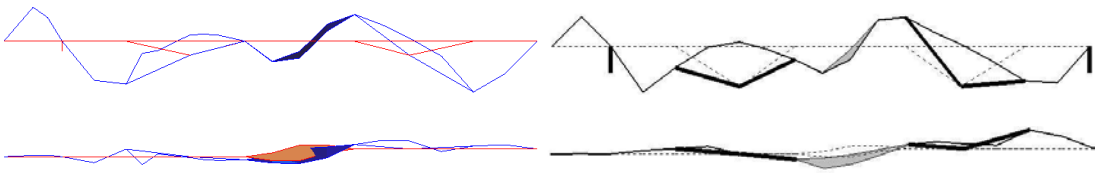

6th mode

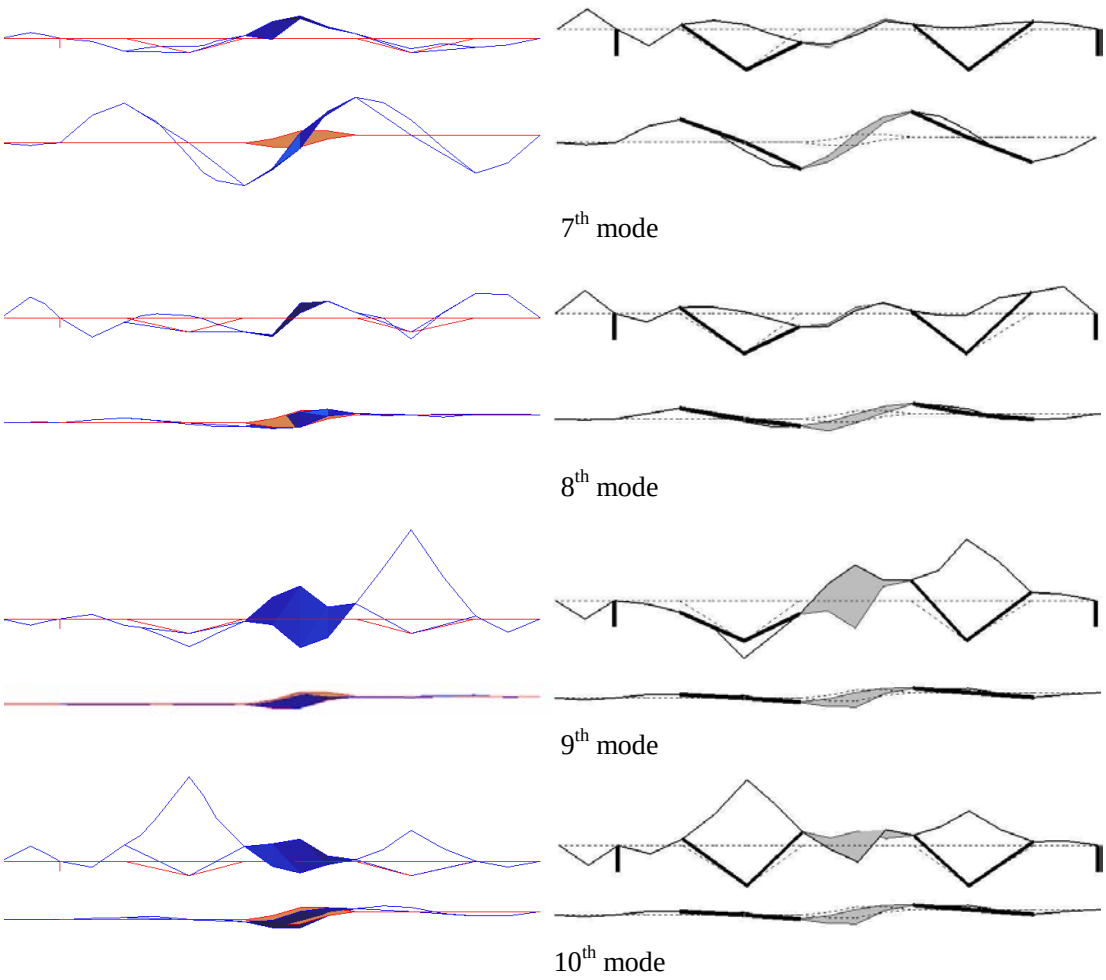

Figure 4.20 Mode shapes identified by OMA of experimental data collected before (left side) and after (right side) installation of TMDs and non-structural elements

The comparison of frequencies of different modes shown in Figure 4.21 (a), (b) reflects the slight decrease of frequencies caused by TMDs and additional non structural elements, including the handrails, glass panels and the timber pavements. These elements introduce essentially additional mass on the footbridge and nearly no extra stiffness, because the contribution of the handrails to the overall stiffness of the footbridge was almost negligible (Caetano et al, 2010b).

Figure 4.21 (c) proves the irregular change of estimated damping ratios before and after installation of TMDs and additional non-structural elements, which could not reflect the change of damping ratios as described in (Caetano et al, 2010b). Possible explanations are the following: First, the ambient excitation was too low to activate the TMDs because both ambient vibration tests were performed during the construction phase. Secondly, only intermittent damping may be introduced by TMDs as consequence of sporadic transient

excessive vibrations.

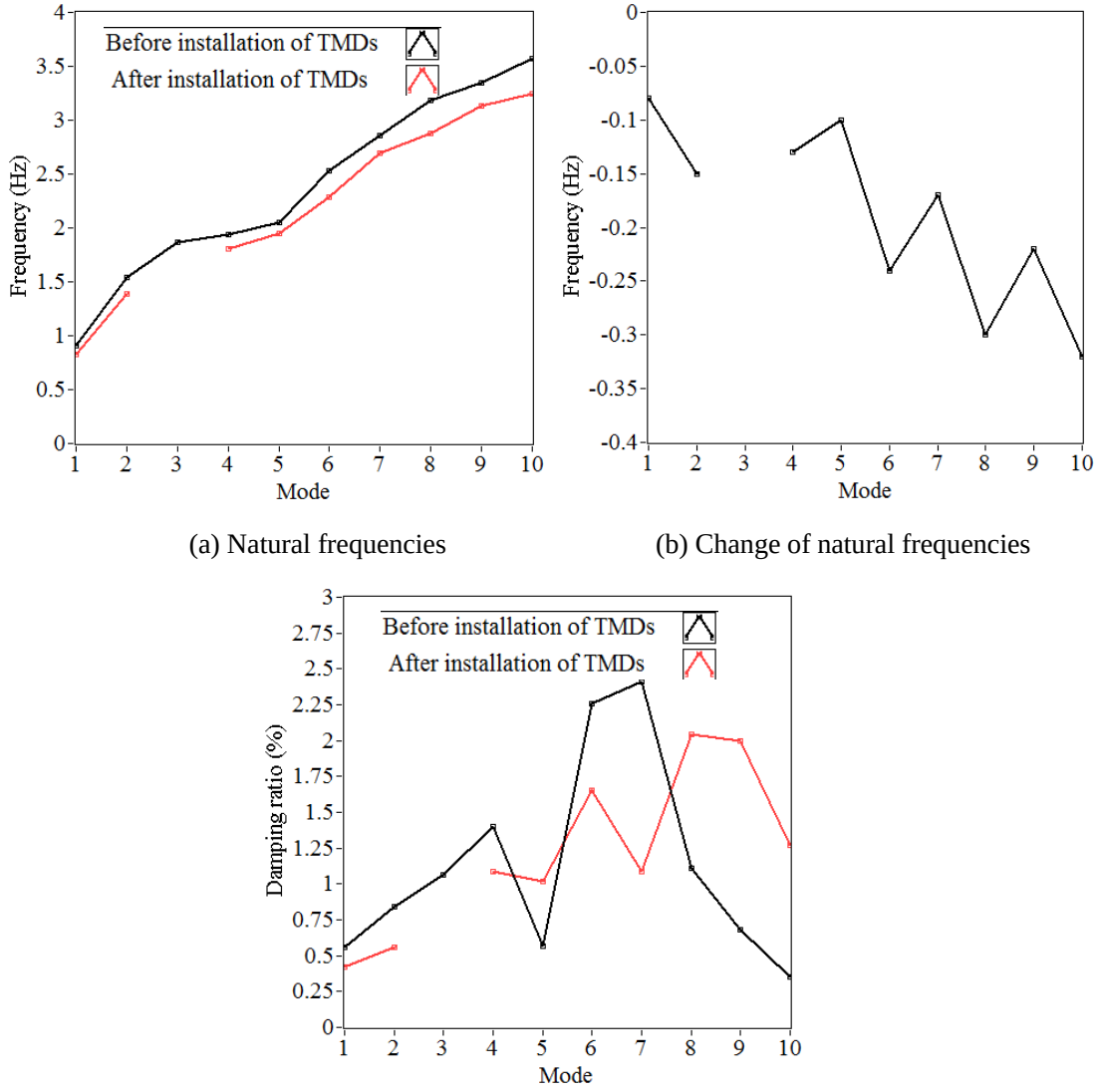

(a) Natural frequencies

(b) Change of natural frequencies

(c) Damping ratio

Figure 4.21 Comparison of identified frequencies and damping ratios before and after installation of TMDs and non-structural elements (SSI-COV method)

From OMA of case 1 and case 2, it is possible to observe that the natural frequencies are sensitive to structural changes, which means that these frequencies can be used as structural health indices. However, in practice it is interesting to detect early damage instead of fatal damage caused by a loss of structural resistance or modification of mass or boundary conditions. Unfortunately, the structural changes caused by early damage are often disturbed by changes induced by environmental and operational variations (Sohn, 2007). In next section, OMA of a lively footbridge in FEUP campus of Faculty of Engineering will demonstrate that the environment factors may mask the subtle change of frequencies caused by early damage.

4.4 OMA OF FEUP CAMPUS FOOTBRIDGE

4.4.1 Description of FEUP campus footbridge

The bridge, which establishes a link between the main buildings of FEUP and the students' canteen, was designed by ENCIL (ENCIL, 1998). The deck is a very slender stress-ribbon concrete slab, continuous over two spans (Figure 4.22). Figure 4.23 presents the elevation and cross section of the footbridge. The slab embeds all four prestressing cables and takes a catenary shape over the two spans, with a circular curve over the intermediate support, which is made of four steel pipes forming an inverted pyramid hinged at the base. The two spans 28m and 30m long and the 2m rise from the abutments to the intermediate pier were the starting points for the definition of the bridge structural geometry. The constant cross-section is approximately rectangular with external design dimensions of 3.80mx0.15m.

The construction method suggested by the bridge designer comprised the following steps: (i) installation and progressive prestressing of all cables to about 750kN each; (ii) hanging of 1m long precast segments from the cables, starting from the abutments and ending at the external limits of the deviating saddle over the intermediate support; (iii) casting of the concrete slab, with formwork provided by the precast segments; casting should be made continuously in an approximately symmetric fashion with respect to the intermediate support, and it should be followed by an injection of the joints between precast segments; (iv) eventual modification of final prestressing in all cables, for correction of geometry; (v) injection of all prestressing ducts with cement grout.

One particular feature of this stress-ribbon bridge is that its stability and stiffness are determined by the axial forces in the tensioned longitudinal cables, the corresponding geometric configuration being defined by the equilibrium conditions of these elements under dead loads. The use of slender deck allows low curvatures. It is worth noting, however, that low curvatures are associated with high cable forces and on the other hand, small modifications of the geometric structural configuration lead to significant changes of axial forces. This characteristics have been already demonstrated by the numerical analysis

performed simulating all the construction phase (Caetano and Cunha, 2004).

(a) Location of Faculty of Engineering of University of Porto (FEUP)

(b) FEUP campus and the footbridge

(c) Global view of FEUP Campus footbridge

(d) Upper view of the deck

Figure 4.22 Overview of FEUP campus footbridge

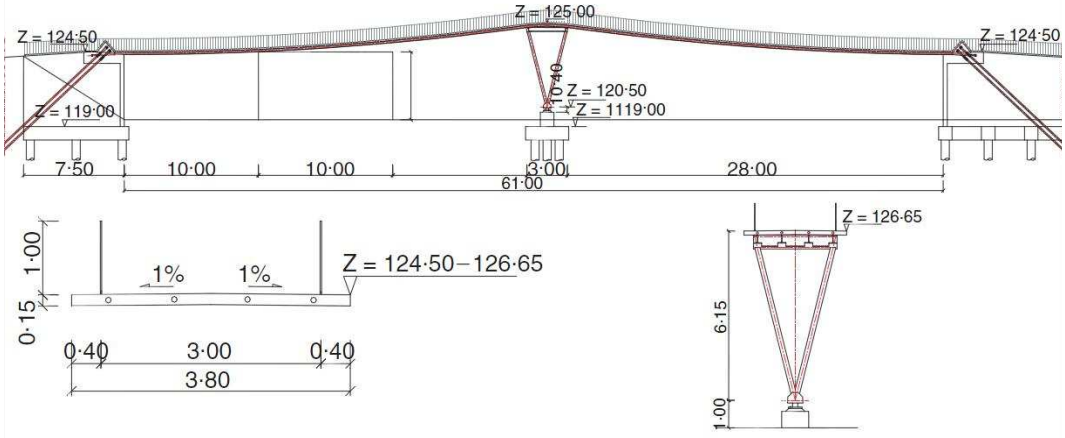

Figure 4.23 Schematic representation of FEUP campus footbridge

4.4.2 Ambient vibration tests

Two previous ambient tests were performed on the 28th March 2003 and the 5th October 2004 in order to calibrate Finite Element models (Caetano and Cunha, 2004) as well as enable coherent comparison of estimates extracted through different identification techniques. (Cunha et al, 2005).

Those ambient vibration tests were based on the use of 4 triaxial seismographs duly synchronized by GPS, provided with 18 bit A/D converters (Figure 4.24). Two of them were placed at fixed positions 2 and 18 (reference points at 1/3 span), while the other two were successively placed at the other measurement points indicated in Figure 4.25 (a). The sampling frequency was 100Hz and the time of acquisition was at least 10 minutes in each setup.

On the 3rd October 2009, a new ambient vibration test was performed with purpose of calibrating the continuous monitoring system installed in the footbridge and building a baseline for long term monitoring (Hu et al, 2010). Another intention was to make a comparison with the modal results estimated based on the previous ambient tests, attempting to detect possible variation of frequencies that might stem from structural degradation. It was developed with six seismographs duly synchronized using GPS sensors. Four of the seismographs were used as references and constantly located at one half and one-third of each of the two spans for different measurement sequences (points 9, 26, 100, 101), while the other two seismographs were placed progressively at the remaining instrumented sections (Figure

4.25 (b)). More measurement points were used to increase the spatial resolution, so that the higher order modal shapes might be identified smoothly. The sampling frequency was 100Hz and the time of acquisition 16 minutes in each setup. A typical vibration signal collected in one setup is shown in Figure 4.26.

Figure 4.24 Seismograph and external GPS

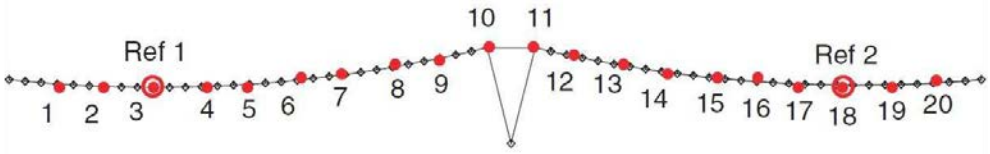

(a) Measurement points in test developed on the 5th October 2004

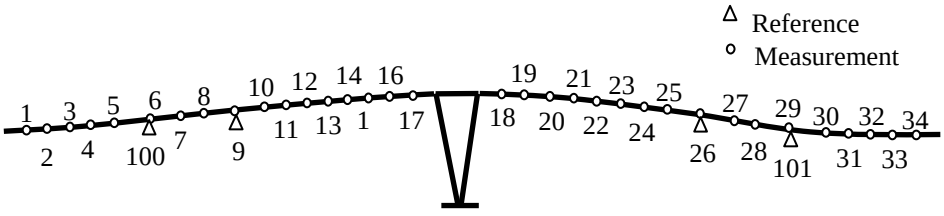

(b) Measurement points in test developed on the 3rd October 2009

Figure 4.25 Measurement points in the ambient vibration tests

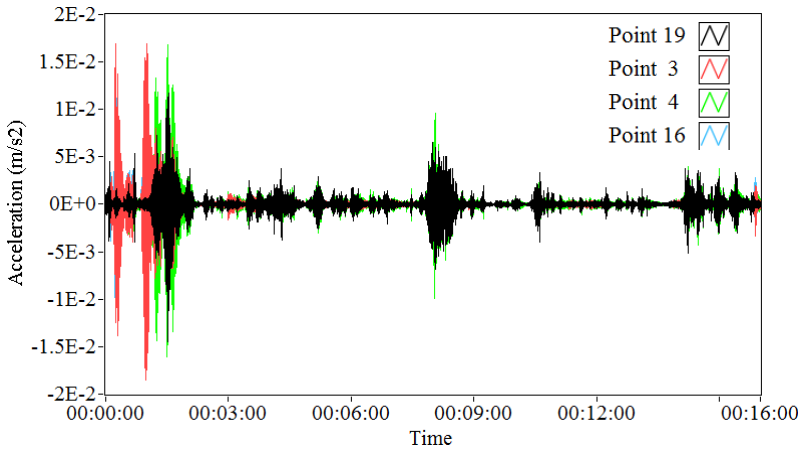

Figure 4.26 Measured acceleration signal

4.4.3 Operational Modal Analysis of FEUP campus footbridge

The data acquired in the three ambient vibration tests was treated with the SSI-COV method. The stochastic subspace model was calculated with the time lag parameter *i* equal to 50. The data was fitted using stochastic subspace models of order between 2 and 100. Using criteria of 1% for frequencies and mode shape correlations, 3% for damping ratios, the stabilization diagrams were produced by the Covariance driven SSI method as shown in Figure 4.27. Table 4.5 lists the estimates of modal parameters as well as results from a finite element analysis calibrated based on experimental results achieved with the ambient vibration test performed on the 28th March 2003. It is observed from Table 4.5 that all natural frequencies decreased with time, which may stem from some structural degradation or environmental effects.

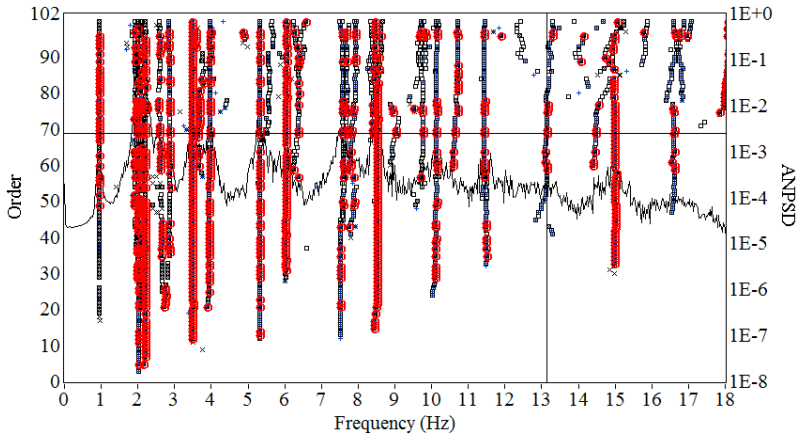

Figure 4.27 OMA of ambient vibration test data

Table 4.5 Comparison of modal parameters identified by SSI-COV based on different ambient vibration test data

Mode	Modal identification results						FE results
	03/10/2009 (SSI-COV)		05/10/2004 (SSI-COV)		28/03/2004 (SSI-COV)		
	Freq (Hz)	Damp (%)	Freq (Hz)	Damp (%)	Freq (Hz)	Damp (%)	Freq
1	0.951	1.03	0.965	1.14	0.983	1.28	0.949
2	1.989	1.09	2.012	1.45	2.084	1.29	1.990
3	2.034	1.16	2.038	1.48	2.136	2.37	2.143
4	2.289	2.05	2.342	1.59	2.415	1.77	2.417
5	3.520	1.87	3.590	2.08	3.746	2.16	3.869
6	3.965	1.71	4.105	1.87	4.245	2.38	4.381
7	5.346	1.80	5.412	1.70	5.709	2.20	5.915
8	6.037	2.03	6.176	2.12	6.530	2.27	6.820
9	7.500	2.01	7.656	2.00	8.137	2.38	8.227
10	8.582	2.12	8.730	1.41	9.300	2.41	9.560
11	10.072	1.89	10.245	2.63	11.059	2.52	12.487
12	11.624	2.18	11.704	1.08	12.676	2.49	14.908
13	13.131	2.15	13.488	2.48	14.424	2.69	16.462
14	14.983	2.08	15.334	1.32	16.451	2.54	18.475
15	16.458	1.96	17.213	1.68	18.220	2.72	20.337

Figure 4.28 compares the frequencies and damping ratios of all modes. It is noted from Figure 4.28 (a) that, after 5 years, frequencies of all modes decrease, the frequency of the 1st mode decreasing from 0.965Hz to 0.951Hz, while the frequency of the 15th mode reduces from 17.213Hz to 16.458Hz. Figure 4.28 (b) provides the frequency changes of all modes. The general tendency is that the frequencies of higher modes are more sensitive to structural or environmental changes. Irregular change of estimated modal damping ratios is also noticed in Figure 4.28 (c).

Initially, the environmental effects were assumed to be ignored, because both ambient vibration tests were performed in nearly the same days of different years (3 Oct 2009 and 5 Oct 2004). However, combining the previous results with those achieved with continuous monitoring system subsequently implemented in the bridge, and described in chapter 5. The effects of temperature on the modal properties are clarified, showing that they can clearly disturb the variation of natural frequencies induced by structural changes.

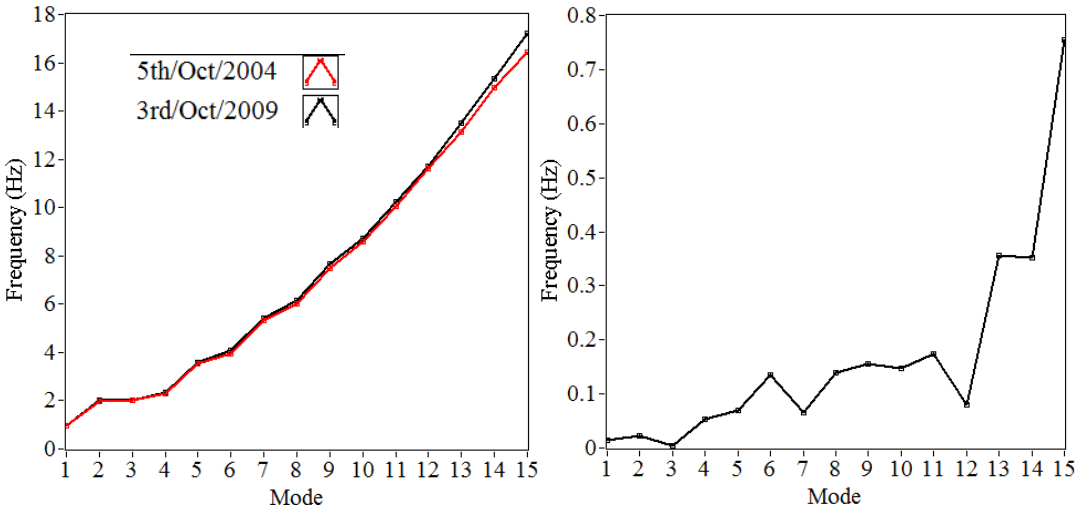

(a) Natural frequencies (b) Change of natural frequencies

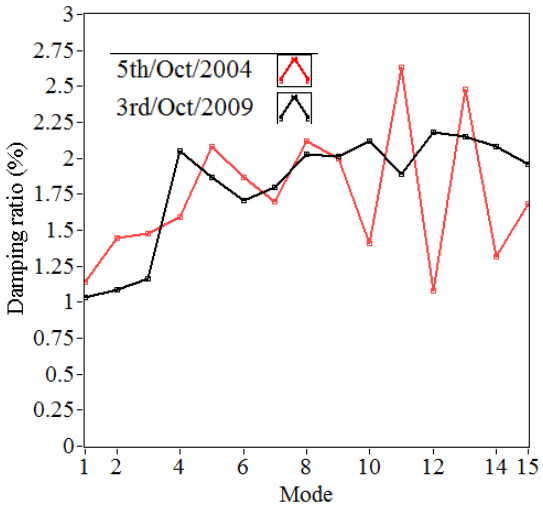

(c) Damping ratios

Figure 4.28 Comparison of identified frequencies and damping ratios based on ambient vibration tests performed on 03 Oct 2009 and 05 Oct 2004

In Figure 4.29 (a), the green and blue solid lines represent the 1st natural frequency estimates 0.951Hz and 0.965Hz, obtained from the ambient vibration tests performed in 2004 and 2009. Both temperature data and identified 1st natural frequency values in the period of 1-7 October 2009 are plotted in black dotted and red solid lines. It is clear that during this week, the 1st natural frequency oscillates between 0.931Hz and 1.001Hz mainly due to the variation of temperature. This means that, if the ambient test were performed on the 5th Oct 2009, the identified 1st frequency would be higher than that from the test performed on the corresponding day 5years ago. In Figure 4.29 (b), the 1st identified frequency of 0.983Hz, obtained from the ambient tests conducted on the 28th March 2003, is still within the range

from 0.957Hz to 1.012Hz measured in the last week of March 2010. The 1st frequency is still observed to be mainly driven by the variation of environmental temperature.

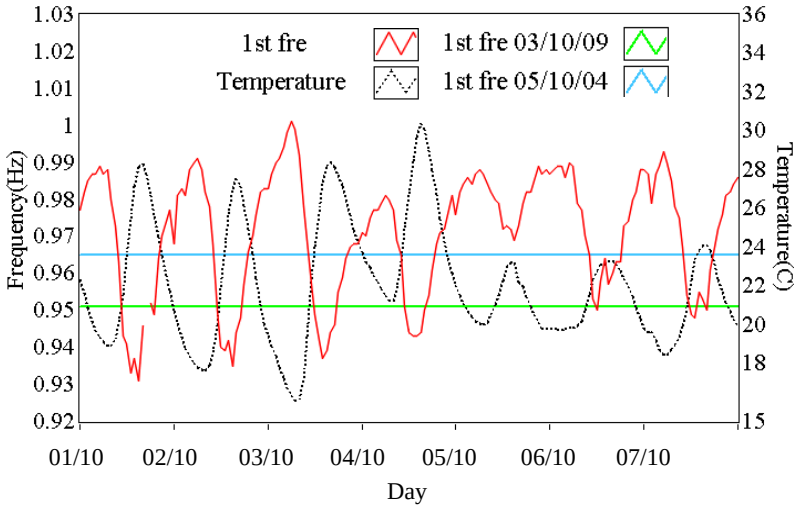

(a) Comparison of 1st natural frequency indentified by two ambient vibration tests (2004 and 2009) and continuous dynamic monitoring estimates

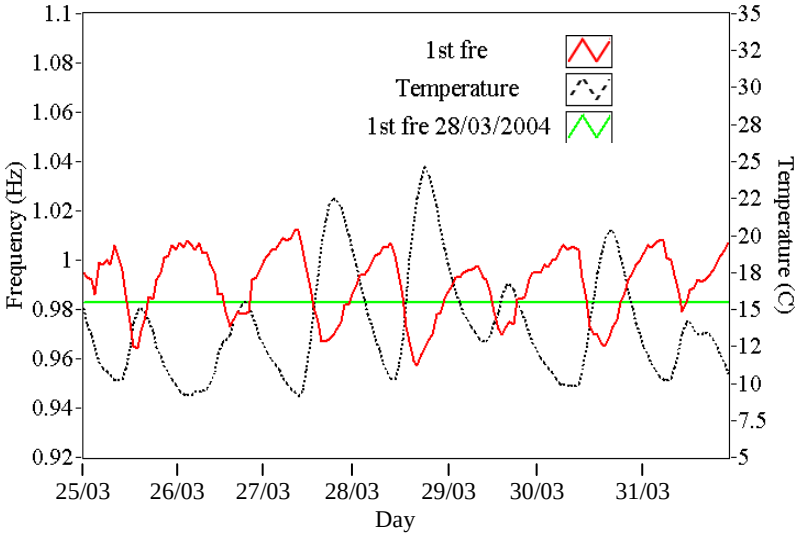

(b) Comparison of 1st natural frequency indentified by ambient vibration test (2003) and continuous dynamic monitoring estimates

Figure 4.29 1st natural frequency estimated from ambient vibration tests and continuous dynamic monitoring

It is demonstrated that apart from the structural changes discussed in cases 1 and 2, environmental factors may influence the variation of frequencies identified under operational conditions and have adverse effects on the implementation of structural health monitoring system in terms of modification of frequencies. Therefore, the implementation of continuous monitoring system requires collecting the structural response, environmental and operational

data over a long enough period of time, covering all possible normal operational conditions, with the purpose of analyzing and removing the environmental influences and building a baseline for damage detection.

Figure 4.30 depicts the mode shapes calculated by finite element analysis (Caetano and Cunha, 2004) and experimentally identified on the basis of the ambient vibration test conducted in 2009. All experimental identified mode shapes are smooth and in good agreement with the numerical ones, except for the 2nd and 3rd modes with closely spaced frequencies around 2 Hz. It is interesting to note that the first two modes are clearly globe modes, the remaining are involving essentially the motions of one of the spans.

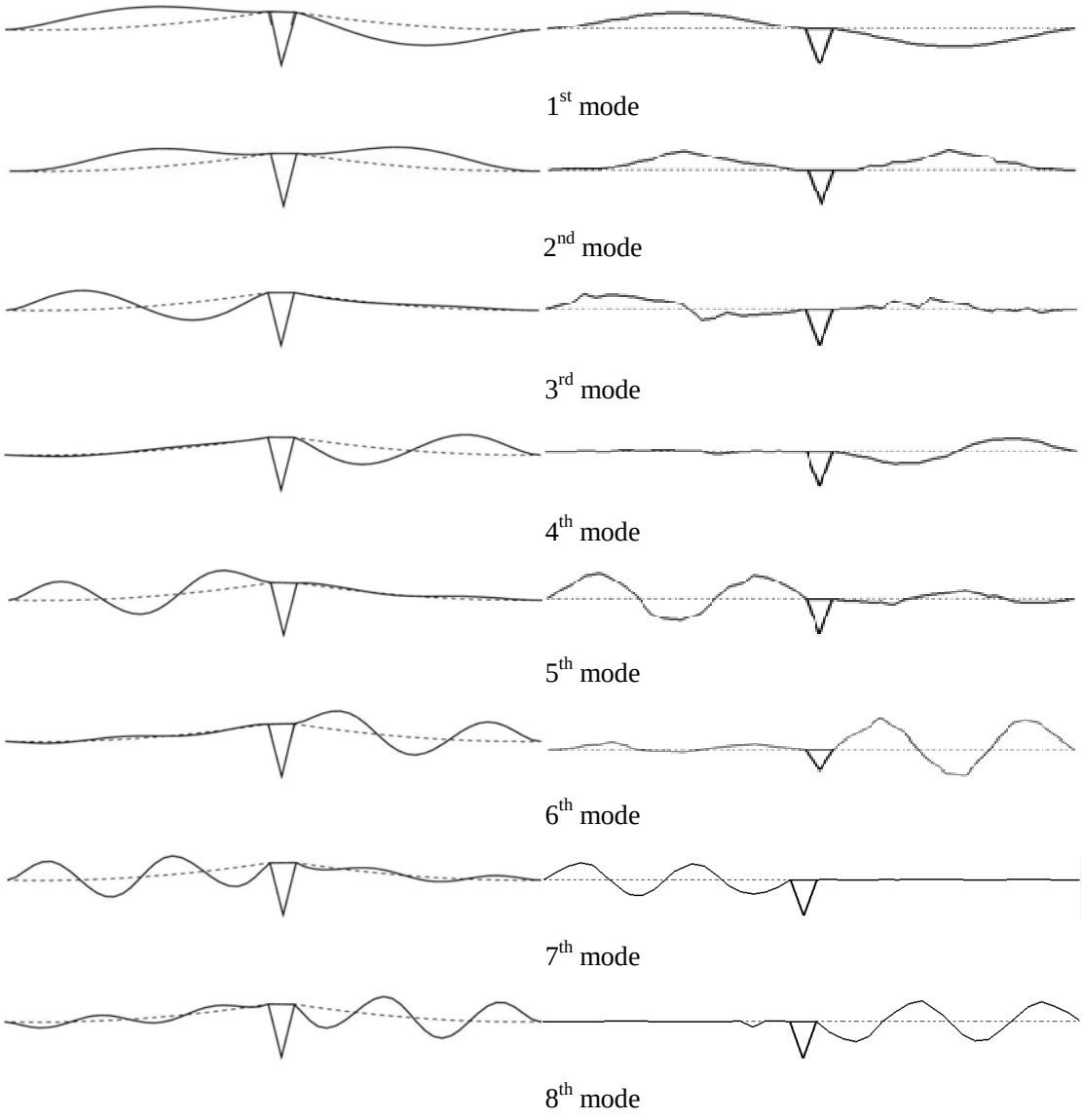

Figure 4.30 Mode shapes calculated by finite element analysis (left side) and identified by SSI-COV method (right side)

4.5 CONCLUSION

This chapter presents the operational modal analysis of Pinhão roadway bridge, Pedro e Inês footbridge and FEUP campus footbridge under different conditions. It is concluded that structural changes, namely related with rehabilitation works or with the installation of additional components, can induce variations of natural frequencies that can be accurately measured. The general tendency is that higher order frequencies are more sensitive than those of lower modes. The modification of frequencies may reflect the structural changes including possible variation of stiffness, mass and boundary conditions, which is the theoretical principle of vibration-based structural health monitoring. However, comparison of modal identification results estimated by ambient vibration tests conducted under different environmental conditions reveals that the structural frequencies are also influenced by environmental factors, which may mask the subtle change induced by small structural changes. As a result, we conclude that the efficiency and success of the implementation of continuous dynamic monitoring systems of bridges requires the analysis of the analysis of the long term behaviour under operational conditions, with the purpose of investigating and removing the environmental effects and build reliable damage indices which are only sensitive to the structural change. In this context, next chapter mainly introduces the continuous monitoring systems implemented in both Pedro e Inês footbridge and FEUP campus footbridge, characterizing the most relevant results achieved with the two applications.

5

CONTINUOUS DYNAMIC MONITORING OF BRIDGES

5.1 INTRODUCTION

In the previous chapter, it was shown that the variations of natural frequencies reflect structural changes, which suggests that they may be used to obtain a damage index for structural health monitoring. Unfortunately, the variations of natural frequencies are also sensitive to environmental and operational factors, such as temperature, traffic loads, wind, boundary conditions, etc. Such change caused by environmental and operational factors may mask subtle variations induced structural changes (Sohn, 2007). Accordingly, it is important to investigate the long term behaviour of bridges under operational conditions and remove the environmental and operational effects on modal parameters, with the purpose of extracting features only sensitive to structural damage.

Considerable efforts have been devoted to investigate environmental effects on modal variability. A 3-span RC footbridge was tested for a 3-year period and found that about 10% seasonal changes were repeatedly observed for each year, which may be partially attributed to the variation of ambient temperature (Askegaard and Mossing , 1988). It is proved in (Rücker et al, 1995) that the temperature effects on the dynamics of a 7-span highway bridge in Berlin can not be neglected. Rohrmann et al (1999) observed that variation of this bridge caused by temperature may reach 10% according to three years continuous monitoring. It was also noted that when a bridge structure is obstructed from expanding or contracting, the expansion joints can be closed significantly modifying the boundary conditions. A dynamic test was conducted

on a skewed 3-span box girder bridge and it was found that there was a 4-5% change in the natural frequencies during spring and winter time (Wahab and De Roeck, 1997). In (Peteers and De Roeck, 2000), the first 3 natural frequencies of Z24 highway bridge was found to vary from 14-18% based on one year monitoring results. A bilinear relationship between environmental temperature and the first two natural frequencies was observed. It was concluded that such bilinear relations are caused by the change of Young's modulus of 16cm thickness asphalt layer with temperature. It was reported in (Farrar et al, 1997) that the first natural frequency of a 7-span composite bridge varies approximately 5% during a 24 hours time period. It was observed that normal environmental change accounts for variation in the first ten modal frequencies from 0.20-1.52% based on one year monitoring of a 1177m long cable stayed bridge (Ni et al, 2005). In (Liu and Dewolf, 2007), it was presented that 3 identified frequencies of a 3-span curved highway bridge suffered changes of 5-6% induced by temperature during one full year. Finally, Magalhães et al (2010) reported annual variations due to temperature on the first 12 natural frequencies of a concrete arch bridge with a span of 280 m, Infante D. Henrique Bridge, around 1.5-2.5%.

Traffic loads may be another important operational variable affecting the dynamic properties of in-service structures. The influence of traffic loads on modal parameters of bridge structures has been also investigated. It was documented in (Kim et al, 1999) that the heavy traffic may account for the 5.4% decrease of natural frequencies of a 46m simply supported plate girder bridge, because of the added traffic mass loading. Magalhães et al (2010) observed that the traffic intensity induce variations on the natural frequencies of the Infante D. Henrique Bridge: traffic jams (stable load) over the bridge lead to a decrease of some natural frequencies (about 0.4% for the first mode), the intensity of the circulating traffic has impact on the level of the bridge vibrations and this has consequences on the natural frequency of the first bending mode (daily variations of about 1%). Regarding footbridges, most of traffic loads are due to pedestrians. The dynamic properties of footbridges under moving people are still less researched. In (Ellis and Ji, 1994), it was found that a person running and jumping on the spot can not change dynamic characteristics of the structure and therefore should be treated only as load. However, this investigation was conducted using a simply supported beam having a fundamental frequency of 18.68Hz, higher

than typical footbridge natural frequencies.

In addition, wind-induced vibrations may also affect structural modal properties, especially for long-span bridges. In (Fujino et al, 2000), the fundamental frequency of a suspension bridge was observed to reduce as the wind speed increased. On the other hand, the modal damping increased when the wind velocity exceeded a certain level. It was found that the maximum difference in the measured natural frequencies under low wind speed conditions and under typhoon conditions is 0.51% (Zhou et al, 2005).

Damping ratios are also reported to be influenced by operational factors. It is well-known that the presence of a stationary (standing or sitting) person increases the structural damping (Živanović et al, 2005).In (Zhang et al, 2002), the damping ratio was observed to be sensitive to the traffic mass, especially when the deck vibration exceeded a certain level. It was concluded that the damping ratio increased because the energy dissipation capacity in materials and at the joint increased due to higher traffic load. Recently, Magalhães (2010) documented that the modal damping ratios of all the modes of Infante D. Henrique Bridge increase due to traffic jam (about 50% for the second mode).

Brief summary of reported examples of environmental and operational variability reveals that they have potential adverse effects on vibration-based damage detection methods. Thus, the structure must be monitored continuously at least one full cycle of operating conditions in order to examine the long term structural behaviour, as well as environmental and operational factors, investigate the effects of environmental and operational variability on dynamic properties and extract features only sensitive with possible structural damage by removing such adverse influences.

In this context, this chapter mainly presents continuous dynamic monitoring results of Pedro e Inês footbridge, in Coimbra, and FEUP campus footbridge, in Porto, investigating the effects of environmental and operational factors, such as temperature and pedestrian traffic, on the dynamic characteristics of both footbridges.

Another important objective of the continuous dynamic monitoring of these footbridges consists in the evaluation of the footbridge serviceability by examining maximum acceleration amplitudes in normal operational conditions. The excessive human induced vibration is generally considered as a serviceability problem for footbridges (Živanović et al, 2005). The

prime example of such problem may arise from the infamous excessive lateral swaying of the new Millennium Bridge in London caused by crowd walking during its opening day on 10 June 2000 (Dallard et al, 2001). In the case of Pedro e Inês footbridge, it is anticipated at design level that it would be vulnerable to vertical and lateral vibrations based on preliminary finite element modelling, which was subsequently verified in crowd tests performed after construction (Caetano et al, 2010 a,b). As a result, it was decided to install Tuned Mass Dampers (TMDs) to control vibrations and a continuous dynamic monitoring system to observe the structural response during a period of 5 years after construction, with purpose of evaluating the serviceability of this footbridge in operational conditions. Besides, the stress ribbon footbridge of FEUP campus was selected as a case study of the European research project "Advanced Load Models for Synchronous Pedestrian Excitation and Optimized Design Guidelines for Steel Footbridges" (SYNPEX,2008), coordinated by RWTH Aachen. One of the tasks of this research was to characterise the corresponding dynamic response due to several passages of a single pedestrian and groups and flows of pedestrians, and evaluate the level of importance of human induced vibrations, from the human comfort point of view. However, the response of the footbridge under normal operational conditions was still unknown. Thus, this chapter describes further research on the continuous monitoring of maximum acceleration amplitudes of these two footbridges in-service conditions.

The chapter is mainly divided into three parts: the first two parts are dedicated to introduce the continuous monitoring results and investigate the environmental effects on the variation of modal parameters in operational conditions. Each part begins with a brief summary of previous results and characteristics of the continuous dynamic monitoring systems installed in the footbridges. Subsequently, the long-term monitoring results are presented, including the maximum vibration level, distribution of frequency components, averaged vibration level, variation of modal parameters, as well as environmental and operational variables. Afterwards, the investigation of the environmental effects on modal parameters based on continuous monitoring results under operational conditions is performed, laying a solid foundation for removal of such adverse effects and detection of possible damage, which will be discussed in detail in next chapter. At last, some conclusions of this chapter are synthesized.

5.2 CONTINUOUS DYNAMIC MONITORING OF PEDRO E INÊS FOOTBRIDGE

5.2.1 Previous research results

The structural features and basic dynamic properties of Pedro e Inês footbridge have been presented in section 4.3. During the design and construction phases, numerical and experimental investigations on the dynamic effects induced by pedestrians were conducted (Caetano et al, 2010a). Regarding lateral vibrations, the numerical analysis indicated that the first lateral mode of vibration was the most critical for the 'lock-in' effect of this footbridge. During the crowd tests performed before the installation of passive control device, it is observed that a maximum lateral acceleration of 1.2m/s^2 under the passage of a group of 145 pedestrian. With regard to vertical vibrations, several modes in the range of 1.5-4 Hz could lead to excessive vibrations when excited by the first or second harmonic of pedestrians in a crowded situation, or by groups of pedestrians walking, running or jumping on the spot. Results obtained during the dynamic tests performed after construction show that relative high accelerations in the vertical direction were recorded when groups of pedestrians jumped (simulation of vandal excitation). The maximum vertical accelerations were found at the middle points of two local arches, corresponding to the positions where accelerometers AV3 and AV6 were installed (Figure 3). The recorded maximum accelerations were 1.11 m/s^2 and 1.94m/s^2, respectively. However, recently released guidelines for design of footbridges, such as Service d'Études Techniques des Routes et Autoroutes (SETRA, 2007) and Human induced Vibration of Steel Structures (HIVOSS, 2007), recommended that lateral acceleration is limited in any case to 0.10m/s^2 to avoid the 'lock-in' effect, as well as acceleration range associated with degree of comfort as shown in Table 5.1.

It is noted that both vertical maximum accelerations previously monitored fall in the range of minimum degree of comfort, whereas the recorded maximum lateral vibration of 12m/s^2 far exceeds 0.1m/s^2, which might lead to unaccepted 'lock-in' phenomenon. Thus, additional Tuned Mass Dampers (TMDs) were installed to constrain possible excessive

vibrations induced by pedestrians in operational conditions.

Table 5.1 Defined comfort classes with acceleration range

Degree of Comfort	Vertical a_{limit}	Lateral a_{limit}
Maximum	<0.5m/s^2	<0.1m/s^2
Medium	0.5-1.0m/s^2	0.1-0.3m/s^2
Minimum	1.0-2.5m/s^2	0.3-0.8m/s^2
Unacceptable discomfort	>2.5m/s^2	>0.8m/s^2

Table 5.2 Natural frequencies, modal masses and characteristics of installed TMDs

Mode no.	Frequency (Hz)			Modal mass (kg)	M_{TMD} (kg)	K_{TMD} (N/m)	C_{TMD} (Ns/m)	Location, number and mass (kg)
	0.5p/m^2	Measured	TMD*					
1	0.83	0.83	0.77	202324	14790	349304	21411	Mv, 6x2465
2	1.42	1.39		170358				
3	1.80	1.81	1.79	773166	2777	352668	2285	Tlt, 2777
4	1.74	1.81	1.73	921010	2777	329928	2026	Tlt, 2777
5	1.90	1.95		444273				
6	2.34	2.28	2.27	117751	3376	689670	9591	Tlt, 2x1688
7	2.68	2.68		637758				
8	2.74	2.89	2.70	445215	7269	2085781	18807	Ttr, 3x2423
9	3.07	3.11	3.01	120763	2270	813742	7018	Teq 1x2270
10	3.17	3.25	3.07	72099	2270	846406	9093	Tdt, 1x2270

* optimal frequency of TMD

Figure 5.1 Horizontal TMD installed at the mid-span section

Figure 5.1 shows the horizontal TMD installed at mid-span. The design properties of TMDs are listed in Table 5.2 and the corresponding positions are shown in Figure 5.3 (a), aiming to control the modes 1, 3/4, 6, 8,9 and 10 that contribute to significant dynamic response of the footbridge (Caetano et al, 2010a). The corresponding modal shapes calculated

by SOVIA software and estimated by operational modal analysis using SMI toolkit are shown in Figure 5.2.

(a) 1st mode

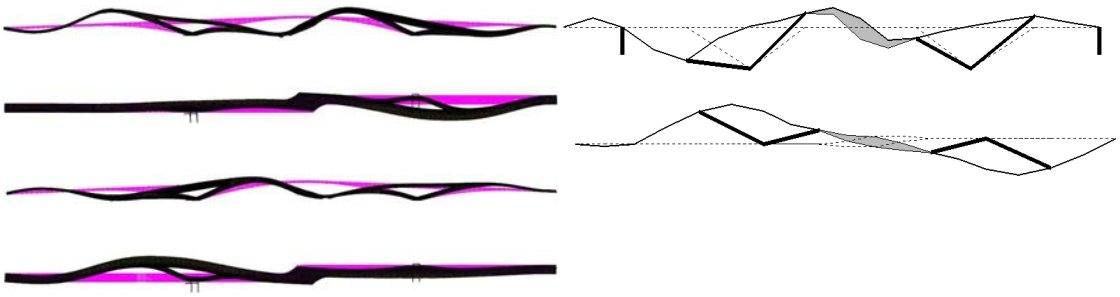

(b) 3rd/4th modes

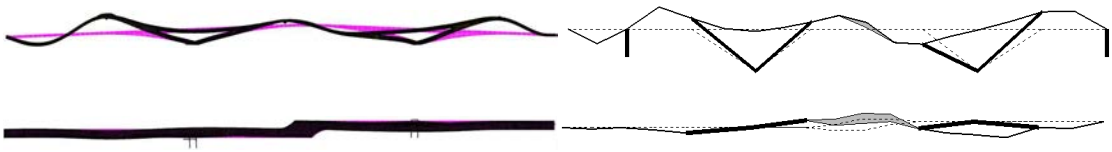

(c) 6th mode

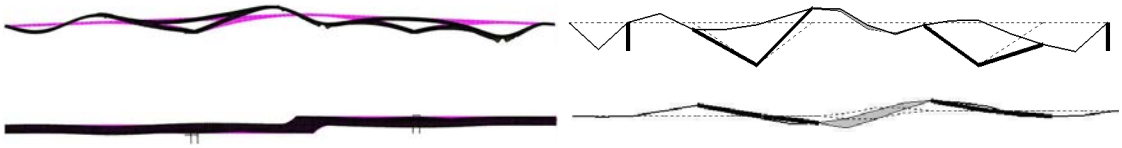

(d) 8th mode

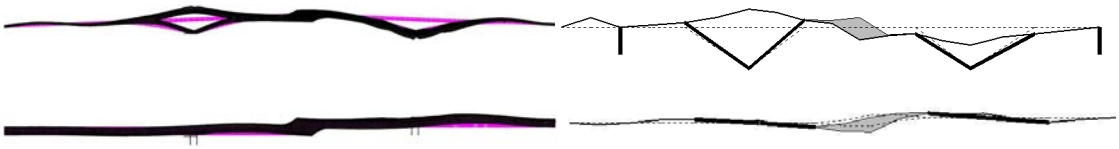

(e) 9th mode

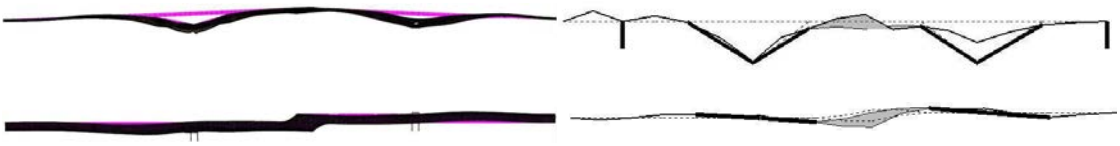

(f) 10th modes

Figure 5.2 Modes selected for control: calculated and identified modal shapes

5.2.2 Continuous dynamic monitoring system

Aiming the permanent characterisation of vibration levels after construction, the bridge owner required the implementation of a continuous dynamic monitoring system, which has been in operation since June 2007. This system was subsequently enhanced for research purposes, in order to include routines for automatic system identification and management of the processed results. This effort led to the organization on three modules, one for signal acquisition and transmission, a second one for automatic signal processing and modal identification, and a third one for results management and visualization (Hu et al, 2008). The second and third modules have been implemented in CSMI (Continuous Structural Modal Identification) toolkit and presented in Chapter 2. In this section, the module for signal acquisition and transmission is briefly introduced (Moutinho et al, 2008).

The signal acquisition module comprises six uniaxial piezoelectric accelerometers PCB-393C (Figure 5.4 (a)) installed in correspondence with the location of the vertical and lateral TMDs (Figure 5.3 (a)). Five of the accelerometers measure vertical accelerations (AV1 to AV3, AV5 and AV6), whereas the last one measures lateral vibrations at mid-span (AT4). All the sensors are mounted inside the steel box and are wired to a signal conditioner PCB-481A01, then connected to a digital computer that incorporates an analogue to digital converter. The acquisition system includes also a UPS system and is located inside one of the abutments (Figure 5.4 (b), (c)). An automatic signal acquisition toolkit was implemented in LabVIEW environment to record the acceleration signals with a sampling frequency of 100Hz and generate data files every 20 minutes. With the purpose of preparing an automatic signal processing, three successive setup files acquired in 20 minutes are concatenated to obtain one hour response file in order to achieve more stable estimation results of modal parameters.

The data transmission module is configured to search the latest acceleration and temperature files and send them to a computer located at FEUP, about 110km away from Coimbra, using an ADSL line via Internet. To reduce the size of signal files and fasten the data transmission, the acceleration signals are decimated, reducing the sampling frequency to 20Hz.

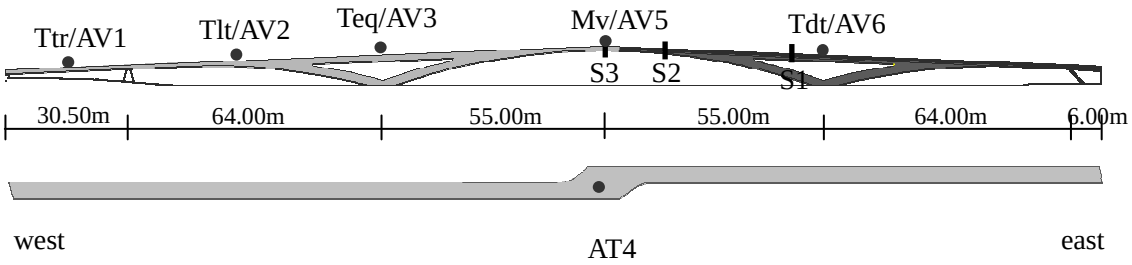

(a) Pedro e Inês footbridge: Longitudinal section and top view, deployment of accelerometers (AV1-AV3, AT4,AV5-AV6) and sections (S1-S3) instrumented with temperature sensors

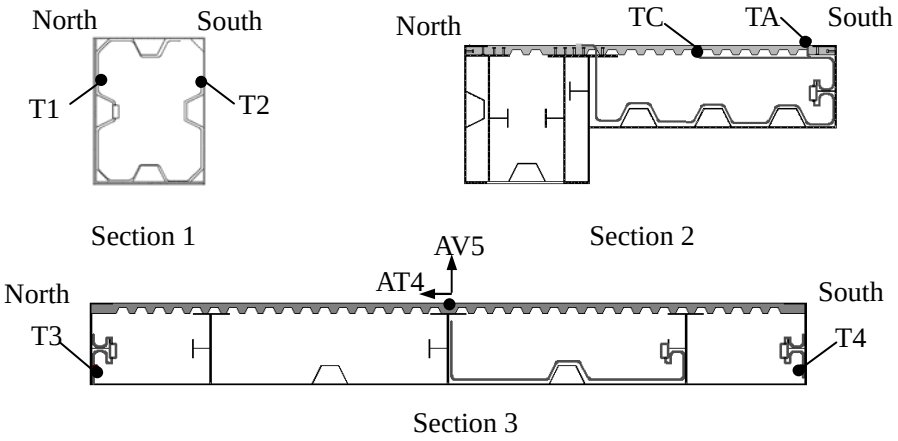

(b) Location of temperature sensors (T1 to T4, TC and TA) in cross sections

Figure 5.3 Pedro e Inês footbridge and deployment of TMDs, accelerometers and temperature sensors

(a) (b) (c)

(a) Accelerometers in deck

(b) Signal conditioner, signal acquisition card, digital computer and UPS

(c) General view of acquisition and conditioning system inside the abutment

Figure 5.4 Components of the continuous dynamic monitoring system

The signal acquisition and transmission module has been operating from the 1st of June 2007 to the 30th of May 2010, except for occasional stops due to small technique problems. It leads to the accumulation of a huge amount of data that needs to be processed, analysed and

interpreted. CSMI toolkit processes these signals automatically and generates the continuous monitoring results depicting long term behaviour of footbridge in operational conditions.

5.2.3 Continuous dynamic monitoring results

a) *Maximum vibration levels and distribution of frequency components*

In order to avoid possible adverse effects of electrical 'spike' noise and accurately evaluate the maximum vibration levels, they are detected by calculating the averaged vibration levels of the absolute envelope in a short interval, instead of picking the peaks of recorded acceleration signals directly. A typical vibration signal acquired from one accelerometer within 20 minutes is shown in Figure 5.5 (a). The zoomed part around the peaks is plotted in Figure 5.5 (b). During 1 second, the absolute envelope values are averaged and shown in Figure 5.5 (c), and the peak of acceleration amplitudes from one accelerometer are determined by picking the maximum value of the averaged absolute envelope values.

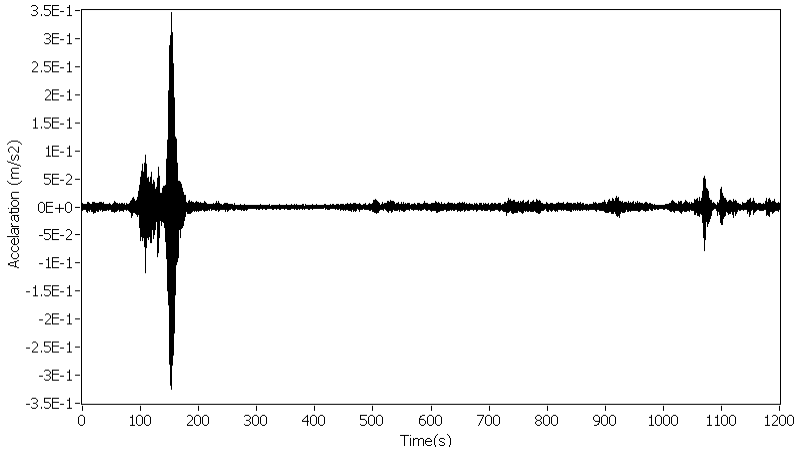

(a) Typical vertical vibration signal within 20 minutes

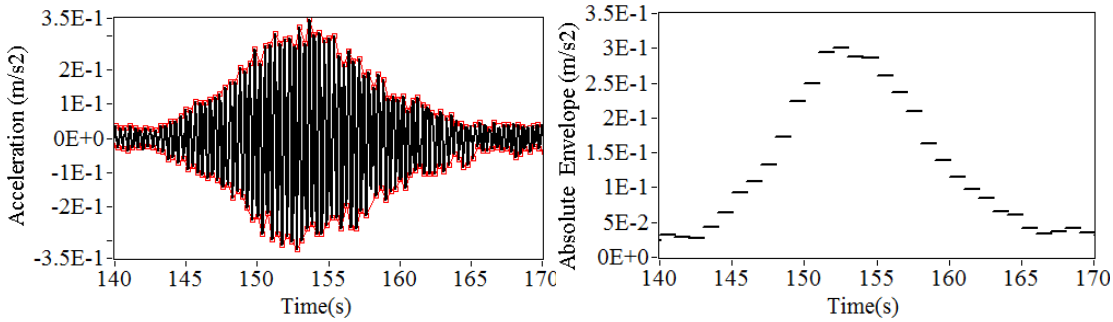

(b) Part of envelope around peak (c) Averaged absolute envelope within 1s

Figure 5.5 Typical vibration signal, envelope and averaged absolute envelope

The maximum lateral acceleration is determined from AT4 directly, while the maximum vertical acceleration is defined by finding the largest maximum acceleration from the 5 vertical accelerometers. The maximum lateral and vertical accelerations were detected automatically from each setup file of 20 minutes by CSMI toolkit. Based on the results from each setup within one day, the corresponding maximum daily lateral and vertical accelerations were also obtained, enabling the preparation of figures representing the evolution of these quantities along each month and each year, as well as the corresponding statistical distributions.

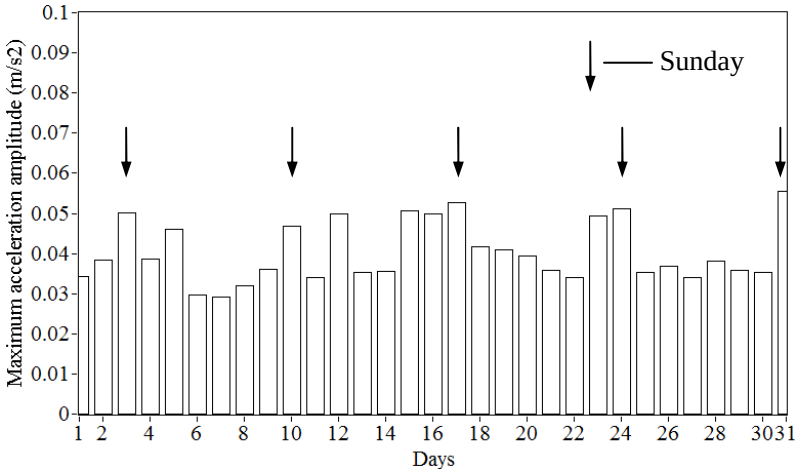

(a) Maximum daily lateral acceleration amplitude in one month

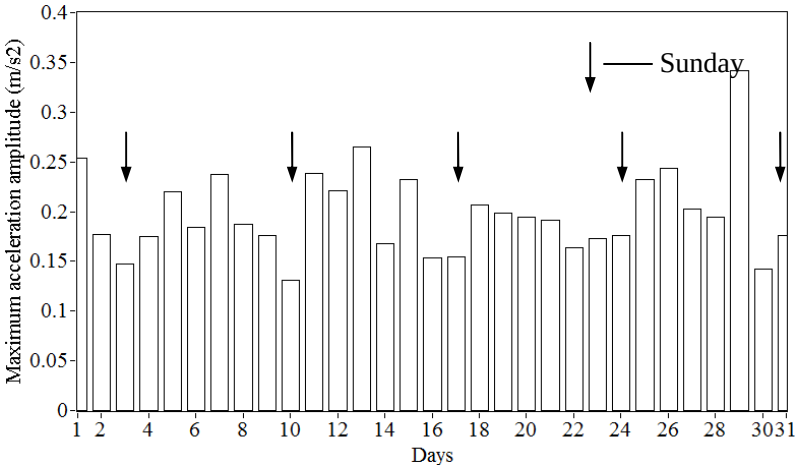

(b) Maximum daily vertical acceleration amplitude in one month

Figure 5.6 Maximum daily vibration amplitude in one month

Figure 5.6 shows the evolution of the maximum daily vibration amplitude during one month in both lateral and vertical directions. It is found that during one month, nearly all recorded maximum lateral acceleration amplitudes occurred on Sunday, whereas maximum

vertical amplitudes are noted in workdays. This may be explained taking into account the different types of pedestrian excitation that tend to induce maximum vibration levels in different directions. As reported in (Caetano et al, 2010a,b), lateral vibrations increase with the raising number of pedestrians crossing the footbridge. On Sundays, it is reasonable to expect that more people use the footbridge, because it links two areas of the city park along the river. As a result, with raising number of pedestrians on the footbridge, larger maximum lateral vibration levels are then observed. On the contrary, the relatively high vertical vibration levels are more associated with running or jumping of pedestrians, which may have a more significant contribution during workdays, where a more reduced number of pedestrians cross the bridge.

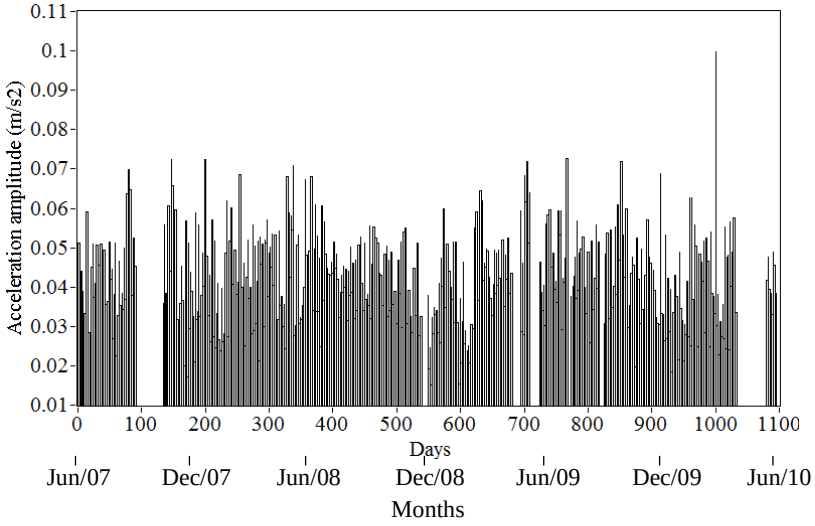

(a) Maximum daily lateral acceleration amplitude

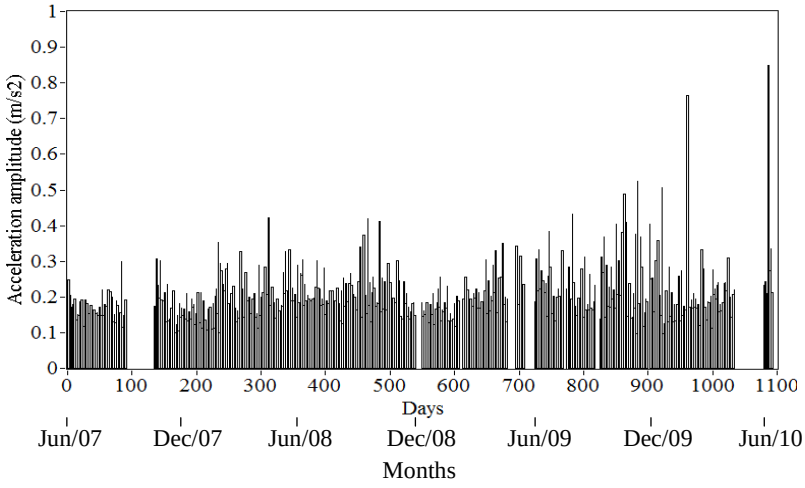

(b) Maximum daily vertical acceleration amplitude

Figure 5.7 Maximum daily vibration amplitude from 1st June 2007 to 31st May 2010 during day light

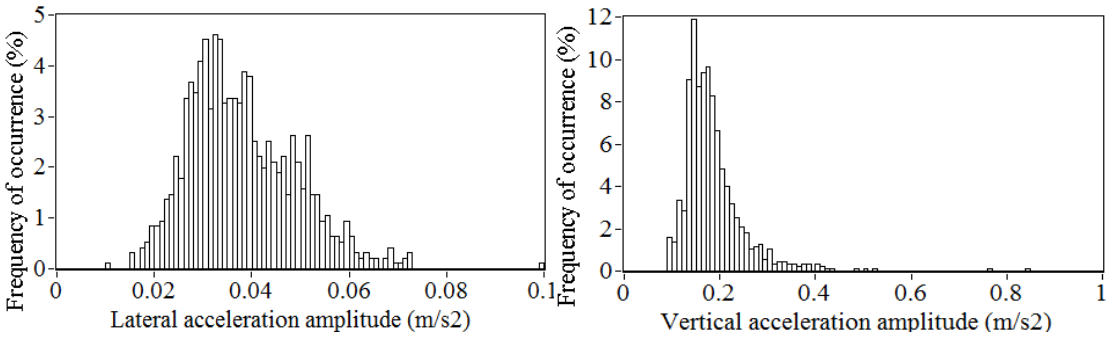

(a) Lateral acceleration amplitude (b) Vertical acceleration amplitude

Figure 5.8 Histograms of maximum daily acceleration amplitudes from 1st June 2007 to 31st May 2010 during day light

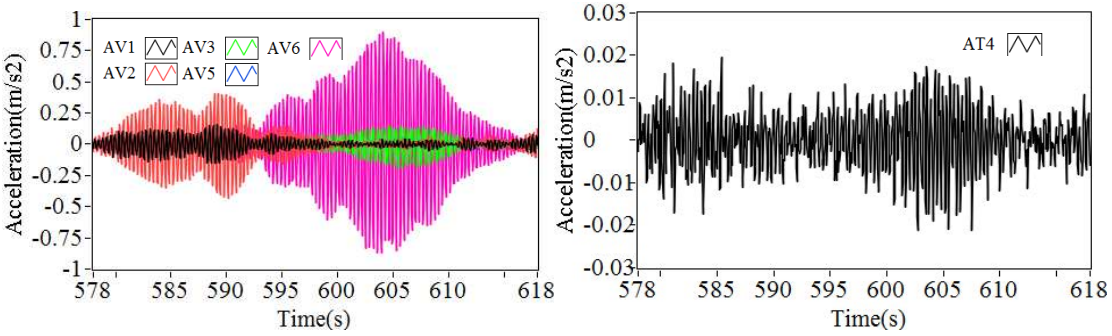

(a) Maximum vertical signals and corresponding lateral signal

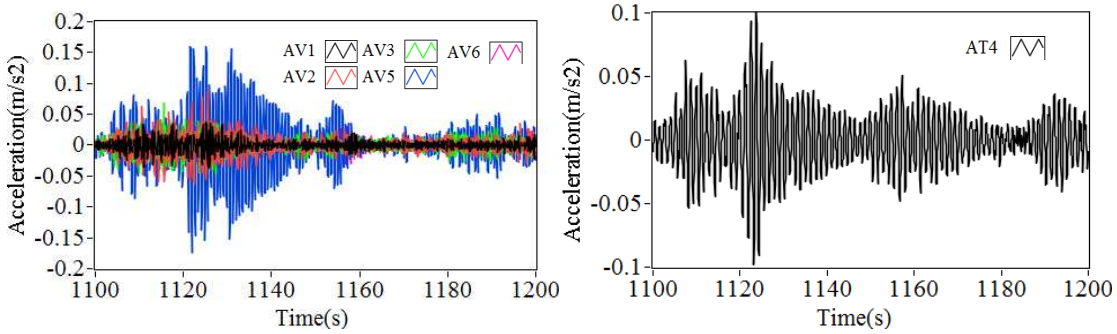

(b) Maximum lateral signal and corresponding vertical signals

Figure 5.9 Observed maximum acceleration signals

Figure 5.7 shows plots with the maximum daily lateral and vertical accelerations measured during 3 years (from June 2007 to May 2010), whereas the corresponding histogram is shown in Figure 5.8. Figure 5.9 shows that the maximum lateral acceleration is 0.099m/s^2, captured at 8:40 AM on the 27th Feb 2010, and the vertical acceleration is 0.849m/s^2, acquired from AV6 at 9:00 AM on the 25th May 2010. The signals recorded in other accelerometers are also included in Figure 5.9. Inspection of Figures 5.7 and 5.8, as well as comparison with comfort limits recommended by SYNPEX and SETRA guidelines (Table

5.1), it is found that all maximum lateral accelerations and nearly all vertical counterparts fall in the range of maximum comfort levels. It can be concluded that no serviceability problem is observed in this footbridge under normal operational conditions during 3 years, as consequence of the implementation of the corresponding passive control devices.

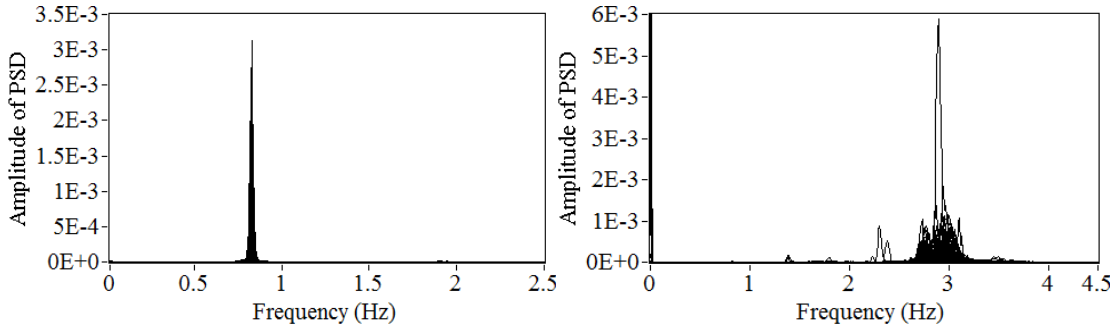

(a)Spectra of lateral signals (b) Spectra of vertical spectrums

Figure 5.10 Power spectra of signals corresponding to maximum accelerations observed from 1st June 2007 to 31st May 2010 during day light

In order to better characterize the behaviour of this footbridge when maximum vibrations are observed, the frequency content of acceleration signals is analyzed, selecting the corresponding maximum 20 minutes acceleration. Taking the signals shown in Figure 5.9 (a), for example, the 20 minutes acceleration signal from AV5 is picked, because the maximum vibration amplitude is observed in this sensor. The power spectra are produced using a Hanning window with 2048 points, and 50% overlap, with a resolution of 0.0097Hz (20Hz/2048). Figure 5.10 (a) shows that the peaks of power spectra related with maximum are around 0.83Hz, which coincides with the prediction from the design phase, indicating that the first lateral mode would be critical for the maximum lateral acceleration amplitude. Figure 5.10 (b) shows that most of the peaks of the spectra relate with maximum vertical vibrations are in the range of 2.7-3.2Hz, which means that natural frequencies in this range are excited by running or jumping of pedestrians. This is also in agreement with conclusion drawn at stages of design and testing. Besides, the finite element analysis indicates that the 8^{th}-10^{th} modes contribute to the significant vertical accelerations (Caetano et al, 2010a). Tab 5.2 lists the corresponding modal frequencies, which are 2.89Hz, 3.11HZ and 3.25Hz that match with the frequency range 2.7-3.2Hz where the maximum vertical vibrations were observed. This evidences that in operational conditions the high vertical responses of the footbridge stem from contributions of the 8^{th}-10^{th} modes as predicted in design. The suggestion of waterfall

plots could further clarify this conclusion.

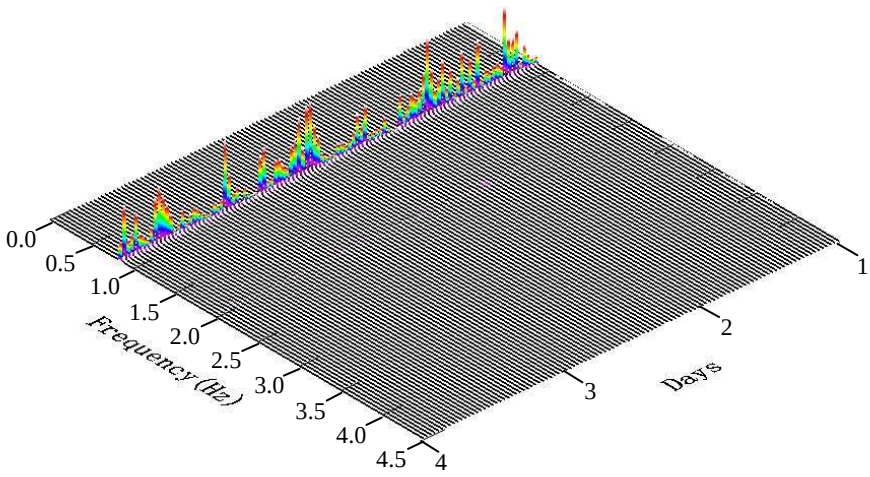

(a) Waterfall plot of lateral acceleration signals (linear scale)

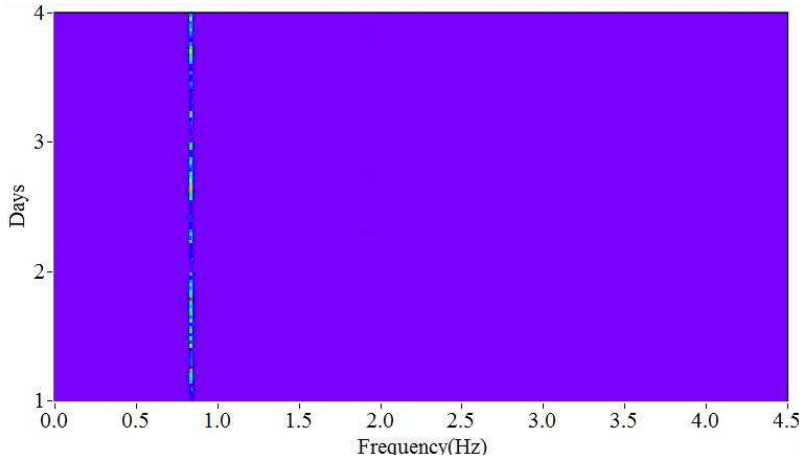

(b) Top view of (a)

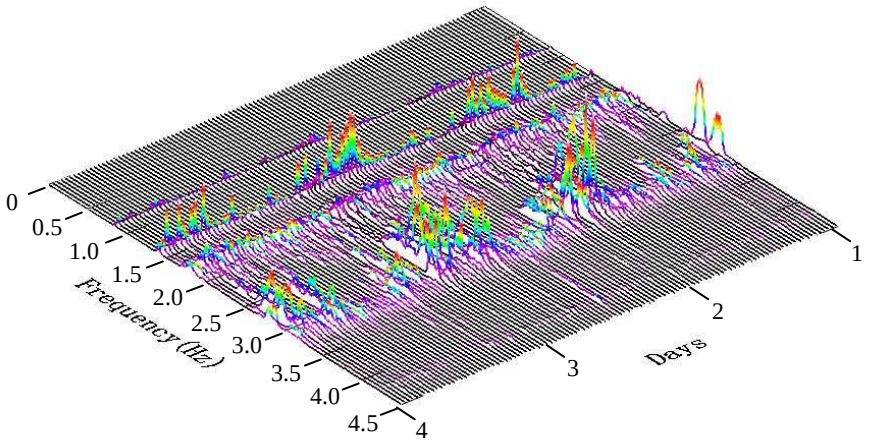

(c) Waterfall plot of vertical acceleration signals (linear scale)

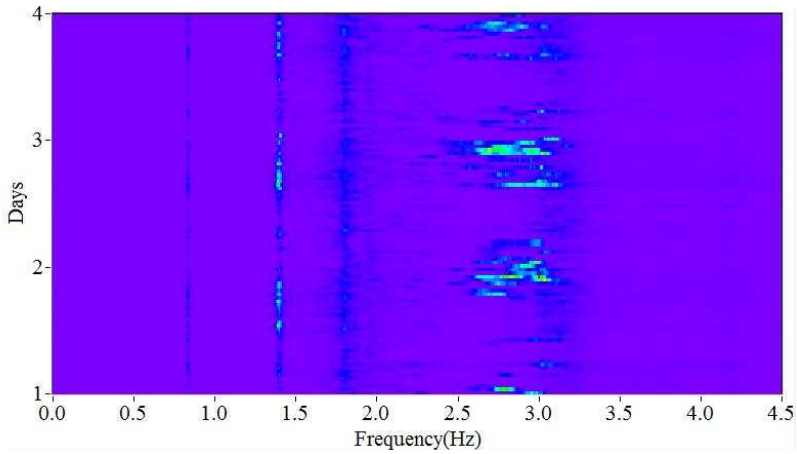

(d) Top view of (c)

Figure 5.11 Waterfall plots of acceleration signals in 3 consecutive days

The waterfall plot is obtained by arranging sequences of power spectral estimates besides each other, which allow to depict the frequency contents of the response, identifying different intensity periods and allowing the observation of the time variation of natural frequencies. Figures 5.11 (a), (c) show the lateral and vertical waterfall plots based on the power spectra (linear scale) of acceleration responses acquired in 3 consecutive days. Top views of them are shown in Figures 5.11 (b) and (d). Vertical acceleration responses recorded in 20 minutes from AV1-AV3 and AV5-AV6 are used to generate every averaged normalized power spectra, while each lateral power spectra is produced by the signal from AT4. The power spectra are obtained using a Hanning window with 2048 points, and 50% overlap, the frequency resolution being 0.0097Hz (20Hz/2048).

From Figures 5.11 (a) and (b), it is observed that the peaks of the spectra are around 0.83Hz, which means that the first lateral mode (0.83Hz) is well excited, contributing to the significant lateral acceleration response during operational conditions. Figure 5.11 (c) and (d) show clear peaks at 1.39Hz, corresponding to the second natural frequency. On the contrary, the peaks for frequencies higher than 1.6Hz are not so clearly defined, which may reflect the damping introduced by several vertical TMDs tuned for frequencies in the range 1.8-3.4Hz. However, the relative high amplitudes of spectra are observed in the range of 2.7-3.2Hz, which may reflect the large energy introduced by pedestrian behaviour, such as running or jumping. It may further prove that the 8^{th}-10^{th} modes within the range of 2.7-3.2Hz are easily excited and contribute to the main vertical response, as indicated in the previous dynamic

analysis. Besides, inspection of Figure 11 (c) and (d) show that the peaks around 1.39Hz in the afternoon are higher than those in the morning, which may indicate that the pedestrian traffic intensity is higher during the afternoon.

b) *Variation of environmental/operational factors and modal parameters*

For in-service structures, the variation of dynamic properties can be the result of time-varying environmental conditions. The environmental and operational factors mainly consist of the temperature, humidity and wind, as well as traffic loading and ambient loading on the structures. In this section, the monitored temperature data during 3 years from 6 thermal sensors installed on different positions are presented. The pedestrian loading is approximately evaluated by hourly averaged acceleration amplitudes and also described. Finally, the variation of identified frequencies and modal damping ratios is reported to characterize the long term dynamic prosperities of the footbridge.

Six temperature sensors are installed in different positions of the footbridge (Figure 5.3 (b)). T1 and T3 are mounted on the north surface of the steel box girder at the arch and at the middle of the footbridge, respectively. On the contrary, T2 and T4 are mounted in the south surface. TC and TA record the concrete deck internal temperature and ambient temperature. Figure 5.12 (a) shows temperature records from 6 thermal sensors during 3 years, sharing similar seasonal variations. The maximum and minimum values are 42.6ºC and -0.85 ºC, recorded in TA and T2, respectively. However, the different temperature records during both summer time and winter time are also perceived, as shown in Figures 5.12 (b) and (c). It is observed that during summer time the air and concrete deck temperatures are relatively high, while in the winter time higher temperatures are noted from south sensors. It is inferred that the difference among the 6 temperature records are caused by the orientation of the footbridge and solar angle. Figure 3 displays that the footbridge approximately east-west direction. As a result, in most of time of summer period, the sunlight shines the concrete deck where TA and TC are mounted, producing relative high temperature records. Whereas, during winter time, the sensors installed in south surface are more exposure to the sunlight due to the smaller solar angle, resulting in temperature differentials. A clear time lag between the concrete deck inner temperature with regard to other records is observed. The possible reason is that it

would take a longer time for the concrete deck to reflect the change of temperature. The difference of temperature is found to be correlated with the natural frequencies in different relations, which will be discussed in next section.

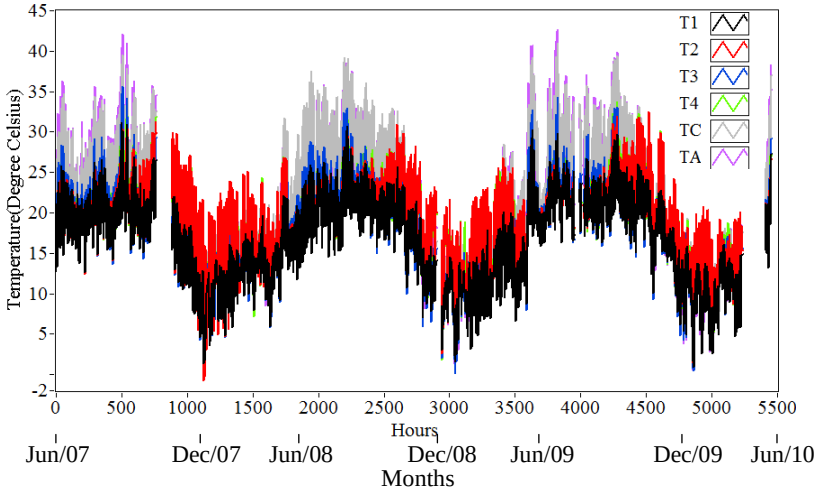

(a) Temperature record in different positions from 1st June 2007 to 31st May 2010 during day light

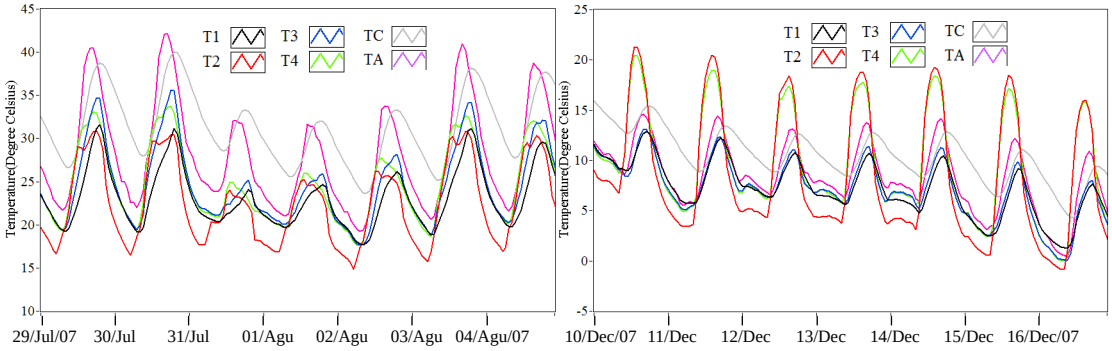

(b) Temperature in summer time (c) Temperature in winter time

Figure 5.12 Temperature record

Concerning the pedestrian excitation, the hourly averaged lateral acceleration amplitude was used in this work to characterise the pedestrian traffic intensity. In (Caetano et al, 2010 a,b), it is reported that the lateral vibration will increase with the raising number of people crossing the bridge. Therefore, it is reasonable to assume that higher lateral vibration levels in each hour are mainly a result of more moving people crossing the footbridge. The detailed algorithm of evaluation of vibration levels has already been described in Chapter 3. In every hour, the absolute values of the envelope of the lateral accelerations measured by AT4 installed at the mid-span (Figure 5.3), are averaged, as shown in Figure 5.13 (a). It is noticed that the lateral vibration levels in the afternoon are higher than those in the morning, which agrees with the observation from Figure 5.11 (d) that pedestrian intensity is higher during the

afternoon. At noon, the vibration levels are relatively lower, possibly because less people cross the footbridge at launch time. Such trend of daily variation of hourly averaged lateral accelerations during daylight is further confirmed by overlapping all corresponding plots during one month, as shown in Figure 5.13 (b). The larger vibration levels caused by more pedestrian are observed in the afternoon, and a clear gap is also found at noon. Plotting all hourly averaged accelerations of each day during one month consecutively (Figure 5.13 (c)), it is interesting to note that the larger lateral vibration levels are found on Sundays, which clearly stems from the higher pedestrian intensity on Sundays in this footbridge linking two sectors of the city park. Figure 5.13 (d) plots hourly averaged lateral accelerations during 3 years, showing that lateral accelerations tend to increase in summer time and decrease in winter time, which seems reasonable as less pedestrian use the footbridge during rainy winter.

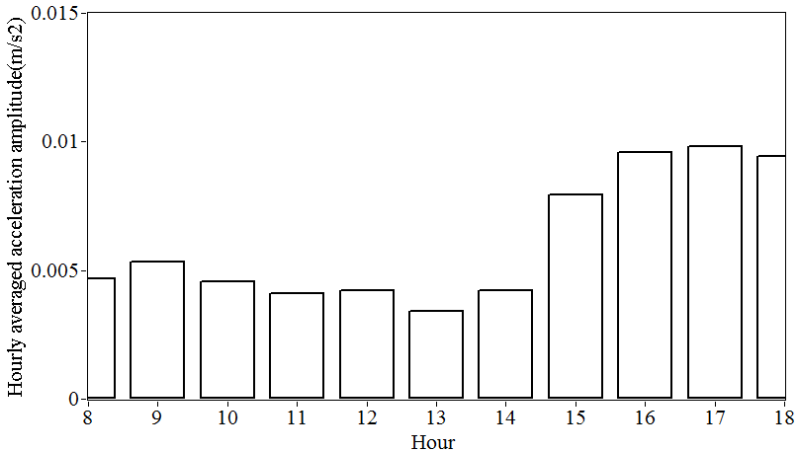

(a) Hourly lateral averaged acceleration amplitude during one day (daylight)

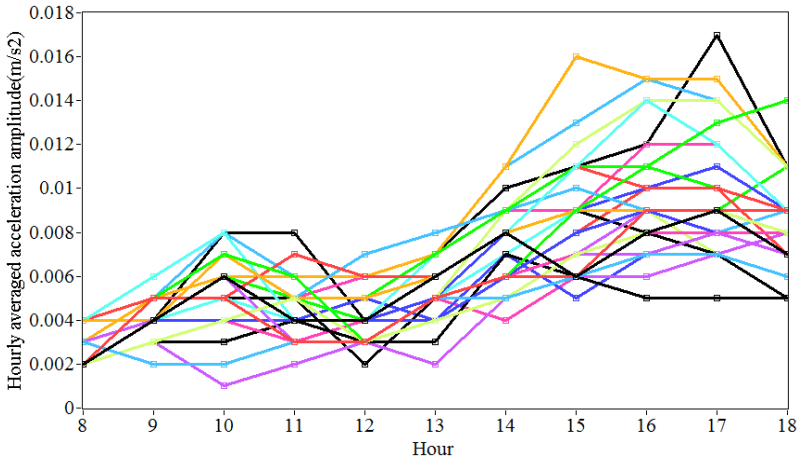

(b) Monthly lateral averaged acceleration amplitude (overlapping of 31 daylight period)

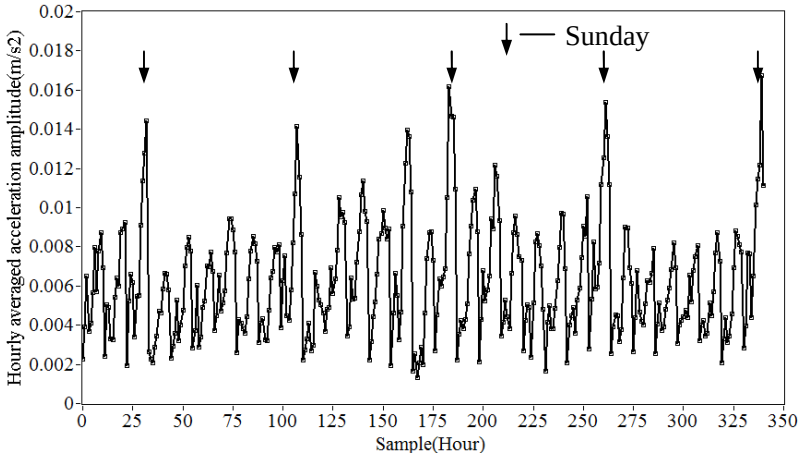

(c) Monthly lateral averaged acceleration amplitude (consecutive period of 31 daylights)

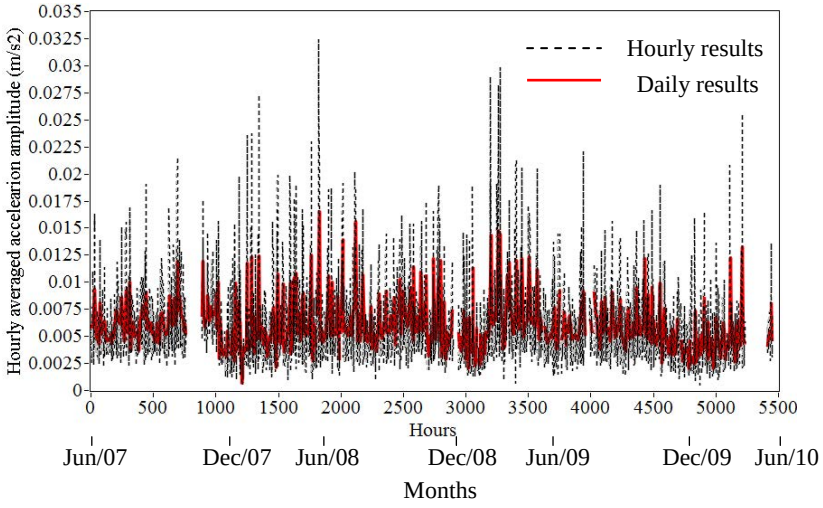

(d) Lateral averaged acceleration amplitude from 1st June 2007 to 31st May 2010 during day light

Figure 5.13 Hourly lateral averaged acceleration amplitude

Figures 5.14 (a) and (b) show acceleration signals from the 6 sensors in the hours corresponding to the maximum and minimum averaged lateral vibrations observed. The assumption that higher lateral vibration levels are mainly a consequence of more people moving over the footbridge may be partially validated by selected lateral acceleration signals. Figure 5.14 (a) displays relative large lateral accelerations which are probably associated with streams of pedestrians, resulting in high lateral vibration level in one hour. It is also interesting to refer that the amplitude of lateral acceleration varies frequently in this hour while the vertical counterparts are relatively stable, which may indicate the intermittent activation of the lateral TMDs. Comparing with the acceleration signals shown in Figure 5.14 (a), the vibration levels of Figure 5.14 (b) in both vertical and lateral direction are quite small.

The reason is that the minimum averaged vertical vibration was recorded at 8:00-9:00 on the 4th Jan 2008 and very few people use this footbridge in a cold winter morning.

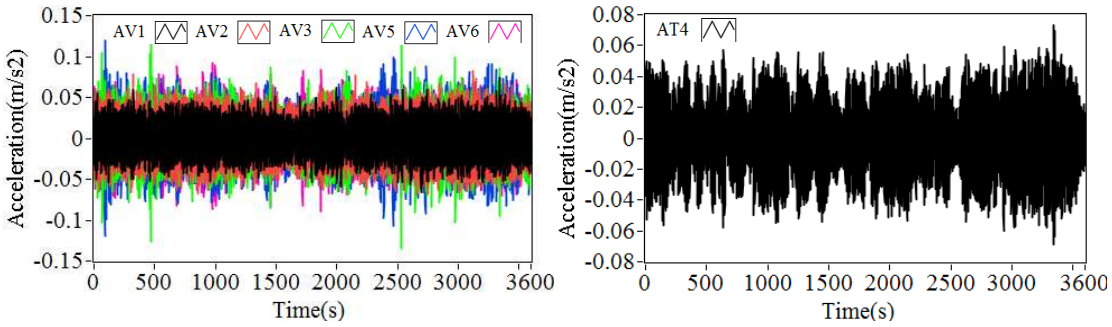

Vertical Lateral

(a) Signals corresponding to the maximum averaged vertical accelerations

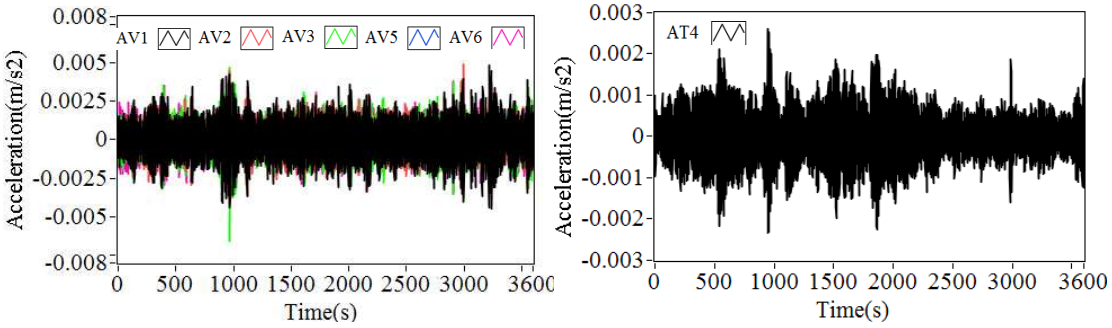

Vertical Lateral

(b) Signals corresponding to the minimum averaged vertical accelerations

Figure 5.14 Acceleration signals acquired in the hours corresponding to maximum and minimum averaged lateral accelerations observed

The modal parameters are identified from vibration signals acquired from the 6 accelerometers using the automatic SSI-COV algorithm, which is implemented in the CSMI toolkit, described in Chapter 3. With the purpose of preparing an automatic signal processing, three successive setup files acquired in 20 minutes are concatenated to obtain a one hour response file and achieve more stable results. A typical stabilization diagram stemming from the application of the automatic system identification procedure to continuous monitoring data is presented in Figure 5.15. An averaged normalized Power Spectrum Density plot is overlapped to reflect frequency domain information. Inspection of Figure 5.15 shows that very clear alignments of stable poles can be found in the frequency ranges 0-1.5Hz and 4-10Hz, leading to very accurate modal estimates. Less clear results are found in the frequency range 1.5-4Hz, probably owing to the damping introduced by the several vertical TMDs.

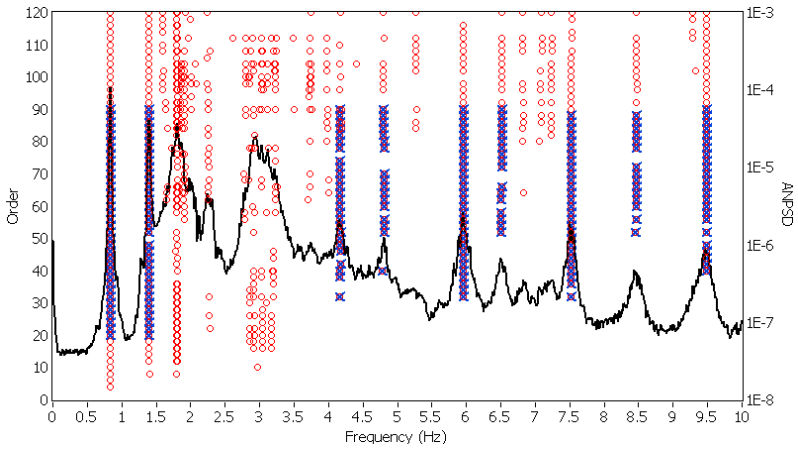

Figure 5.15 Typical stabilization diagram produced by the automatic SSI-COV algorithm using one hour signals

Figure 5.16 (a) shows the identified frequencies of 8 modes in the range 0-10Hz from the 1st June 2007 to the 31st May 2010. Figure 5.16 (b)-(i) plots the time evolution of frequency estimates of each mode individually. In order to clearly depict the general variation trend during three years, the hourly frequency results within one day are averaged again to produce the daily averaged frequencies. They are also presented as the solid line in red. The variation of frequencies is caused by environmental/operational factors, which will be discussed in next section.

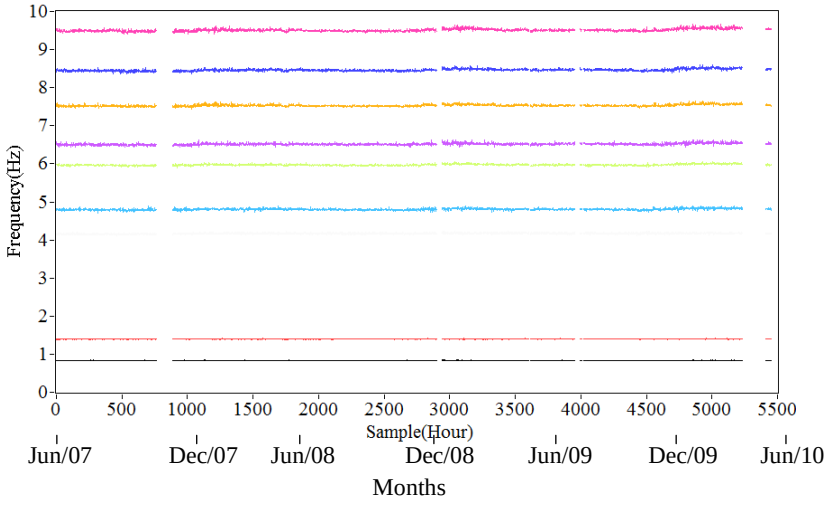

(a) All identified frequencies

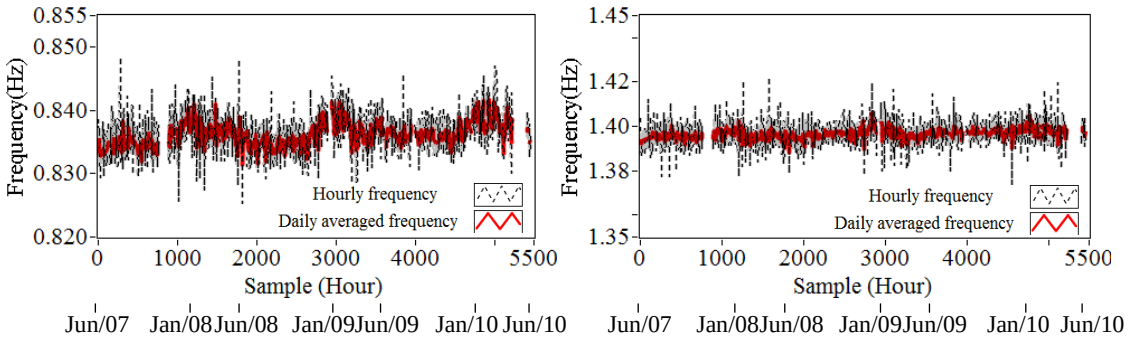

(b) 1st frequency

(c) 2nd frequency

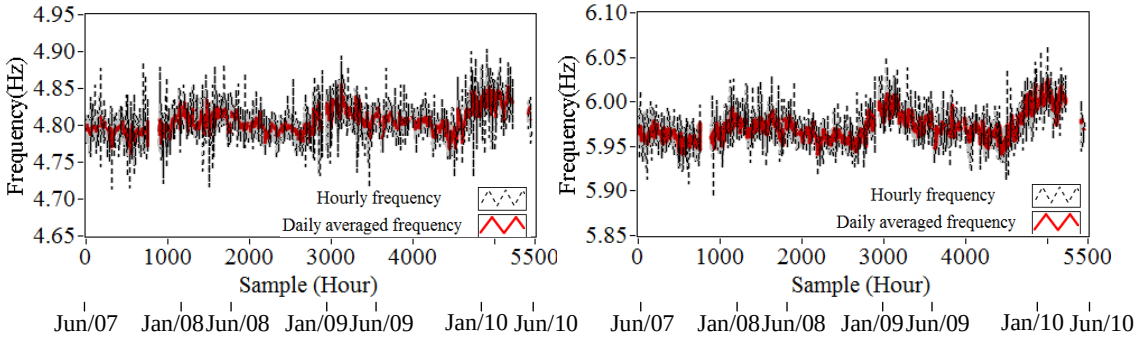

(d) 12th frequency

(e) 13th frequency

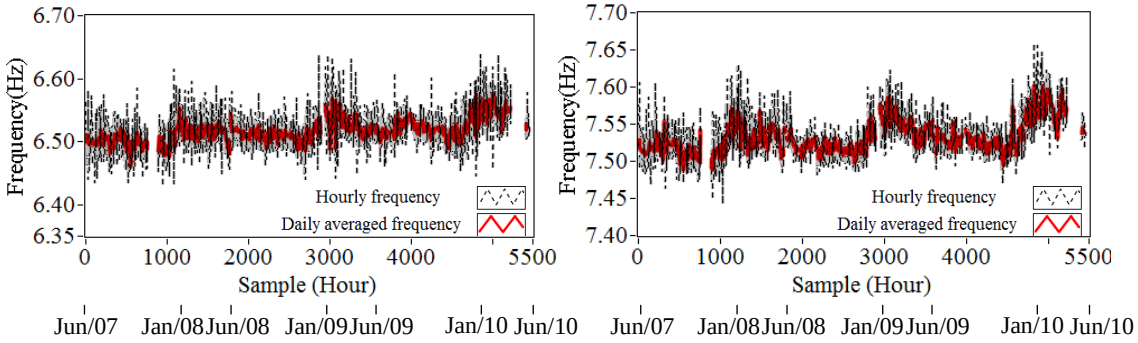

(f) 14th frequency

(g) 15th frequency

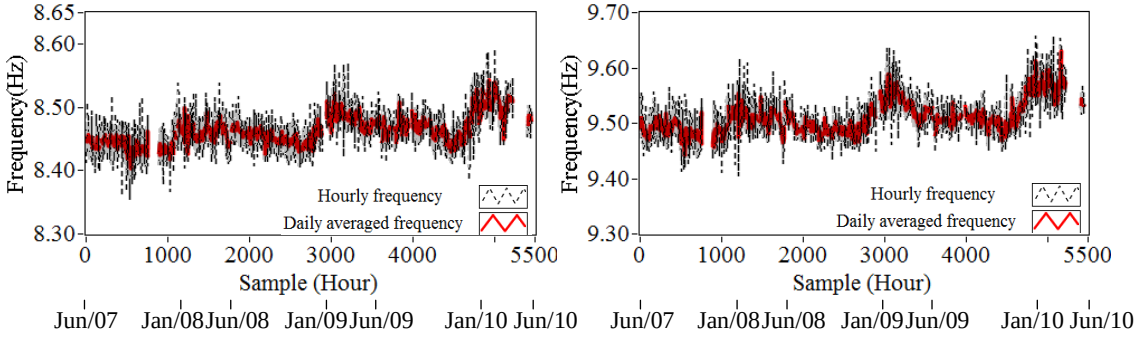

(h) 16th frequency

(i) 17th frequency

Figure 5.16 Identified frequencies from 1st June 2007 to 31st May 2010 during day light

Table 5.3 summaries the statistical information of all identified natural frequencies. It is observed that the changes of environmental/operational conditions lead to relative variations in the frequencies in the range of 2.7%-3.9% in the period of 3 years.

Table 5.3 Statistics of identified natural frequencies

Averaged frequency(Hz)	Frequency range(Hz)	Maximum difference(%)	Standard deviation(Hz)
0.836	0.824-0.848	3.0	0.003
1.397	1.370-1.422	3.7	0.004
4.807	4.714-4.903	3.9	0.022
5.973	5.893-6.064	2.8	0.019
6.518	6.418-6.644	3.5	0.026
7.533	7.435-7.676	3.2	0.026
8.465	8.347-8.593	2.9	0.029
9.512	9.402-9.662	2.7	0.034

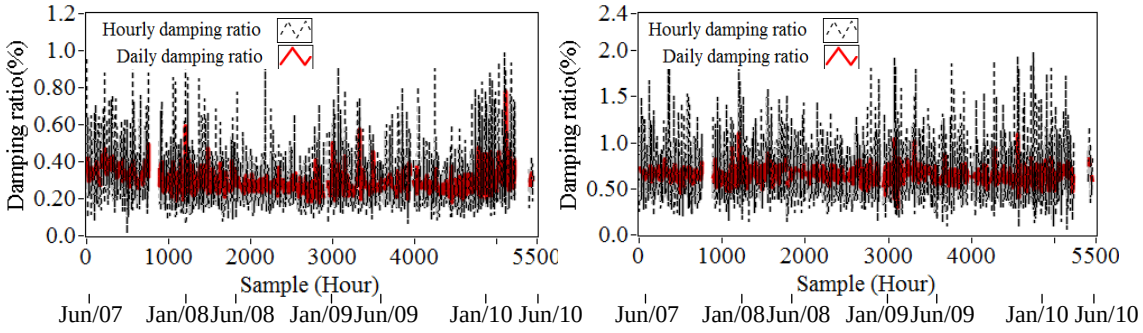

(a) 1st modal damping ratio (b) 2nd modal damping ratio

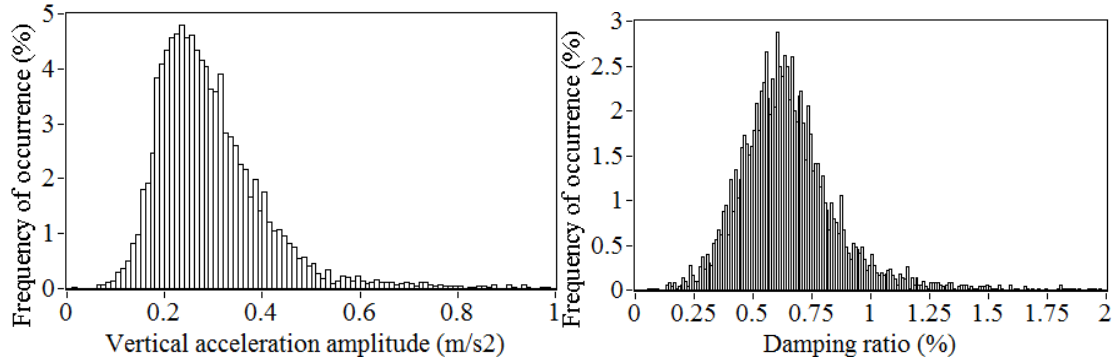

(c) Histogram of 1st modal damping ratio (d) Histogram of 2nd modal damping ratio

Figure 5.17 1st and 2nd modal damping ratio and corresponding histograms from 1st June 2007 to 31st May 2010 during day light

The black dash line in Figures 5.17 (a) and (b) shows the damping ratio of the first 2 modes of vibration, estimated from signals acquired in one hour from 5 vertical accelerometers and 1 lateral. The solid line in red means daily averaged results, clarifying the

long term variation tendency. The corresponding histograms of modal damping estimates are plotted in Figures 5.17 (c) and (d), respectively. Inspection of Figures 5.17 (a) and (c) shows that the first damping ratio estimates distributes are around the 0.30% (averaged damping ratio during 3 years), which is even slightly lower than 0.41% estimated from operational modal analysis (Table 4.4). This can stem from two reasons. One is that the lateral component is dominated in the first mode (Figure 4.20), but only one accelerometer (AT 4) was used to acquire lateral signal, which reduce the accuracy in the identification of the modal damping ratio. Another reason is that bias errors may also exist in estimated damping ratios when the excitation is quite low. It is observed that the 2nd modal damping ratio scatters around 0.64% (averaged damping ratio during 3 years) and is close to 0.57% identified by operational modal analysis. Although the vertical component dominates in this mode and 5 accelerometers record vertical response, the estimated damping ratio under conditions of low excitation may be questionable.

c)*Correlation between environmental/operational factors and modal parameters*

According to previous investigation summarised in the introduction (section 5.1), the temperature may be the principal factor affecting the variation of natural frequencies under operational conditions. Also, it is noted that, for this footbridge, 6 thermal signals recorded in different positions along the footbridge have distinct trend of variation. The correlation coefficients fitting linear regression models between the 6 temperature records and the frequency estimates of different mode orders are listed in Table 5.4. Inspection of each column of this table clearly shows that the coefficients between temperature readings from T4 and frequencies f_{12}-f_{17} are larger than those from other sensors, which means that the temperature record from the south surface at midspan of the footbridge can better reflect a significant effect on the change of natural frequencies than other temperature sensors. Therefore, the temperature readings from T4 were selected as the most representative to investigate the temperature effect.

Figures 5.18 (a)-(h) display the relation between temperature recorded by T4 and identified natural frequencies $f_{1,}$ $f_{12\text{-}17}$. As shown, all natural frequencies decrease with the temperature increase. From a statistical viewpoint, the relations between temperature and all

natural frequencies can be identified as approximately linear. The linear regression model was then developed to represent the natural frequencies as a function of temperature, which can be mathematically described as f_i=a+bt, where a and b are coefficients to be estimated, t representing the samples of temperature and f_i being the corresponding natural frequencies. The resulting curve fitting is also plotted as the red solid lines in Figure 5.18. It is also noted from Table 4 that the correlation coefficient between natural frequencies f_2 and temperature is quite small. It may be inferred that f_2 is less sensitive to temperature effect. Inspection of Figure 5.16 (c) shows the variation of f_2 during 3 years which is relatively small compared with other mode results.

Table 5.4 Correlation coefficients between the temperature records in different positions and identified frequencies

Frequency	f_1	f_2	f_{12}	f_{13}	f_{14}	f_{15}	f_{16}	f_{17}
T1	0.70	0.25	0.52	0.66	0.41	0.67	0.49	0.64
T2	0.65	0.22	0.62	0.73	0.50	0.74	0.62	0.69
T3	0.73	0.28	0.53	0.68	0.43	0.69	0.50	0.64
T4	0.69	0.24	0.63	0.75	0.51	0.75	0.62	0.70
TC	0.68	0.26	0.49	0.62	0.36	0.61	0.41	0.59
TA	0.72	0.28	0.54	0.67	0.42	0.67	0.48	0.63

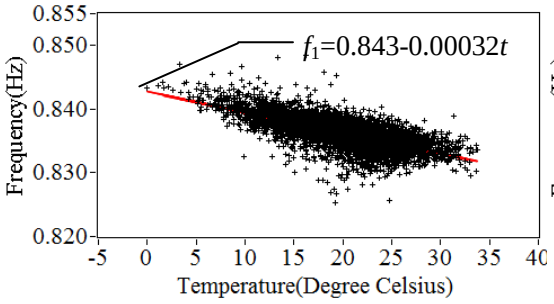

(a) 1st frequency

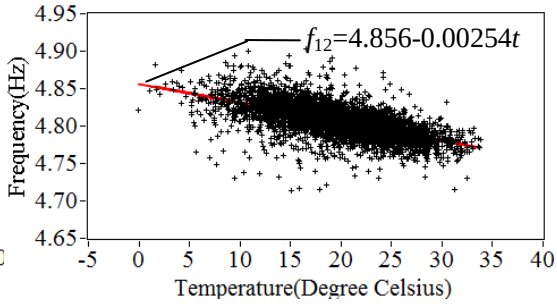

(b) 12th frequency

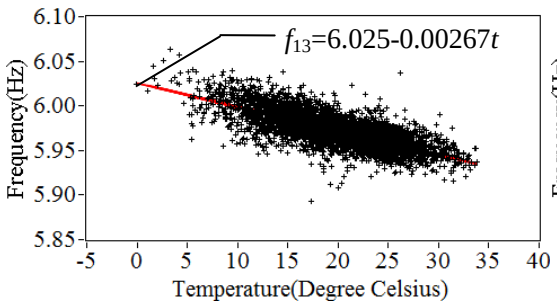

(c) 13th frequency

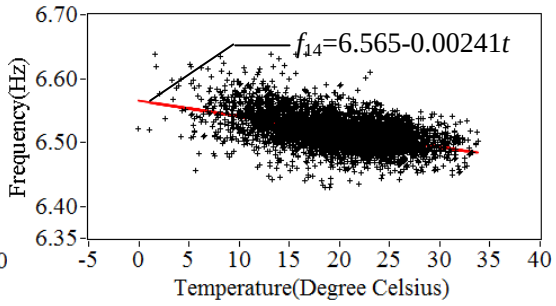

(d) 14th frequency

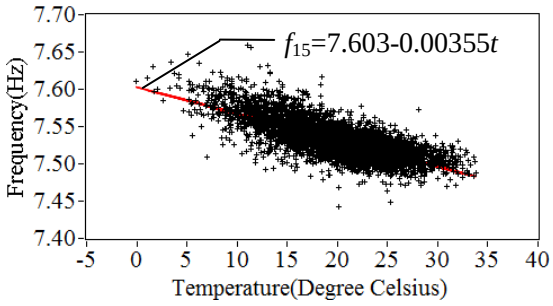

(e) 15th frequency

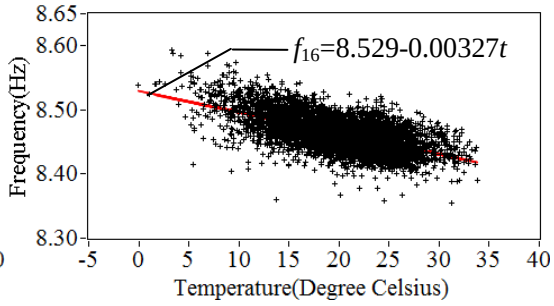

(f) 16th frequency

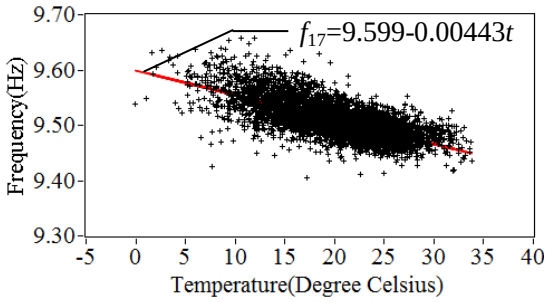

(g) 17th frequency

Figure 5.18 Identified frequencies versus temperature recorded at T4 from 1st June 2007 to 31st May 2010 during daylight

Beyond temperature, pedestrian traffic may also affect the variation of frequency estimates. In (Caetano et al, 2010a), it is pointed that during dynamic tests performed before installation of TMDs, a slight decrease of the first natural frequency was observed when 'lock-in' phenomenon occurred due to more pedestrians over the footbridge. A possible reason for reduction of frequency is also the nonlinear behaviour of the foundations. In (Caetano et al, 2010b), after installation of TMDs , it is also observed that activation of lateral TMD due to high vibration levels also reduce the first natural frequency. Based on the long term monitoring results, the correlations between identified frequencies and hourly averaged acceleration level were evaluated to reflect the effects of traffic intensity, as shown in Figure 5.19. The correlation coefficients fitting linear regression model between hourly averaged lateral vibration level and frequency of different orders are listed in Table 5.5.

Table 5.5 Correlation coefficients between the hourly lateral averaged acceleration level and identified frequencies

Frequency	f_1	f_2	f_{12}	f_{13}	f_{14}	f_{15}	f_{16}	f_{17}
Lateral vibration level	0.52	0.40	0.14	0.20	0.14	0.26	0.23	0.23

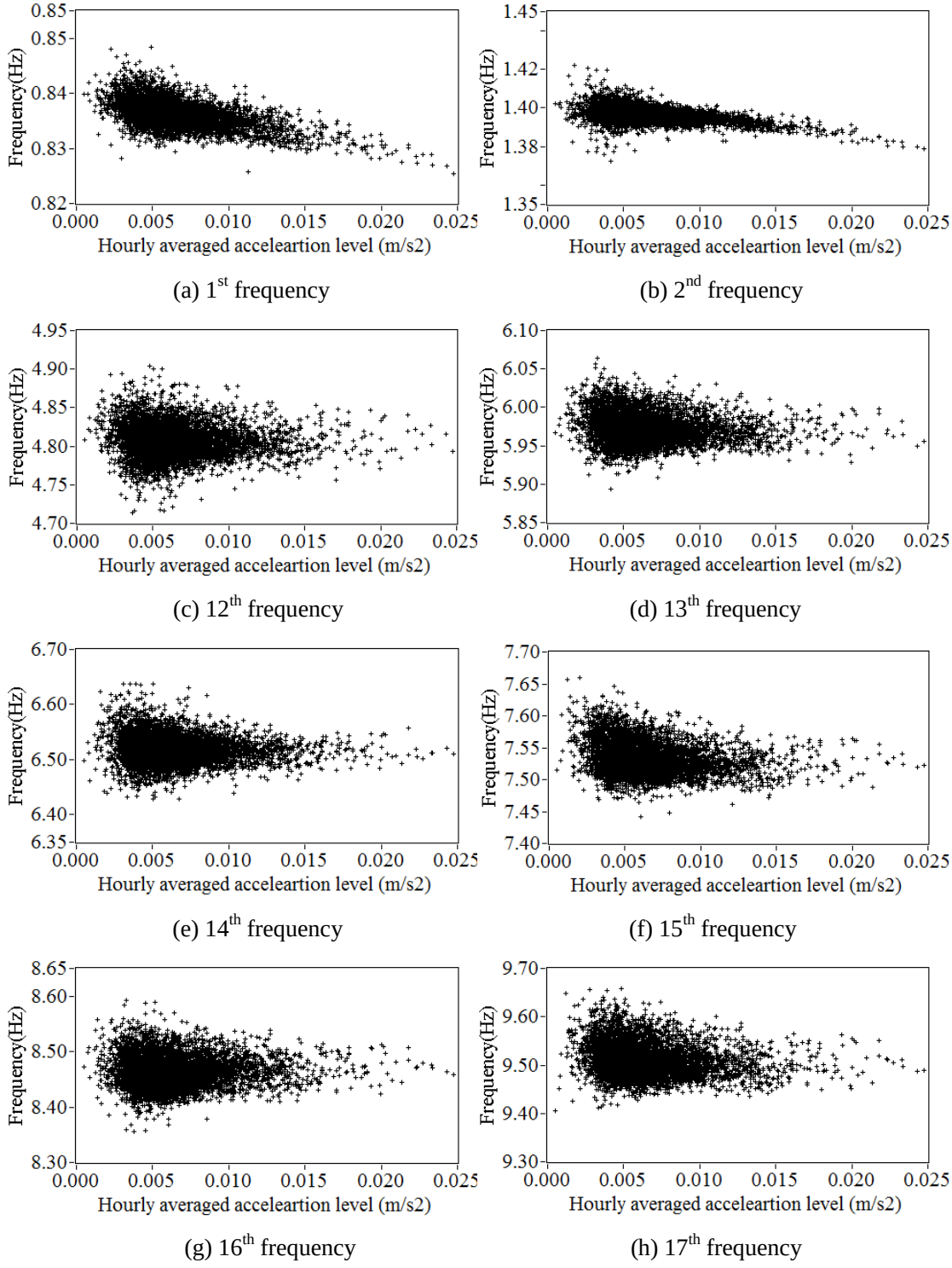

(a) 1st frequency (b) 2nd frequency

(c) 12th frequency (d) 13th frequency

(e) 14th frequency (f) 15th frequency

(g) 16th frequency (h) 17th frequency

Figure 5.19 Identified frequencies versus hourly averaged acceleration amplitude from 1st June 2007 to 31st May 2010 during day light

It is observed from Figures 5.19 (a) that the frequencies of the first modes decrease slightly with increase of hourly vibration level the corresponding correlation coefficients being 0.52. This conclusion agrees with the experimental observations in (Caetano et al, 2010a, b), showing that more pedestrians crossing bridge may lead to reduction of the first

two frequencies. On the contrary, no clear relations are observed in the frequencies of higher modes (Figures 5.19 (c)-(h)) and the correlation coefficients are quite low. This means that a large number of pedestrians would not change the frequencies of high order modes.

The effect of pedestrian traffic on natural frequency estimates may be identified in a more clear way separating the estimates corresponding to two different ranges of vibration amplitude, and projecting those two clusters on the plane frequency-temperature .In Figure 5.20 (a)-(h) one can find pairs of plots, reflecting the influences of lateral vibration response and temperature on natural frequency estimates of different orders, respectively. The plots on the left-side depict the relation between hourly averaged lateral response and natural frequencies, while the graphs on the right side correlate the temperature and the frequency results.

In order to reveal the influence of both pedestrian traffic and temperature, the samples of the left-side plots are divided into two individual clusters artificially. One cluster of samples (in black), whose hourly averaged lateral accelerations are in the range 0-0.012m/s^2, represents frequency results under low vibration levels, while the other cluster (in red) characterizes the frequency results identified, with large vibration levels with averaged accelerations larger than 0.012m/s^2. Selecting the corresponding temperature records of the two clusters and plotting them against with frequency results, one obtains the plots on the right-side. It is observed from the right side-plot of Figure 5.20 (a) that the samples representing high vibration levels (in red) scatter in the low boundary of the correlation plots between 1st frequency and temperature, which shows that high vibration levels induced by a high numbers of pedestrians lead to reduce the frequency. Such observation coincides with the conclusion drawn in (Caetano et al, 2010a). Figure 5.20 (b) also shows that natural frequency estimates of the lower boundary of the correlation plot correspond to higher vibration levels. However, it is estimated from Figure 20 (c)-(h) that the frequency estimates associated to the two clusters have not a distinct representation in the plane frequency-temperature. It may be concluded that the higher order frequencies are not sensitive to pedestrian traffic but only affected by temperature changing.

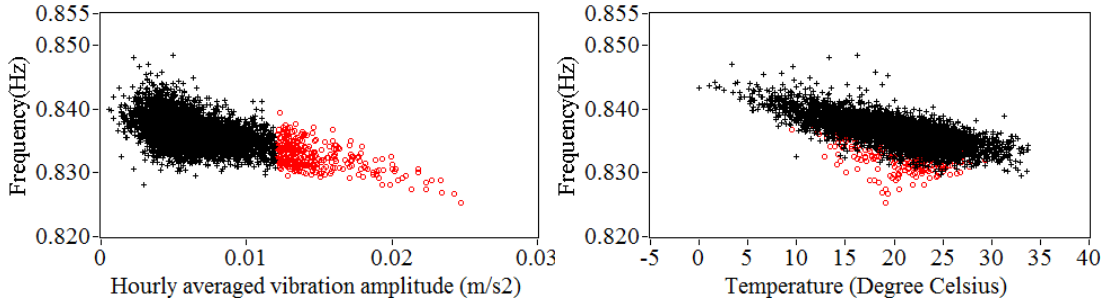

(a) 1st frequency

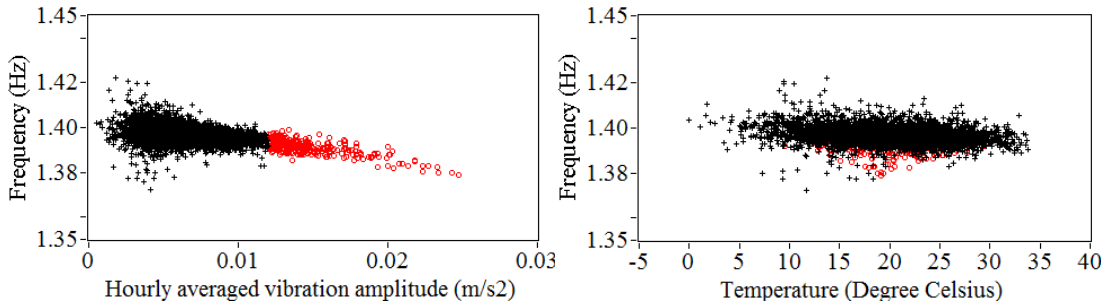

(b) 2nd frequency

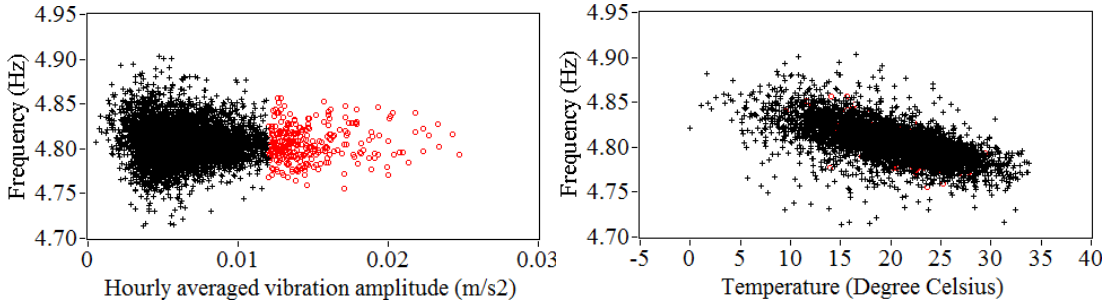

(c) 12th frequency

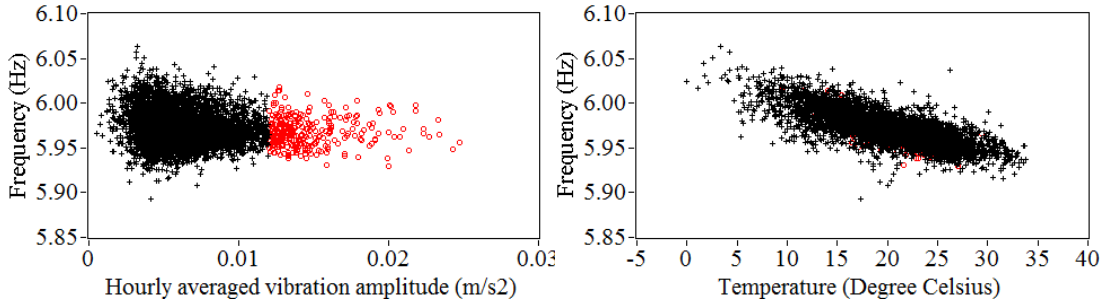

(d) 13th frequency

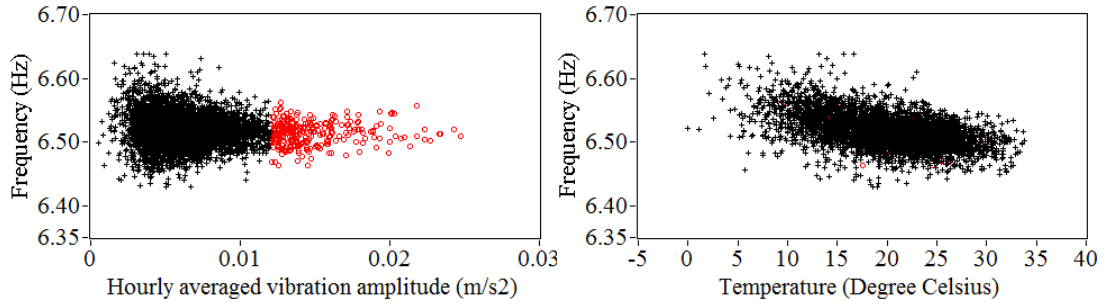

(e) 14th frequency

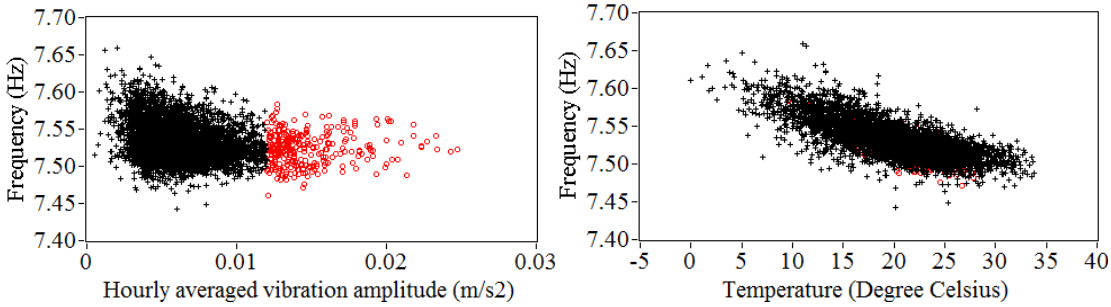

(f) 15th frequency

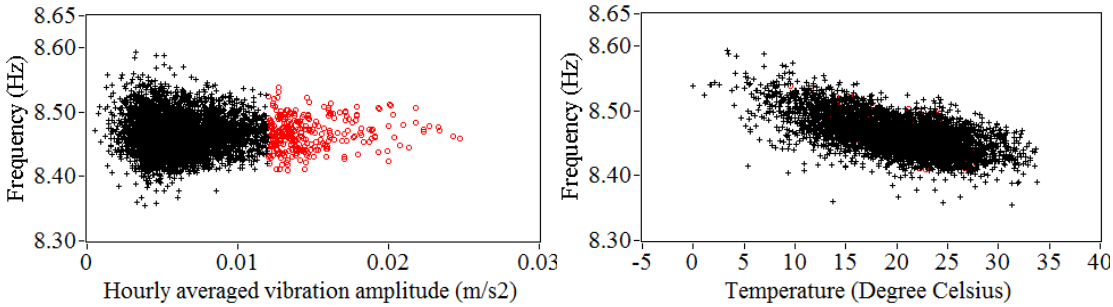

(g) 16th frequency

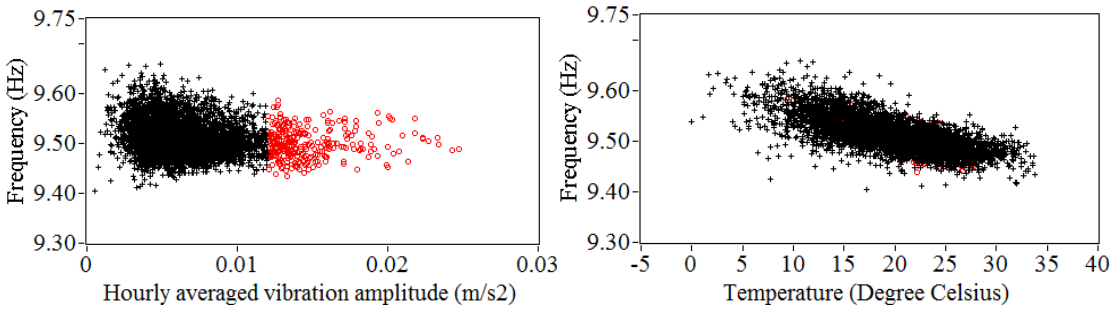

(h) 17th frequency

Figure 5.20 Effects of averaged lateral acceleration amplitude on identified frequencies

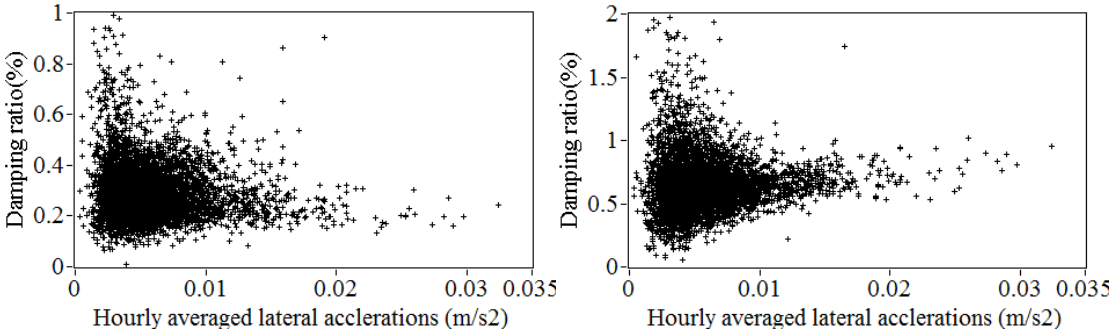

(a) 1st modal damping ratio (b) 2nd modal damping ratio

Figure 5.21 Identified damping ratio versus hourly averaged acceleration amplitude from 1st June 2007 to 31st May 2010 during day light

In addition, the possible effects of operational factors on damping ratio estimates are also investigated. Figure 5.21 displays the relation between the hourly averaged lateral acceleration and the first two modal damping rations. It is shown in Figure 5.21 (a) that no clear influence of lateral vibration level on 1st damping ratio is observed. Within the range of low vibration levels, the damping ratio varies from 0.1-1%, which indicates the inaccuracy of damping ratios estimates with low excitation under operational conditions. It must be noted that the lateral component dominates the 1st mode, and that signals from only one lateral accelerometer were used to identify the damping ratio. For the 2nd mode, inspection of Figure 5.21 (b) shows that, in the range of low vibration levels (0-0.012m/s^2) relatively large biased errors of modal damping ratios are observed.

5.2.4 Summary

This section mainly presents the continuous dynamic monitoring system and 3 years dynamic monitoring results of Pedro e Inês footbridge, as well as an investigation on the effect of the environmental/operational factors on modal parameters estimates. Firstly, the potential and reliability of the economical continuous dynamic monitoring system installed is proved by the signals acquired along 3 years. From the 1st June 2007 to 31st May 2010, no excessive lateral vibrations and very few immoderate vertical responses were recorded. The frequency domain analysis of time series indicates that the 1st mode is critical for lateral vibration and the modes around 3Hz contribute mainly to vertical accelerations, validating the prediction made in the stage of design of TMDs. Hourly averaged lateral acceleration is proposed to approximately evaluate the pedestrian traffic intensity. Modal parameters related

with 8 modes were automatically identified by CSMI toolkit, and it is observed that the natural frequency estimates are sensitive to environmental/operational factor, the maximum differences for modes of different orders varying from 2.7%-3.9%. Investigation of continuous recorded temperatures shows that variations of these signals are different because of the positions of the temperature sensors. As a result, the level of correlation between those temperature records and natural frequency estimates is also dissimilar. Correlation analysis demonstrates the approximate linear influence of temperature on natural frequencies of different modes except the 2nd one. Besides, it is also observed that the frequency of the 1st mode is influenced by the pedestrian traffic intensity, which agrees with previous conclusion drawn during the dynamic tests performed in the period of design of TMDs. Estimates of the first two modal damping ratios are also presented, but it seems the results are questionable under level of excitation.

5.3 CONTINUOUS DYNAMIC MONITORING OF FEUP CAMPUS FOOTBRIDGE

5.3.1 Previous research results

The characteristics of FEUP campus footbridge were introduced in section 4.4.1. One particular feature of this footbridge is that it is a stress-ribbon bridge and its stability and stiffness are determined by the axial forces in the tensioned longitudinal cables. Therefore, the structural behavior of the footbridge shows a great dependence on the geometric configuration. In (Caetano and Cunha, 2004), this characteristic is demonstrated by numerical analysis. Comparison of modal parameters estimated by OMA based on two ambient tests was presented in section 4.4.3, indicating that resonant frequencies of different modes are subject to the effect of temperature, which motivated the installation of a continuous dynamic monitoring system for investigation of the long term behaviour of the footbridge. Besides, human-induced vibration of this stress-ribbon footbridge was also examined in (Caetano and Cunha, 2004, 2005). It is documented that a group of 22 persons jump at 2Hz at a position in the vicinity of one-third the larger span produced an oscillation with amplitude of almost

6.6m/s^2(Figure 5.22), which far exceeds the recommended unacceptable discomfort limit 2.5m/s^2 (Table 5.1, Page 148). Therefore, the maximum vertical acceleration is also monitored to evaluate the serviceability of the footbridge under operational conditions.

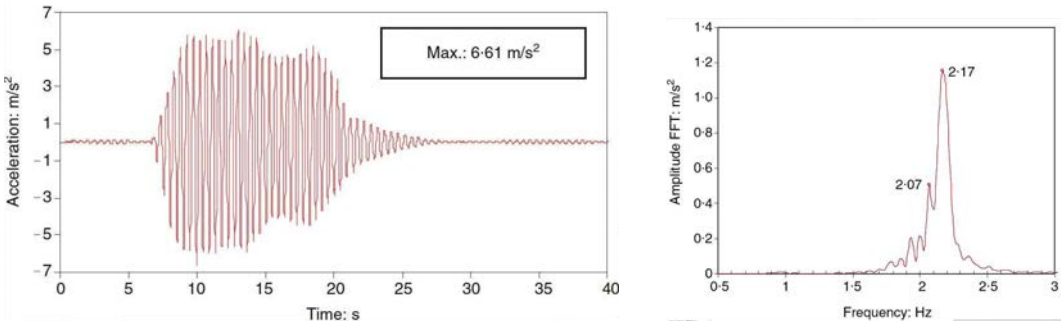

(a) Time response (b) Fourier Spectrum

Figure 5.22 Measured maximum vertical acceleration induced by a vandal load

5.3.2 Continuous dynamic monitoring system

The continuous dynamic monitoring system comprehends signal acquisition, transmission and processing modules. The signal processing modules have been implemented in the CSMI (Continuous Structural Modal Identification) toolkit and were described in Chapter 3. In this section, the module for signal acquisition and transmission is briefly introduced. (Hu et al, 2010).

The signal acquisition system comprises sensors and data acquisition devices. Each sensor unit comprises an accelerometer PCB-393C, a signal conditioner PCB-488A03 and a PT100 thermal sensor. Four units are mounted separately on the lower surface of the bridge deck at both half and 1/3 of each span (Figures 5.23 (a) and (c), Figure 5.24 (a)). Acceleration signal conditioners and thermal sensors are connected via cable with National Instruments Ethernet data acquisition (DAQ) devices, which are incorporated in a steel box installed beneath the deck at the intermediate support (Figure 5.23 (b), Figure 5.24 (b)). The NI Ethernet DAQ unit consists of a NI ENET-9215 data acquisition device transmitting output acceleration signals with a sampling frequency of 5kHz under operational conditions and a NI ENET-9219 universal input device acquiring temperature information with a sampling frequency of 1Hz, both carriers are connect to a Ethernet switch, which transmits acquired data into a computer at FEUP library through a power-line bridge. The NI Ethernet DAQ

device is driven by a signal acquisition toolkit, which resamples acceleration signals to 50Hz, generating nearly a real-time zipped acceleration signal file every 10 minutes and a temperature file every 30 minutes continuously. All signal files acquired under operational conditions are conveniently accessed via Internet.

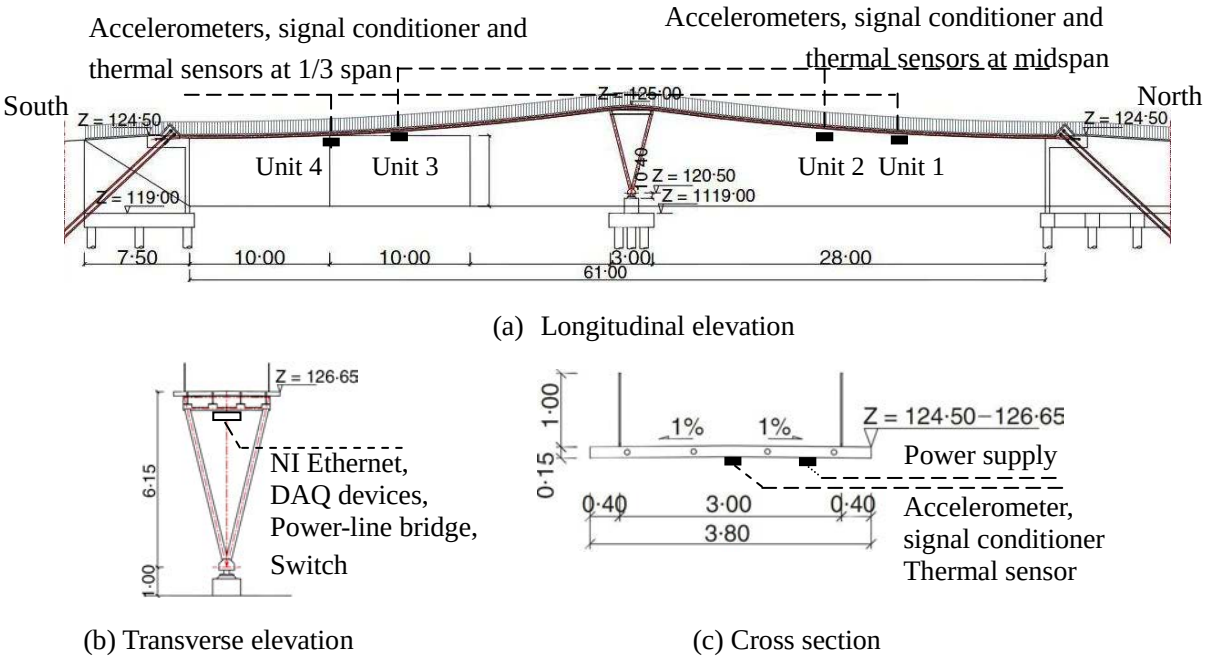

(a) Longitudinal elevation

(b) Transverse elevation

(c) Cross section

Figure 5.23 Elevations and cross section of the footbridge, with indication of the components of the installed continuous dynamic monitoring system

(a) Accelerometer installed at the bottom surface of the footbridge deck

(b) NI Ethernet, DAQ devices, power-line bridge and switch

Figure 5.24 Images of components of the continuous dynamic monitoring system

The signal acquisition and transmission module has been operating from the 1st of June 2009 to now, except for occasional stops due to small technical problems. It leads to the accumulation of a huge amount of data that needs to be processed, analyzed and interpreted.

CSMI toolkit processes these signals automatically and generates the continuous monitoring results. To achieve a better estimation of the structural properties, six consecutive signal files are concatenated to obtain the response in one hour for processing.

5.3.3 Continuous dynamic monitoring results

a) *Maximum vibration levels and distribution of frequency components*

The similar procedure for detection of maximum vertical vibration amplitude that has been used at Pedro e Inês footbridge is also applied to vertical responses acquired from the 4 accelerometers. A typical acceleration signal and detected envelope are plotted in Figure 5.25 (a). The zoom part around a peak is shown in Figure 5.25 (b). Within 1 second, the absolute values of the envelope are averaged and plotted in Figure 5.25 (c). The peak of vertical response from one accelerometer is approximately determined by picking the maximum value of the averaged absolute envelope values. By comparing the maximum vertical levels from the 4 accelerometers, the maximum vertical acceleration in one hour is detected. According to the results in every hour, the daily maximum vertical acceleration is recorded.

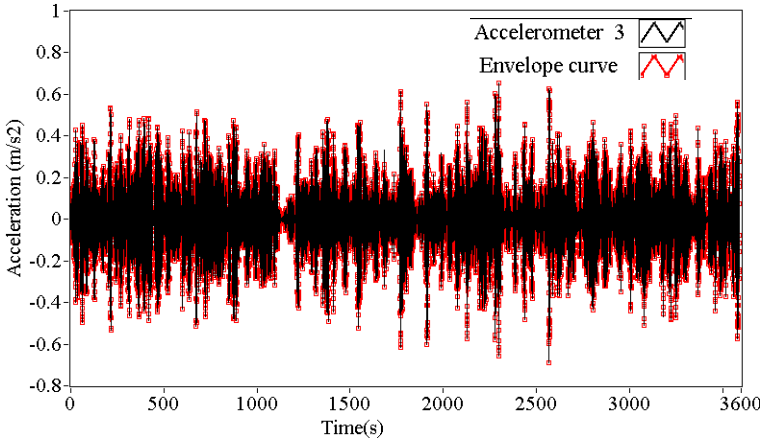

(a) Signal and its envelope

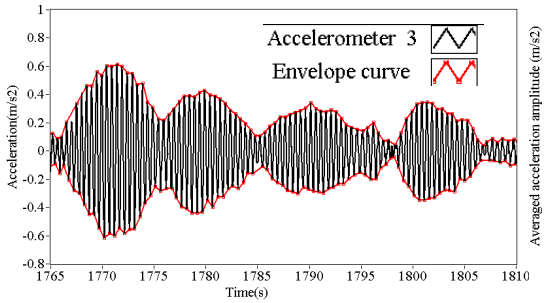

(b) Part of signal and its envelope

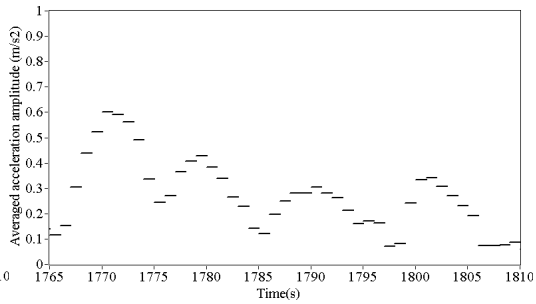

(c) Averaged absolute envelope within 1s

Figure 5.25 Signal from one accelerometer and its envelope

Figure 5.26 displays the distribution of the maximum daily vertical acceleration in one month. The maximum accelerations observed on weekends are much lower than those in workdays. It should be noted that this footbridge is located in FEUP campus, linking the main buildings and the canteen. The fact that relative few people use the footbridge during the weekend results in lower maximum vibration levels.

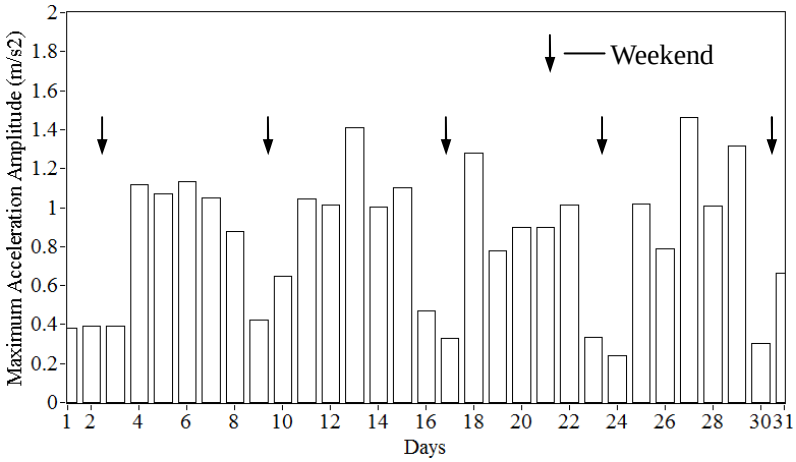

Figure 5.26 Maximum daily vertical acceleration in one month

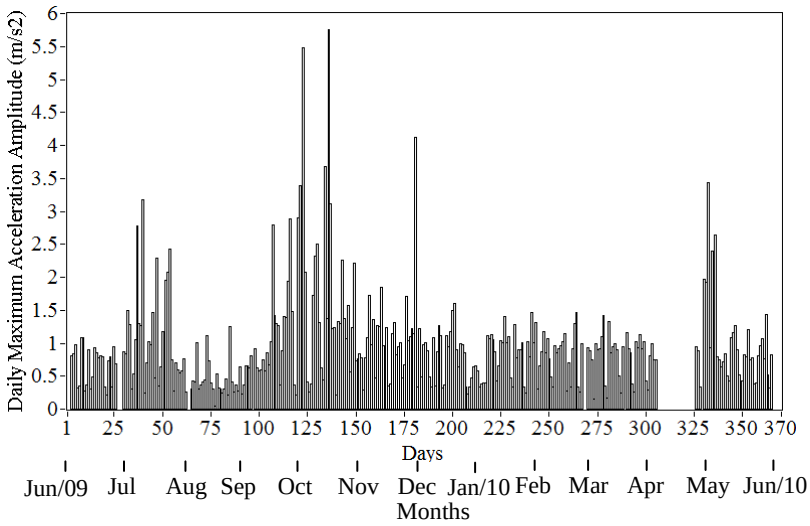

Figure 5.27 Maximum vertical acceleration amplitude from 1st June 2009 to 31st May 2010

Figure 5.27 shows the maximum daily vertical accelerations measured from June 2009 to May 2010 and the corresponding histogram is shown in Figure 5.28. Figure 5.29 shows the maximum vertical vibration level achieved of 5.7m/s^2, captured at 1/3 of larger span at 16:00 on the 14th October 2009. Comparing the monitored maximum daily vertical accelerations and the comfort limits recommended by SYNPEX and SETRA guidelines, it is observed that there were 117 days in which the maximum vertical vibration level exceeded the medium degree of comfort (1m/s^2) within one year. Actually, it is quite easy to feel the vertical vibration when

crossing this footbridge under operational conditions. However, the serviceability is still acceptable though relatively large vertical vibrations are monitored frequently. As indicated in (Caetano and Cunha, 2005) that the maximum vertical accelerations exceeding 2m/s^2 are induced by vandal loads corresponding to jumping of group of students.

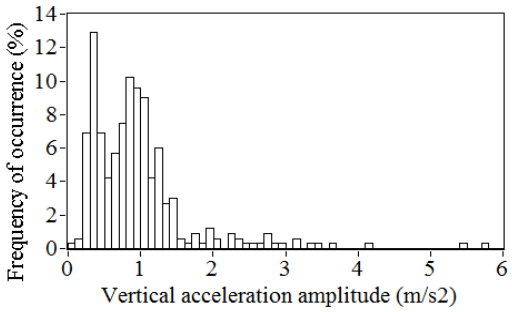

Figure 5.28 Histogram of Figure 5.27

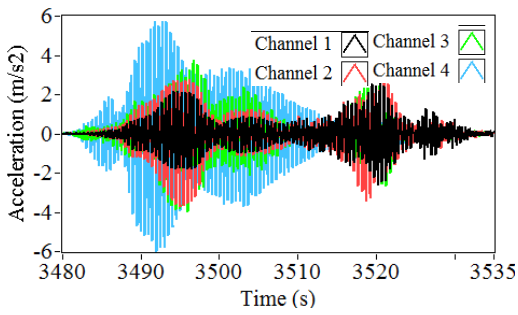

Figure 5.29 Maximum acceleration signals

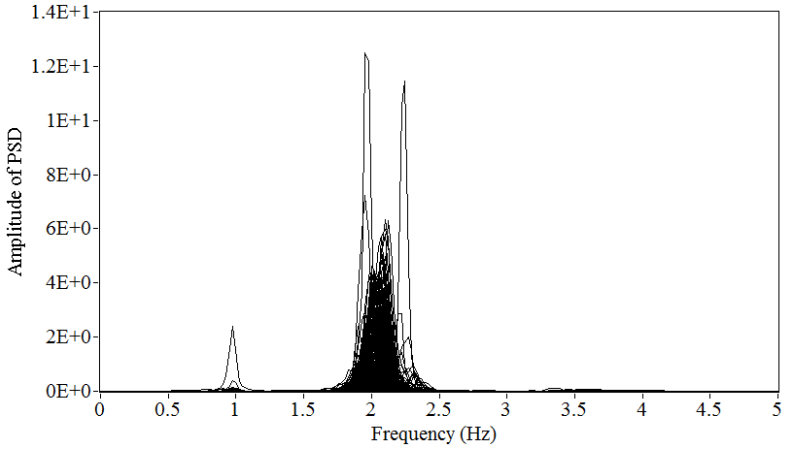

Figure 5.30 Power spectra of signals corresponding to maximum observed accelerations

The frequency domain analysis of time series is also performed in order to better characterize the long term dynamic behaviour of this footbridge. Figure 5.30 shows the power spectra of the acceleration signals in one hour when the maximum daily vertical vibration is observed. The power spectra are calculated using a Hanning window with 4096 points, and 50% overlap, the frequency resolution being 0.0122Hz (50Hz/4096). It is observed from Figure 5.31 that the peaks of spectra fall in the range of 1.9Hz-2.3Hz and most of them around 2.0Hz-2.2Hz. It is also recalled that two adjacent natural frequencies around 2Hz, associated with the 2nd and 3rd modes, are listed in Table 4.5. The spectra clearly evidence the proneness of this footbridge to vibrations induced by pedestrians and the frequencies around 2Hz are critical for the maximum vertical vibration during operational conditions, which also agrees with the conclusion drawn in (Caetano and Cunha, 2004). The shift of peaks of the

spectra within 1.9Hz-2.3Hz may result from the temperature effect. For example, In Table 4.5 the 2nd natural frequency varies from 1.989Hz to 2.084Hz and the 3rd natural frequency changes from 2.034Hz to 2.136Hz because of different temperature conditions.

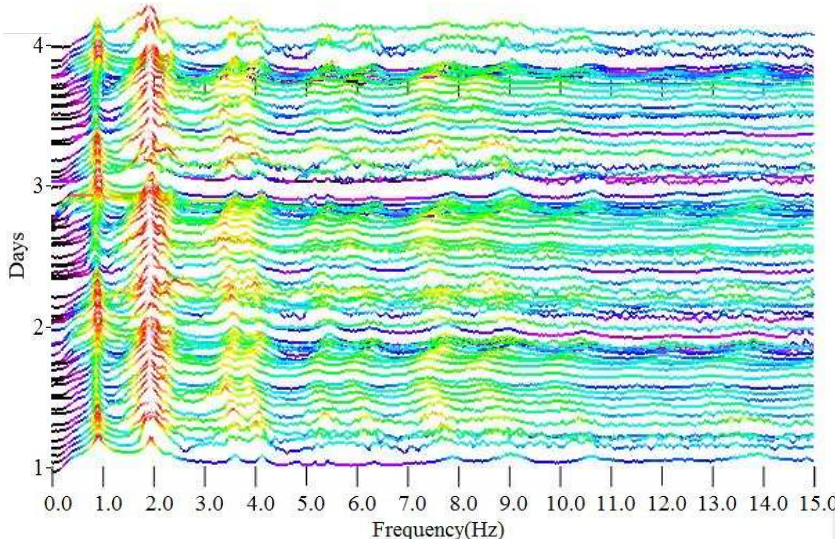

(a) Waterfall plot of acceleration signals (logarithm scale)

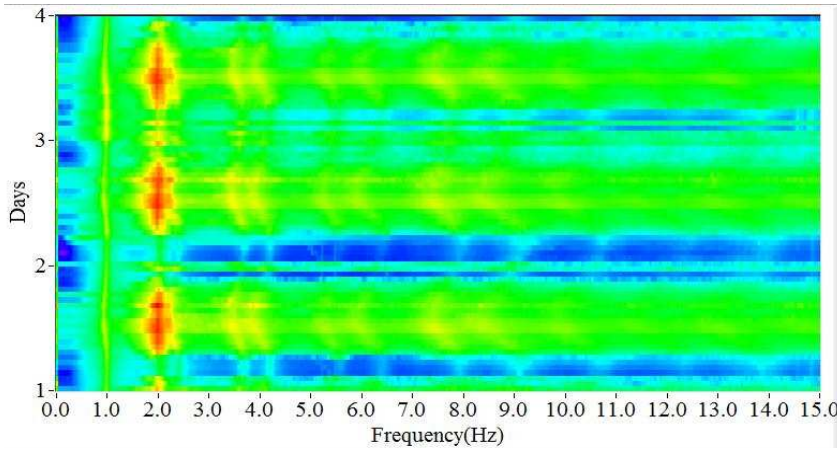

(b) Top view of (a)

Figure 5.31 Waterfall plots of acceleration signals in 3 consecutive days (logarithm scale)

Waterfall plots are also used to disclose the distribution of frequency contents, identify the intensity period and observe the variation of natural frequencies under normal conditions. Every ANPSD (averaged normalized power spectral density) of time series is generated based on responses from the 4 accelerometers within one hour. The ANPSD is generated using a Hanning window with 4096 points and 50% overlap. The frequency resolution is 0.0122Hz (50Hz/4096). Figure 5.31 (a) shows the waterfall plot by putting sequences of ANPSD estimates in 3 consecutive days besides each other. Top view of it is shown in Figure 5.31 (b). Inspection of Figure 5.31 (a) and (b) shows that the peaks of each spectrum are around 2Hz,

indicating that two adjacent modes around 2Hz are easily excited, these two modes contributing significantly to the acceleration response. Besides, the areas in red and yellow around 2 Hz represent high energy, because of large excitation exerted by more pedestrians, whereas those in blue and green, in the vicinity of 2Hz, reflect low energy. The intermittent observations of these two different areas may indicate the high and the low pedestrian traffic intensity. Finally, it is also observed that for the peaks around 0.99Hz, the frequencies at noon are lower than those at other time. Similar tendency is even clear for the peaks around 4Hz, 6Hz and 8Hz. The variation of frequencies suggests the environmental effects as discussed in section 4.4.

b) *Variation of environmental/Operational factors and modal parameters*

The same research procedure used in Pedro e Inês footbridge is applied to FEUP campus footbridge. Firstly, the variations of ambient temperature and hourly averaged vertical accelerations are presented. Subsequently, the variations of frequencies and modal damping ratios are described.

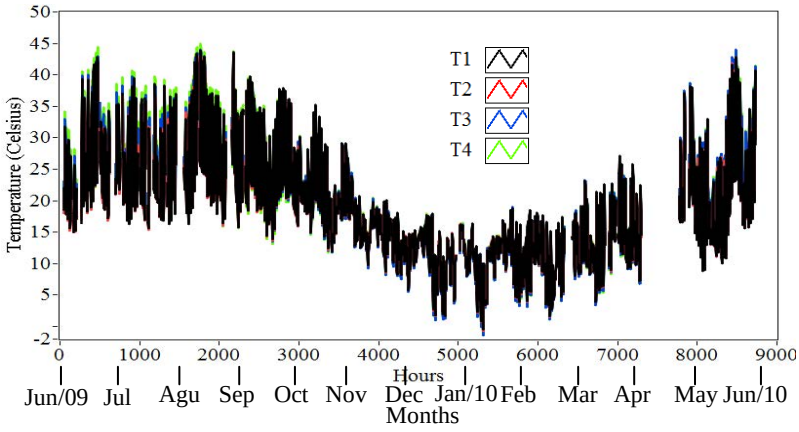

(a) Temperature record in different positions from 1st June 2009 to 31st May 2010

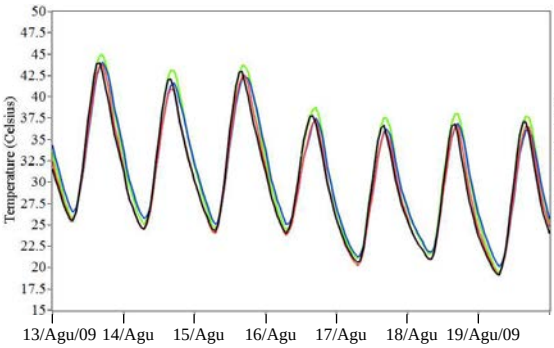

(b) Temperature in summer time

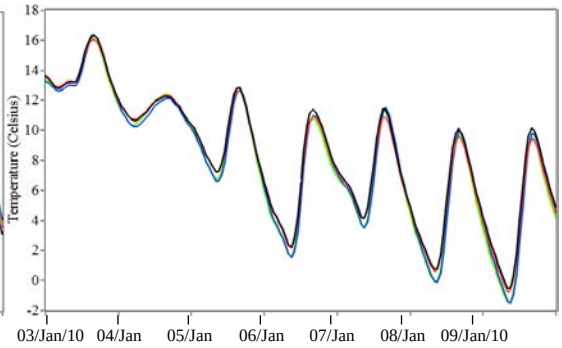

(c) Temperature in winter time

Figure 5.32 Annual variation of temperature

Figure 5.32 (a) displays the temperature records from the four sensors installed in different positions at the lower surface of the bridge deck, from the 1st of June 2009 to the 31st of May 2010. During nearly one year, the highest measured temperature was 45.7℃, while the lowest was -1.5 °C, slightly below the freezing point. Inspection of Figure 5.32 (b) and (c) shows that these four temperature series have similar trends in both winter time and summer time, because the length of the footbridge is only 61m and all 4 thermal sensors are mounted on the low surface of bridge decks. Therefore, averaged temperature of the records from the four thermal sensors is used to investigate the environmental effects.

In order to investigate the effect of pedestrians on the frequencies of the lively stress-ribbon footbridge under normal operational conditions, the procedure of evaluation of averaged vibration amplitude described in Chapter 3 is applied to continuous monitoring signals. Figure 5.33 (a) shows the distribution of averaged acceleration amplitudes from each accelerometer in one day. Averaged acceleration amplitudes from the four accelerometers are averaged again to approximately evaluate vibration levels in every hour, as shown in Figure 33 (b). It is observed that the values are much lower at night (from 00.00 to 6.00 and from 19.00-23.00), and that the averaged vibration amplitude in each accelerometer increases in the morning and decreases in the afternoon. The peaks appear around noon since more people cross the bridge to commute between the main buildings of FEUP and the canteen, which agrees with the observation from the waterfall plot in Figure 5.31. Figure 33 (c) plots the averaged acceleration amplitudes in one month. It is clearly observed that consecutive peaks are presented in five working days and low vibration levels are exhibited during weekends. Figure 33 (d) depicts the annual variation of the averaged vibration amplitude, an operational factor that is influenced by the change of the number of peoples crossing the footbridge along the academic year. In effect, the very significant reduction of vibration levels during August, early period of September and at the end of the year early stems from the occurrence of Summer and Christmas holidays periods, in which only very few pedestrians use this campus footbridge. Large numbers of pedestrians during the five working days and rare people at weekends result in significant fluctuations of vibration levels. Figures 34 (a) and (b) show responses corresponding to the maximum and minimum hourly averaged accelerations from June 2009 to May 2010. They were captured at 13.00-14.00 on the 16th Nov 2009 and at

4.00-5.00 on the 8th Aug 2009, respectively.

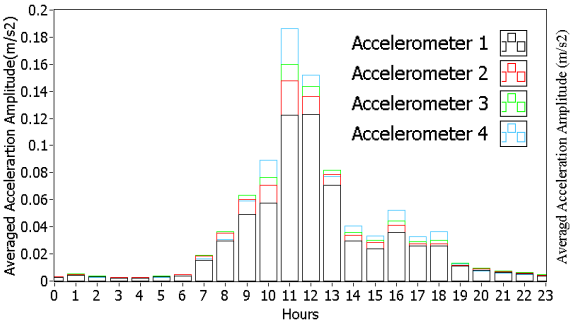

(a)Averaged acceleration amplitudes at each accelerometers

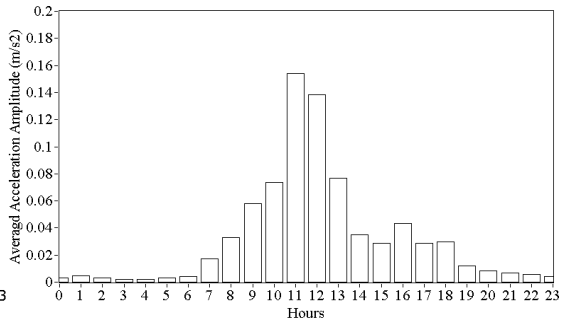

(b)Averaged acceleration amplitudes from the 4 accelerometers

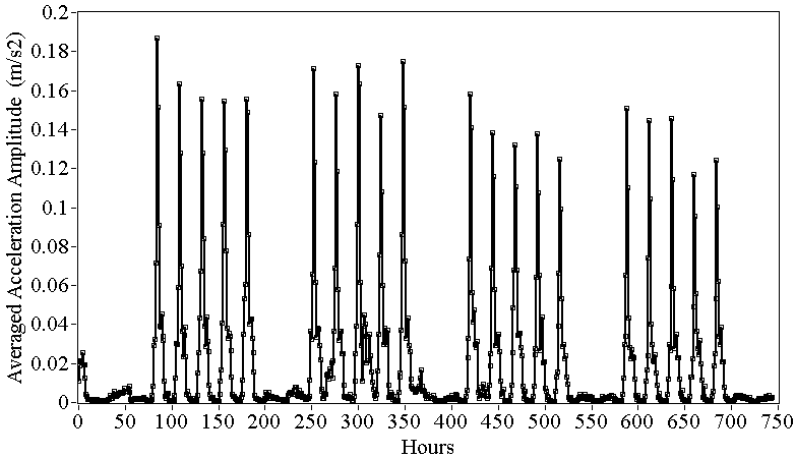

(c) Monthly averaged acceleration amplitudes

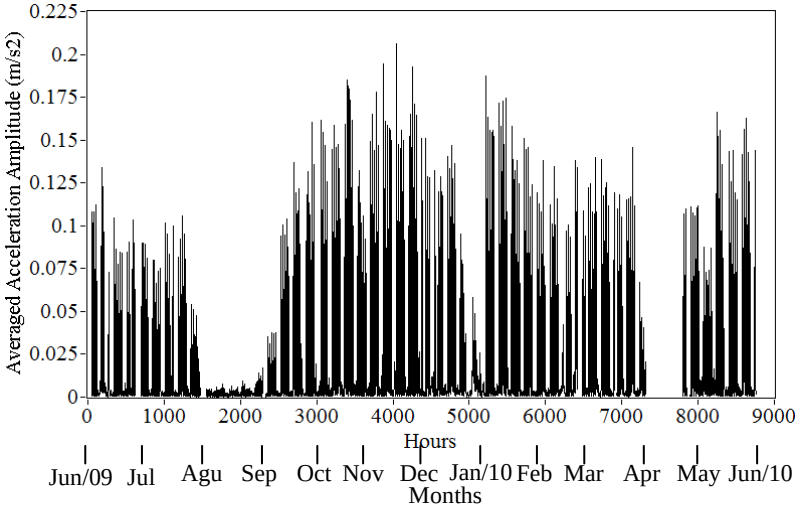

(d) Annual averaged acceleration amplitude from 1st June 2009 to 31st May 2010

Figure 5.33 Averaged acceleration amplitudes

Figure 34 (a) reveals that the maximum averaged vibration level results from constant high acceleration along one hour caused by relatively stable streams of pedestrian crossing the

footbridge during launch time. On the contrary, Figure 34 (b) reflects that the minimum response is composed of intermittent micro vibration that may result from frequently gentle breeze or passages of cars under the bridge before dawn of quiet summer night.

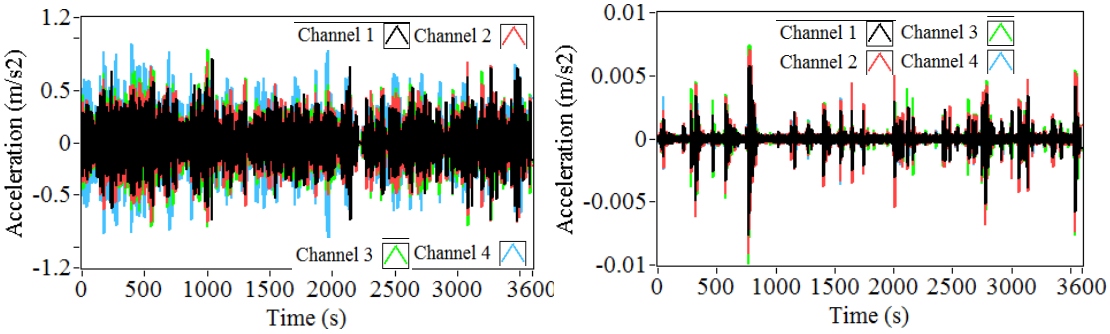

(a)Signals corresponding to the maximum averaged vertical accelerations

(b)Signals corresponding to the minimum averaged vertical accelerations

Figure 5.34 Acceleration signals acquired in the hour when maximum and minimum averaged acceleration was observed

According to Figures 5.33 and 5.34, the vibration levels under normal operational conditions are appraised efficiently by hourly averaged acceleration. It is also reasonably assumed that the hourly averaged acceleration is correlated with the number of pedestrians crossing the footbridge.

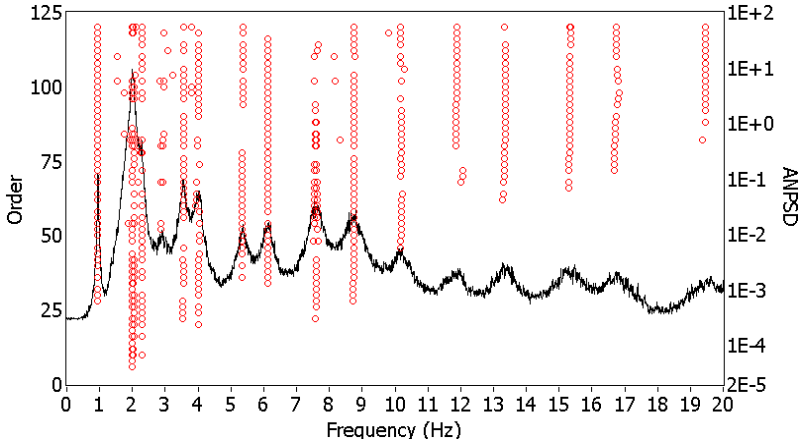

Figure 35 Typical stabilization diagram generated by the automatic SSI-COV algorithm using one hour signals

The automatic SSI-COV procedure implemented in CSMI toolkit was applied to the continuous monitored signals. Figure 5.35 displays a typical stabilization diagram and overlapped ANPSD. It is noticed that the alignments of stable poles around frequencies of different modes are clear except for the modes around 2Hz. The probable explanation is that noise poles are introduced due to pedestrian pace frequencies of about 2Hz, which further results in the difficulty of accurate identification of modal parameters around 2Hz.

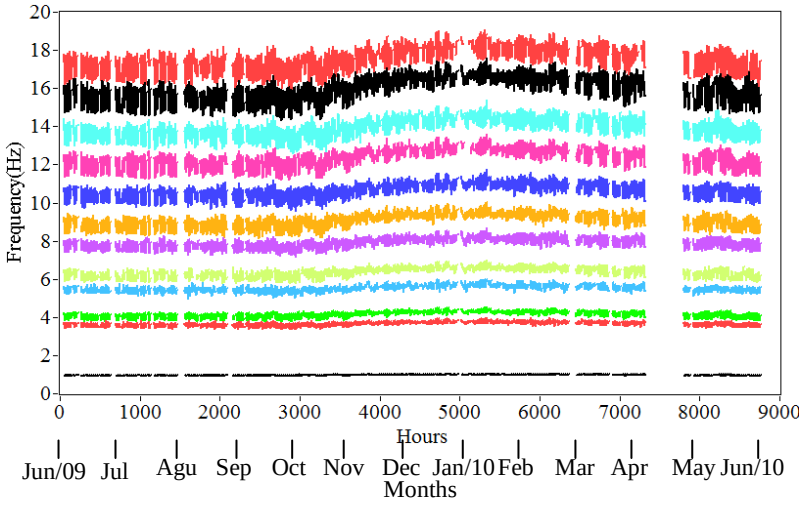

(a) All identified frequency estimates

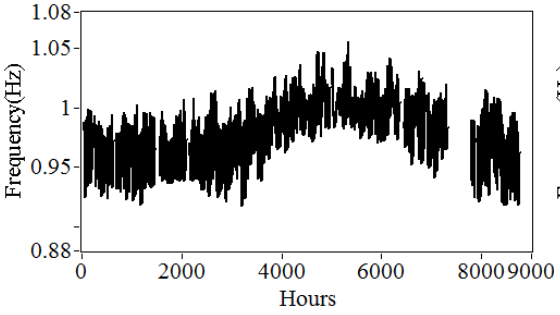

(b) 1st frequency

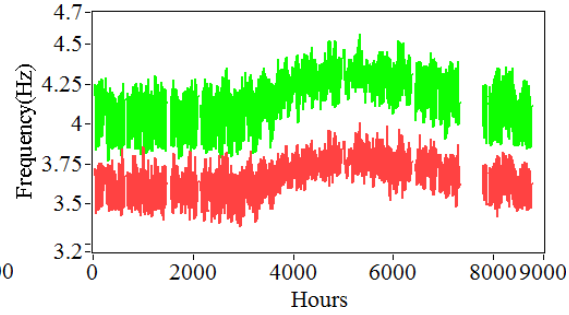

(c) 5th and 6th frequencies

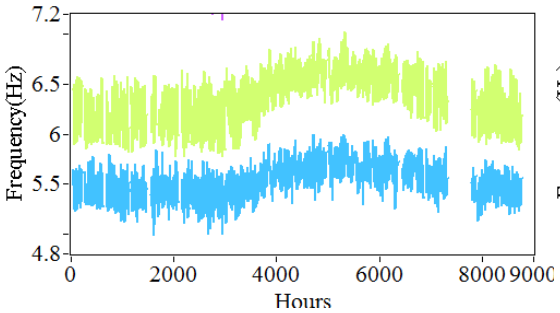

(d) 7th and 8th frequencies

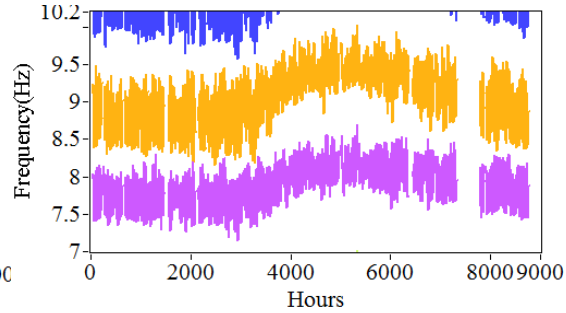

(e) 9th and 10th frequencies

Figure 5.36 Identified frequencies from 1st June 2009 to 31st May 2010

All identified frequency estimates of 12 modes in the range of 0-20Hz from June 2009 to May 2010 are shown in Figure 5.36. The variations of frequency estimates of high order modes are quite clear. The tendency of increasing in Winter time and decreasing in Summer time reflects the seasonal environmental effects. In particular, the analysis of the temperature effect on the 1st mode by comparing OMA results from two tests performed in different years is clarified in section 4.4. Figures 5.36 (b)-(e) show the annual variation of frequencies of lower order modes, revealing that they are also susceptible to environmental effects.

Table 5.5 Statistics of the identified natural frequencies

Averaged frequency(Hz)	Frequency range(Hz)	Maximum difference(%)	Stardard deviation(Hz)
0.982	0.917-1.055	14.0	0.024
3.674	3.359-4.007	17.6	0.107
4.179	3.768-4.563	19.0	0.149
5.515	4.987-5.999	18.3	0.160
6.399	5.771-7.021	19.5	0.252
7.921	7.148-8.693	19.5	0.260
9.116	8.418-10030	20.6	0.341
10.644	9.577-11.758	20.5	0.377
12.369	11.213-13.624	19.5	0.484
13.944	12.572-15.382	20.2	0.485
16.030	14.330-17.597	20.4	0.629
17.538	15.859-19.073	18.3	0.610

Table 5.5 lists the statistical information of all identified frequencies, indicating that the annual maximum relative difference of frequency estimates in mode of different orders varies from 14.0% to 20.6%. It further proves the dependence of natural frequencies with regard to environmental factors under normal operational conditions.

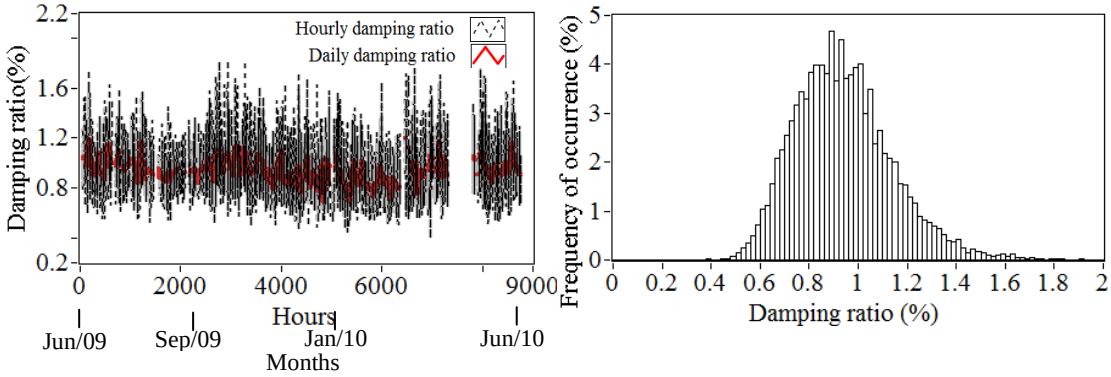

(a) 1st modal damping ratio estimates (b) Histogram of 1st modal damping ratio estimates

Figure 5.37 1st modal damping ratio estimates and corresponding histogram from 1st June 2009 to 31st May 2010

Figure 5.37 (a) and (b) plots the annual variation of the 1st modal damping ratio and corresponding histogram. Daily averaged damping ratios are also plotted as red line in Figure 5.37 (a), in order to clarify the tendency of the annual modal damping ratio estimates. No clear relation between damping ratios and environmental factors is observed from Figure 5.37 (a) as will be discussed in later. Inspection of Figure 5.37 (b) shows that the long term modal

damping ratio estimates vary around 0.94% (annual averaged damping ratio), slightly smaller than 1.15% which is the averaged value of damping ratio estimated by 3 modal tests performed in different time (Table 4.5, Page 135).

c)*Correlation between environmental/operational factors and modal parameters*

In order to understand the long term behaviour of FEUP campus footbridge under changing environmental conditions, the effects of both temperature and vibration level on continuous monitoring frequencies were investigated.

In Figure 38, the relations between averaged concrete temperature values from the four thermal sensors and natural frequencies of different modes are analyzed. Generally, the frequency decreases when the temperature increases, but there is a 'turning point' approximately situated around 30°C. Similar nonlinear relations are also observed for the other modes. Below 30°C, the bridge stiffness normally increases with decreasing temperature in a linear manner. While above 30°C, the identified frequencies of all modes do not change and seem stable with increasing temperature. The particular phenomenon may be further explained by considering the effect of pedestrian traffic.

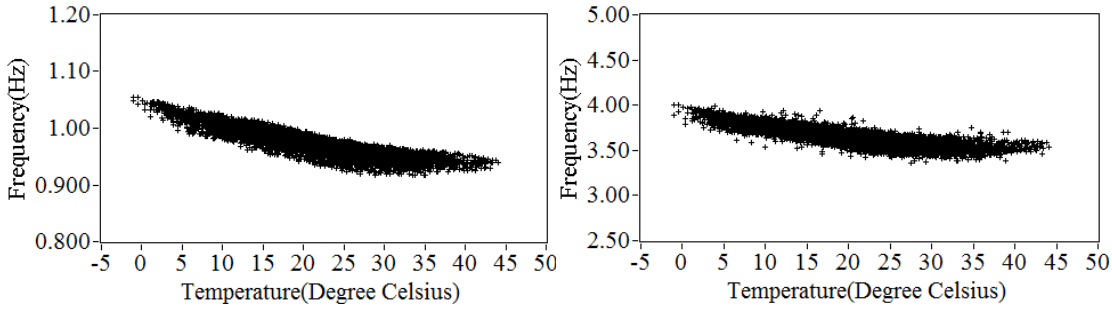

(a) 1st frequency

(b) 5th frequency

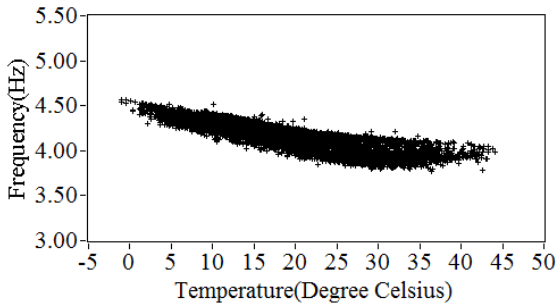

(c) 6th frequency

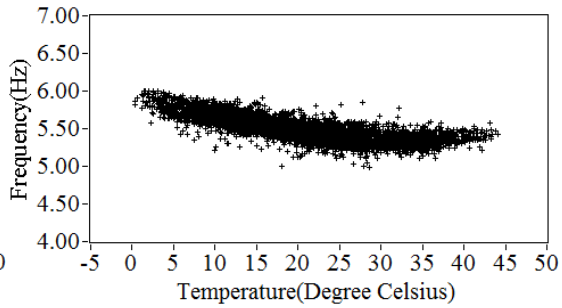

(d) 7th frequency

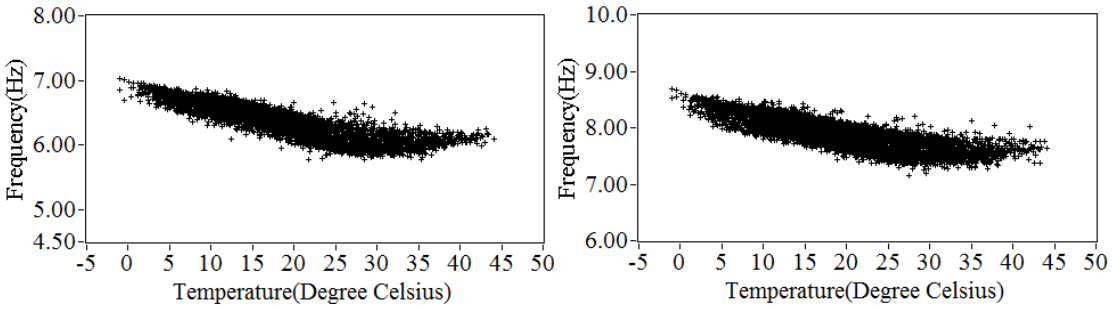

(e) 8th frequency (f) 9th frequency

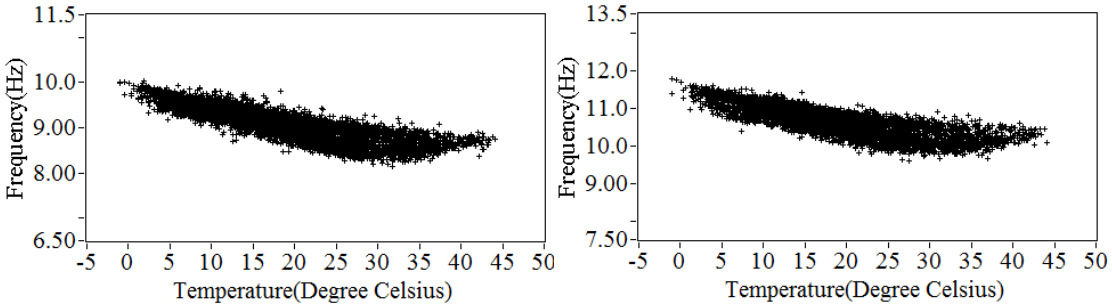

(g) 10th frequency (h) 11th frequency

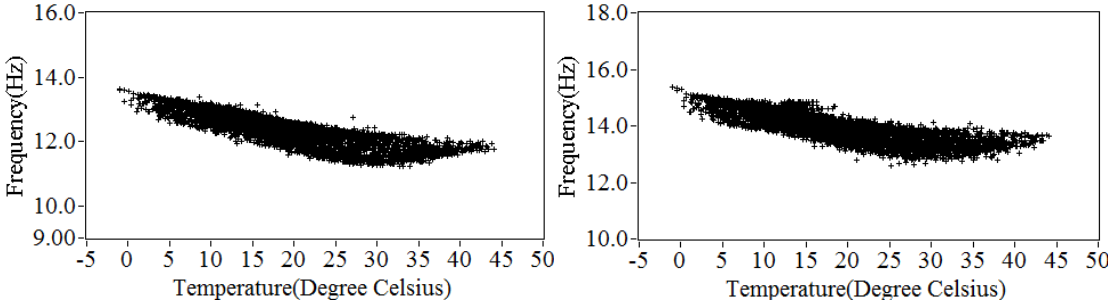

(i) 12th frequency (j) 13th frequency

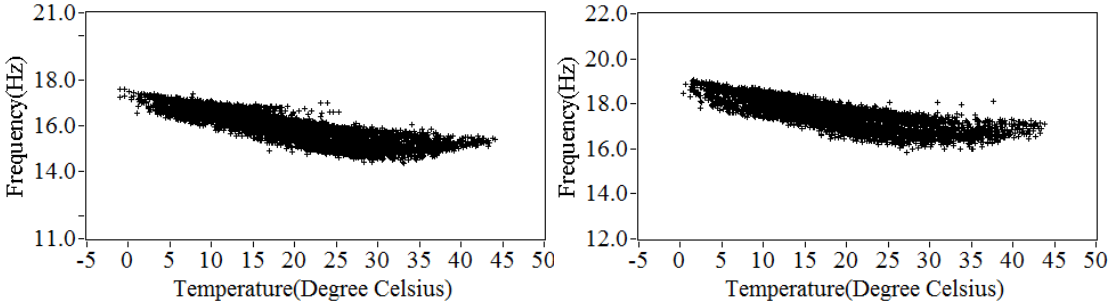

(k) 14th frequency (l) 15th frequency

Figure 5.38 Identified frequencies versus averaged temperature record from 1st June 2009 to 31st May 2010

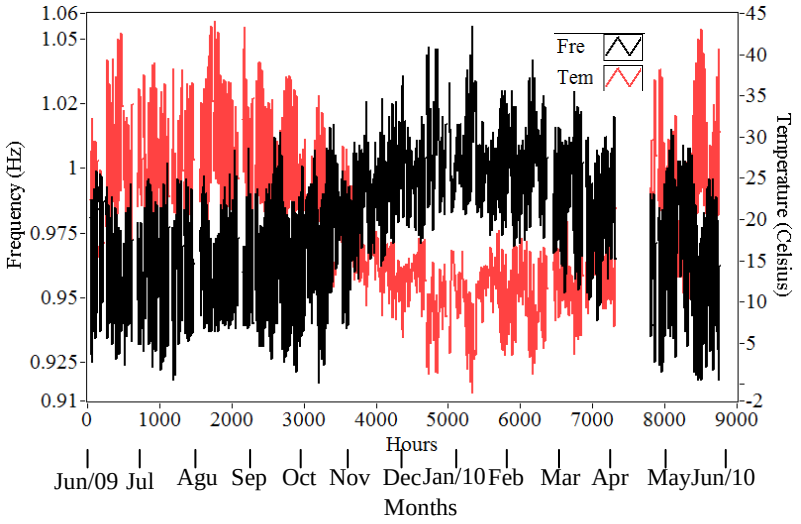

(a) 1st frequency vs ambient temperature in one year

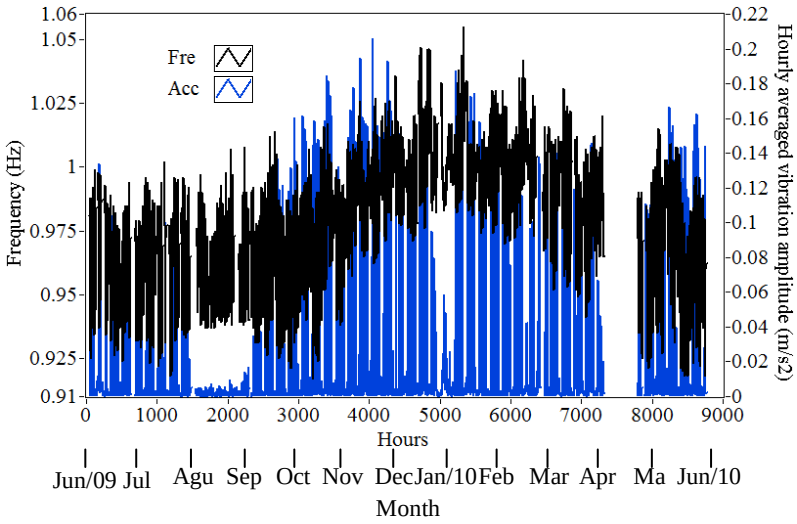

(b) 1st frequency vs averaged acceleration amplitude in one year

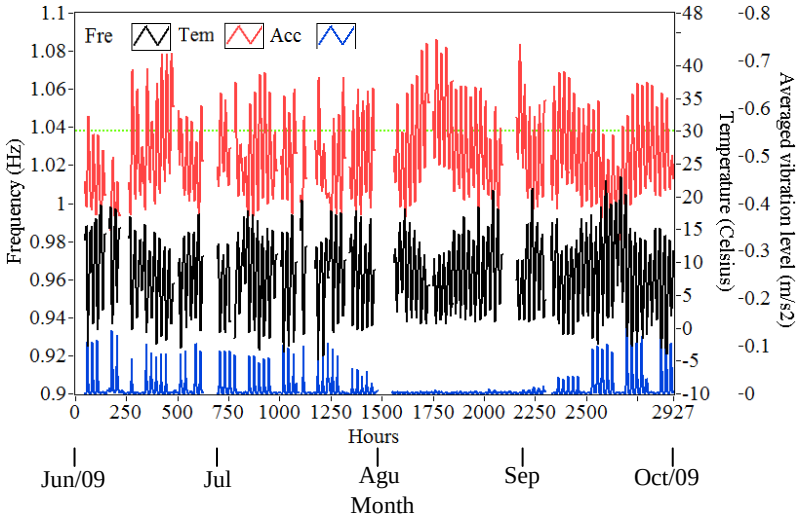

(c) Relation between 1st frequency and temperate as well as averaged vibration level from June/2009 to September/2009

Figure 5.39 Evolution of the 1st frequency estimates versus temperature and averaged acceleration amplitude during one month

Figure 5.39 compares the time evolution of the 1st frequency estimates versus concrete temperature and the averaged acceleration amplitude. The subplots (a) and (b) investigate the annual variation of these three attributes, while subplot (c) only focuses their local changes from June to September in 2009. The black line in Figure 5.39 shows the variation of the 1st natural frequency estimates, and the lines in red and blue are overlapped to reflect the corresponding changes of temperature and averaged acceleration amplitudes, respectively. Figure 5.39 (a) shows that generally the frequency and the temperature change in an opposite way. On the contrary, it is noted from Figure 5.39 (b) that no obvious trend between vibration level and frequency can be observed over the period of one year. As a result, one conclusion may be that from long term monitoring point of view concrete temperature has a stronger influence on the annual variation of the structural natural frequencies. Taking that into account, as the temperature records during the Summer Holiday (August) are higher, lower values of the natural frequencies were expected during this period. However, it is observed in Figure 5.39 that during the Summer Holiday the lower bound of the frequency results is even higher, conflicting with that expectation. Such observation could be further clarified by overlapping the three variables and inspecting them in the period of June/2009-September/2009 as shown in Figure 5.39 (c). For example, it is noticed that the temperature in August (around 1750 hours) is higher than in June (around 450 hours), whereas the lower bound of frequencies in the former period is obvious higher than in the latter. This may stem from the lower vibration levels of the footbridge due to very few pedestrians in Summer holidays. At the same time, it is also interesting to refer that the low bound of frequencies in August seems rather stable and unchanged with regard to the variation of temperature, comparing with the one in June, July and September. However, the high bound that reflects the bridge properties at nighttime, still exhibits the tendency of frequencies decrease with increase of temperature, regardless of difference of averaged accelerations. This could be further clarified by correlating individual monthly results of temperature and identified frequencies.

Figure 5.40 (a)-(d) present correlation plots using monthly variations of temperature and of the 1st frequency estimates. Inspection of these plots shows a clear ‘turning point’ at about 30ºC. It is also observed that the plots corresponding to June, July and September exhibit similar relations, whereas some difference between them and the plot of August is also noted,

as the low boundary of the correlation plot of August is higher than the plots of other months. To illustrate the difference, Figure 5.40 (e) overlaps the correlation plots of June and August. It is obvious that the low boundary of the plot of June is lower than the one of August, which argues with the observation reflected by Figure 5.39 and may be partially explained by the effect of higher averaged accelerations in June, July and October.

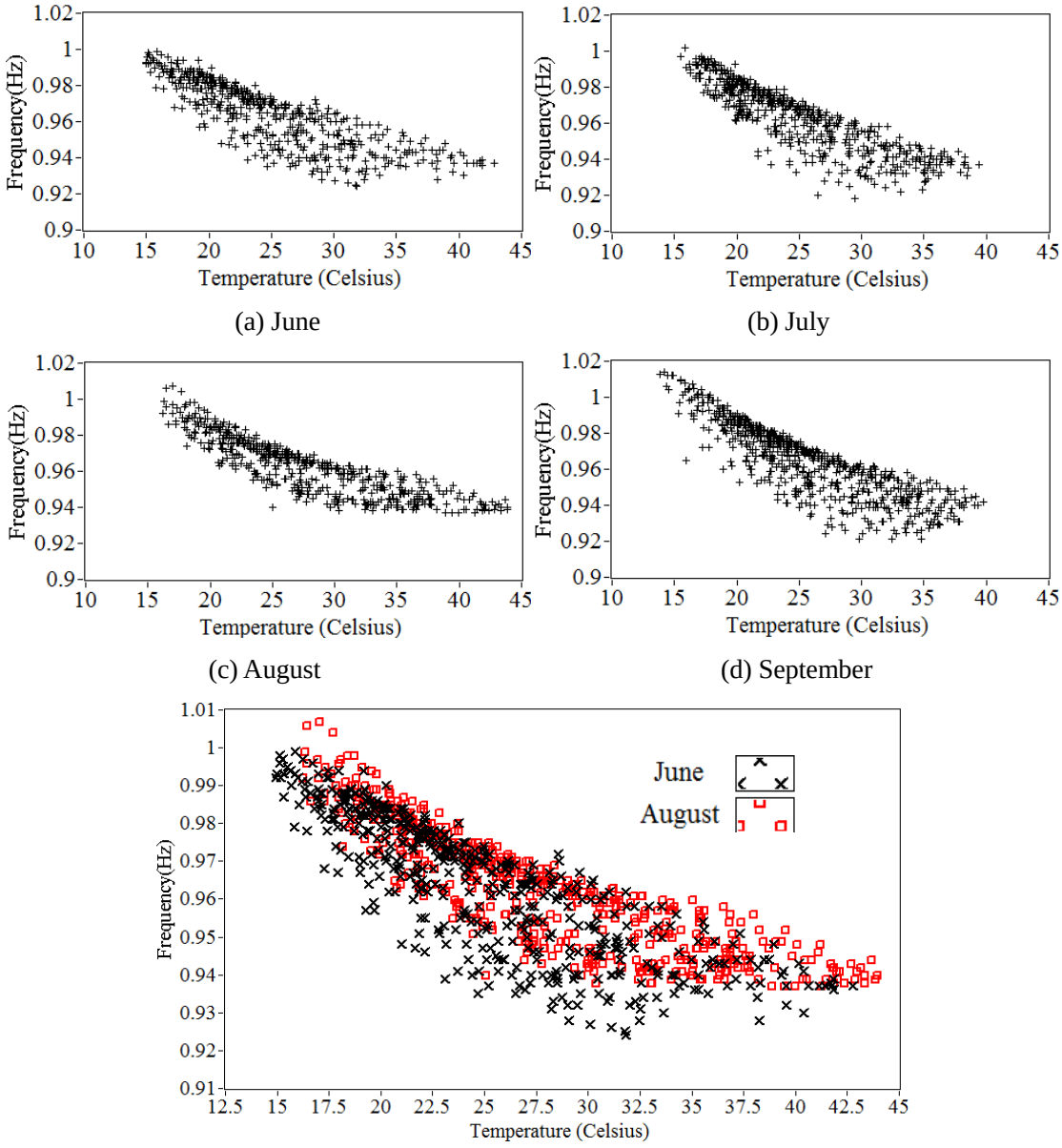

(a) June (b) July

(c) August (d) September

(e) Comparison of correlation plots of both June and August

Figure 5.40 Correlation between temperature and the 1st frequency estimates using individual monthly results

All those observations from Figures 5.39 and 5.40 suggest that for this stress-ribbon footbridge, vibration level may also affect the change of frequencies beyond temperature. Moreover, the nonlinear relation between frequency estimates and temperature exhibits some

turning point in temperature at around 30ºC, which probably stems from the geometric nonlinear behaviour of this structure. This aspect was not explored in this thesis, but deserves further research in the near future.

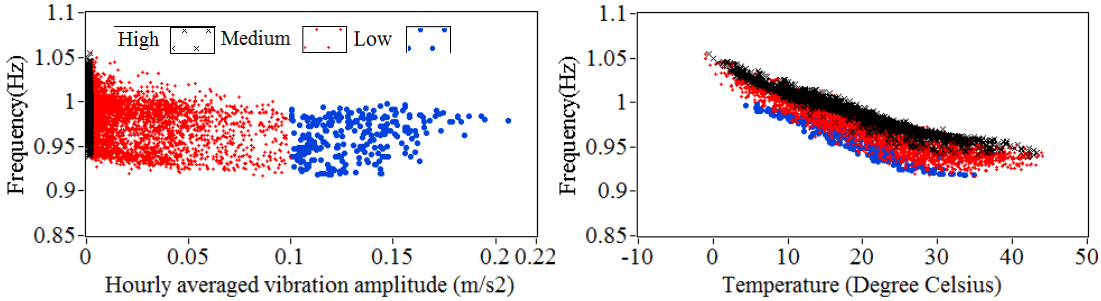

(a) 1st frequency

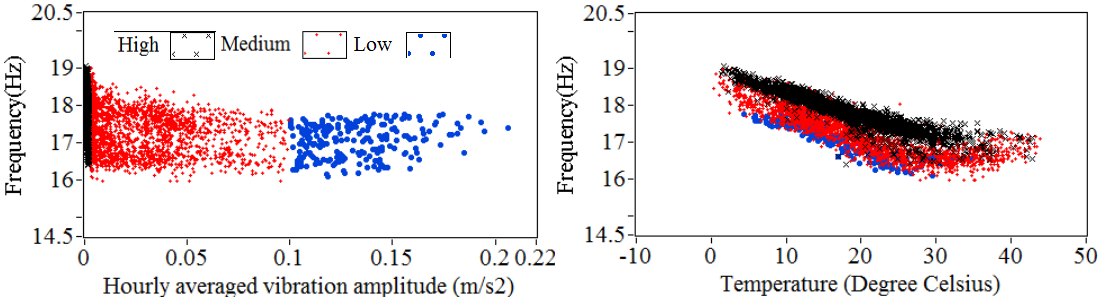

(b) 15th frequency

Figure 5.41 Effect of averaged acceleration amplitude and temperature on identified frequencies

With intention to further manifest the effect of vibration level, the one year monitoring frequency estimates were objectively divided into three clusters, according to the corresponding vibration levels. One of them corresponds to the frequency results estimated from footbridge responses in one hour when the averaged acceleration amplitude is lower than 0.002m/s^2. The second cluster is a group of frequency results whose corresponding hourly averaged acceleration amplitude is larger than 0.1m/s^2. The last cluster is formed by the remaining frequency results reflecting the medium vibration levels. The correlation plots between hourly averaged amplitude and frequency (1st and 15th orders as examples), shown in the left side graphs of Figure 5.41, reveal the distribution of frequency results in terms of the corresponding vibration levels. The clusters in black, red and blue represent annual frequency results with low, medium and high hourly averaged vibration amplitude, respectively. Combining with the corresponding temperature records of these three clusters, the correlation plots between temperature and frequency (1st and 15th orders as examples) are characterized by the right side graphs of Figure 5.41. It is observed that the frequency results with low

vibration levels (in black) scatter along the high boundary of the graphs whereas the frequency results representing high vibration level distribute in the low bound (in blue), suggesting the effects of the hourly averaged accelerations on frequencies. Such observation also prove the conclusion drawn from comparison of correlations between temperature and the 1st frequency estimates in terms of monthly monitoring results from June 2009 to September 2009 (Figure 5.40).

Finally, it is important to state that, though the raising vibration levels are believed to reduce frequencies according to the above analysis, the true reasons are still uncertain. That can probably result from the fact that higher values of averaged acceleration amplitudes are caused by a larger number of pedestrians, which may not only add mass to the structure, but also induce some slight nonlinear behaviour of this stress-ribbon footbridge.

In order to compare the effects of temperature and vibration levels, the scales of Y axis (Frequency) used in Figure 5.42 are considered the same as those used in Figure 5.38. Comparison of these two figures indicates that from the long term monitoring point of view the effects of vibration level on frequencies are far less obvious than those caused by temperature, which coincides with the conclusions drawn from analysis of continuous monitoring results of Pedro e Inês footbridge and other cases summarized in section of Introduction.

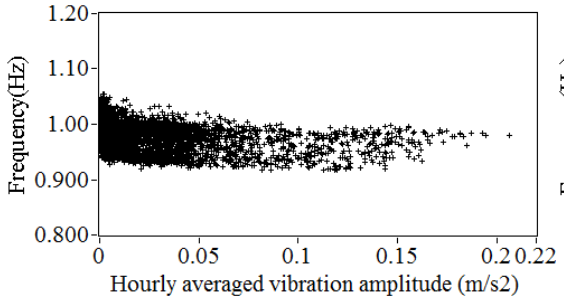

(a) 1st frequency

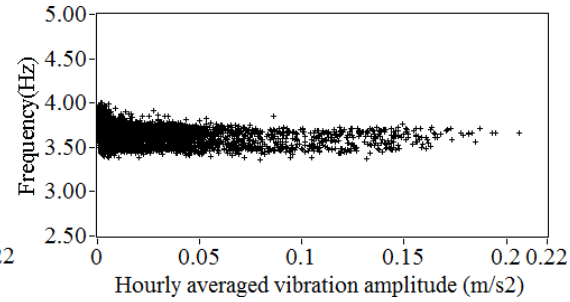

(b) 5th frequency

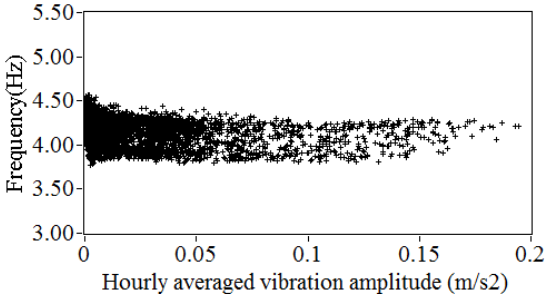

(c) 6th frequency

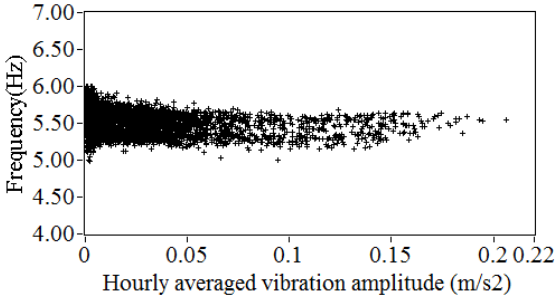

(d) 7th frequency

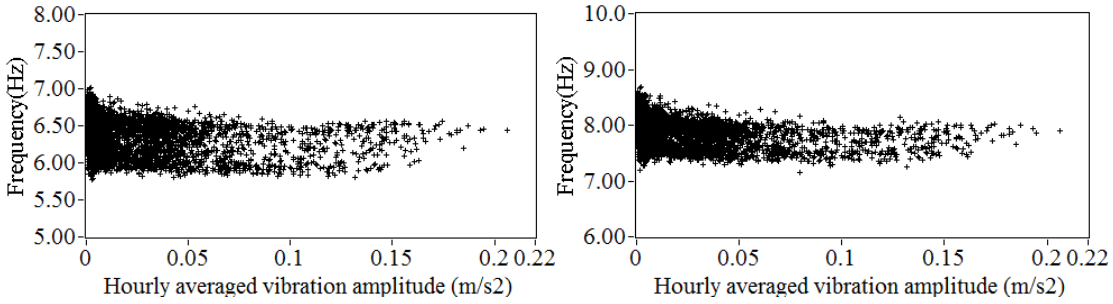

(e) 8th frequency

(f) 9th frequency

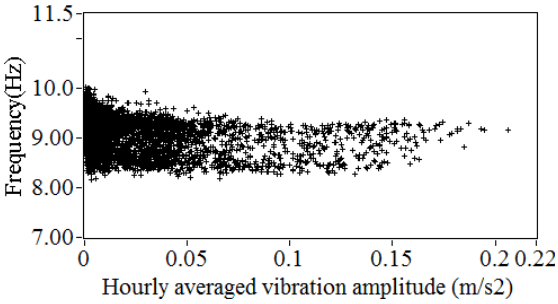

(g) 10th frequency

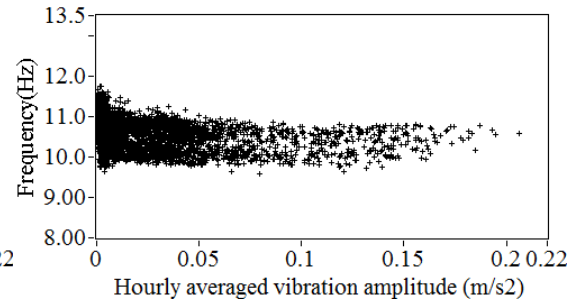

(h) 11th frequency

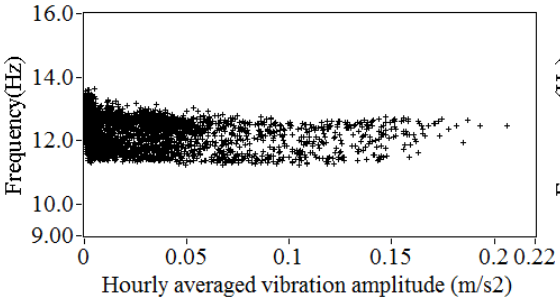

(i) 12th frequency

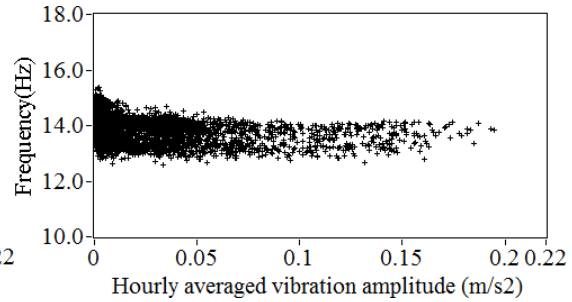

(j) 13th frequency

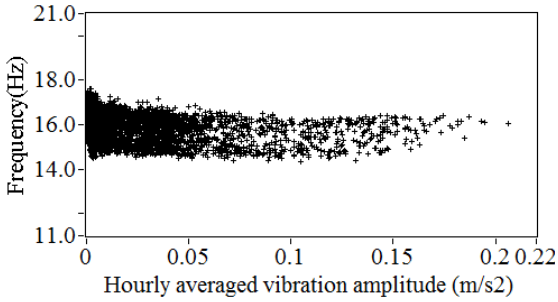

(k) 14th frequency

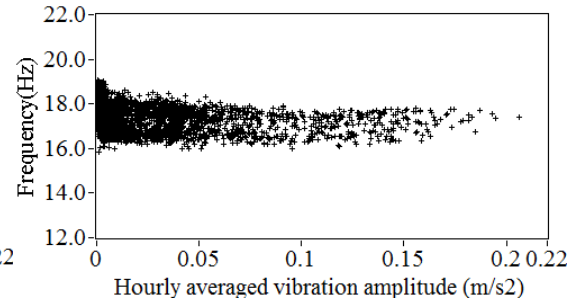

(l) 15th frequency

Figure 5.42 Identified frequencies versus hourly averaged acceleration amplitude from 1st June 2009 to 31st May 2010

Beyond the investigation of the effect of environmental factors on resonant frequencies, the relations between vibration levels and the first modal damping ratio estimates were also analyzed. Figure 5.43 displays the correlation plots between all hourly averaged accelerations in one year. No obvious tendency is observed.

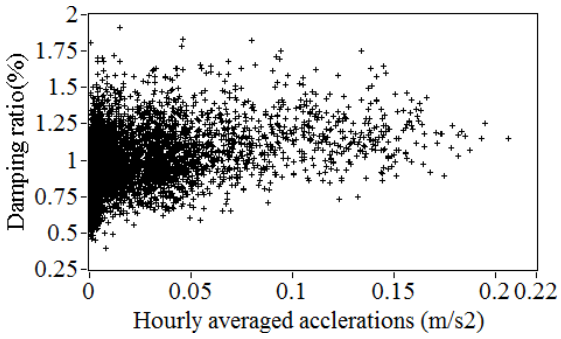

Figure 43 Identified 1st modal damping ratio versus hourly averaged acceleration amplitude from 1st, June, 2009 to 31st May 2010

5.3.4 Summary

In this section, efforts were developed to investigate the continuous dynamic monitoring results of FEUP campus footbridge, as well as the effect of environmental factors on dynamic properties. Firstly, a compact continuous dynamic monitoring system is described, mainly consisting of signal acquisition, transmission and processing modules. The potential and efficiency of this system is illustrated by the annual monitoring of vertical accelerations and temperature starting on the 1st June 2009. Subsequently, the maximum daily vertical vibration levels are presented as a serviceability index for footbridge under normal use. It is found that the daily maximum accelerations in 117 days of one year exceed 1 m/s^2 (maximum limit for medium degree of comfort) and that the maximum vibration level reached 5.7m/s^2, indicating the bridge is prone to high acceleration levels induced by vandal loads . Frequency domain analysis reveals that modes around 2Hz are easily excited, because they tend to coincide with the pacing rate of pedestrians. Hourly averaged vertical accelerations are used to approximately characterize the response levels of the footbridge and evaluate the traffic intensity. The proposed method reflected reasonable daily variations of vibrations and showed that the estimated response levels in working days are more significant than those observed in weekends or in holidays. In the third part of this section, the annual variation of temperature, hourly averaged vertical accelerations and modal parameters are analyzed and estimated with intention of depicting the environmental effects on dynamic properties under operational conditions. This investigation shows that the identified frequencies of 10 modes are all sensitive with variation of temperature, the corresponding estimates presenting an annual maximum relative difference oscillating between 14% and 20.6%. Similar nonlinear relations

between concrete temperature and frequencies are examined with a clear 'turning point' situated approximately around 30ºC. Additionally, relatively slight effects of pedestrian loads on frequencies are also observed though the degree of influence is less apparent than temperature. Conclusion is drawn that, from the continuous monitoring point of view, temperature has a primary influence on the variation of frequencies of all modes.

5.4 CONCLUSION

In the context of investigation of long term behaviour of bridges and special structures, compact and economic continuous dynamic monitoring systems were applied at the Pedro e Inês footbridge, in Coimbra, and at FEUP campus footbridge, in Porto. They consist of data acquisition and transmission hardware, as well as the CSMI toolkit for the processing of collected signals and organization of results. It is demonstrated that such systems can provide not only important instantaneous dynamic information about the footbridge, but also serves as an effective tool for long term bridge health monitoring.

Continuous dynamic monitoring results are presented, including accelerations and temperature. Regarding the Pedro e Inês footbridge, in Coimbra, the maximum recorded vertical and lateral vibration levels are 0.849m/s^2 and 0.099m/s^2, during 3 years, much less than 1.94m/s^2 and 1.2/m/s^2, which were the corresponding maximum responses observed during a crowd test performed before installation of control devices. Those values evidenced the efficiency of the TMDs under operational conditions. At FEUP campus footbridge, the maximum vertical vibration level reached 5.7m/s^2 during one year, certainly induced by vandal loads. In addition, in 352 days of one year the recorded maximum daily vertical vibration levels are clearly below 2.5m/s^2, which means that unacceptable vertical vibrations do not frequently occur, according to guidelines, such as of Service d'Études Techniques des Routes et Autoroutes (SETRA,2007) and Human induced Vibration of Steel Structures (HIVOSS, 2007). Maximum vertical accelerations clearly above the limits are induced by vandal loads, as described in (Caetano and Cunha, 2005).

The frequency domain analysis of time series collected at these two footbridges shows that the higher levels of vibration recorded are caused by some resonance related with one or

more modes of vibration, as some bridge natural frequencies are close to the dominant frequencies of the human-induced excitation. With regard to Pedro e Inês footbridge, in Coimbra, the most easily excited vertical frequency range is around 3Hz, which not only accords with running or jumping behaviour of pedestrians but also coincides with bridge natural frequencies around 3Hz. This observation also confirms the predictions from the preliminary design of the control devices. Regarding to FEUP campus footbridge, the frequency domain analysis shows that peaks around 2Hz are most frequently observed due to the proximity between step frequencies of pedestrians and bridge natural frequencies around 2Hz.

Hourly averaged acceleration amplitude was used to evaluate the vibration levels, preparing for the correlation analysis with modal parameters estimated from structural response collected in one hour. The efficiency of this method is illustrated by reasonable daily and seasonal variations of vibration level. Long term variations of temperature information are also presented. It is concluded that the temperature records from different positions have different tendencies, depending on the orientation of the bridge and solar angle, as well as leading to diverse effects on frequencies.

Modal parameters were identified automatically by application of SSI-COV algorithm implemented in the CSMI toolkit. Frequencies of a significant number of modes are estimated by hourly accelerations recorded from the Pedro e Inês footbridge in Coimbra and the FEUP campus footbridge in Porto. Approximately linear and nonlinear relations between frequencies and temperature are observed in these two footbridges. With raising temperature, the frequencies of all modes decrease. Temperature is also concluded as the primary environmental factor affecting variation of frequencies of different modes. Statistical analysis of frequency results shows that the maximum relative difference of frequency estimates of Pedro e Inês footbridge oscillates in the range 2.7%-3.9%, far less than 14%-20.6%, which is the counterpart of FEUP campus footbridge.

In addition, vibration levels evaluated by hourly averaged accelerations are also proved to affect frequency estimates of the first two modes of Pedro e Inês footbridge and of all modes of FEUP campus footbridge. The tendency of reduction of frequency estimates with increasing vibration levels is observed in both footbridges. Although the effects of frequencies

from vibration levels are promising, the true reason is still uncertain and worth further investigation in future.

6

DAMAGE DETECTION USING CONTINUOUS DYNAMIC MONITORING DATA

6.1 INTRODUCTION

Detection of slightly abnormal structural changes under normal operational conditions, rather than fatal damage leading to a transient loss of structural resistance, is vital for structural health monitoring. In reality, environmental and operational parameters oscillate in time, and induce alterations of vibration features. Unfortunately, the changes of features caused by environmental and operational parameters may be of an order of magnitude equal or even greater than those induced by slight structural damage. If the effects of those parameters are not taken into account in the damage detection process, false damage diagnoses on the basis of continuous dynamic monitoring data may occur and thus it becomes unreliable. Accordingly, it is critical to remove such adverse effects from environmental and operational factors and build a reliable healthy indicator which is sensitive to early abnormal structural modification (Deraemaeker et al, 2007).

The several approaches to solve such problem may be generally classified in three types. The first one attempts to directly model the environmental and operational influences on the dynamic characteristics of the structure. It is a difficult procedure because, on the one hand, many environmental and operational factors may be considered, and on the other hand, the accurate environmental model is still unknown. To overcome this difficulty, instead of

building the mathematical model, an alternative method consists in identifying it on the basis of the '*input*' (environmental variable) and the '*output*' (dynamic features). It returns to the '*system identification*' problem, as described at the beginning of Chapter 2. The models representing accurately the relationship between *input* and *output* can be identified. Examples of this method are the use of a linear filter for the Alamosa Canyon bridge (Sohn et al, 1999), the application of an Auto Regressive model for the Z24 bridge (Peeters and De Roeck, 2001) and the implementation of Support Vector Machine for the Ting Kau bridge (Ni et al, 2005). In these cases, the authors restricted their investigations to the modelling of the relationship between temperature and the first frequency. However, one drawback of this method is that the model can not be derived from a physical law and thus the meaning of the models is not clear. Moreover, the optimal locations of temperature sensors may be difficult to determine or reach (Kullaa, 2001). For example, in (Ni et al, 2005), 20 temperature measurements were selected among a set of 83 temperature sensors installed on a cable-stayed bridge. Also, as mentioned in Chapter 5, some difference was observed in only 6 thermal sensors mounted in the Pedro e Inês footbridge. In order to overcome these drawbacks, a set of methods have been proposed to remove the environmental variables without measuring them. For example, a linear factor analysis is applied to eliminate environmental and operational effects from the healthy system (Kullaa, 2001). A more popular approach is based on Principal Component Analysis (PCA). In this method, the measurement of the environmental variables is not required because the environmental effects are treated as embedded variables. The underlying assumption of this method is that changes in the measurement features due to environmental variations are different from those caused by structural damage, and may be accounted for using PCA and can be distinguished. Considerable research efforts have been devoted to the application of this method. It has been applied to the monitoring data of a composite panel in an environmental chamber (Mason, 2002). It is reported in (Yan et al, 2005a, b) that this approach was implemented in a scaled laboratory model and further developed the non-linear PCA technique to identify the damage in Z24 bridge. This method was implemented in (Deraemaeker et al, 2007) to detect the simulated damage on a numerical model of a bridge subject to environmental change. In (Girado et al, 2006), a PCA-based method is developed to locate the damage of an analytical model of a four story building under varying environmental

conditions. Recently, this approach was applied to remove the unknown environmental and operational effects after linear regression analysis (Magalhães, 2010). The efficiency and robustness of the PCA-based method was verified, with the purpose of removing the environmental effects and detect structural damage. However, the applications of this technique using continuous dynamic monitoring data are still rare. In reality, it seems that the environmental factors have specific effects on different structures. For example, in Chapter 5, the linear effects on the frequencies are observed in Pedro e Inês footbridge while a nonlinear trend is noticed in FEUP campus footbridge. In this thesis, an effort of implementation of PCA-based methodology in the continuous monitoring of these two footbridges is presented.

This chapter mainly consists of three parts: The first part is dedicated to generally model the environmental effects from the point of view of statistical analysis, with intention of removing the environmental and operational effects. It should be noted that it is not strictly a mathematical model characterizing the relations between environmental variables and dynamic features, or a model describing the relations between input and output referred in *system identification*. The general model intends to assist to understand the PCA based method for removal of the environmental effects. Subsequently, the theory is introduced. To illustrate the complex equations, a geometrical interpretation is also presented in order to highlight the essence of this method. In the second part, the proposed methodology is applied to the continuous monitoring data of the two footbridges in order to remove the environmental and operational effects and detect simulated damage. Finally, some conclusions are summarized.

6.2 GENERAL ENVIRONMENTAL MODEL AND REMOVAL OF ENVIRONMENTAL EFFECTS

6.2.1 General environmental model

Due to the difficulty of accurately modelling the influence of environmental factors on the extracted features, it is expected to remove such influence without measuring environmental variables. The basic idea is that changes in the extracted features due to

environmental variations are different from those caused by structural damages. The former may be accounted for using PCA by identifying the linear subspace where the environmental effects exist. Projecting the features in the subspace orthogonal to the identified linear subspace allows removing the environmental effects. Moreover, the effect of noise or occasional abnormal identification may be mitigated when a large number of samples is employed for statistical analysis. A general environmental model proposed in (Deraemaeker et al, 2007) is presented to illustrate the underlying physical meaning of PCA-based method.

It is assumed that all features are collected in a matrix Y

$$Y=f(T, L, W\ldots)+g(\eta) \tag{6.1}$$

where f $(T, L,W\ldots)$ is a function of the environmental and operational variables (i.e. temperature T, traffic intensity L, wind W, ….) as well as η is a variable which is associated with structural damages and noise. It is noted that it is difficult to derive the theoretical function f directly. However, the general function f can be approximately decomposed into two mappings as shown in Figure 6.1.

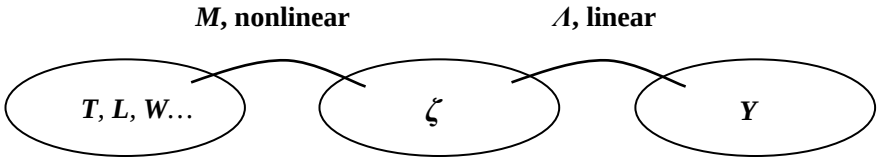

Figure 6.1 Function f decomposed into a nonlinear mapping M and a linear mapping Λ

The environmental and operational factors $(T, L, W\ldots)$ are transformed into *unobservable factors* ζ by means of a non-linear mapping M:

$$f\ (T,\ L,W\ldots)=\ \Lambda(M(T,\ L,W\ldots)) \tag{6.2}$$

The nonlinear mapping is generally unknown and does not need to be identified. The *unobservable factors* ζ are assumed to be statistically zero-mean independent variables. A linear mapping Λ is used between the *unobservable factors* and the vibration features, then equation (6.1) becoming

$$Y=\Lambda\zeta+g(\eta) \tag{6.3}$$

In order to identify the linear mapping Λ between the unobservable factors and the features, it is necessary to measure the features vector from the healthy structure under operational conditions for a full period of time that manifest the environmental effects, for

example, continuous monitoring a bridge after construction during a one year period of time, whereas the influence of the other factors η is relatively small. It could be expressed as residual part ε:

$$\varepsilon = g(\eta) \ll \Lambda\zeta \tag{6.4}$$

and equation (6.3) becomes:

$$Y = \Lambda\zeta + \varepsilon \tag{6.5}$$

The relations underlying equation (6.5) can be further illustrated by Figure 6.2.

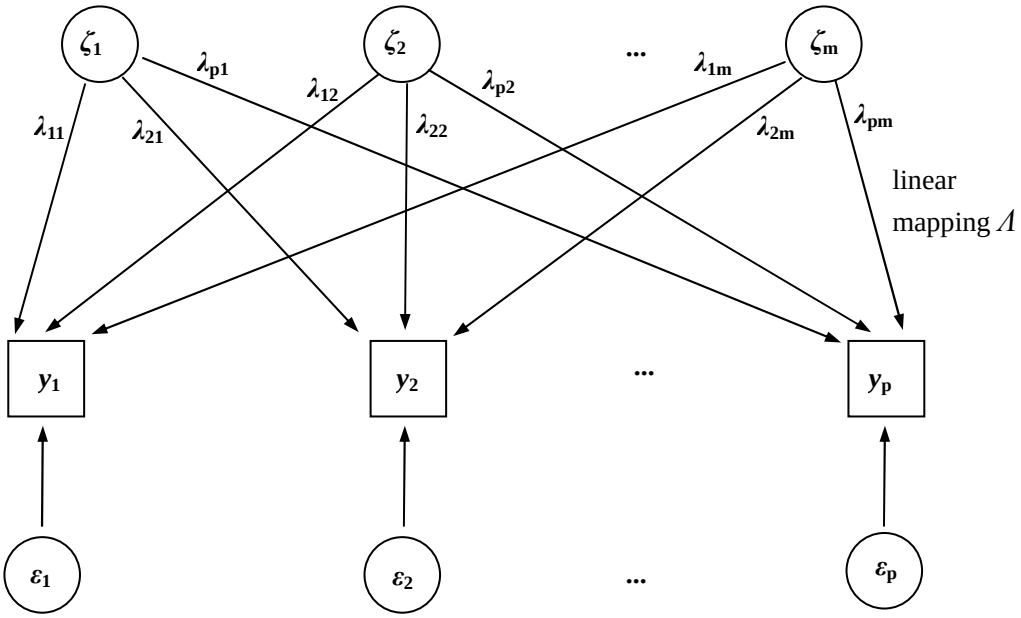

Figure 6.2 Representation of feature matrix Y
using a linear mapping of unobservable factors ζ and a residual part ε

It should be emphasised that the linear mapping Λ can be identified by Principal Component Analysis (PCA), only if the number of ζ factors is smaller than the number of features. If the number of *unobservable factors* is equal to the number of features, the new mapping Λ is identical to function f and ε=0. In this case, the environmental factors can not be removed. Therefore, the restriction of PCA based method is that the dimension of *unobservable factors* ζ must be smaller than the number of features.

6.2.2 Removal of environmental effects

Let us consider the matrix $Y \in R^{n \times N}$, whose column vectors y_k are the identified n-order natural frequencies at time t_k (k=1,2,…..,N) during a cycle of monitoring time. The covariance matrix between feature matrices Y is given by:

$$\Sigma=E[YY^T]=E[(\Lambda\zeta+\varepsilon)(\Lambda\zeta+\varepsilon)] \tag{6.6}$$

where E is the mathematical expectation. It is assumed that *unobservable factors* ζ have zero-mean and its covariance matrix is identity, as well as the residual part is far small as $\varepsilon \ll \Lambda\zeta$. Equation (6.6) becomes:

$$\Sigma=\Lambda\Lambda^T+\Psi \tag{6.7}$$

where Ψ is the covariance matrix of residual part ε. On the basis of above equation, it is possible to split the covariance matrix of features into the contribution of environment and the residual part.

A singular value decomposition of the covariance matrix of Y is expressed as

$$\Sigma=USU^T \tag{6.8}$$

$$S=\begin{bmatrix} S_1 & 0 \\ 0 & S_2 \end{bmatrix},\ U^TU=I \tag{6.9}$$

where U is an orthonormal matrix ($UU^T=I$), whose columns define the principal components and form a subspace spanning the data, and S is the singular values matrix representing the active energy of the associated principal components. Matrix S can be split in two parts: $S_1=diag(\sigma_1^2,\sigma_2^2...\sigma_m^2)$ is a diagonal matrix with the square of the first m singular values on the diagonal, ranked by decreasing order, and $S_2=diag(\sigma_{m+1}^2,\sigma_{m+2}^2...\sigma_n^2)$. In practice, the elements of S_2 are much smaller comparing with elements of S_1. However, they are not equal to zero due to the influences of noise or the minor nonlinear effects. An indicator can be defined as:

$$I=\sum_{i=1}^{m}\sigma_i^2 \Big/ \sum_{i=1}^{n}\sigma_i^2 \tag{6.10}$$

Parameter m is determined as the lowest integer such as $I>e$ (%), where e is a threshold value (e.g. 95%). The meaning of this threshold is the following: m unobserved factors contribute to e% of the variance in the observed data. In other words, m factors have a strong influence on the variation of the vibration features and have to be retained, whereas the other factors whose influence may be negligible (e.g., noise). From the point of view of geometry, the extracted features of the structure vary mainly along the directions of the m principal components associated with the highest energies, that is, the extracted features approximately

remain in the hyper-plane defined by the *m* principal components. For example, in some cases temperature may be the only significant environmental and operational factor, which means that *m* is equal to 1 (Yan et al, 2005a).

Accordingly, matrix U is also split in two parts as:

$$U= [U_1\ U_2] \tag{6.11}$$

where U_1 is the first *m* columns of U.

This splitting allows to identify the Λ and Ψ

$$\Lambda=U_1\sqrt{S_1} \tag{6.12}$$

$$\Psi= U_2S_2U_2^{\mathrm{T}} \tag{6.13}$$

In order to remove the environmental/operational effects, *unobservable factors* ζ can further solved by classical least-square estimator by minimizing

$$Y-\Lambda\zeta \tag{6.14}$$

ζ can be estimated as the Moore-Penrose pseudo-inverse of Λ

$$\tilde{\zeta} = (\Lambda^{\mathrm{T}}\Lambda)^{-1}\Lambda^{\mathrm{T}}Y \tag{6.15}$$

The estimated $\Lambda\overline{\zeta}$ can be given by substituting equation (6.12) into (6.15)

$$\Lambda\tilde{\zeta} = \Lambda\ (\Lambda^{\mathrm{T}}\Lambda)^{-1}\Lambda^{\mathrm{T}}Y \tag{6.16}$$

Because of the properties of the *SVD* ($U_1^{\mathrm{T}}U_1=I$), this expression reduces to

$$\Lambda\tilde{\zeta} = U_1\sqrt{S_1}\ (\sqrt{S_1}^{\mathrm{T}}U_1^{\mathrm{T}}\ U_1\sqrt{S_1})^{-1}\sqrt{S_1}\ \ U_1^{\mathrm{T}}Y$$

$$=U_1U_1^{\mathrm{T}}Y \tag{6.17}$$

According to (6.5), the new feature matrix is given by ε

$$\varepsilon=Y-\Lambda\tilde{\zeta} =Y-U_1U_1^{\mathrm{T}}Y \tag{6.18}$$

It corresponds to the dynamic features from which the environmental effects have been removed.

6.2.3 Damage detection

The Novelty Detection technique can be applied to analyse the residual error ε in order to detect possible structural damage. Initially, Novelty Detection is simply to identify from

measured data if a machine or structure has deviated from normal condition, that is if the data is novel. The concept of Novelty Detection is not entirely new, however, the new terminology is justified by the fact that novelty detection provides a unifying framework for techniques from a wide range of disciplines involving with condition monitoring, pattern recognition and multivariate statistics. (Worden et al, 2000).

In the procedure of damage detection, Novelty Detection first builds an internal representation of system's normal condition, and then examines subsequent data to observe if they significantly depart from the normal condition. It can be summarized as following steps:

1. The Mahalanobis norm of residual error matrix ε is calculated as Novelty Index (*NI*):

$$NI_k = \sqrt{\varepsilon_k^T R^{-1} \varepsilon_k} \tag{6.19}$$

where R is given by equation $R=(YY^{\mathrm{T}})/N$.

2. Once Mahalanobis norm is computed, the control chart (Montgomery, 2005) is used to process the calculated *NI* vector. In statistical analysis, control charts plot some relevant index as a function of the samples. The charts have low and upper limits, which are computed from those samples, recorded when the process is assumed to be in control. When unusual sources of variability are present, sample statistics will deviate from controlled state and plot outside the control limits. In (Kullaa, 2003), several univariate and multivariate control charts for damage detections are compared.

To detect possible damage, an *X*-bar control chart (Yan et al, 2005; Giraldo et al, 2006) is constructed by drawing two lines: a centre line (*CL*) and an additional horizontal line corresponding to an upper limit (*UCL*), which are given by:

$$CL = \overline{NI} \tag{6.20}$$

$$UCL = \overline{NI} + \alpha\sigma \tag{6.21}$$

where $\overline{NI}$ and σ are the mean value and the standard deviation of *NI* in the reference healthy state, respectively. In the present application α is taken as 3, which corresponds to 99.7% confidence.

Two criteria can be employed as damage warning: (1) outlier analysis, counting for the percentage of the *NI* laying outside the *UCL* and (2) ratio of $\overline{NI}$ between healthy and damage state. In the healthy state, the new vibration features should stay in the hyperplane spanned by the features in reference state, so the percentage of the *NI* overpassing *UCL* should be small and ratio of $\overline{NI} \to 1$. On the contrary, with the emergence of damage, the new vibration features will depart from the hyper-plane in the reference healthy state, which will cause the percentage of outlier to increase significantly and lead to relatively large ratio of $\overline{NI}$ (Worden et al, 2000; Yan et al, 2005; Giraldo et al, 2006) .

6.2.4 Geometric interpretation

In order to better understand the methodology, a simple two-dimensional example is presented to help visualizing how the principal components characterize the variation of the extracted features when affected by environmental factors, and how this technique can be used to distinguish their effects. Similar explanations can be also found in (Yan et al, 2005; Giraldo et al, 2006).

Figure 6.3 shows a geometric interpretation of a two-dimensional case (two features y_1 and y_2). The circles (in black) represent the distributions of features y_1 and y_2 in healthy state. A single point *Z* (a cross in red) is identified in damage state and the corresponding point in healthy state is a circle *Y* (a circle in red). It is assumed that the data is affected by multiple environmental factors.

The application of PCA determines two principal components (PC-I and PC-II) in terms of which the data in healthy state disperses. PC-I is associated with the higher singular value and is responsible for the great variation of the features and corresponds to the main environmental factor, while PC-II represents the effect of other factors. Due to the existence of the main environmental factor, the circles vary along the PC-I, whereas other factors make these circles slightly vary in other direction. This step of application of PCA corresponds to the equations (6.6-6.11).

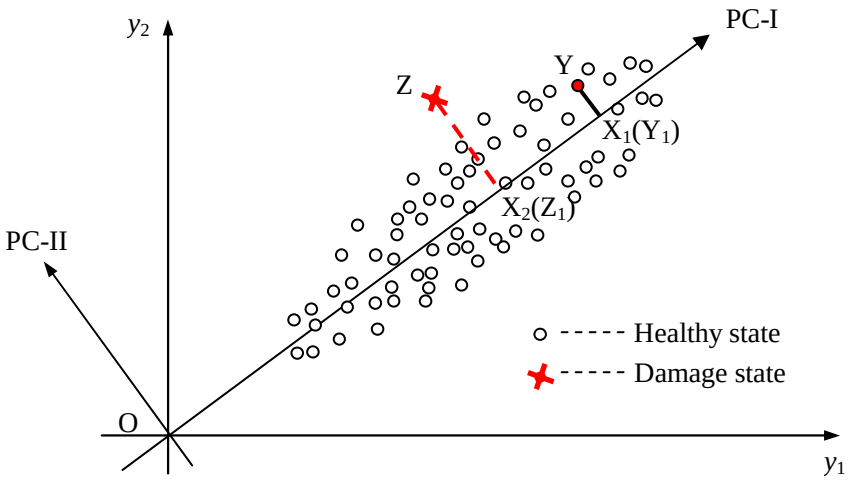

Figure 6.3 Features of the two-dimensional example

Using equation (6.12), these data in healthy state can be expressed in terms of the principal components. The point *Y* (the circle in red) is taken as an example. Using only the first principal component, it is projected into a new space spanned by PC-I resulting in a scalar equal to OX_1. The point X_1 is remapped into the original 2D space and the point Y_1 is obtained. The corresponding residual error defined by equation (6.18) can be evaluated by the length of segment Y_1Y in the original 2D space spanned by two features y_1 and y_2. If the damage occurs, the new features depend in a different way on the environmental factors comparing with the reference feature. For example, the point *Y* shifts to point *Z*. Applying the similar projection procedure of point *Y* according to equations (6.16-6.18) leads to new residual error Z_1Z. It increases significantly comparing with the Y_1Y in healthy state. It is pointed out that all points in healthy state would shift to new positions because of the structural damage. By comparing their residual errors in both healthy and damage states, the environmental effects are approximately eliminated and damage may be detected.

In this section, the general environmental model is proposed to illustrate the PCA-based method of removal of the environmental effect, which also is described. The geometry interpretation assists to clarify the several steps of the proposed methodology. After eliminating the environmental effects, the statistical indicator is only sensitive with the structural change or damage. In the next section, this method will be applied to continuous dynamic monitoring results, in order to remove the environmental effects and detect simulated damage.

6.3 REMOVAL OF ENVIRONMENTAL EFFECTS AND DAMAGE DETECTION

6.3.1 Application to continuous dynamic monitoring results from Pedro e Inês footbridge

It is recalled that, in section 5.2.3 of Chapter 5, the approximate linear effects of environmental and operational factors, on the natural frequencies of Pedro e Inês footbridge are observed and frequencies of higher modes (f_{12}-f_{17}) are sensitive to the change of temperature. The corresponding maximum relative difference in three years varies from 2.7%-3.9% and may mask the subtle changes caused by structural damage. As a result, the frequency estimates of f_{12}-f_{17} are used to constitute the frequency matrix *Y*, in order to apply PCA to remove environmental effects and prepare for damage detection. As Pedro e Inês footbridge is a new structure and no obvious structural damage is observed, possible damage was simulated based on the modification of the finite element model. As described in Chapter 4, the central arch is supported by two groups of vertical piles with a depth of about 30m. The stiffness provided by these foundations is low due to poor mechanical characteristics of soil layers beneath the river bed. The supports provided at the abutments allow the longitudinal displacement of the deck and block the transversal movements. Thus, in the finite element analysis, boundary conditions of support of the arch were simulated with spring elements in the horizontal and longitudinal directions, and the supports of the left abutment were only modelled with longitudinal spring element. Due to the inaccuracy of numerical simulation results associated with frequencies of relatively higher modes, for example, f_{16} and f_{17} , the features matrix *Y* was established with f_{12}-f_{15} and corresponding mean frequencies (4.81Hz, 5.97Hz, 6.52Hz and 7.53Hz,respectively).

In the finite element analysis, the transversal and longitudinal boundary conditions at the supports of the arch, as well as at the supports of the left abutment are modelled with spring elements. The simulated damage scenarios are created by decreasing their stiffness 5%, 10%, 15%, 20% and 30% of the original values. The induced changes of calculated frequencies are listed in Table 6.1.

Table 6.1 Change of calculated natural frequencies caused by simulated damage (Percentage of mean identified frequencies)

Natural frequencies		f_{12}	f_{13}	f_{14}	f_{15}
Decrease of longitudinal stiffness (arch)	5%	0.000	0.012	0.003	0.080
	10%	0.000	0.024	0.006	0.192
	15%	0.000	0.037	0.011	0.347
	20%	0.000	0.051	0.017	0.592
	30%	0.000	0.083	0.034	1.056
Decrease of transversal stiffness (arch)	5%	0.002	0.027	0.002	0.075
	10%	0.002	0.068	0.005	0.249
	15%	0.002	0.137	0.013	0.461
	20%	0.004	0.269	0.025	0.640
	30%	0.006	1.618	0.029	0.844
Decrease of longitudinal stiffness (abutment)	5%	0.031	0.000	0.003	0.025
	10%	0.076	0.002	0.006	0.055
	15%	0.120	0.003	0.011	0.090
	20%	0.166	0.003	0.015	0.130
	30%	0.269	0.007	0.025	0.236

The continuous monitoring results during the 1st year (from June 2007 to May 2008) are selected as reference and the frequency results f_{12}-f_{15} in the second year (from June 2008 to May 2009) are affected with the change of these frequencies caused by simulated damage.

Calculation of equations (6.6-6.10) using continuous monitoring results leads to the square of singular values (157.6, 2.6E-4, 1.9E-4 and 8.3E-5, respectively), demonstrating that the first singular value makes I>99.99%, which indicates only one factor, certainly, temperature, having a primary effect on the long term frequency results. It agrees with the analysis in section 5.2.3. One principal component is considered in the application of equations (6.12-6.21). Novelty index *NI* (grey points) and centre line *CL* (in different colours) in reference state for different damage levels are plotted in Figure 6.4-6.6. The corresponding damage detections based on outlier analysis and ratio of $\overline{NI}$ are characterised in Table 6.2-6.4. The upper limit (*UCL*) is defined with *CL* and σ of the reference state on the basis of equation (6.21).

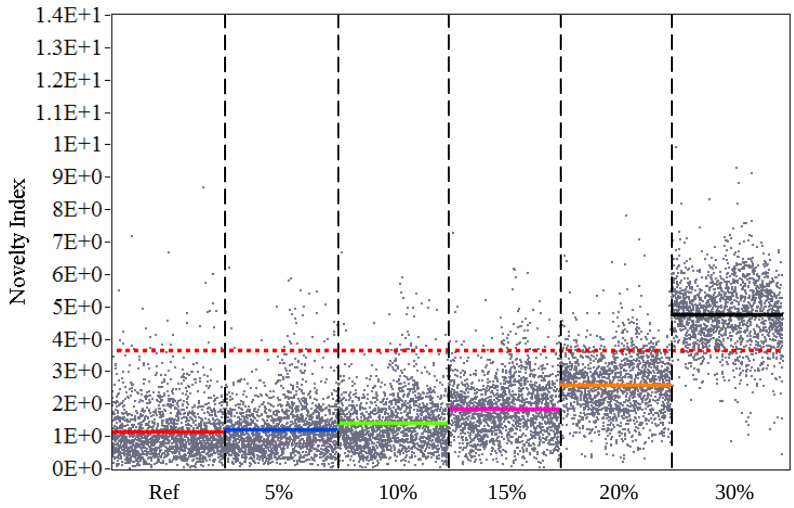

Figure 6.4 Detection of simulated damage by decreasing the stiffness of longitudinal spring element of support of the arch

Table 6.2 Outlier analysis and ratio of mean of NI of different damage scenarios shown in Figure 6.4

Damage	Ref	5%	10%	15%	20%	30%
Outlier analysis	1.8%	1.8%	2.2%	3.6%	13.4%	88.9%
Ratio of $\overline{NI}$	1	1.05	1.21	1.62	2.35	4.17

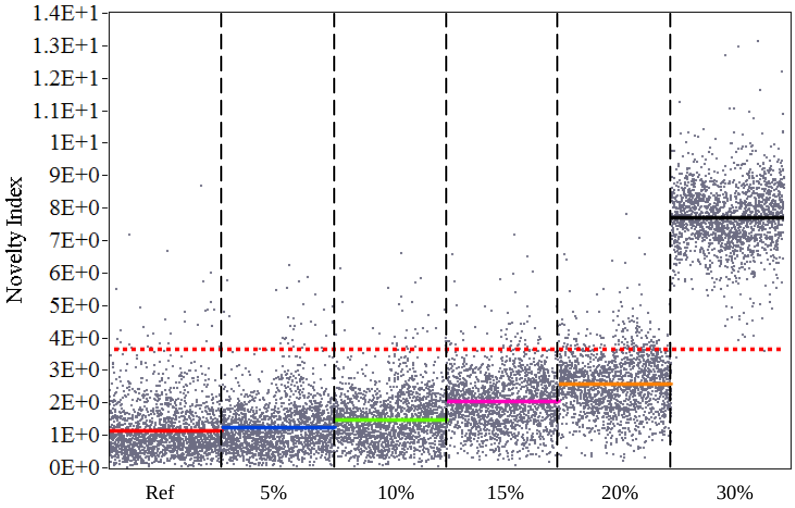

Figure 6.5 Detection of simulated damage by decreasing the stiffness of transversal spring element of support of the arch

Table 6.3 Outlier analysis and ratio of mean of NI of different damage scenarios shown in Figure 6.5

Damage	Ref	5%	10%	15%	20%	30%
Outlier analysis	1.8%	1.9%	1.9%	3.4%	9.2%	99.9%
Ratio of $\overline{NI}$	1	1.09	1.30	1.78	2.24	6.74

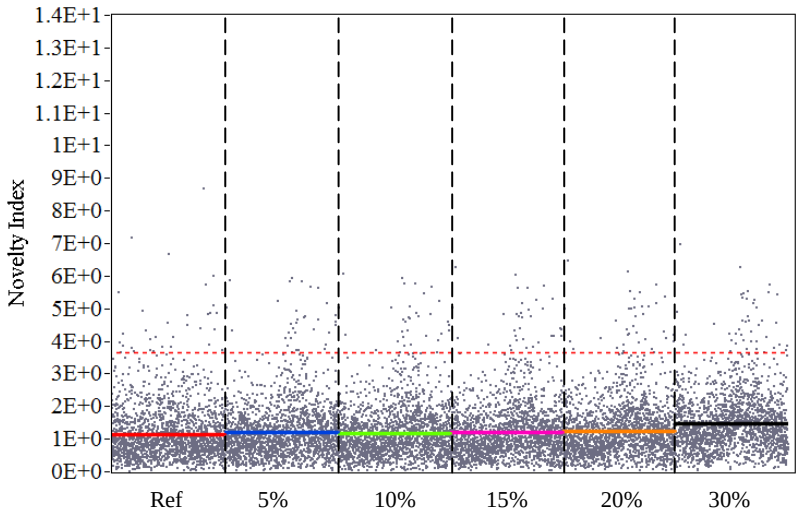

Figure 6.6 Detection of simulated damage by decreasing the stiffness of spring element in supports of left abutment

Table 6.4 Outlier analysis and ratio of mean of NI of different damage scenarios shown in Figure 6.6

Damage	Ref	5%	10%	15%	20%	30%
Outlier analysis	1.8%	1.8%	1.8%	1.9%	2.0%	2.4%
Ratio of $\overline{NI}$	1	1.04	1.03	1.04	1.09	1.27

Regarding the simulated damage in the longitudinal and transversal springs of support of the arch, it is shown in Table 6.2-6.3 that, with the increasing reduction from 5% to 30% of original stiffness of the spring elements in different positions, the ratios of $\overline{NI}$ increase from 1.05 to 4.17 and from 1.09 to 6.74, as well as the outlier analysis presents similar trends. In

Figures 6.4-6.5, the *CL* lines also deviate clearly from the reference state. So, the simulated damages in different levels are efficiency detected by the PCA-based method.

On the contrary, regarding the longitudinal spring on the abutment, there is only a slightly difference in the ratio of $\overline{NI}$ and outlier analysis, as well as a not significant departure of the *CL* for the increasing damage degrees, as shown in Table 6.4 and Figure 6.6. The possible reason may be that only frequencies of higher modes are sensitive to the change of longitudinal spring elements on the abutment, but these frequency results were not included in the present investigation of damage detection. Inspection of Table 6.1 also shows that in the situation of reduction of spring stiffness from 5% to 30% of original stiffness of the spring elements, the induced maximum variation of the frequencies is only 0.269%, which is far less than the counterpart of other damage scenarios with respect to the reduction of spring elements in arch support.

The application of PCA-based method to 3 years monitoring frequency results leads to the Novelty Index (*NI*) and centre line (*CL*) for each year shown in Figure 6.7. It is noted that no clear long term variation of Novelty Index are observed and thus the environmental effects are removed. The healthy indicator *CL* is nearly at the same level during the three years and the outlier analysis evidences a similar trend, as listed in Table 6.5. It may be inferred that from June 2007 to May 2010 no obvious damage is observed and the footbridge continues in a healthy condition.

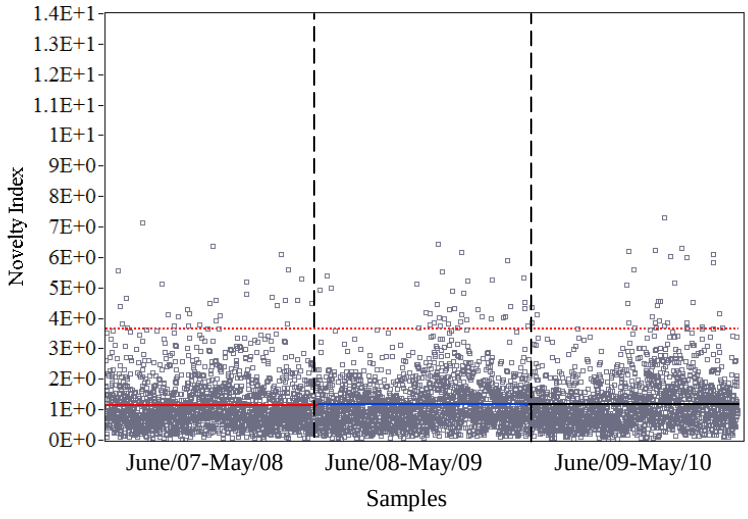

Figure 6.7 Calculated Novelty Index and center lines using 3-years frequency results

Table 6.5 Outlier analysis and ratio of mean of NI of different years

Damage	June/07-May/08	June/08-May/09	June/09-May/10
Outlier analysis	1.8%	1.9%	1.9%
Ratio of $\overline{NI}$	1	1.03	1.03

6.3.2 Application to continuous dynamic monitoring results from FEUP campus footbridge

In (Hu et al, 2011), continuous monitoring data from June 2009 to March 2011 are reported. The environmental and operational nonlinear effects on natural frequencies of different model orders are similar to those observed in Chapter 5. The corresponding maximum relative difference in nearly two years varies from 15.3%-21.4% and certainly mask the early changes caused by structural damage.

Although temperature and pedestrian traffic affect the natural frequencies in a nonlinear manner, the strong linear relations between frequencies of different modes are observed, as proved by the large correlation coefficients listed in Table 6.6 (the correlation coefficients matrix is symmetrical and only the upper parts are retained). Beyond the large correlation coefficients, the correlation plots between frequencies of different modes also demonstrate the strong linear relations. For example, Figure 6.8 displays the correlation plot between the normalized 1^{st} natural frequency estimates and the 5^{th}, as well as 15^{th} natural frequency estimates, respectively. Therefore, it may be concluded that although the nonlinear environmental and operational effects on all frequency results are observed, the linear subspace $\boldsymbol{A}$ representing environmental and operational variables (independent variables) exists and can still be identified by linear PCA, as well as such effects can be also removed by projecting the vibration features into the space of the independent variables.

A three dimensional finite element model of FEUP Campus footbridge was developed and conveniently calibrated on the basis of modal identification tests with the purpose of investigating the dynamic behaviour of this bridge under the crossing of groups and flows of pedestrians, as well as of vandal loads (Caetano et al, 2005). In the current research, this finite

element model is used to simulate the possible occurrence of structural damage.

Table 6.6 Correlation coefficients between the frequency estimates of different modes

	f_1	f_5	f_6	f_7	f_8	f_9	f_{10}	f_{11}	f_{12}	f_{13}	f_{14}	f_{15}
f_1	1.00	0.93	0.95	0.90	0.94	0.92	0.94	0.93	0.95	0.93	0.96	0.93
f_5	/	1.00	0.92	0.85	0.90	0.91	0.91	0.92	0.93	0.93	0.93	0.93
f_6	/	/	1.00	0.84	0.92	0.91	0.93	0.92	0.94	0.93	0.94	0.92
f_7	/	/	/	1.00	0.85	0.84	0.84	0.85	0.86	0.86	0.85	0.85
f_8	/	/	/	/	1.00	0.90	0.92	0.91	0.94	0.91	0.94	0.91
f_9	/	/	/	/	/	1.00	0.91	0.92	0.92	0.93	0.93	0.93
f_{10}	/	/	/	/	/	/	1.00	0.92	0.95	0.93	0.95	0.92
f_{11}	/	/	/	/	/	/	/	1.00	0.93	0.94	0.93	0.94
f_{12}	/	/	/	/	/	/	/	/	1.00	0.94	0.96	0.94
f_{13}	/	/	/	/	/	/	/	/	/	1.00	0.95	0.95
f_{14}	/	/	/	/	/	/	/	/	/	/	1.00	0.94
f_{15}	/	/		/	/	/	/	/	/	/	/	1.00

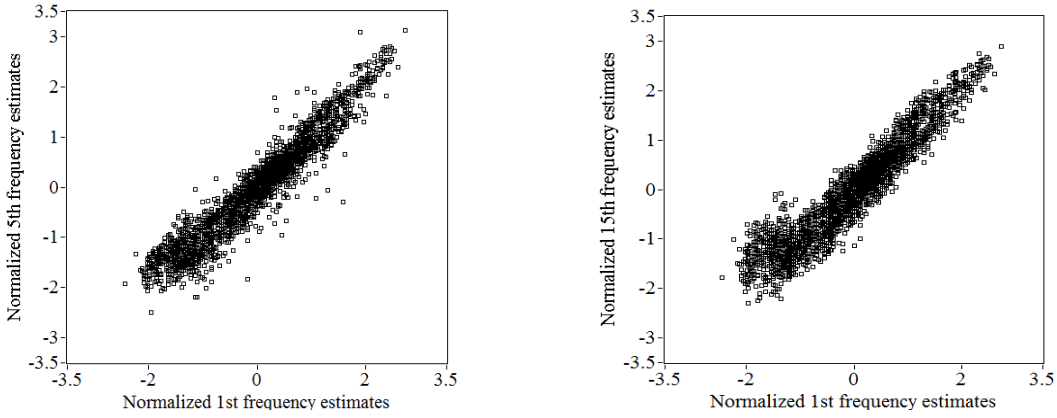

(a) The 1st versus 5th frequency (b) The 1st versus 15th frequency

Figure 6.8 Linear relations between the 1st natural frequency estimates and the 5th and the 15th natural frequency estimates

On the basis of the structural features introduced in section 4.4.1, two series of parallel truss elements at a distance of 3.80m are used to idealize the four cables, with an initial tension of about 2000kN and clamped in both abutments. Beam and shell elements with a length of 0.99m alternate with beam and shell elements 0.01m long, the former simulating the concrete deck and the latter representing the joints between precast elements.

Possible damage scenarios are simulated by replacing the clamped boundary conditions with spring elements. In order to represent different levels of damage, the corresponding stiffness constants are defined as K_1= 1E13 kN·m/rad, K_2= 1E10 kN·m/rad and K_3= 1E7 kN·m/rad. The induced changes of percentage of the corresponding mean frequencies are listed in Table 6.7. The continuous monitoring results during the 1st year (from June 2009 to March 2010) are selected as reference and the frequency estimated in the second year (from June 2010 to March 2011) are loaded with the change of these frequencies caused by simulated damage.

Table 6.7 Change of calculated natural frequencies caused by simulated damage (Percentage of mean identified frequencies)

Mode	K_1	K_2	K_3
1	1.60	5.6	12.5
5	0.07	5.0	9.8
6	3.13	6.1	10.1
7	0.06	5.2	9.2
8	3.35	6.2	9.3
9	0.06	5.1	8.3
10	3.42	6.0	8.4
11	0.07	5.0	7.7
12	3.47	5.8	7.8
13	0.06	4.1	6.3
14	2.25	2.6	3.1
15	0.04	1.9	3.5

Equations (6.6-6.10) lead to squares of the singular values as: 1264.290, 0.031, 0.020, 0.014, 0.011, 0.010, 0.009, 0.006, 0.005, 0.002, 0.001 and 0.0007. This suggests that the variations of frequency estimates can be explained just by one environmental factor. As indicated in section 5.3.3 of Chapter 5, from the point of view of continuous monitoring, ambient temperature may be the primary influence source though the relatively weak effects from pedestrian traffic are also noted. However, in the current analysis the first two principal components are retained with attempt to efficiently remove the effects of both temperature and pedestrian traffic.

Figure 6.9 shows the Novelty index *NI* (grey points) and centre line *CL* of reference state (in red) and three different damage scenarios (in blue, purple and black, respectively). Obvious deviation of *CL* comparing with the reference state is noted when releasing the

rotation with decreasing stiffness constants of spring elements at both abutments. It is shown in Table 6.8 that the corresponding ratios of $\overline{NI}$ increase from 1.39 to 3.31 and the outlier analysis presents similar trend. It means that such damage can be clearly detected.

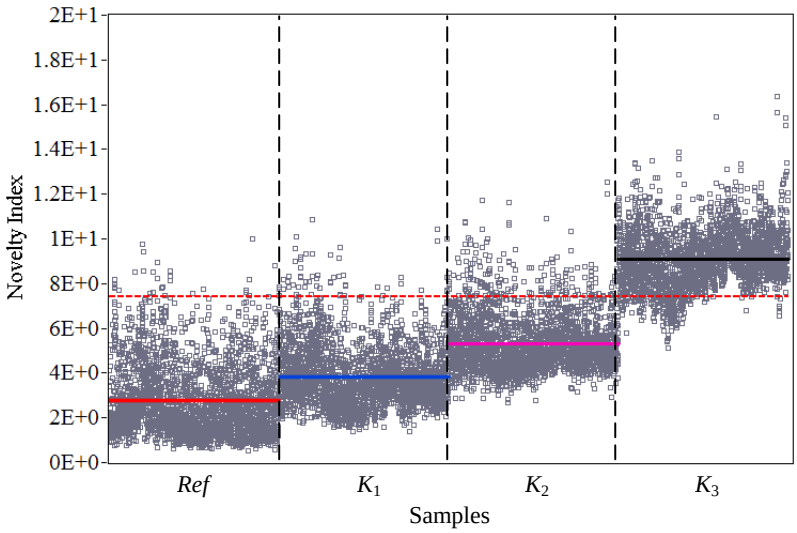

Figure 6.9 Detection of simulated damage by decreasing the stiffness of spring element in abutment

Table 6.8 Outlier analysis and ratio of mean of *NI* of different damage scenarios shown in Figure 6.10

Damage	Ref	K_1	K_2	K_3
Outlier analysis	1.1%	2.1%	7.1%	9.2%
Ratio of $\overline{NI}$	1.00	1.39	1.93	3.31

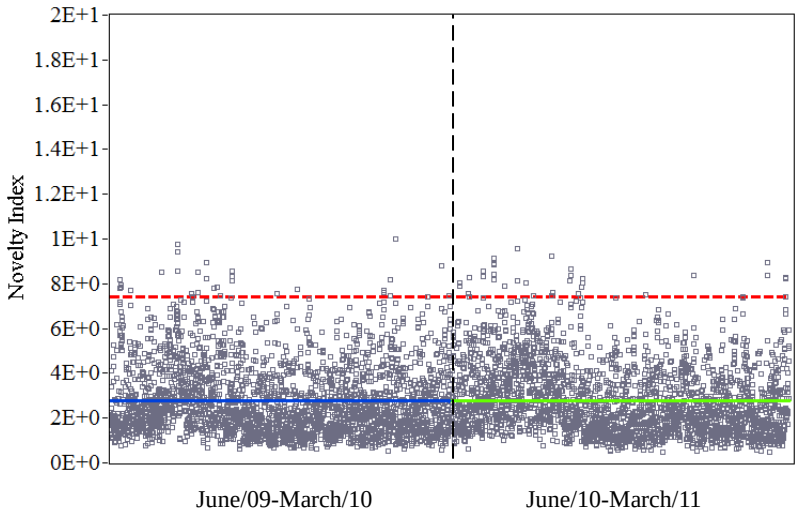

Figure 6.10 Calculated Novelty Index and centre lines using nearly two years frequency estimates

Table 6.9 Outlier analysis and ratio of mean of NI of different years

Damage	June/09-March/10	June/10-May/11
Outlier analysis	1.1%	1.2%
Ratio of $\overline{NI}$	1	1.01

Figure 6.10 shows the Novelty Index (*NI*) and centre line (*CL*) for each year calculated on the basis of frequency estimates in nearly two years. The environmental and operational effects are efficiently removed because no obvious variations of *NI* are noted. It is observed from Table 6.9 that the healthy indicators *CL* in two years are at the same level and the outlier analysis evidences a similar trend. It may be concluded that from June 2010 to March 2011 there is not obvious structural changes, comparing with the reference state from June 2009 to March 2010.

6.4 CONCLUSION

This chapter is focused on investigations for detection of simulated structural damage, on the basis of continuous dynamic monitoring data of two lively footbridges under operational conditions. It begins with the introduction of PCA-based methodology. The general environmental model and geometry interpretation assist to help clarifying the theory of this proposed method.

In Chapter 5, correlation analysis between natural frequencies and temperature, as well as vibration levels, reveals that from the point of view of long term monitoring, temperature has a primary effect on the variations of frequencies, in a linear manner for Pedro e Inês footbridge whereas nonlinear manner for FEUP campus footbridge. Due to the linear influence of environmental and operational factors regarding the Pedro e Inês footbridge, linear PCA naturally is used to remove such adverse effects and simulated damage is successfully detected according to 3 years monitoring results. Moreover, although nonlinear effects of those factors are observed in the long term monitoring results of FEUP campus footbridge, the linear relations between frequencies of different orders indicate the possibility of application of linear

PCA. Such feasibility is validated by the efficiency of removal of environmental effects and detection of simulated damage using nearly two years monitoring results.

7

CONCLUSIONS AND FUTURE WORKS

7.1 CONCLUSIONS

This thesis is focused on the following main points:

- development of LabVIEW based toolkits for OMA and automated OMA;
- implementation of continuous dynamic monitoring systems;
- investigation on a PCA-based damage detection procedure and its application on two existing lively footbridges in Portugal, with the purpose of establishing a vibration-based SHM system for footbridges, capable of not only providing accurate information regarding the long term dynamic behaviour, but also evaluating the current health state of the footbridges under operational conditions.

The main conclusions of this research can be summarized as:

(i) Based on PCB vibration measurement equipments and National Instruments data acquisition and transmission hardware, economical and compact continuous dynamic monitoring systems were implemented in two footbridges and have been operating efficiently for a relatively long period of time. The nearly real-time acceleration signals and ambient temperature information are continuously collected by accelerometers and thermal sensors respectively, and are automatically transmitted through Internet from the bridges to FEUP in Porto, preparing for further processing and analysis;

(ii) Nearly all frontier output-only modal identification methods are summarized. The corresponding theoretical basis is clarified by application to the experimental data from an

ambient vibration test of a metallic frame performed in the laboratory. A toolkit for ambient vibration testing is developed by implementing PP, EFDD, SSI-COV and SSI-DATA methods and is applied to OMA of different bridges. By balancing the efficiency and accuracy of different approaches, a toolkit mainly dedicated to automated OMA is further implemented on the basis of SSI-COV method by interpreting the stabilization diagrams excluding user interactions. Combining with other functions, such as detection of maximum vibration level, evaluation of averaged vibration level and production of waterfall plot, this toolkit becomes an automatic signal processing sub-toolkit that is a core part in vibration-based SHM systems;

(iii) By comparing the frequencies results estimated by OMA of ambient vibration test data of Pinhão bridge before and after rehabilitation, as well as of Pedro e Inês footbridge before and after installation of TMDs, it is concluded that natural frequencies are efficient features reflecting structural modifications. However, the significant environmental effects under operational conditions are also observed by OMA of experimental data of FEUP campus footbridge;

(iv) The serviceability of two footbridges under operational conditions was assessed on the basis of the continuous monitoring data. Regarding the Pedro e Inês footbridge, in Coimbra, the maximum recorded vertical and lateral vibration levels are 0.849m/s^2 and 0.099m/s^2 during 3 years. Comparing with the different comfort limits recommended by HIVOSS and SETRA guidelines, it is found that all maximum lateral and nearly all vertical acceleration fall in the range of the medium comfort acceleration limits. It can be concluded that no serviceability problem is observed in this footbridge under normal operational conditions during these 3 years, as consequence of implementation of the corresponding control devices. For FEUP campus footbridge, the maximum vertical vibration level reached 5.7m/s^2 during one year, certainly induced by vandal loads. In addition, in 352 days of one year the recorded maximum daily vertical vibration levels are clearly below 2.5m/s^2, which mean that unacceptable vertical vibrations do not frequently occur.

(v) The frequency domain analysis of time series collected at these two footbridges shows that the higher levels of vibration recorded are associated to some resonance related with one or more modes of vibration, as some bridge natural frequencies are close to the dominant frequencies of the human-induced excitation. With regard to Pedro e Inês footbridge,

in Coimbra, the main vertical bridge responses are dominated by frequencies at around 3Hz, which not only accords with running or jumping behaviour of pedestrians but also coincides with bridge natural frequencies around 3Hz. While for FEUP campus footbridge the recorded daily maximum vertical vibration signals are mainly dominated by frequency components around 2Hz due to the proximity between step frequencies of walking pedestrians and bridge natural frequencies around 2 Hz.

(vi) Modal parameters are continuously identified automatically by SSI-COV algorithm. Frequencies of a significant number of modes are estimated based on hourly acceleration records from the Pedro e Inês and the FEUP campus footbridges. Statistical analysis of frequency results shows that the maximum relative difference of frequency estimates of Pedro e Inês footbridge varies from 2.7% to 3.9%, far less than the variation of 14%-20.6% of FEUP campus footbridge, meaning that the influence of temperature on modal frequencies is much more relevant in this case. Approximately linear and nonlinear relations between modal frequencies and temperature are observed in these two footbridges. Temperature is also identified as the primary environmental factor affecting variation of frequencies of different modes, though the resonant frequencies of the first two modes of Pedro e Inês footbridge and those of all modes of FEUP campus footbridge are also influenced by the vibration levels;

(vii) An attempt to remove the influences of environmental and operational factors on natural frequency estimates was performed by applying linear PCA and novelty analysis on the residual errors to build a statistical damage indicator for long term structural health monitoring. In the application of Pedro e Inês footbridge, the linear environmental and operational effects are efficiently removed by PCA and simulated progressive damages are successfully detected. Regarding FEUP campus footbridge, PCA-based approach is still effective to remove the observed nonlinear influences of environmental and operational factors due to the high linear relations between frequencies of different orders. Such feasibility is validated by the efficiency of removal of environmental effects and detection of simulated damages using monitoring results in nearly two years.

7.2 FUTURE WORKS

The final purpose of vibration-based SHM is to build a robust, automatic and generally applicable system in order to determine the system health condition and quantify the extent of damage. In the sequence of the present research, the following aspects can be further explored:

(i) A more complete continuous dynamic monitoring system can be developed by integrating more data acquisition hardware in order to provide more complete information regarding the structural response and environmental factors. For example, wind speed measurements are needed in order to investigate the influence of wind on structural dynamic properties. A video camera system can be used to quantify the relation between pedestrian traffic and the structural response under operational conditions. The monitoring of dynamic strain in critical cross sections can be also useful for fatigue assessment.

(ii) An innovative frequency domain modal identification algorithm, p-LSCF, can be implemented in the toolkits for ambient vibration testing and automated OMA considering its better performance in the identification of modal damping ratios. The estimation results can be tested by the continuous dynamic monitoring data from the two footbridges analysed and compared with those from SSI-COV methods in time domain. Furthermore, it has been demonstrated that the automatic identification of modal properties has to be complemented with algorithms for extraction of the influence of environmental variables, like temperature, and operational factors, like the traffic intensity, so that changes of modal parameters can be well correlated with structural damages. It is then expected that a computational model to eliminate the environmental effects, sufficiently robust to work on an on-line or nearly real time basis, can be improved in order to determine the structural health state efficiently and confidently.

(iii) In this thesis, the purpose has been only to detect whether the damage occurs or not, based on resonant frequencies shifts. It would be important to extend the monitoring capabilities, combining the mode shape information and analytical models, trying to localize and quantify the structural damage.

REFERENCE

Akaike, H. (1974) Stochastic Theory of Minimal Realization, *IEEE Transaction on Automatic Control*, AC-19, 667-674.

Allemang, R. J.; Brown, D. L. (1998) A Unified Matrix Polynomial Approach to Modal Identification, *Journal of Sound and Vibration*, 211(3), 301-322.

Andersen, Palle (1997) *Identification of Civil Engineering Structures using Vector ARMA Model*, Ph.D. Thesis, Aalborg University, Denmark, 1997

Aoki M. (1987) *State Space Modelling of Time Series*. Springer-Verlag, Berlin, Germany.

ARTeMIS (2010) *Ambient Response Testing and Modal Identification Software*, Structural Vibration Solution A/S, Alborg, Denmark.[http://www.svibs.com/]

Askegaard, V.; Mossing, P. (1988) Long Term Observation of RC-Bridge using Changes in Natural Frequencies. *Nordic Concrete Research*, 7, 20-27.

Bendat, J.; Piersol, A. (1980) *Engineering Applications of Correlation and Spectral Analysis*. John Wiley & Sons, USA.

Benveniste,A. and Fuche, J.J. (1985) Single Simple Modal Identification of a Nonstationary Stochastic Process, *IEEE Transactions on Automatic Control*, AC-30 (1), 66-74.

Boller, C.; Chang, F.-K.; Fujino, Y. (2009) *Encyclopaedia of Structural Health Monitoring*. Wiley.

Brown, D.L.; Allemang, R.J.; Zimmerman, R.D.; Mergeay, M. (1979) Parameter Estimation Techniques for Modal Analysis, *SAE Paper*, *No.*790221, *SAE Transactions* 88,828-846.

Brincker, R.; Ventura, C.; Andersen, P. (2001) Damping Estimation by Frequency Domain Decomposition. In *Proceedings of IMAC XIX*, Kissimmee, USA.

Brincker, R.; Zhang, L.; Andersen, P. (2000) Modal Identification from Ambient Responses Using Frequency Domain Decomposition. In *Proceedings of IMAC XVIII*, San Antonio, USA.

Caetano, E; Cunha, A (2004) Experimental and numerical assessment of the dynamic behaviour of a stress-ribbon footbridge, *Structural Concrete*, 5(1), 29-38.

Caetano, E; Cunha, A (2005) Study of the potential of collapse of a footbridge under vandal loads, In *IABSE Symposium on Structures and Extreme Events*, Lisbon, Portugal.

Caetano, E.; Cunha, A; Magalhães, F.; Moutinho, C. (2010a) Studies for controlling human-induced vibration of the Pedro e Inês footbridge, Portugal. Part 1: Assessment of dynamic behaviour. *Engineering Structures*, 32(4), 1069-1081.

Caetano, E.; Cunha, A.; Moutinho, C.; Magalhães, F. (2010b) Studies for controlling human-induced vibration at the Pedro e Inês Footbridge, Portugal. Part 2: Implementation of tuned mass dampers. *Engineering Structures*, 32(4), 1082-1091.

Caetano, E.; Cunha, A.; Hoorpah, W; Raoul, J. (2009) *Footbridge Vibration Design*. CRC Press.

Cauberghe, B. (2004) *Applied Frequency-Domain System Identification in the Field of Experimental and Operational Modal Analysis*. PhD Thesis, Vrije Universiteit Brussel, Belgium.

Cooley, J. W.; Tukey, J. W. (1965) An Algorithm for the Machine Calculation of Complex Fourier Series. *Mathematics of Computation*, 19(90), 297-301.

Costa, B; Dimande, A; Félix, C; Figueiras, J (2008) Assessment of Pinhão Bridge Behaviour during the Field Tests Carried Out to Support the Strengthening and Rehabilitation Design, In *the 7th International Conference on Steel Bridges*, Guimarães , Portugal.

Cunha, A.; Caetano, E. (2006) Experimental Modal Analysis of Civil Engineering Structures. *Sound and Vibration*, 6(40), 12-20.

Cunha, A.; Caetano, E.; Magalhães, F. (2007) Output-only Dynamic Testing of Bridges and Special Structures. *Structural Concrete (Fib)*, 8(2), 67-85.

Cunha, A.; Caetano, E.; Moutinho, C.; Magalhães, F. (2005) Damping identification in a stress-ribbon footbridge. In *the proceedings of EURODYN '2005, the 6th European Conference on Structural Dynamics*, Paris, France

Dallard, P.; Fitzpatrick, A.J.; Flint, A.;Le Bourva, S.; Low, A; Ridsdill-Smith, R.M.; Willford, M. (2001) The London Millennium Footbridge. *Structural Engineer* 79 (22), 17–33.

Deraemaeker, A.; Reynders, E.; De Roeck, G.; Kullaa, J. (2008) Vibration-based structural health monitoring using output-only measurements under changing environment. *Mechanical Systems and Signal Processing*, 22(1), 34-56.

Dimande, A; Pimentel, M; Félix, C; Figueiras, J (2011) Monitoring System for Execution Control Applied to a Steel Arch Footbridge, *Structure and Infrastructure Engineering: Maintenance, Management, Life-Cycle Design and Performance*, in press, doi :10.1080/15732471003649585

Ellis, B.R.; Ji, T. (1994) Floor Vibration Induced by Dance-Type Loads: Verification. *The Structural Engineer*, 72(3), 45-50.

ENCIL (1998) *Passagem para Peões-Project Base de Fundaçes e Estruturas*, U.P.Pólo.

Ewins, D. J. (2000) *Modal Testing: Theory and Practice*. Research Studies Press, U.K.

Farrar, C. R.; Doebling, S. W.; Cornwell, P. J.; Straser, E. G. (1997) Variability of Modal Parameters Measured on the Alamosa Canyon Bridge In *Proceedings of IMAC XV*, Orlando, Florida, USA.

Farrar, C.R.; Lieven, N (2007) Damage Prognosis: the Future of Structural Health Monitoring. *Philosophical Transactions of The Royal Society A*, 365, 623-632.

Farrar, C. R.; Worden, K. (2007) An Introduction to Structural Health Monitoring. *Philosophical Transactions of the Royal Society A*, 365, 303-315.

Felber, A. J. (1993) *Development of a Hybrid Bridge Evaluation System*. PhD Thesis, University of British Columbia, Vancouver, Canada.

Friswell M.I. and Mottershead J.E. *Finite Element Model Updating in Structural Dynamics*. Kluwer Academic Publishers, Dordrecht, The Netherlands, 1995.

Fujino, Y.; Abe, M.; Shibuya, H.; Yanagihara, M. ; Sato, M. (2000) Monitoring of Hakucho suspension bridge using ambient vibration. In *Proceedings of Workshop on Research and Monitoring of Long Span Bridges*. Hong Kong, pp. 142–149.

Fukuzono, K. (1986) *Investigation of Multiple Reference Ibrahim Time Domain Modal Parameter Estimation Technique*, M.S. Thesis, Dept. of Mechanical and Industry Engineering, University of Cincinnati.

Giraldo, D.F.; Dyke, S.J. ;Caicedo, J.M. (2006) Damage Detection Accommodating Varying Environmental Conditions. *Structural Health Monitoring*, 5(2), 155-172.

Guillaume, P.; Pintelon, R.; Schoukens, J. Parametric (1996) Identification of Multivariable Systems in the Frequency Domain - A Survey. In *Proceedings of ISMA 21, the International Conference on Noise and Vibration Engineering*, Leuven, Belgium.

Guillaume, P., Verboven, P., and Vanlanduit, S. (1998) Frequency-Domain Maximum Likelihood Identification of Modal Parameters with Confidence Intervals. In *Proceedings of ISMA 23, the International Conference on Noise and Vibration Engineering*, K.U.Leuven, Belgium.

Guillaume P., Hermans L., and Van der Auweraer H. (1999) Maximum Likelihood Identification of Modal Parameters from Operational Data. In *Proceedings of IMAC XVII*, Kissimmee, USA.

Guillaume, P.; Verboven, P.; Vanlanduit, S.; Van der Auweraer, H.; Peeters, B. (2003) A Poly-Reference Implementation of the Least-Squares Complex Frequency-Domain Estimator. In *Proceedings of IMAC XXI*, Kissimmee, USA.

Hermans, L., Guillaume, P., and Van der Auweraer, H. (1998) A Frequency Domain Maximum Likelihood Approach for the Extraction of Modal Parameters from Output-only Data, In *Proceedings of ISMA 23, the International Conference on Noise and Vibration Engineering*, K. U. Leuven, Belgium.

Hermans, L.; Van der Auweraer, H. (1999) Modal Testing and Analysis of Structures under Operational Conditions: Industrial Applications. *Mechanical Systems and Signal Processing*, 13(2), 193-216.

Heylen. W., Lammens. S., and Sas P. (1995) *Modal Analysis Theory and Testing*. Department of Mechanical Engineering, Katholieke Universiteit Leuven, Leuven, Belgium.

HIVOSS (2008) Human Induced Vibrations of Steel Structures: Design of Footbridges Guideline. 31pp.

Ho B.L.; Kalman R.E. (1966) Effective Construction of Linear State-Variable Models from Input/Output Data. *Regelungstechnik*, 14, 545-548.

Hu, W.-H.; Cardoso, A., Magalhães, F.; Caetano, E; Cunha, A. (2010) Environmental Effects on Modal Variability of a Stress-Ribbon Footbridge under Operational Conditions, In *Proceedings of ISMA'2010, the International Conference on Noise and Vibration Engineering*, Leuven, Belgium.

Hu, W.-H.; Caetano, E.; Cunha, A (2007) Experimental Modal Identification: A Toolkit for LabVIEW, In *Proceeding of EVACES'07, the 2nd International Conference on Experimental Vibration Analysis for Civil Engineering Structures*, Porto, Portugal.

Hu, W.-H.; Caetano, E.; Cunha, A (2011) Investigation on damage detection of a stress-ribbon footbridge under operational conditions, In *Proceeding of SMART'11, the 5th ECCOMAS Thematic Conference on Smart Structures and Materials*, Saarbrücken, Germany.

Hu, W.-H.; Cunha, A; Caetano, E; Magalhães, F; Mountinho, C (2010) LabVIEW Toolkits for Output-only Modal Identification and Long-term Dynamic Structural Monitoring. *Structure and Infrastructure Engineering: Maintenance, Management, Life-Cycle Design and Performance*, 6(5), 557-574.

Hu, W.-H.; Moutinho, C. Cunha. A; Caetano E. (2008) A Signal Result Management and Visualization System for Evaluation of Long Term Dynamic Behaviour of Bridges. In *Proceeding EWSHM'08, the 4th European Workshop of Structural Health Monitoring*, Cracow, Poland.

James, G. H.; Carne, T. G.; Lauffer, J. P.; Nard, A. R. (1992) Modal Testing Using Natural Excitation. In *Proceedings of IMAC X*, San Diego, USA.

Juang, J.-N. (1994) *Applied System Identification*. Prentice Hall Englewood Cliffs, New Jersey, USA.

Juang, J.-N.; Pappa, R. S. (1985) An Eigensystem Realization Algorithm for Modal Parameter Identification and Model Reduction. *Journal of Guidance, Control, and Dynamics*, 8(5), 620-627.

Kailath, T., 1980, *Linear Systems*, Prentice-Hall, New Jersey.

Kim, C. Y.; Jung, D. S.; Kim, N. S.; Yoon, J. G. (1999) Effect of Vehicle Mass on the Measured Dynamic Characteristics of Bridges from Traffic-Induced Test. In *Proceedings of IMAC XIX*, Kissimmee, USA.

Kullaa, J. (2001) *Elimination of Environmental Influences from Damage-Sensitive Features in a Structural Health Monitoring System*, in: Fu-Kuo Chang (Ed.), Structural Health Monitoring—the Demands and Challenges, CRC Press, 742–749.

Kullaa, J. (2003) Damage detection of the Z24 bridge using control charts, *Mechanical Systems and Signal Processing*, 17 (1), 163-170.

Kung S.Y. (1978) A New Identification and Model Reduction Algorithm via Singular Value Decomposition. In *Proceedings of the 12th Asilomar Conference on Circuits, Systems and Computers*, pp. 705-714, Asilomar, USA.

LabVIEW,Getting started with LabVIEW. 2010. [http://www.ni.com/]

Liu, C.; DeWolf, J. T. (2007) Effect of Temperature on Modal Variability of a Curved Concrete Bridge under Ambient Loads. *Journal of Structural Engineering*, 133(12), 1742-1751.

Ljung, L. (1999) *System Identification: Theory for the User*. Prentice Hall, New Jersey.

Longman, R.W. and Junag, J.-N. (1989) Recursive Form of the Eigensystem Realization Algorithm for System Identification. *Journal of Guidance, Control and Dynamics* 12, 647-652.

MACEC (2011) *MACEC 3.2: A Matlab Toolbox for Experimental and Operational Modal Analysis User's Manual*, Department of Civil Engineering, Faculty of Engineering, Katholieke Universiteit, Leuven, Belgium. [http://bwk.kuleuven.be/bwm/macec]

Manson,G. (2002) Identifying Damage Sensitive, Environment Insensitive Features for damage detection, In *Proceedings of the 3rd International Conference on Identification in Engineering Systems.* Swansea, UK.

Magalhães, F. (2010) Operational Modal Analysis for Testing and Monitoring of Bridges and Special Structures. Ph.D. Thesis, University of Porto, Portugal.

Magalhães, F; Costa, B; Cunha, A; Caetano E (2006) Experimental Validation of the Finite Element Modeling of Pinhão Bridge, In *the 3rd European Conference on Computational Mechanics: Solids, Structures and Coupled Problems in Engineering,* Lisbon, Portugal.

Magalhães, F.; Caetano, E.; Cunha, A. (2007a) Dynamic Testing of the New Coimbra Footbridge before Implementation of Control Devices. In *Proceedings of IMAC XXIV*, Orlando, Florida, USA.

Maia, N.; Silva, J. (1997) *Theoretical and Experimental Modal Analysis*. Research Studies Press Ltd.

Montgomery, D (2005). *Introduction to Statistical Quality Control*. John Wiley & Sons, Inc.

Moutinho, C.; Hu, W.-H.; Caetano, E.; Cunha, A. (2008) Implementation of a Dynamic Monitoring System at Coimbra Footbridge", *In the Proceedings of IMAC XXVI*, Orlando, Florida, USA.

Ni, Y. Q.; Hua, X. G.; Fan, K. Q.; Ko, J. M. (2005) Correlating Modal Properties with Temperature using Long-term Monitoring Data and Support Vector Machine Technique *Engineering Structures,* 27, 1762-1773.

Parloo, E. (2003) *Application of Frequency-Domain System Identification Techniques in the Field of Operational Modal Analysis*. PhD Thesis, Vrije Universiteit Brussel, Belgium.

Peeters, B. (2000) *System Identification and Damage Detection in Civil Engineering*. PhD Thesis, Katholieke Universiteit Leuven, Belgium.

Peeters, B.; De Roeck, G. (2001) One-year monitoring of the Z24-Bridge: environmental effects versus damage events. *Earthquake Engineering and Structural Dynamics,* 30(2), 149-171.

Peeters, B.; Van der Auweraer, H. (2005) PolyMax: a Revolution in Operational Modal Analysis. In *Proceedings of IOMAC*, Copenhagen, Denmark.

Peeters, B.; Van der Auweraer, H.; Guillaume, P.; Leuridan, J. (2004) The PolyMAX Frequency-Domain Method: a New Standard for Modal Parameters Estimation? *Shock and Vibration* (11), 395-409.

Pintelton R.; J. Schoukens (2001) *System Identification – a Frequency Domain Approach*, IEEE Press, New York.

Prevosto, M. (1982) *Algorithmes D'Identification des Caractéristiques Vibratoires de Structures Mecaniques Complexes*. PhD Thesis, Université de Rennes I, France.

Rainieri, C.; Fabbrocino, G. (2009) Automated Output-Only Dynamic Identification of Civil Engineering Structures. *Mechanical System and Signal Processing*, doi:10.1016/j.ymssp.2009.10.003.

Rohrmann, R. G.; Baessler, M.; Said, S.; Schmid, W.; Ruecker, W. F. (2000) Structural Causes of Temperature Affected Modal Data of Civil Structures Obtained by Long Time Monitoring. In *Proceedings of IMAC 18*, San Antonio, USA.

Rytter A. (1993) *Vibration Based Inspection of Civil Engineering Structures*. PhD thesis, Department of Building Technology and Structural Engineering, Aalborg University, Denmark.

Rücker, W.F.; Said, S.; Rohrmann, R.G. ; Schmid, W. (1995) Load and condition monitoring of a highway bridge in a continuous manner. In *Proceedings of the IABSE Symposium on Extending the Lifespan of Structures*, San Francisco, USA.

SDTools (2008) *Structural Dynamics Toolbox User Guide Version 6.1*, SDTools Company, Paris, France. [http://www.sdtools.com/]

SÉTRA/ AFGC (2006) Footbridges: Assessment of vibrational behaviour of footbridges under pedestrian loads", 131pp.

Shih, C. Y.; Tsuei, Y. G.; Allemang, R. J.; Brown, D. L. (1988) Complex Mode Indicator Function and its Application to Spatial Domain Parameter Estimation. *Mechanical Systems and Signal Processing*, 2(4), 367-377.

Sohn, H. (2007) Effect of environmental and Operational Variability on Structural Health Monitoring. *Philosophical Transactions of the Royal Society*, 365, 539-560.

Sohn, H.; Dzwonczyk, M.; Straser, E.; Kiremidjian, A.; Law, K.; Meng, T. (1999) An Experimental Study of Temperature Effect on Modal Parameters of the Alamosa Canyon Bridge, Earthquake Engineering and Structural Dynamics, 28, 878–897.

Sohn, H.; Farrar, R.; Hemez, M.; Czarnecki, J.; Shunk, D.; Stinemates, W.; Nadler, R. (2003) *A review of Structural Health Monitoring Literature: 1996-2001*. Los Alamos National Laboratory Report, LA-13976-MS, Los Alamos, USA.

SYNPEX (2008) Advanced Load Models for Synchronous Pedestrian Excitation and Optimised Design Guidelines for Steel Footbridges- Final Report, EUR 23318, European Commission, ISBN 978-92-79-08303-7.

Turkey, J.W.; Blackman, R.B. (1959) *The Measurement of Power Spectra*, Dover Publications Incorporated.

Van Overschee, P.; De Moor, B. (1996) *Subspace Identification for Linear Systems*. Kluwer Academic Publishers, Leuven, Belgium.

Verboven, P., (2002) *Frequency Domain System Identification for Modal Analysis*, Ph.D. Thesis, Vrije Universiteit Brussel, Belgium, 2002.

Verboven, P.; Parloo, E.; Guillaume, P.; Van Overmeire, M. (2002) Autonomous Structural Health Monitoring - Part I: Modal Parameter Estimation and Tracking. *Mechanical Systems and Signal Processing*, 16(4), 637-657.

Vold, H; Kundrat, J; Rocklin, T; Russell, R (1982) A Multi-Input Modal Estimation Algorithm for Mini-Computers, *SAE Paper No*. 820194, *SAE Transactions* 91,815-821.

Wahab, M.; De Roeck, G. (1997) Effect of Temperature on Dynamic System Parameters of a Highway Bridge. *Structural Engineering International*, 7(4), 266-270.

Welch, P. D. (1967) The use of Fast Fourier Transform for the Estimation of Power Spectra: a Method based on Time Averaging over short Modified Periodograms. *IEEE Transaction on Audio and Electro-Acoustics*, AU-15(2).

Worden, K; Farrar, C.R. (2007) Structural Health Monitoring. *Philosophical Transactions of the Royal Society*, 365, 299-632.

Worden, K; Manson, G.; Fieller, N.R.J. (2000) Damage detection using outlier analysis. *Journal of Sound and Vibration*. 229, 647-667.

Yan, A.-M.; Kerschen, G.; Boe, P. D.; Golinval, J.-C. (2005a) Structural Damage Diagnosis under varying Environmental Conditions - Part I: A Linear Analysis. *Mechanical Systems and Signal Processing*, 19, 847-864.

Yan, A.-M.; Kerschen, G.; De Boe, P.; Golinval, J.-C. (2005b) Structural damage diagnosis under varying environmental conditions - part II: local PCA for non-linear cases. *Mechanical Systems and Signal Processing*, 19, 865-880.

Zeiger H.P. and McEwen A.J. (1974) Approximate Linear Realization of Given Dimension via Ho's Algorithm. *IEEE Transactions on Automatic Control*, AC-19(2), 153.

Zhang, Q. W., Fan, L. C. & Yuan, W. C. (2002) Traffic-induced variability in dynamic properties of cable-stayed bridge. *Earthquake Engineering and Structural Dynamics*. 31, 2015–2021.

Zhou, H.-F.; Ni, Y.-Q..; Ko, J.-M. (2005) Performance of neural network for simulation and prediction of temperature-induced modal variability. In *Proceeding of Smart Structures and Materials (SPIE)*, Bellingham, USA.

Živanović, S.; Pavic, A.; Reynolds, P. (2005) Vibration Serviceability of Footbridge under Human-Induced Excitation: A Literature Review. *Journal of Sound and Vibration*, 279, 1-74.